

Waveguide lasers in rare earth doped planar silica

A thesis submitted for the degree of Doctor of Philosophy in
the Faculty of Engineering, University of Glasgow.

by

James R. Bonar

September, 1995

© James R. Bonar

ProQuest Number: 13832101

All rights reserved

INFORMATION TO ALL USERS

The quality of this reproduction is dependent upon the quality of the copy submitted.

In the unlikely event that the author did not send a complete manuscript and there are missing pages, these will be noted. Also, if material had to be removed, a note will indicate the deletion.



ProQuest 13832101

Published by ProQuest LLC (2019). Copyright of the Dissertation is held by the Author.

All rights reserved.

This work is protected against unauthorized copying under Title 17, United States Code
Microform Edition © ProQuest LLC.

ProQuest LLC.
789 East Eisenhower Parkway
P.O. Box 1346
Ann Arbor, MI 48106 – 1346

Thesis
10388
Cp 1

GLASGOW
UNIVERSITY
LIBRARY

This thesis is dedicated to my family.

Acknowledgements

I would like to express my extreme gratitude to my academic supervisor and friend Dr Stewart Aitchison. His constant help and enthusiasm have been invaluable throughout the duration of the project. I would also like to thank Professor P. J. R. Laybourn for the use of the facilities in the Department of Electronics and Electrical Engineering.

Special thanks go to my industrial supervisors Dr Graeme Maxwell and Jim Ainslie at BT Laboratories, Ipswich. Their assistance far exceeded that required of any industrial supervisor. I would also like to thank Graeme, for feeding me on a Thursday night, whilst working at BT, for the small sum of a bottle of wine.

The technical support given during the project was first class and I would like to extend my thanks to Tom Wright and his staff.

In particular I would like to thank Ian McNicholl, Jimmy Young and Tommy Cairns for the maintenance and up-grade of the flame hydrolysis deposition equipment. Ian is thanked for his marriage guidance counselling. Many thanks to Kas Piechowiak for his expertise in cutting and polishing of waveguides. I would also like to acknowledge Dougie Irons and 'the boys' in the mechanical workshop. Special thanks to Hugh Moy and Joe Smith for their joviality and encouragement. All the cleanroom staff are thanked for their help. In particular Joan Carson. Jim Gray is acknowledged for his help with the laser systems, even although he tried to undermine my golf game by losing my clubs. Robert Harkins his golfing partner in crime, is also recognised for his valuable assistance in the production of masks. All the people in the dry etch section and the electronic workshop are thanked for their help. In particular Peter McKenna. Laurence Bradley is also thanked for providing the tea-break facilities and for his banter.

I have made many friends during my studies and I would like to thank them all for making my stay at Glasgow University enjoyable, especially on a Friday night. A special thanks to my colleague John Bebbington, for his help and advice and for being such a good friend.

Financial support was provided by a Science and Engineering Research Council Case award with BT Laboratories, which is gratefully acknowledged.

I would especially like to thank my family for their constant support throughout my 'long' academic career. My wife Gillian is thanked for her love, patience and provision of hot dinners.

Jim Bonar.

Abstract

The aim of this project was to realise rare earth doped silica waveguide lasers. Particular attention was focused on the doping of the neodymium and erbium ions into the host glass.

The host glass employed to fabricate low loss rare earth doped devices was based on the binary $\text{SiO}_2\text{-P}_2\text{O}_5$ system. This was fabricated by the flame hydrolysis of SiCl_4 and PCl_3 . This was subsequently updated for the metal halide POCl_3 . The deposited soot from the hydrolysis reaction was typically sintered at temperatures of $1375\text{ }^\circ\text{C}$ in a furnace for time durations of 15 minutes to produce high quality, low loss planar waveguides.

To form suitable cladding material for both passive and active devices, research concentrated on $\text{SiO}_2\text{-P}_2\text{O}_5\text{-B}_2\text{O}_3$ glass films. As a result, suitable cladding layers were possible which were thick ($20\text{ }\mu\text{m}$), index matched to the buffer and possessed low sintering temperatures ($1100\text{ }^\circ\text{C}$).

Rare earth doping of the $\text{SiO}_2\text{-P}_2\text{O}_5$ films was based on two techniques, namely solution and aerosol doping. The aerosol technique was developed during the project. Comparisons were drawn between the two techniques. For both techniques the loss of the planar films was dependent on the fabrication conditions. In particular it was found to be dependent on the P_2O_5 codoping level, the thermal history of the sample and the rare earth concentration. Aerosol doping a one step procedure, although still a relatively immature technique, also offered more flexibility in relation to selective area doping.

Ridge waveguides were fabricated employing a combination of photolithographic and reactive ion etching techniques. As a result, it was possible to produce low loss channel waveguides with reduced etch wall roughness. Further investigations resulted in large etch rates. The insertion loss of doped channel waveguides 6 cm long was measured to be as low as 1.5 dB at 632.8 nm.

Optical assessment of the rare earth doped channel waveguides included fluorescence, absorption and fluorescence lifetime measurements. The lifetime measurements

supplied important information pertaining to the ion-ion interactions. Consequently, doping levels and codopant material were studied to provide the optimum devices.

As a result of the optical assessment, Nd^{3+} doped silica waveguide lasers were fabricated using both the solution and aerosol doping techniques. The solution doped sample exhibited a lower threshold and a higher slope efficiency than compared to other similar reported devices. The first successful demonstration of a Nd^{3+} doped silica waveguide laser fabricated by aerosol doping was also observed. Finally, a long path length Er^{3+} doped silica waveguide laser was fabricated by the solution technique.

Index

Acknowledgements

Abstract

Chapter 1	Introduction	1
1.1	Introduction	1
1.2	Thesis outline	2
	References	4
Chapter 2	Flame Hydrolysis Deposition	5
2.1	Introduction	5
2.2	Fabrication methods for silica fibres	5
	2.2.1 Modified chemical vapour deposition (MCVD)	6
	2.2.2 Outside vapour deposition (OVD)	7
	2.2.3 Vapour axial deposition (VAD)	8
2.3	FHD technology and system	9
	2.3.1 Gas supply	10
	2.3.2 Chemical cabinet	12
	2.3.3 Deposition chamber	13
	2.3.4 Scrubber unit	20
	2.3.5 Consolidation furnace	20
2.4	Conclusions	22
	References	23
Chapter 3	Fabrication of planar waveguides - material and optical analysis	26
3.1	Introduction	26
3.2	Synthesis, deposition and sintering of fine glass particles	29
3.3	Binary $\text{SiO}_2\text{-P}_2\text{O}_5$ glass system	32
3.4	Binary $\text{SiO}_2\text{-B}_2\text{O}_3$ glass system	37
3.5	Ternary $\text{SiO}_2\text{-GeO}_2\text{-B}_2\text{O}_3$ glass system	45

3.6	Conclusions	46
	References	48
Chapter 4	Channel waveguide fabrication and assessment	50
4.1	Introduction	50
4.2	Planar waveguide fabrication	50
	4.2.1 Sample preparation	50
	4.2.2 Deposition process	51
	4.2.3 Assessment of planar waveguides	53
4.3	Photolithography	65
4.4	Reactive ion etching (RIE)	71
	4.4.1 CHF ₃ etch	73
	4.4.2 C ₂ F ₆ + O ₂ etch	75
	4.4.3 CHF ₃ + C ₂ F ₆ etch	76
4.5	Waveguide cutting and polishing processes	78
4.6	Channel waveguide loss measurements	80
4.7	Summary	83
	References	85
Chapter 5	Assessment of techniques for rare earth doping	87
5.1	Introduction	87
5.2	Rare earth doped fibres	88
	5.2.1 Solution doping	88
	5.2.2 Volatile halide methods	89
	5.2.3 Aerosol doping	90
	5.2.4 Rod-in-tube method	90
5.3	Rare earth doping of planar waveguides	90
	5.3.1 Solution doping	92
	5.3.2 Aerosol doping	96
	5.3.3 Optical properties of rare earth doped waveguides	97
	5.3.4 Electron microprobe	113
	5.3.5 Lifetime results	117
	5.3.6 Nd ³⁺ doped planar waveguide lasers	123
	5.3.7 Er ³⁺ doped planar waveguide laser	134
	References	138

Chapter 6	Monolithic integration for future rare earth doped silica waveguide devices	144
6.1	Introduction	144
6.2	Grating devices	144
	6.2.1 Introduction	144
	6.2.2 Holographic system	147
	6.2.3 Electron beam system	149
6.3	Selective area doping	155
6.4	Waveguide devices	158
	6.4.1 Multimode interference (MMI) couplers	158
	6.4.2 Ring resonators	161
	References	166
Chapter 7	Conclusions and future work	168
7.1	Conclusions	168
7.2	Future work	173
	References	175

Chapter 1 Introduction

1.1 Introduction

It was not until 1966 that serious attention was paid to the idea of an optical communication system based on the propagation of light within circular dielectric waveguides¹. This concept took a long time to be developed, considering that in 1870, John Tyndall demonstrated light could be guided within a water jet².

At the present time, optical fibres, based on fused silica, are the transmission medium of choice for long distance, high bit rate transmission in telecommunications networks. The improvements in glass fibre quality and semiconductor laser reliability have made possible the information superhighway. It is envisaged that services such as telepresence, teleconferencing and multimedia will become more common in both the work and home environments. To provide such services an inexpensive and robust technology will be needed, to perform all optical signal processing functions. Silica based planar lightwave circuits (PLC) offers this capability.

The term Integrated Optics (IO) was first introduced by S. E. Miller of Bell Laboratories based on the concept of optical circuits³. Subsequently, PLCs have been fabricated in various materials. The major market driving forces in the adaptation to PLCs into an optical network are cost, performance, reliability and mass production. Such PLCs can be fabricated by a combination of flame hydrolysis deposition (FHD) and reactive ion etching (RIE). The optical waveguides fabricated have the added advantages of high quality which are low loss and compatible with fibre. The fabrication technique enables precise control of the waveguide structure such that the field overlap between the modes of the fibre and the waveguide are similar resulting in low waveguide to fibre coupling losses. It is also a relatively simple process to fibre pigtail devices for packaging, as V-grooves can be precisely defined in the Si substrate using anisotropic etching⁴. Moreover, FHD procedures can be modified to produce monolithically integrated active and passive structures.

1.2 Thesis outline

The objectives of this thesis were to fabricate and characterise rare earth doped silica waveguide lasers. The flame hydrolysis deposition (FHD) technique was employed to fabricate silica waveguides. Two methods were developed for incorporation of rare earth ions into the glass matrix. Subsequently, analysis was performed to compare the two techniques.

Chapter 2 reviews several fabrication methods for silica fibres. The development from the fibre technology to a planar format using the flame hydrolysis deposition (FHD) technique is highlighted. An in depth analysis of the FHD apparatus is presented. The developments undertaken on the system to provide safe and reproducible depositions are described in detail.

The fabrication of high silica planar waveguides are described in Chapter 3. In particular, results are presented for phosphosilicate and borosilicate binary glass systems. The optimisation of the fabrication procedures to produce low loss, bubble free waveguides are described. Particular attention is given to the deposition and sintering conditions.

Optical inspection of silica based planar waveguides are detailed in Chapter 4. Techniques are defined for swift qualitative measurements. The fabrication of channel waveguides is illustrated. Photolithographic, reactive ion etching and sawing processes are reported. RIE processes to provide relative high etch rates are also detailed.

Chapter 5 details the optical properties of rare earth doped silica channel waveguides. A review is given for both rare earth doped fibre and planar manufacture. Solution doping and aerosol doping (the latter was a technique developed during the course of this study), are described. Particular emphasis is placed on aerosol doping and analysis undertaken to compare it to the more established solution doping process. The doping parameters are optimised to reduce ion-ion interactions for both techniques. Consequently, the first successful demonstration of a neodymium doped silica waveguide laser fabricated by aerosol doping is described. Results are also presented for both neodymium and erbium doped silica waveguide lasers formed by solution doping.

Chapter 6 describes work on various passive components. Bragg reflectors based on etched gratings are described. Selective area doping to facilitate monolithic integration

Chapter 1 Introduction

of passive and active functions are illustrated. Design and fabrication conditions for multimode interference couplers, ring resonators and integrated optic waveguide pressure sensors are also detailed.

Finally, in Chapter 7, a summary of the thesis is presented, and suggestions for future work are given.

References

- 1 Kao K. C. and Hockham G. A., Proc. IEEE, 1966, **113**, 1151.
- 2 Tyndall J., Royal Institution of Great Britain Proceedings, 1870-1872, **6**, 189.
- 3 Miller S. E., Bell Syst. Tech. J., 1969, **48**, 2059.
- 4 Bean K. E., IEEE Trans. on Electron Devices, 1978, **ED -25**, 1185.

Chapter 2 Flame hydrolysis deposition

2.1 Introduction

The advent of optical fibre communications and the phenomenal growth achieved over recent years have resulted in a growing demand for fibre compatible planar lightwave circuits (PLC's). Flame hydrolysis deposition (FHD) has been one of the main techniques investigated for both active and passive functions. This produces high silica content waveguides with tailored indexes and dimensions to match that of fibres. Already, devices such as 1x8 splitters are openly available on the market¹.

The fabrication of planar silica samples by FHD is an adaptation of fibre preform techniques. The technique is basically a Chemical Vapour Deposition (CVD) process. The starting materials consist of volatile halides, e.g. PCl_3 , POCl_3 , BCl_3 and GeCl_4 . Using such volatile metal chlorides ensures added purity since any absorption by transition metals is negligible owing to their smaller saturated vapour pressure.

2.2 Fabrication methods for silica fibres

Transparent articles of silica fabricated at low temperatures with a high degree of purity originated with the work of Hyde in the early 1930's². This was an outside process involving flame hydrolysis of SiCl_4 and other dopant precursors. However, the first attempts at forming multicomponent high-purity glass fibres involved the so-called double-crucible technique³. Conventional glass melting was adapted to specially prepared soda-lime-silica and sodium borosilicate glasses. To provide high purity silica, transition metals such as iron and copper, the two principal contaminants, were reduced using ion exchange, electrolysis or solvent extraction until the levels were below parts per billion.

Contamination during the glass melting stage raised the level of impurities. Some degree of improvement was obtained by optimising the process, the result was losses of lower than 5 dB/km at 0.9 μm . However, low losses were not achieved in the 1.3 to 1.55 μm spectral region. The major problem was caused by severe OH^- inclusion, which resulted in absorption bands. Subsequently, this technique was superseded by vapour deposition techniques, to produce silica glasses.

As mentioned interest evolved from the outside process with two technologies- outside vapour deposition (OVD)⁴ and vapour axial deposition (VAD)⁵ developed. Simultaneously, inside processes based on chemical vapour deposition (CVD) methods used in the electronics industries, resulted in the modified chemical vapour deposition (MCVD) process⁶.

2.2.1 Modified chemical vapour deposition (MCVD)

Bell Laboratories developed the MCVD process for optical fibre fabrication, adopting the thin SiO₂ process used in the semiconductor industry⁷. The MCVD process was developed to overcome the problems of uniform soot thickness and OH⁻ contamination.

MCVD technique was derived from a combination of the CVD process and inside soot deposition (ISD) process. The technique involves a silica glass tube rotating on a glass working lathe. High-purity metal halides are injected into a rotating tube, the vapours being transported by oxygen gas. An oxy-hydrogen flame is traversed along the outside of the tube at temperatures of typically 1500 - 1650 °C. Figure 2.1 illustrates the basic principle for making MCVD fibres. During each traversal a homogeneous gas reaction takes place, the halide vapour materials are oxidised to fine glass particles in the hot zone and deposited downstream on the inner surface of the silica tube. The temperature of the flame is high enough to sinter the fine glass particles but low enough not to deform the tube. Finally, the tube is thermally collapsed, with the deposited silica

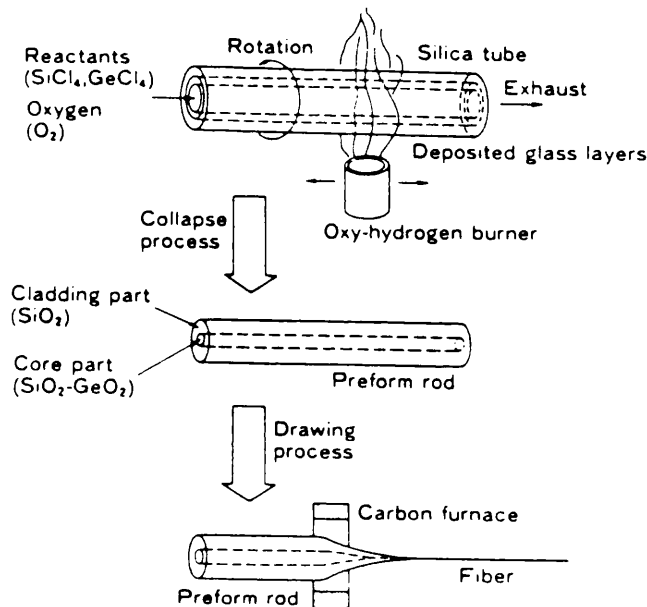


Figure 2.1 MCVD process for making fibres taken from ref. 28.

Chapter 2 Flame hydrolysis deposition

forming the core and the silica tube the outer cladding. The preform is then subsequently drawn into a fibre in a high temperature furnace.

MCVD results in low loss fibres since the material is essentially hydroxyl-free⁸. The halide vapours are easily tailored to give either step-index or graded-index fibres. Single-mode operation is also possible with precise core sizes and refractive indexes defined⁹.

2.2.2 Outside vapour deposition (OVD)

OVD is one of two outside processes. This was developed by Corning Glass Works and produced the first successful high silica fibre. A schematic of the process is shown in Figure 2.2. A vapour mixture of halides is reacted in an oxy-hydrogen flame to form a glass soot which is deposited on a rotating mandrel. The temperature is sufficiently high to partially sinter the particles and form a porous silica layer. The mandrel also traverses the lathe enabling the glass particles to be controlled layer by layer and thus allowing step-index and graded-index fibres to be readily achieved.

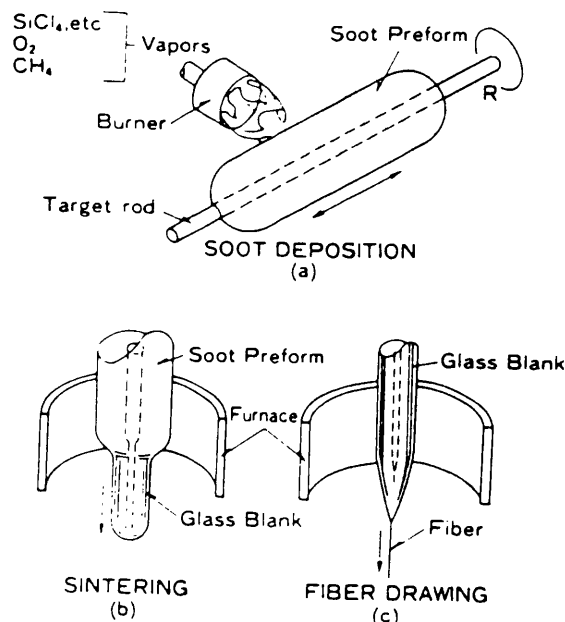


Figure 2.2 OVD process for making fibres taken from ref. 28.

After the deposition is complete the porous preform is slipped off the ceramic mandrel and sintered to form a transparent preform. Care must be taken when removing the rod

from the porous preform to avoid cracking taking place. For this process it is also necessary to grow the cladding material, which is typically undoped SiO_2 . The preform is then drawn into a fibre.

2.2.3 Vapour axial deposition

The VAD technique was developed by a consortium of Japanese cable makers and The Nippon Telephone and Telegraph Corporation. This process was developed from OVD and introduced simplified fabrication processes and fibre preform mass production.

The VAD process is an axial method with the soot deposited end on as shown in Figure 2.3. Once again halide materials blown from an oxy-hydrogen torch are oxidised to form a soot by flame hydrolysis. However, two torches are used to simultaneously deposit the core and cladding glasses onto the end of a rotating target rod. Consequently the preform does not have a central hole as is the case for OVD. The fibre preform is then retracted slowly through a high temperature furnace for consolidation. The thermal mismatch between core and cladding is resolved for this process.

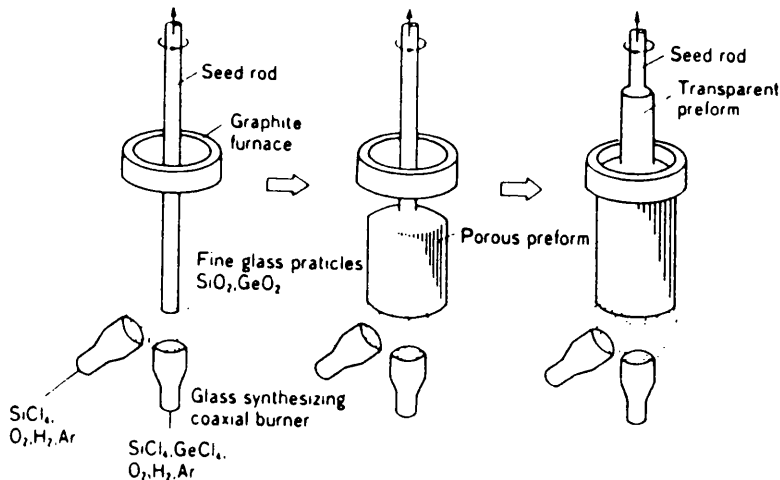


Figure 2.3 VAD process for making fibres taken from ref. 28.

2.3 FHD technology and system

FHD is a technology developed from the outside fibre preform techniques and modified to produce a planar waveguide geometry¹⁰. The high-silica technology offers the potential of integrating a number of passive functions on a silicon chip, as well as the possibility of hybrid integration of both active and passive devices onto a silicon motherboard¹¹. Integrated optics, in the form of these planar lightwave circuits (PLCs), offer ruggedness, mass producibility and low cost compared to bulk-optic and fibre-optic configurations.

To form silica-based PLCs various techniques have been employed. Instead of giving a thorough description to all the techniques developed the interested reader is referenced to a suitable publication¹². Some of the successful technologies have been ion-exchange in glass¹³, plasma enhanced CVD (PECVD)¹⁴, low pressure CVD (LPCVD)¹⁵, high pressure oxidation (HIPOX)¹⁶ and plasma activated CVD (PACVD)¹⁷. Developments have also taken place in polymer waveguides in recent years¹⁸.

FHD offers many features which are attractive for the fabrication of integrated-optic components. It lends itself to planar integrated circuits due to its well controlled core dimensions and index profile which can be matched to standard fibre technology¹⁹. It is also an inexpensive technique suitable for batch processing, and is also compatible with microelectronics industry. The devices themselves are reproducible and involve only a few fabrication steps, with photolithography, etching annealing etc. adapted from the microelectronics industry. The silicon which is used as a substrate, allows the production of aligned V-grooves for passive waveguide to fibre coupling²⁰. The silica can be doped with rare earths, such as neodymium and erbium, to produce active regions which enable planar laser and amplifiers to be fabricated^{21,22}. Such devices have potential applications as transparent splitters, delay lines and integrated lasers. Selective area doping is also possible offering the integration of passive and active silica devices on the same silicon motherboard. Other positive aspects are the flexibility in the thickness which range from 2 μm to 200 μm , and the thick cladding layers which can be deposited to completely bury etched waveguides²³. Vertical integration has also been demonstrated²⁴, potentially increasing the number of functions on a chip as well as waveguides with circular cross-sections which decrease the coupling losses to fibres²⁵. It is therefore, no surprise that with all these advantages, that the high-silica technology has received a lot of attention by the optoelectronics researchers. The improved performance over existing technologies has attracted industrial investment and resulted

Chapter 2 Flame hydrolysis deposition

in this technology developing from the prototype stage, to the point where packaged devices such as 1xN splitters are available.

The next section intends to give the reader a detailed overview of the FHD system developed and maintained by the author. A brief introduction is however presented. The required reagents are transported to the deposition chamber using an inert carrier gas. The subsequent raw material vapours are fed into an oxy/ hydrogen torch. Fine glass particles synthesised by flame hydrolysis are deposited directly onto suitable substrates placed on a turntable. The deposited soot is then removed to a furnace for consolidation into a transparent film. Consolidation using CO₂ lasers is also possible due to the glass being deposited in the form of fine particles²⁶. A picture of the deposition laboratory is given in Figure 2.4.

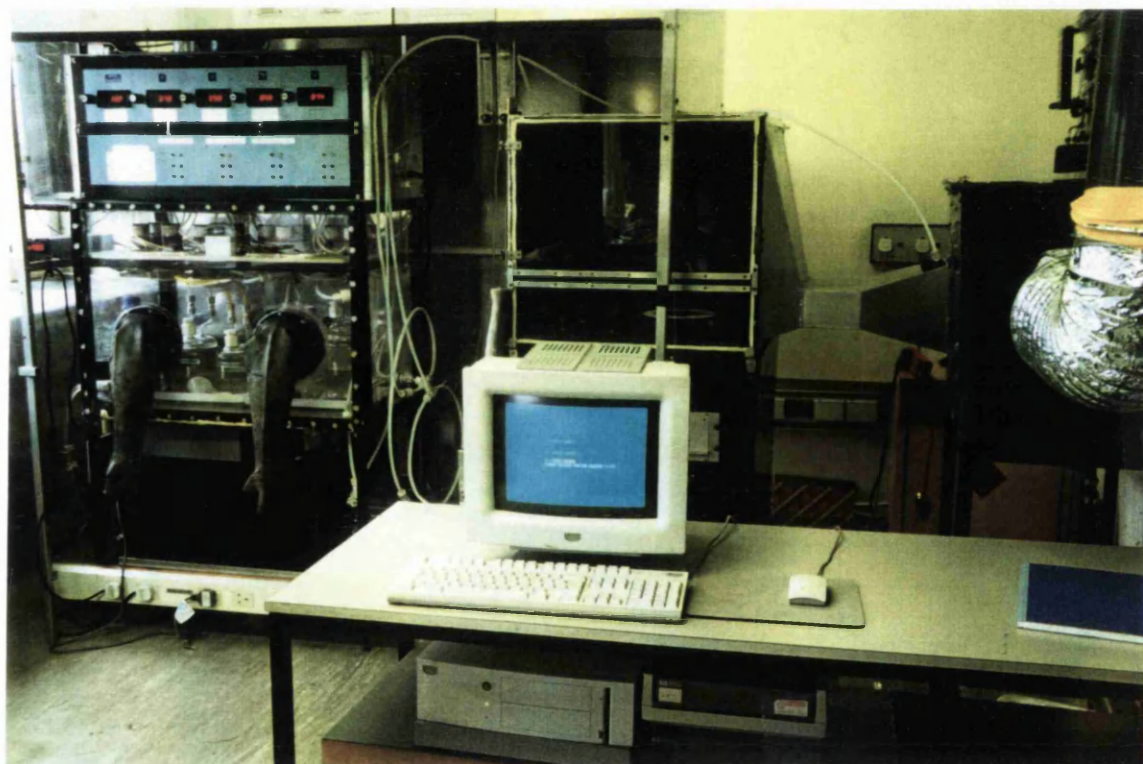


Figure 2.4 FHD laboratory.

2.3.1 Gas supply

For FHD it is important that the chemical cabinet, where the metal halides are housed is permanently purged to produce a 'dry' atmosphere. This is a preventive method to stop hydrolysis of the reactive compounds taking place as well as flushing the chemical box of residual vapours for when the Drechsel bottles are refilled. The cabinet purging line is installed with a flow regulator, allowing the flow rate to be temporarily increased after the refilling operation. This is possible, with an electronic switch over system

allowing two of four bottles to continually supply the cabinet with zero grade nitrogen at a constant pressure of 50 psi allowing two empty bottles to be replaced whilst other two continue to supply. The necessary solenoids, regulators and stainless steel piping are installed and frequently tested. The mass flow controllers (MFCs) are supplied with N_2 ensuring that there is always a positive pressure and that no moisture is fed down the pipes from the oxy-hydrogen torch to cause hydrolysis. A picture of the nitrogen supply and electronic switch gear is shown in Figure 2.5.



Figure 2.5 Nitrogen gas supply assembly.

Zero grade nitrogen is also used as the carrier gas for the halides, the quality of the gas ensuring that the risk of hydrolysis within the piping is minimised preventing the unwanted hydrolysis and blockage of the pipework. Economically, it is found that the system can supply the system for approximately six continuous days at the standard pressure of 50 psi and at a flow rate of 4 l/min. For future development dryers have been incorporated into the gas supply which can filter out particle sizes of 2 μm thus,

Chapter 2 Flame hydrolysis deposition

allowing the incorporation of cheaper standard nitrogen grade bottles or the installation of a N₂ compressor. At the moment the dryers are by-passed.

Hydrogen and oxygen, the necessary gases for hydrolysis, are installed with the relevant safety precautions followed such as the hydrogen and oxygen are stored in separate rooms. The pipework is made from stainless steel as are the regulators. Flash-arrestors are fixed in the line to prevent catastrophic accidents. Helium is supplied to the deposition laboratory, this is fed to the furnace to aid consolidation of the soot layers, as described in subsequent chapters.

2.3.2 Chemical cabinet

The chemical cabinet consists of a sealed perspex box which contains the metal halides. The cabinet is sealed using silicone sealant, sticky ribbon and silicone rubber. Numerous screws are fitted to give a good seal. The cabinet is permanently purged with N₂ and the temperature is maintained at 23 °C using a heater and thermostat, this prevents condensation and hydrolysis taking place in the pipes.

Optipur grade halides are kept in Drechsel bottles. The bottles are placed on a PTFE tray for spillage purposes. Silicone oil is pumped round the bottles at 20 °C to maintain the same vapour pressure within the bottles. A reservoir is used for filling the oil, this is necessary to allow any air bubbles trapped in the system to be removed as this would damage the flow heater. The temperature is constant so that the N₂ flow rate can be set and the relevant vapour transport calculated. The relation for the chloride vapour transported by the nitrogen from the Drechsel bottles, F_v, is given by:

$$F_v = (F \times V) / (P - V)$$

where,

F is the carrier gas flow (N₂)

V is the saturated vapour pressure of the metal chloride

P is the pressure above the halides.

All pipe fittings within the cabinet are formed from polytetrafluoroethylene (PTFE). Sil type fittings with ferrule assemblies incorporating a Viton 'O' ring are used for improved coupling. PTFE check-valves are placed in the input to each bottle to ensure that no return vapour is allowed into the system to attack the pneumatic bellow valves (PBV's) and mass flow controllers. The bellow valves situated within are a special type, the central assembly being made from polyvinylidene fluoride (PVDF). This material was used due to the chlorides corroding the normal stainless steel design. Solenoid

Chapter 2 Flame hydrolysis deposition

valves were used to direct the gas flow through the valves. The control gas for the PBV's is once again N_2 which is either directed to the bubblers, or the waste. The PBV to the waste is normally in the open position whilst both the inlet and outlet to the bubblers are in a normally closed position for safety reasons. Only, during a deposition are the PBV's changed.

The cabinet is fitted with detachable rubber gloves for working within the cabinet. This is to protect the operator from the corrosive halides, when bottles are refilled or piping replaced. Tools for the removal of piping and lids are housed within the cabinet, spare halide solutions are also kept within, as well as sodium carbonate for the neutralisation of spillages.

Above the cabinet the mass flow controllers (MFC's), digital volt meters and check valves are placed. Check-valves are fitted before the MFC's ensuring uni-directional of the gas flow. The MFC's are designed to give a precisely controllable laminar flow with fast response times. A solenoid valve controlled by a dc voltage is used to alter the flow rate. The outputs are displayed on digital voltmeters indicating the amount of N_2 carrier gas being bubbled through the bubblers. An MFC acting as a master is installed, this ensures that the piping is dry, residual vapours are removed to a halide collecting bottle and that a positive pressure is always set up in the halides gas line i.e. prevents moisture infiltration from the open gas line end. A manometer is used to measure the pressure of the N_2 , to indicate partial or complete blockage. The flow rate to the torch is always maintained at a standard 850 sccm, the master being altered to give the desired flow rate. A picture of the chemical and mass flow cabinets is given in Figure 2.6.

2.3.3 Deposition chamber

The reaction phase of the FHD deposition takes place in the deposition chamber. The chamber consists of a transparent Perspex door, which is hinged allowing the operator complete access for cleaning, fitting and removal of the torch. The door is also designed with a flap for loading and unloading the samples (Figure 2.7). This ensures added cleanliness with the removal of sliding parts which in the past have caused contamination. The flap is sealed tightly when performing a deposition. The remaining panels are coated in Xylan, a commercial coating which is resistant to HCl, the main by-product of the reaction. In an effort to increase the yield of quality samples as much as possible, the equipment within the chamber was designed to withstand the HCl, thus reducing the risk of contamination within the chamber.

Chapter 2 Flame hydrolysis deposition

The holder for the torch is manufactured from anodised aluminium and the screws from nylon. Flexible tubing feeds the halides, hydrogen, oxygen and shrouding gas to the silica torch. Various torches from two suppliers - Heraeus (Wickbold burner) and Baumbach are used, depending on the application. The basics of the design is that there is at least three concentric tubes. The middle orifice is fed with the halides whilst the next two are fed with H_2 and O_2 respectively²⁷. For passive depositions it was discovered that this was the optimum combination since it resulted in the least turbulent



Figure 2.6 Chemical and mass flow cabinets.

flame and complete hydrolysis of the metal chlorides. Nozzles for the Wickbold burners were designed to give directionality to the flame. These were modified to have a narrowing in the waist which improved the flame shape and thus, the deposition quality. The Baumbach burners were discovered to produce comparable results, but at a fraction of the cost. A fourth port was also incorporated into both torch designs to act

as a shroud. N_2 gas is fed to this extra port, effectively shaping the flame and preventing the temperature of the torch nozzle rising to a level where it devitrifies and contaminates the deposited layers. A selection of torches and nozzles are illustrated in Figures 2.8a, b, c and d. Figures 2.9a and b, illustrates the focusing effect of the nozzle on the flame. However a more complete analysis is given later into the reasons for the different designs and the results obtained.



Figure 2.7 Deposition chamber.

A laminar air flow is created in the chamber by having a filtered aperture opposite the extract. This reduces chaotic eddy flows which would result in a turbulent flame and hence uneven depositions. The exhaust system removes the by-product gases HCl and H_2O formed by flame hydrolysis. The extract is situated in line with the torch and deposition table. To create a better extract and a constant extract rate along the torch

traversal an Al-anodised local extract is employed²⁸. This stabilisation technique offers reduced fluctuations in both the deposition thickness and refractive index parameters owing to the steady flame produced across the complete traversal length.

Various turntables are employed for depositing the soot on to numerous substrates. The most common one employed is a silicon carbide turntable, which is very robust and stands up to both the corrosive HCl and the high temperature of the flame. This provides carriage for three 3" wafers and three 30 mm diameter substrates. Typically, 3" silicon substrates with a 10 μm thermally grown oxide layer are employed although other substrates such as 4" or 30 mm Homosil grade silica discs are used for some applications. These are placed on anodised aluminium turntables of varying sizes, the recesses of which are machined to the correct sizes for carriage.

Underneath the turntable there is a heater to facilitate temperature control and provide substrate temperatures which prevent crystalline structures being formed. A variable transformer to control the temperatures is housed under the hard aluminium anodised base plate. An electric fan is also situated below the base plate to prevent overheating of the electrics situated adjacent to the transformer. The electronics housed here consist of two Digiplan stepper motors, the power supplies and control units. The control units are connected to an Ambra 386 PC using a National Instruments interface card. One stepper motor controls the torch traverse whilst the other controls the turntable rotation.



Figure 2.8a Wickbold torch for passive depositions.



Figure 2.8b Baumbach torch for passive depositions.



Figure 2.8c Modified Baumbach torch for active depositions.



Figure 2.8d Fused quartz nozzles.



Figure 2.9a Flame shape without nozzle.



Figure 2.9b Flame shape with nozzle.

As the torch traverses along the rotating turntable the velocity increases as a function of $1 / R$, where R is the radius of curvature. This results in non-uniform layers across the sample. As the radius decreases the period between the sample being exposed to the torch is decreased and as a result a thicker layer is deposited. Consequently a 17% variation in thickness across a 3" wafer is measured for samples deposited with a constant deposition rate. To overcome this, the torch traversal speed is incremented during the deposition as an inverse function of the radii. Results measured a thickness variation of only 4% across a 3" wafer and banding across the wafer, which can be seen by the eye, was not as pronounced.

The torch is fixed to anodised aluminium posts by employing a holder fabricated from nylatron (black nylon), which is easily machined and resistant to the HCl by-product. The pipes carrying the relevant gases are always fixed in the same position by a nylon holder which is machined to accommodate five gas pipes. The pipes themselves consist of flexible Nalgene™ tubing which are connected to the PTFE feed pipes by PTFE couplings. The flexibility prevents tension damaging the pipes. To ensure good coupling to the torch pipes, PTFE tape is used as a sealant. PTFE tape is preferred as there is no oil base which can ignite spontaneously in the presence of oxygen.

2.3.4 Scrubber unit

As mentioned above HCl is a by-product of hydrolysis. This is extracted by a centrifugal fan to a scrubber system illustrated in Figure 2.10. The scrubber is placed between the deposition chamber and the fan. It is made from a plastic design with alternate spray bars and baffles. The extracted vapour is carried over the baffles and through the spray. A pump with a titanium shaft is used to transport the water round the closed loop system to the spray bars. To form a fine mist, high pressure air is supplied which dissolves the HCl. The scrubber is fitted with a drain so that the water can be drained after every deposition and refilled without the acidity of the water becoming too high. This ensures that the scrubber can remain closed and that the seals within the pump are not corroded either from the acidity or the alkali which would have to be added for a neutral base. To ensure that either the spray bars are not blocked or that a mist is being formed a perspex panel top is used and attached with numerous screws. This enables inspection and access to the scrubber chamber. An overflow facility was also introduced into the design to prevent the possibility of flooding.

2.3.5 Consolidation furnace

The final part of the process in planar silica fabrication is the consolidation of the deposited low density silica soot. A vertical loading MF 206 furnace illustrated in Figure 2.11 is used for this part of the process. This replaced a SSL model SC 105/46/1600 furnace which was limited to only one 3" wafer processing at a time owing to the horizontal geometry. The same controller was adapted to the new model which allows programmable temperature control. Due to the compact nature of the furnace and the close proximity of the thermocouple the temperature displayed and the temperature actually measured with a Platinum / Platinum 13% Rhodium thermocouple in the centre of the chamber was typically accurate to 5 °C over the working temperature range. This is in comparison to the old furnace model which had a temperature difference of > 120 °C between the set point temperature on the controller and the value of measured temperature²⁹.

Specially designed quartz carriages, shown in Figure 2.12 were purchased enabling seven 3" wafers to be loaded for batch processing. This effectively allows the user to simultaneously fabricate samples for devices and samples for material analysis in a single run. Wafers can be placed above deposited samples to reduce the risk of contamination from the devitrification of silica furnace liners, which tended to cause quartz particles to drop onto the horizontally supported samples. Also, owing to the

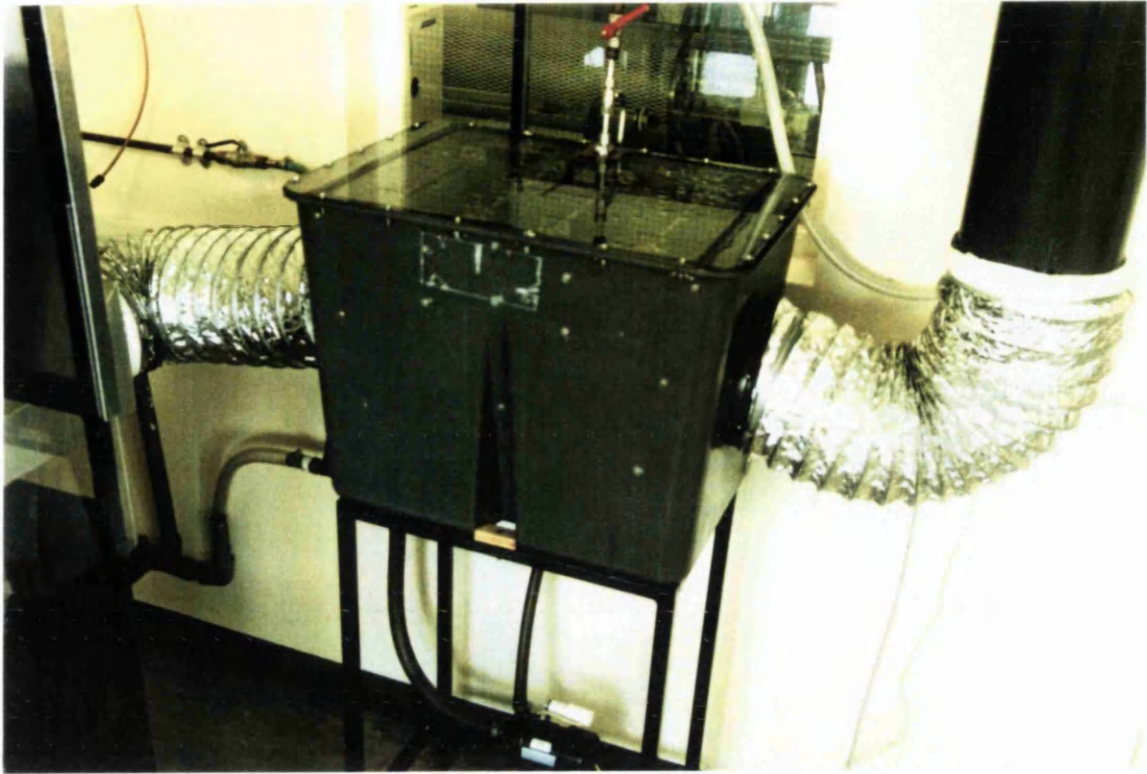


Figure 2.10 Scrubber unit.

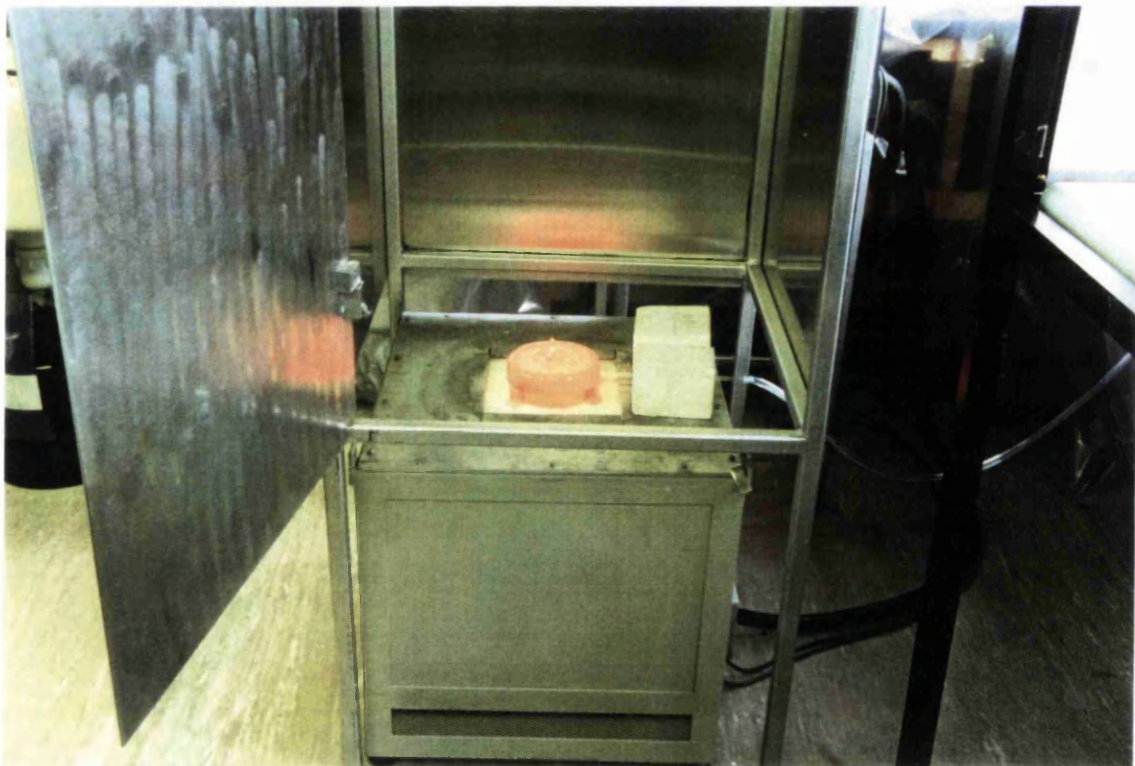


Figure 2.11 Vertical loading MF 206 electrical furnace.

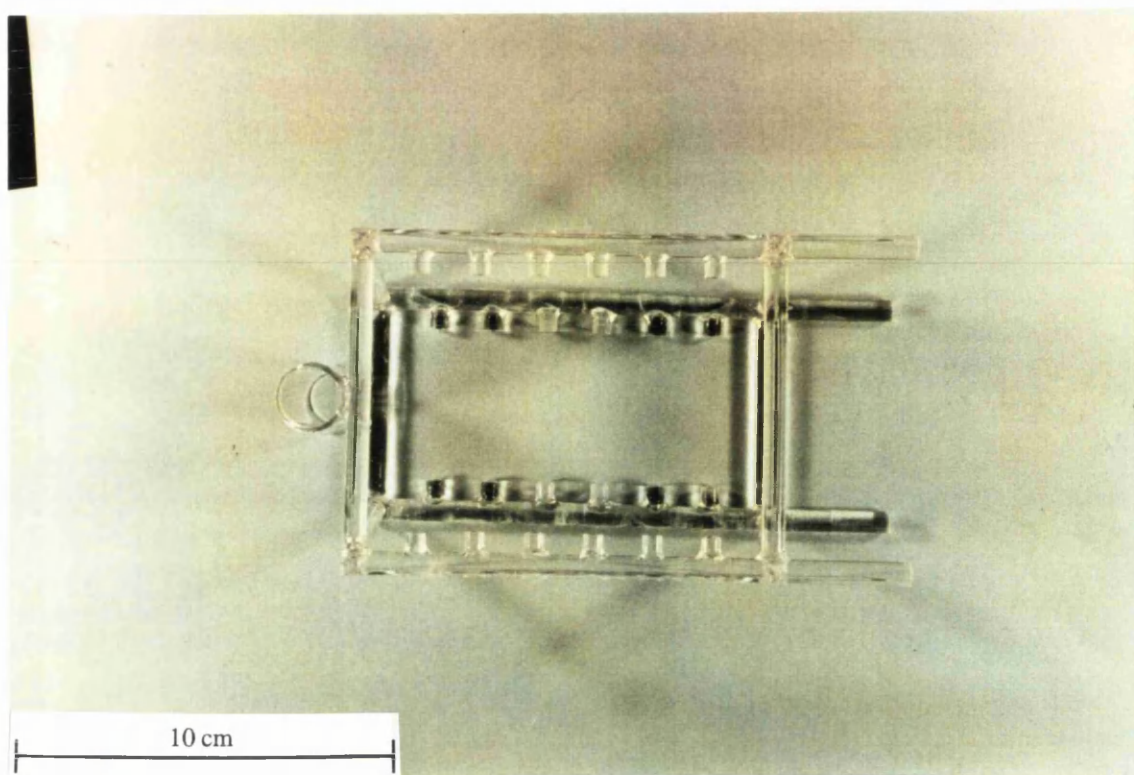


Figure 2.12 Fused quartz carriages for batch processing.

more compact design, furnace liners can be purchased at a fraction of the cost in comparison to the horizontal model. The older model incorporated a mullite ($\text{SiO}_2:\text{Al}_2\text{O}_3$) ceramic furnace liner around the silica liner for support reducing the working bore to 90 mm. The gases helium and oxygen were also piped to the furnace to aid sintering and oxidation of the glass.

2.4 Conclusions

To achieve reproducible results and a high standard of devices it was critically important to run the laboratory in a well-maintained and efficient manner with safety always a paramount issue. Major drawbacks in the fabrication were contamination and downtime of the equipment. Measuring the particle count it was found that the particle count for particles below $0.5\ \mu\text{m}$ and greater than $0.5\ \mu\text{m}$ were 22,000 and 770 respectively. To give an idea to the 'cleanliness' of the deposition laboratory this correlates to Class 100,000. Already, tentative steps are in progress to up-grade the laboratory to at least Class 10,000. Equipment in the laboratory is now thoroughly maintained and inspected at regular intervals and where possible replacements have been purchased. This has dramatically increased the turn-over of devices.

References

- 1 Photonic Integration Research, Inc. (PIRI), Product Catalogue, 1992.
- 2 Hyde J. F., U. S. Patent, no. 2, 272, 342, 1942.
- 3 Pearson A. D. and Day C. R., Bell Lab. Rec., 1972, **50**, 103.
- 4 Keck D. B., Schultz P. C. and Zimar F., U. S. Patent, no. 3, 737, 292, 1973.
- 5 Izawa T. and Inagaki N., Proc. IEEE, 1980, **68**, 1184.
- 6 MacChesney J. B., O'Connor P. B., DiMarcello F. V., Simpson J. R. and Lazay P. D., Proc. Tenth International Congress on Glass, Kyoto, 1974.
- 7 MacChesney J. B., Jaeger R. E., Pinnow D. A., Ostermeyer F. W., Rich T. C. and Van Uitert L. G., Phys. Lett., 1973, **23**, 340.
- 8 Horiguchi M. and Kawachi M., Electron. Lett., 1976, **12**, 310.
- 9 Miya T., Terunama Y., Hosaka T. and Miyashita T., Electron. Lett., 1979, **15**, 106.
- 10 Kawachi M., Yasu M. and Edahiro T., Electron. Lett., 1983, **19**, 583.
- 11 Kobayashi M., Yamada M., Yamada Y., Himeno A. and Terui H., Electron. Lett., 1987, **23**, 143.
- 12 Pliskin W., J. Vac. Sci. Techn., 1977, **14**, 1064.
- 13 Ramaswamy R. V. and Srivastava R., J. Lightwave Techn., 1988, **6**, 984.
- 14 Valette S., J. Modern Opt., 1988, **35**, 993.
- 15 Verbeek B. H., Henry C. H., Olsson N. A., Orlovsky K. J., Kazarinov R. F. and Johnson B. H., J. Lightwave Techn., 1988, **6**, 1011.

Chapter 2 Flame hydrolysis deposition

- 16 Izawa T., Mori H., Murakami Y. and Shimizu N., Appl. Phys. Lett., 1981, **38**, 483.
- 17 Nourshargh N., Starr E. M., Fox N. I. and Jones S. G., Electron. Lett., 1985, **21**, 818.
- 18 Booth B. L., J. Lightwave Techn., 1989, **7**, 1445.
- 19 Kawachi M., Opt. and Quant. Electron., 1990, **22**, 391.
- 20 Bean K. E., IEEE Trans. on Electron Devices, 1978, **ED -25**, 1185.
- 21 Hibino Y., Kitagawa T., Shimizu M., Hanawa F. and Sugita A., IEEE Photon. Tech. Lett., 1989, **1**, 349.
- 22 Kitagawa T., Hattori K., Shuto K., Yasu M., Kobayashi M. and Horiguchi M., Electron. Lett., 1992, **28**, 1818.
- 23 Takato N., Yasu M. and Kawachi M., Electron. Lett., 1986, **22**, 321.
- 24 Barbarossa G. and Laybourn P. J. R., Electron. Lett., 1992, **28**, 437.
- 25 Sun C. J., Myers W. M., Schmidt K. M. and Sumida S., IEEE Photon. Tech. Lett., 1991, **3**, 238.
- 26 Yamada Y., Kawachi M., Yasu M. and Kobayashi M., Appl. Opt., 1985, **24**, 454.
- 27 Izawa T., Sudo S., Hanawa F. and Kobayashi S., ECL Tech. J., 1979, **26**, 2531.
- 28 Izawa T. and Sudo S., Optical Fibers: Materials and Fabrication, Tokyo: KTK Scientific, 1987.

Chapter 2 Flame hydrolysis deposition

29 Maxwell G. D., PhD Thesis, University of Glasgow, 1990.

Chapter 3 Fabrication of planar waveguides - material and optical analysis

3.1 Introduction

Throughout the years, various different types of waveguides have been studied for light transmission. To produce high quality optical fibres, it was necessary to analyse various materials such as liquid, gas, crystal and glass waveguide geometries. Subsequently, glass fibres due to their attractive properties received most attention and now provide the major source for light transmission.

Compared to liquid and gas materials, solid-state devices exhibit a stronger interaction with light waves. However, although this indicates higher loss especially with electronic transitions and molecular vibrations providing absorption in the ultraviolet and infrared red regions respectively, the optical properties are relatively stable. This cannot be said for liquid and gas which encounter problems in controlling the refractive index and are limited to step-index type waveguide structures.

Crystalline materials are low loss, however the growth techniques require a large amount of time and ultimately are expensive with batch-processing generally not feasible. Also, scattering losses can be introduced when cladding such structures, due to the higher index difference.

Amorphous materials such as oxide glasses, demonstrate Rayleigh scattering loss to a higher extent than the materials mentioned above due to density fluctuations within the material. However, glasses offer controllability of the refractive index profile, simple and cheap production as well as mass production. The cladding of glass is easily deposited and provides little surface roughness and hence, a reduction in scattering loss¹.

Glass exhibits a rare quality in its ability to form an amorphous structure when cooled from high temperatures. This super cooling effect results in the molten material not forming a crystalline state. This ability is performed by the network former silica SiO_2 , at temperatures above 1480 °C. To decrease the sintering temperature of silica, modifiers such as P_2O_5 and B_2O_3 can be introduced into the glass matrix. P_2O_5

increases the refractive index of silica, while B_2O_3 has the opposite effect decreases it. In the work detailed in this section particular emphasis has been placed on phosphosilicate and borosilicate binary glass structures. Other network formers are GeO_2 and TiO_2 which increase the refractive index by relatively large amounts, especially TiO_2 ². However, TiO_2 doped silica is found to exhibit scattering losses higher than those observed for other modifiers³. Also, GeO_2 is typically formed in a ternary system and co-doped with either phosphorous or boron to enable complete consolidation below temperatures of 1400 °C which is not possible with the binary SiO_2 - GeO_2 glass. Graphs of both the consolidation temperature⁴ and the refractive index⁵ as a function of the molar content of network formers are shown in Figure 3.1 and Figure 3.2 respectively.

Within this study, material analysis has centred around adopting a suitable recipe for incorporating rare earth ions into the glass matrix and as a result much of the investigation has focused on the problems incurred throughout the development. Thus, in many cases a qualitative description of the solutions necessary to achieve the desired material quality is given.

The main thrust was to produce low loss devices which exhibited, little or no, out of plane and in plane scatter losses. The material has to be reproducible in physical terms e.g. thickness and refractive index, as well as being homogeneous. Not only were samples produced with varying network modifier concentrations but also with a range of consolidation parameters and co-dopants.

Basically, it was found that the necessary foundation stone was to utilise as high as phosphorous content silica as possible. This allowed a relatively high concentration of rare earth ions to be uniformly incorporated into the glass. Several problems resulted owing to the nature of the soft glass (see Figure 3.3) such as core deformation, phosphorous diffusion⁶ etc. Even at relatively low cladding temperatures problems were encountered, which are detailed in more depth in the following chapter as well as other difficulties posed by the core composition. To form the necessary cladding layer which was both of a sufficient thickness and refractive index matched to the buffer layer many depositions took place based on a SiO_2 - P_2O_5 - B_2O_3 glass. As an additional feature silica co-doped with boron and germanium were fabricated. The main aim was to match the core refractive index and thicknesses to that of the phosphorous regime for possible future photorefractive⁷ features in integrated active and passive devices, discussed in Chapter 6. Thus, a small section is devoted to preliminary studies.

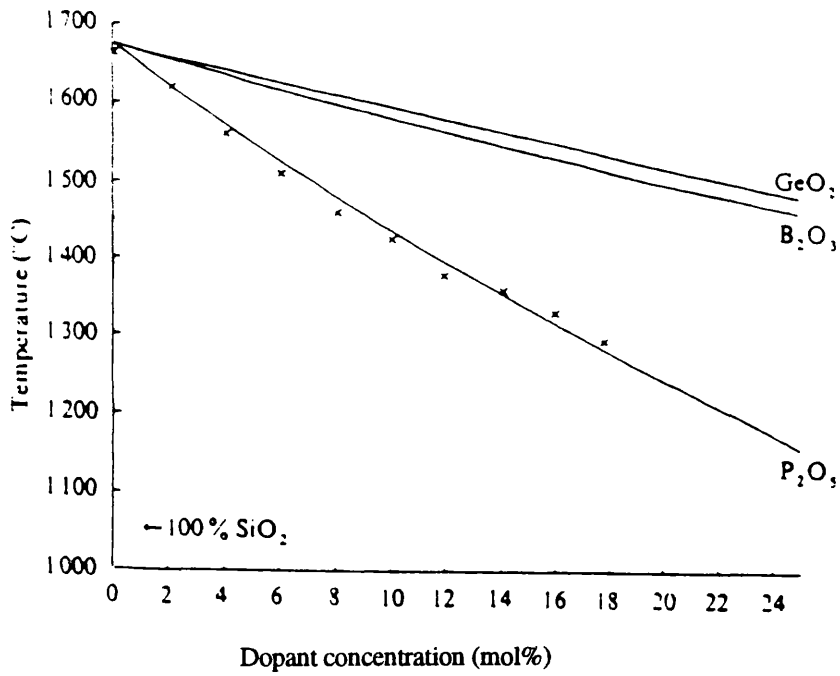


Figure 3.1 Consolidation temperature as a function of composition for SiO₂-P₂O₅, SiO₂-B₂O₃ and SiO₂-GeO₂ binary glasses taken from ref. 4.

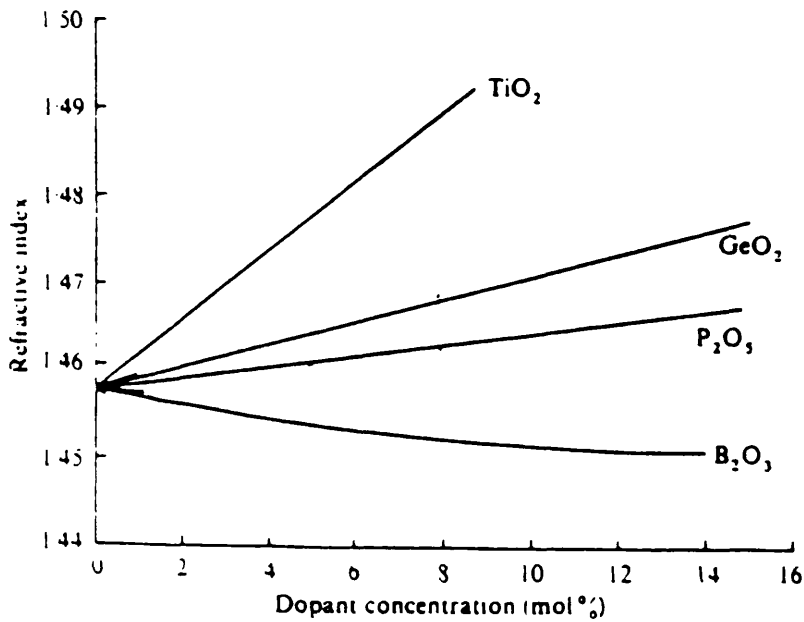


Figure 3.2 Refractive index as a function of composition for SiO₂-P₂O₅, SiO₂-B₂O₃, SiO₂-TiO₂ and SiO₂-GeO₂ binary glasses taken from ref. 5.

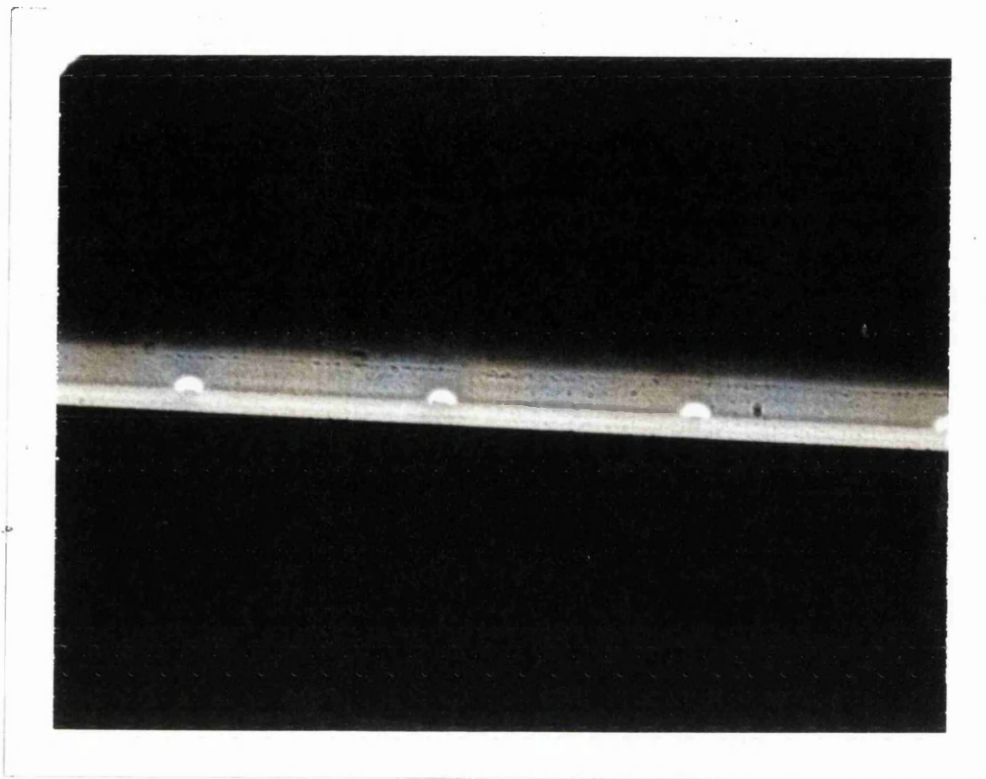
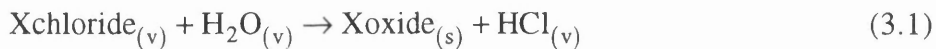


Figure 3.3 Cross-sectional view of waveguides to highlight deformation of SiO₂-P₂O₅ core.

3.2 Synthesis, deposition and sintering of fine glass particles

The basic operation for the forming of the low density soot, involves oxide products (such as SiO₂, P₂O₅) being synthesised by the flame hydrolysis reaction of the starting halide materials such as SiCl₄ and POCl₃. The chemical reaction when the halides are hydrolysed has the following form:



where X, denotes the dopants Si, P, B, Ge and Ti.

The low density soot is deposited onto substrates placed on the turntable. The substrates are then transferred to a high temperature electric furnace for sintering. The samples then undergo the subsequent testing and processing procedures. However, features such as substrate material, metal chloride flow rates, flame temperature, substrate temperature, consolidation atmosphere etc. have to be taken into account when forming low loss glass material. Within this section general behaviour and material properties encountered for the glass systems investigated will be discussed

with the subsequent sections detailing the requirements and differences for the individual glass system.

In general 3" silicon wafers with a 10 μm thermally grown oxide layer were employed as the substrate material. The benefits of Si are many fold: low cost, wide availability, ability to micromachine V-grooves for fibre alignment etc. However, it would appear that forming silica glass layers using FHD on Si would be difficult due to the difference in thermal expansion. This is not the case, as the thermal expansion of Si ($2.5 \times 10^{-6} \text{ deg}^{-1}$) is greater than that of silica ($5.5 \times 10^{-7} \text{ deg}^{-1}$) such that the stress in the silica waveguide is compressive, thus preventing cracking of the fused deposited silica layer.

To fuse the deposited silica it is necessary to reduce the viscosity of the silica by incorporating dopants. As mentioned previously, P_2O_5 is employed to reduce the sintering temperature. In relation to thermal expansion this may seem a surprising choice since the expansion coefficient 25 times larger ($14 \times 10^{-6} \text{ deg}^{-1}$) than that of silica. However, for P_2O_5 concentrations of 45 wt% in silica the expansion coefficient is similar to that of the pure host and as a result, forms a stable glass⁸.

The glass particles deposited on the substrate are oxidised at lower temperatures than that of the oxidation process for the same halide materials. The reasons for this are that the halides do not directly form the oxide but rather undergo intermediate steps. This results in a lower activation energy, as well as the existence of flame radicals which promote the formation reaction of oxide materials⁹. The average size of the particle is determined by the flame temperature and the halide flow rates¹⁰. It is typically found that the particle size becomes smaller for increasing flame temperature. Whereas, in the combustion zone of the torch the factor governing the particle growth is that of Brownian motion. Thus, particles collide and stick forming aggregates which in turn undergo further collisions to form agglomerates. The bonds between the particles are of a physical nature and the glass particles which are deposited onto the substrate are dependent on the spatial concentration.

In general the soot was deposited onto samples placed on a heated turntable, which was maintained at a temperature of 150 °C. The temperature of the turntable was the maximum temperature available and the deposition parameters (flame temperature) were such that the substrate temperature did not increase to cause the evaporation of the dopant due to either melting or sublimation, whilst reduced the possibility of crystalline structures being deposited for certain dopants. Studies based on the $\text{SiO}_2\text{-GeO}_2$, $\text{SiO}_2\text{-B}_2\text{O}_3$ and $\text{SiO}_2\text{-TiO}_2$ systems formed by FHD illustrated the difference in the

binary systems for substrate temperature¹¹. It was found that irrespective of the substrate temperature TiO₂ exhibited no crystalline form. However, both GeO₂ and B₂O₃ were found to have crystalline structures for substrate temperatures below 400 °C. Increasing the temperature of the substrate resulted in an increase in the oxide concentrations dissolved in the SiO₂ matrix. It was deduced that since both the oxide dopants had a high saturated vapour pressure they remained in the vapour phase when deposited onto the substrate. Unlike, the TiO₂ which formed solid particles in the flame such that it was not dependent on the substrate temperature.

The fine glass particles deposited onto the substrate are heated up to between 1200 to 1375 °C in an electric furnace for sintering. From the earliest of times sintering has been used to fabricate metals, such as iron and platinum, which could not be melted. Similarly, glasses are heated to temperatures near their melting point¹²., such that there is a reduction in surface area whilst at the same time an increase in the density¹³. It is the excess free energy of the surface area of the oxide powders which allows consolidation at relatively low temperatures in comparison to solid material. The addition of dopants to the silica reduces the glass viscosity and hence, the sintering temperature. For FHD, densification of the glass involves the fine particles forming necks between adjoining particles, to produce an open network with pores¹⁴. Further densification results with closure of pores until a transparent, bubble free glass is produced. Chapter 5 illustrates different stages of sintering for SiO₂-P₂O₅ films.

Much of the work concerning sintering of porous glass has been based on the OVD and VAD processes for fibre preform production. FHD on a planar format however, has restrictions in comparison to the fibre form. The nature of the substrate means that the highest processing temperature that can be tolerated is 1375 °C, unlike fibre preform production which takes place at higher temperatures. The substrate also can restrict the thermal cycle of the glass due to thermal shock of the substrate in certain conditions. It is thus necessary, to achieve sintering conditions in which planar guides can be produced without diffusion of the dopant, residual gas trapping and crystal formation.

The environment gas in the furnace during sintering is another factor to take into consideration. The set-up for the furnace allowed both He and O₂ to be employed as the environment gas. O₂ was used to promote oxidation, whilst He was adopted due to studies by Sudo et al, which suggested that it would aid sintering by promoting pore collapse¹⁵. This is due to the fact that the critical diameter of the He is large in comparison to the diameter of the pores in the latter stage of sintering. Unlike Ar which possesses a much smaller critical diameter such that it does not diffuse out of the pores but rather inhibits the pore closure to create bubbles.

3.3 Binary SiO₂-P₂O₅ glass system

For the binary SiO₂-P₂O₅ glass system the considerations to take into account were highly phosphorous doped layers, which could be quickly fused to reduced thermal processing, without gas trapping and evaporation of the phosphorous dopant taking place. The thermal mismatch between SiO₂ and P₂O₅ discussed earlier highlighted the potential problem of using P₂O₅ as a dopant. What makes it even more surprising is that it sublimates at 300 °C, melts at 580 °C, is hygroscopic and has a high vapour pressure at elevated temperatures. However, it exhibits no tendency to phase separation or to devitrification, is low loss at telecommunication wavelengths and it is chemically resistant to attack by water.

The phase diagram of the SiO₂P₂O₅ system¹⁶ is given in Figure 3.4. Of importance is the fact that relatively small amounts of P₂O₅ are necessary to reduce the temperature to produce a single liquid phase. Thus, by rapidly cooling it will produce a single phase. To obtain the liquidus line the procedures are different from the processes encountered with FHD, however, it does give a good indication to the behaviour of the system.

To produce SiO₂-P₂O₅ films the halides SiCl₄ and PCl₃ were initially transported to the flame using N₂ as a carrier gas. The hydrogen and oxygen flow rates were 4 and 6 l/min respectively. Figure 3.5 indicates the refractive index difference between the core and buffer as a function of the PCl₃ flow rate. The prism coupler method, discussed in Section 4.2.3, was employed to measure the refractive indices.

There are several points to note. The refractive index range produced was quite large and the index change was proportional to the PCl₃ flow rate. The thickness of the film was also constant irrespective of the PCl₃ flow rate. It was also possible to completely sinter films for relatively low PCl₃ flow rates.

The halide PCl₃ was found to be extremely adequate for forming low loss glass films. However, due to supply constraints, deposition parameters had to be re-calibrated for POCl₃ which is less expensive and more readily available in the quantities required for the FHD system. Since the vapour pressure of POCl₃ (29.55 mm at 21 °C) is approximately one third of PCl₃ (100 mm at 21 °C) it was necessary to install MFC controllers which would be able to cater for flow rates of at least 600 sccm.

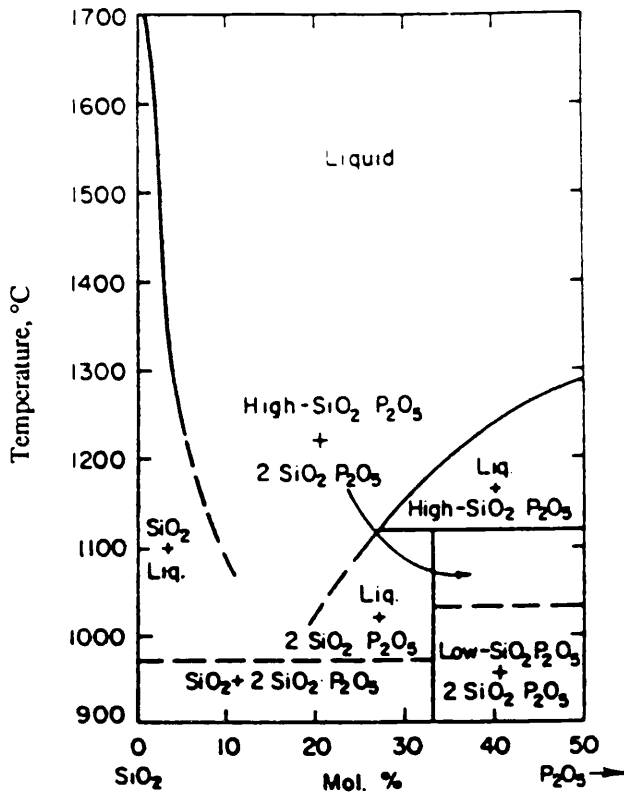


Figure 3.4 Phase diagram of SiO₂-P₂O₅ glass system.

Once again the hydrogen and oxygen flow rates were 4 and 6 l/min respectively. The SiCl₄ was maintained at 150 sccm and the samples were sintered at 1300 °C for 1 hour. Figure 3.6 indicates the refractive index difference as a function of the POCl₃ flow rate.

A similar trend to that observed for PCl₃ was measured, with the refractive index proportional to the flow rate. The thickness of the films were also independent of the POCl₃ flow rates. However, it was found that more P₂O₅ was being incorporated into the glass system. This was borne out with higher index measurements for similar vapour flows carried to the torch. A possible reasons for this phenomenon was that since POCl₃ vapour required a larger gas carrier flow rate to the torch than the PCl₃ system, that the flame temperature was cooler and subsequently the vapour pressure of the P₂O₅ was lower. Hence, the lower temperature would prevent the volatilisation of the P₂O₅ phase, resulting in higher doping levels. To investigate this phenomenon experiments were conducted with hydrogen and oxygen flow rates reduced to 1 and 2 l/min respectively, to produce a cooler flame. Once again the SiCl₄ was maintained at 150 sccm and the samples were sintered at 1300 °C for 1 hour. For FHD the flame temperature can be lower than that typically used in the MCVD process due to the reasons mentioned earlier.

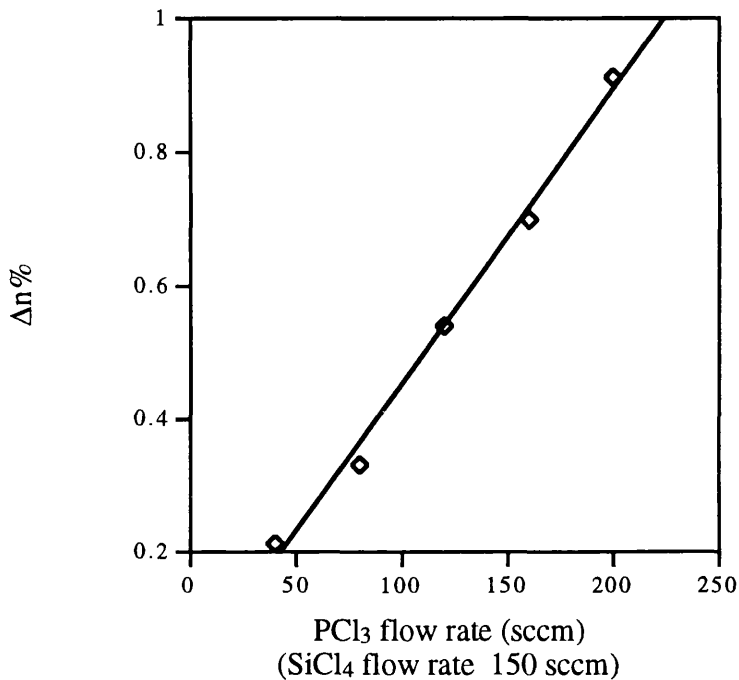


Figure 3.5 Refractive index of $\text{SiO}_2\text{-P}_2\text{O}_5$ film as a function of PCl_3 flow rate.

Figure 3.7 indicates the refractive index difference as a function of the POCl_3 flow rate. From the experimental data it can be seen that the P_2O_5 level is greater with a significant increase in refractive index difference of approximately 0.15%. The lower temperature of the flame is such that the vapour pressure of the oxide component is low enough not to cause volatilisation of the P_2O_5 . The SiO_2 itself is not as readily affected as the P_2O_5 due to its much lower saturated vapour pressure. A decrease in the threshold flow rate of the halide materials for the formation of solid oxide particles is also observed due to the decrease in saturated vapour pressure¹⁷.

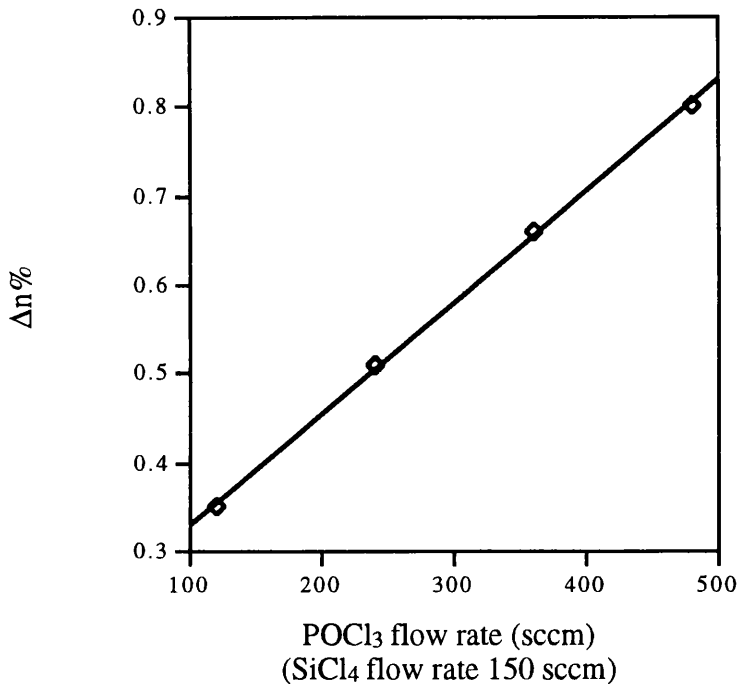


Figure 3.6 Refractive index of SiO₂-P₂O₅ film as a function of POCl₃ flow rate.

For all the graphs showing the refractive index as a function of the phosphorous halide flow rate, the graphs indicate that an index greater than that of thermally grown SiO₂ can be achieved for no additional phosphorous halide flow. Unfortunately, it is not possible to prove this by fabricating SiO₂ by FHD on a silicon substrate, as the temperature necessary to sinter the soot is too high for the substrate to withstand.

In all cases a gel was obtained when the phosphorous halide level was increased to levels greater than that used to produce the maximum refractive index step. As a result, it was not feasible to process such samples. It is the authors opinion that the gel deposited was phosphoric acid. This is possibly due to the high P₂O₅ levels, which being extremely hygroscopic, converts the residual water to phosphoric acid. It is also known that orthophosphoric acid is an 'oily' substance.



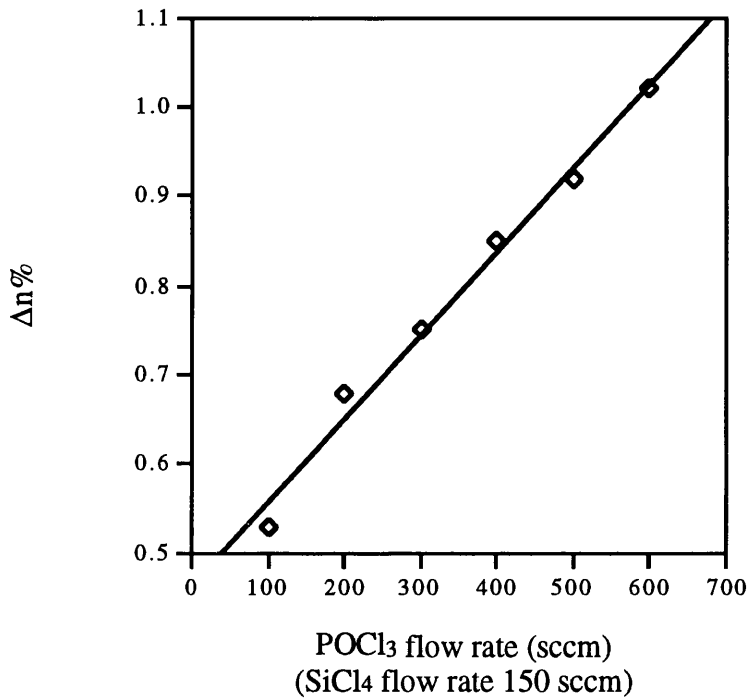


Figure 3.7 Refractive index of SiO₂-P₂O₅ film as a function of POCl₃ flow rate.

Another problem highlighted for the P₂O₅ system was the substrate temperature. It was observed that if the substrate temperature at the start of the deposition was less than 120 °C then the resulting film would have a high density of voids. By implementing a heater with a smaller radius under the turntable it was possible to form a temperature gradient across the Si wafers such that part of the wafer was below 120 °C. As expected the region which was below the temperature produced voids, as illustrated in Figure 3.8. The voids themselves are created due to the mechanical strength of the deposited film being so low that oxide particles flake off¹⁸. The increased temperature of the substrate creates a higher degree of sintering to prevent this. Alternatively, the distance of the flame can be moved closer to the substrate to achieve a higher degree of sintering. Whilst care had to be taken to stop this phenomenon the temperature of the substrate could not be too high in case the P₂O₅ evaporated. The final stage in sintering the SiO₂-P₂O₅ film was designed to be compatible with the rare earth doping process. It was important to be able to sinter the glass in a quick time and at a high temperature, without loss of the P₂O₅ due to evaporation and without residual gas trapping.

For $\text{SiO}_2\text{-P}_2\text{O}_5$ films the nature of the glass is such that the low viscosity results in complete consolidation. However, due to this viscosity, the film is susceptible to consolidating at such a rate that residual gas is trapped and causes bubbles. To overcome this phenomenon the deposited layer can be thinner and the final film produced from a series of depositions. Alternatively, a temperature gradient in the furnace can allow slower fusing conditions. However, it was found that a gradual ramp of the temperature had the undesired effect of allowing the P_2O_5 level to evaporate, to such a level that the deposited soot could not be fully sintered. A possible solution to this, used in investigations of phase relations for glasses, was to place the sample in a platinum box to create a partial pressure. However, this had no effect and did not provide a greater deal of sintering.

Deposited $\text{SiO}_2\text{-P}_2\text{O}_5$ films were able to be fused in He atmospheres at temperatures as high as 1385°C in time durations of between 15 to 120 minutes with no gas trapping, or P_2O_5 out diffusion. Another benefit was that the samples could be quenched at temperatures as high as 1375°C without thermal shock damaging the samples. Figure 3.9 indicates the problems found when trying to consolidate the samples at 1400°C . At 1385°C striations across the sample as well as implosions due to faults in the Si crystal planes were also observed (Figure 3.10).

High P_2O_5 doped samples (~20 wt%) also required a thermal oxide buffer layer of at least $4\ \mu\text{m}$ thick. The thermal mismatch between the Si substrate and deposited film caused severe cracking to take place over the sample. This is shown in Figure 3.11 where a highly doped film was deposited and sintered on a sample with a $1\ \mu\text{m}$ buffer layer.

3.4 Binary $\text{SiO}_2\text{-B}_2\text{O}_3$ glass system

For the $\text{SiO}_2\text{-B}_2\text{O}_3$ system the important factors in the investigation were to fabricate films which would act as suitable claddings for high phosphorous doped cores. This involved, matching the refractive index to that of the buffer and sintering temperatures which would not cause the gross deformation of the core. It was also important to produce thick layers which would embed the core, remembering that the viscous nature of the glass tends to minimise the surface area, and as result 'flows' between the guides¹⁹. This is unlike other silica technologies where cladding layers maintain the shape of the initial design.



Figure 3.8 SEM photograph of void on sintered film.



Figure 3.9 Photograph of deformation of sample consolidated at 1400 °C.

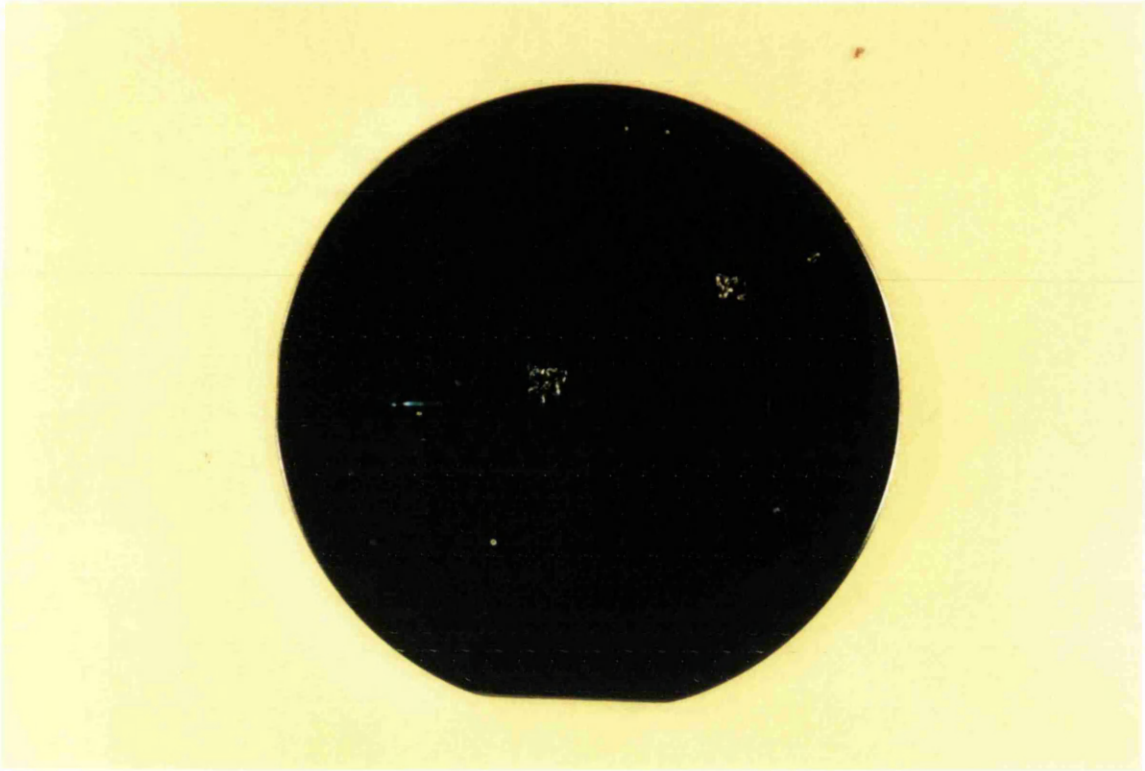


Figure 3.10 Photograph of deformation of sample consolidated at 1385 °C.



Figure 3.11 Photograph of cracking in film deposited on a Si substrate with a 1 μm thick buffer layer.

The phase diagram of the $\text{SiO}_2\text{-B}_2\text{O}_3$ system²⁰ is given in Figure 3.12. There was wide controversy regarding this system, owing to the problems in obtaining reliable equilibrium data²¹. The principal difficulties involved the volatilisation of B_2O_3 , the hydration and the great viscosity of $\text{SiO}_2\text{-B}_2\text{O}_3$. However, a feature noted by the study was the difficulties found in detecting devitrification of the borosilicate glasses.

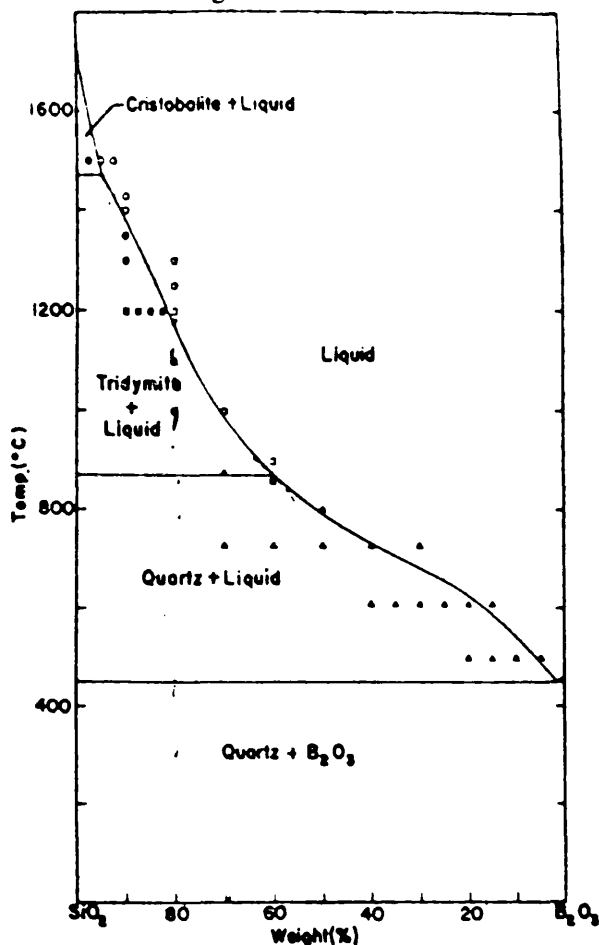


Figure 3.12 Phase diagram of $\text{SiO}_2\text{-B}_2\text{O}_3$ glass system.

To produce $\text{SiO}_2\text{-B}_2\text{O}_3$ films the halides SiCl_4 and BCl_3 were initially transported to the flame. In this case the BCl_3 was gaseous. The hydrogen and oxygen flow rates were 1 and 2 l/min respectively. However, since the refractive index change introduced by B_2O_3 reduces the index, qualitative measurements were undertaken to match the refractive index to that of the thermal oxide.

Measurements involved viewing the cross-section of the planar waveguide by cutting the samples into rectangular pieces after the $\text{SiO}_2\text{-B}_2\text{O}_3$ film had been deposited. The samples were then inspected end-on by fixing the ends of the substrate to cover slips using silver dag. The samples were then investigated under a microscope in transmission mode, such that the planar films were normal to the objective. It was a relatively simple matter to investigate the relative intensities between the thermal oxide

and deposited layer. This is illustrated in Figure 3.13, showing a brighter intensity for the deposited layer and Figure 3.14, showing a similar intensity to that of the thermal oxide. The process also gave an indication of the film thickness.

To maintain the uniformity of the film thickness, the SiCl_4 flow rate was maintained at 150 sccm for all depositions. The BCl_3 flow rate was varied between 0 and 50 sccm. However, even with the maximum BCl_3 flow rate the temperature necessary to consolidate the soot was 1325 °C, for a time of 60 minutes in a He atmosphere²². The addition of POCl_3 to the reaction resulted in an increase in the refractive index and a decrease in the sintering temperature. It was subsequently established, that BCl_3 and POCl_3 flow rates of 50 and 30 sccm provided films with an index approximately equal to that of the thermal oxide which sintered at 1200 °C, for a time of 60 minutes in a He atmosphere. It was also possible to deposit 20 μm thick layers in a single deposition.

As a result of studies based on the optical ageing characteristics of borosilicate fibres, refractive index measurements as a function of temperature were conducted²³. To allow reliable refractive index measurements a high P_2O_5 doped layer was used. This generally gave an index difference in relation to the thermal oxide of 0.75%. The addition of B_2O_3 , to form a $\text{SiO}_2\text{-P}_2\text{O}_5\text{-B}_2\text{O}_3$ glass reduced the refractive index to 0.68%. All the samples were fused at 1300 °C for 60 minutes in a He atmosphere. The samples were then ramped down to various temperatures at a rate of 5 °C/min and removed from the electric furnace to cool down to ambient temperature. Figure 3.15 shows the refractive index measurements as a function of the final temperature on removal from the furnace. Also plotted is the refractive index measured for a sample ramped down to 1100 °C at a lower rate of 3.33 °C/min.

Figure 3.15 indicates that as the temperature is ramped down to below 1100 °C then for this particular system the refractive index begins to rise. The index difference between the high temperatures and the low temperatures relates to an index difference of 4×10^{-3} . Similarly, in the fibre work reported, the index difference was as large as 8.7×10^{-3} . The rise in refractive index also took place at more moderate temperatures of 400 °C.

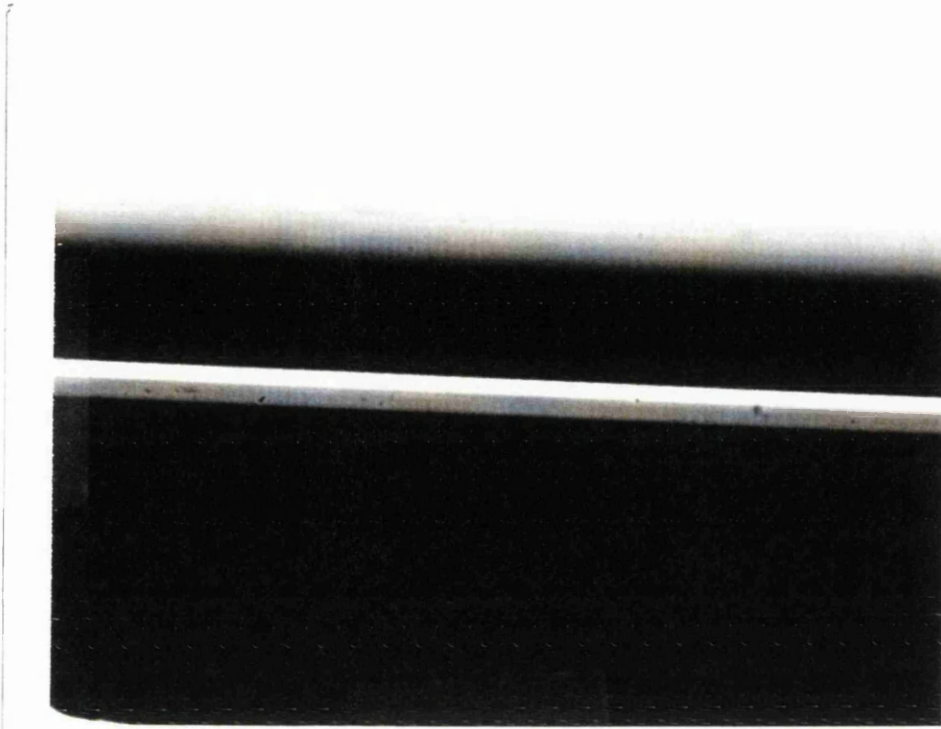


Figure 3.13 Cross-sectional view of $\text{SiO}_2\text{-P}_2\text{O}_5\text{-B}_2\text{O}_3$ planar waveguide.

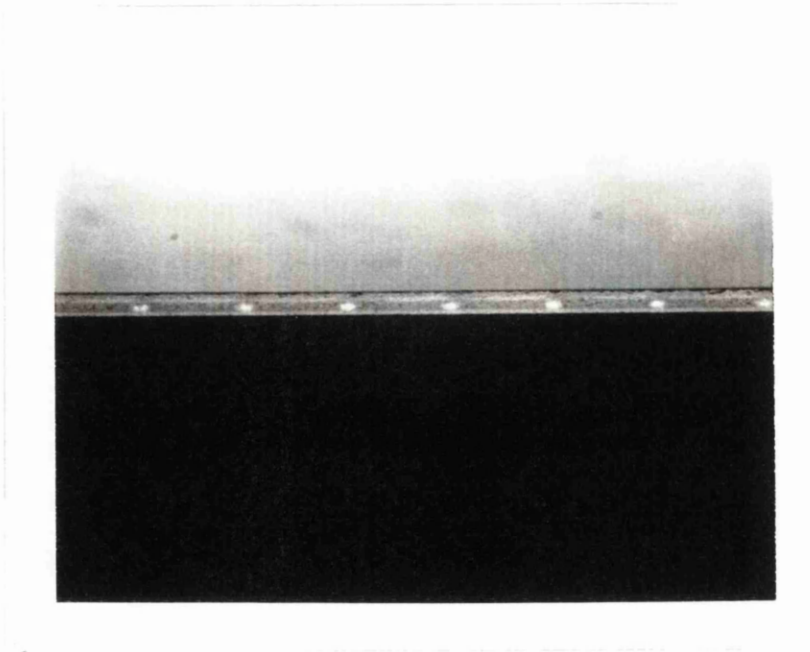


Figure 3.14 Cross-sectional view of $\text{SiO}_2\text{-P}_2\text{O}_5\text{-B}_2\text{O}_3$ planar waveguide.

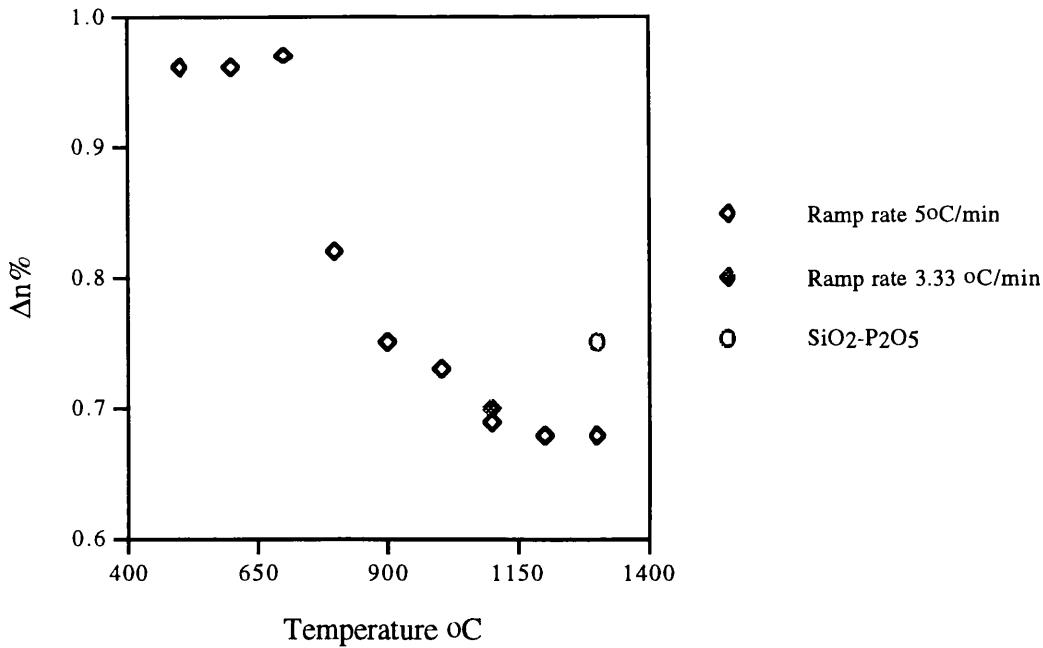


Figure 3.15 Refractive index of $\text{SiO}_2\text{-P}_2\text{O}_5\text{-B}_2\text{O}_3$ film as a function of final temperature.

The low refractive index regime occurs when the glass is quenched whereas at lower temperatures annealing causes an increase in the refractive index. This is attributed to a density increase for the annealed sample²⁴. Compared to the fibre experiment the apparent discrepancies are due to the high doping levels employed for the fibre results. Increasing the boron oxide content results in the glass becoming less rigid such that the glass transition temperature decreases. Of particular note is that for an increase in index for this particular system the sample must be removed at temperatures below 1100 °C. This is less critical for the regime employed for index matched cladding layers, as the B_2O_3 content is greater.

For the $\text{SiO}_2\text{-P}_2\text{O}_5\text{-B}_2\text{O}_3$ system two main problems were encountered. The system was susceptible to gas trapping and when inspecting the deposited material, using the microscope it was found that a dark band was formed next to the buffer layer. The gas trapping was most pronounced when short duration, high temperature cladding films were attempted. Once again, this was to try and minimise the thermal cycle of the rare earth doped cores. The gas trapping was especially bad for planar samples with a high density of devices as shown in Figure 3.16. This problem was alleviated for thick films by plunging the deposited soot at 850 °C and ramping the temperature to 1200 °C at a rate of 15 °C/min. The discontinuity at the interface between the thermal oxide and the deposited soot as illustrated in Figure 3.17 was due to diffusion of the

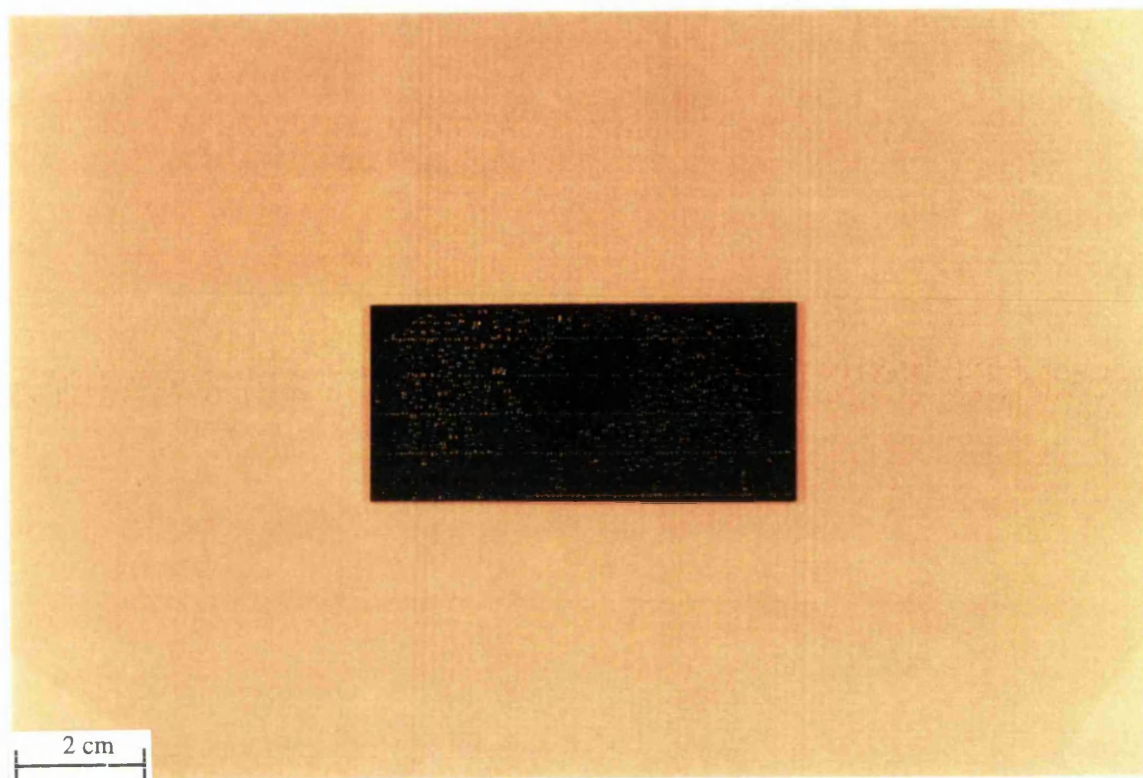


Figure 3.16 Photograph of planar sample devastated with bubbles due to gas trapping.

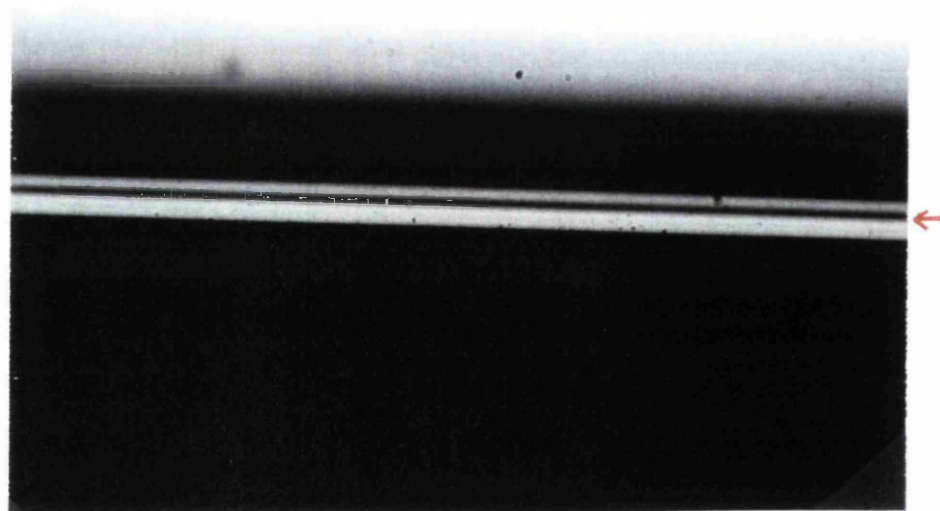


Figure 3.17 Cross-sectionional view showing discontinuity at the interface between the thermal oxide layer and the $\text{SiO}_2\text{-P}_2\text{O}_5\text{-B}_2\text{O}_3$ layer.

B₂O₃. This was as a result of the flame temperature. Once again this phenomenon was reduced by either decreasing the hydrogen flow rate to the torch, or moving the torch further away from the sample.

Another feature of the system was that deformation and interdiffusion between the core and cladding took place. This was attributed to the high P₂O₅ content of the core region. To prevent these problems a Balzer box coater was used to deposit 1 μm thick SiO₂ layers, index matched to that of the buffer layer²⁵. It was shown, that by bleeding an oxygen pressure of 3x10⁻⁶ mbar into the chamber, the desired index was produced. The system itself was quite versatile offering an index range of 0.07. However, due to time constraints no measurements of the reduction in interdiffusion were undertaken. Although, inspecting devices with no capping layers, the P₂O₅ was only seen to diffuse into the clad and not the thermal oxide buffer.

In conclusion it was possible to produce thick cladding material, index matched to that of the buffer layer. Several problems were encountered. However, suitable solutions were found to accommodate difficulties such as gas trapping.

3.5 Ternary SiO₂-GeO₂-B₂O₃ glass system

Towards the end of the project a small amount of time was spent measuring the refractive index change for the SiO₂-GeO₂-B₂O₃ system. This was due to the photosensitive properties reported for this system in both fibre and planar work. Collaboration with Porto University, who have the necessary facilities to treat and expose the samples, has been set-up.

By maintaining the SiCl₄ and BCl₃ flow rates at 150 and 30 sccm, it was possible to measure the refractive index as a function of the GeCl₄ flow rate. The hydrogen and oxygen flow rates were 1 and 2 l/min respectively. Figure 3.18 indicates the refractive index difference as a function of the GeCl₄ flow rate.

For this system a high sintering temperature of 1325 °C was necessary. For this reason, SiO₂-GeO₂ systems could not be tested for FHD, due to the glass sintering temperature necessary. To reduce the sintering temperature either codoping with B₂O₃ or P₂O₅ was necessary²⁶. Since, B₂O₃ reduces the refractive index of the glass this means a larger GeO₂ concentration for similar refractive index values to that produced for samples codoped with P₂O₅ and GeO₂. The B₂O₃ is also reported to aid the photosensitive properties of the glass, such that it was chosen as a suitable codopant²⁷.

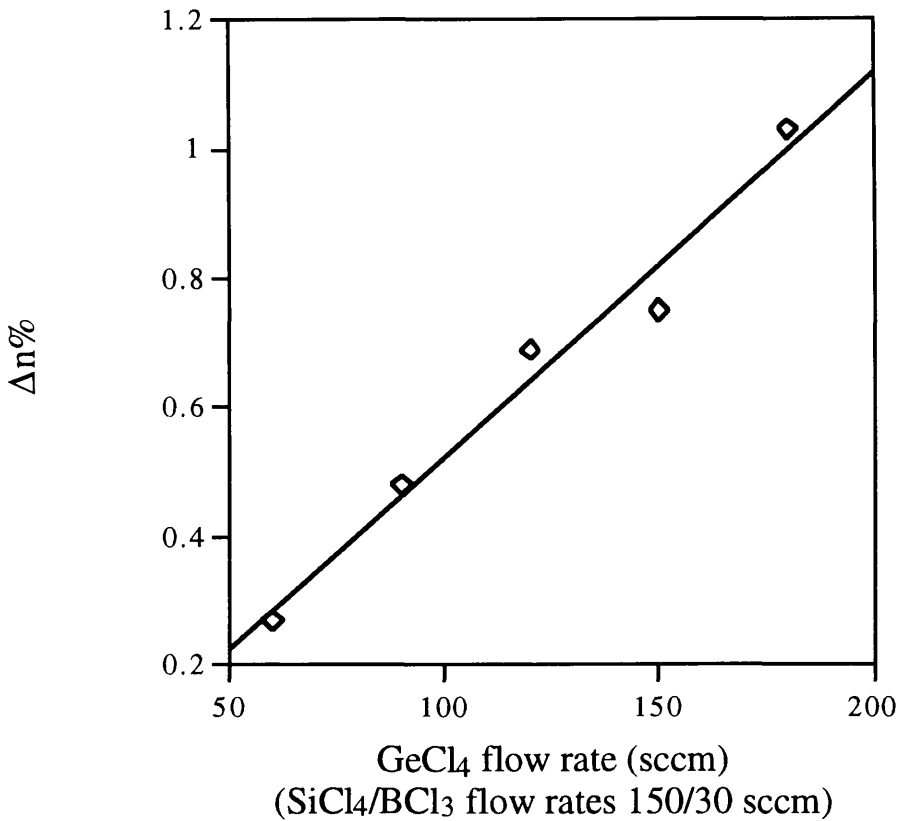


Figure 3.18 Refractive index of SiO₂-GeO₂-B₂O₃ film as a function of GeCl₄ flow rate.

Of particular importance was that it was possible to match the refractive index of the SiO₂-GeO₂-B₂O₃ system to that of the typical index used for rare earth doped samples within the project. This offers the potential of integrating active devices with photosensitive regions to produce such devices as DBR laser structures. Chapter 6 discusses the topic of selective area doping in more detail.

3.6 Conclusion

Various glass systems were fabricated and investigated. The main objective, was to fabricate low loss rare earth doped devices. Consequently, core layers formed from the binary SiO₂-P₂O₅ system were fabricated. High phosphorous content silica was able to be fused at high temperatures in a short time period. The cladding layers were formed from the SiO₂-P₂O₅-B₂O₃ system. A suitable cladding layer, which was thick, index matched to the buffer layer and possessed a low sintering temperature was possible. Problems for both glass systems were highlighted and solutions suggested. Finally, the

SiO₂-GeO₂-B₂O₃ system was characterised, to investigate the photosensitivity of waveguides for novel waveguide designs.

References

- 1 Tien P. K., Appl. Opt., 1971, **10**, 2395.
- 2 Kawachi M., Yasu M. and Edahiro T., Electron. Lett., 1983, **19**, 583.
- 3 Kawachi M., Opt. and Quant. Electron., 1990, **22**, 391.
- 4 Hammond C. R., Phys. and Chem. Glasses, 1978, **19**, 41.
- 5 Beales K. J. and Day C.R., Phys. and Chem. Glasses, 1980, **21**, 5.
- 6 Ishii M., Hibino Y., Sugita A. and Tamamura T., Electron. Lett., 1993, **29**, 1684.
- 7 Hill K. O., Fujii Y., Johnson D. C. and Kawasaki B., Appl. Phys. Lett., 1978, **32**, 647.
- 8 Gambling W. A., Payne D. N., Hammond C. R. and Norman S. R., IEE Proc., 1976, **123**, 570.
- 9 Miller T. J., Potkay E. and Yuen M. J., Fibre Optics: Processing and Applications. AIChE Symposium Series, **83**, 1.
- 10 Ulrich G. D., Combust. Sci. and Technol., 1971, **4**, 47.
- 11 Edahiro T., Kawachi M., Sudo S. and Tomaru S., Jpn. J. Appl. Phys., 1980, **19**, 2047.
- 12 Mackenzie J. K. and Shuttleworth R., Proc. Phys. Soc., London, 1949, **62**, 833.
- 13 Frenkel J., J. Phys. (Moscow), 1945, **9**, 385.
- 14 Scherer G. W., J. Am Ceram. Soc., 1977, **60**, 236.

Chapter 3 Fabrication of planar waveguides - material and optical analysis

- 15 Sudo S., Edahiro T. and Kawachi M., Trans. IECE Jpn., 1980, **E63**, 731.
- 16 Tien T. Y. and Hummel F. A., J. Am Ceram. Soc., 1962, **45**, 422.
- 17 Kawachi M., Sudo S. and Edahiro T., Jpn. J. Appl. Phys., 1981, **20**, 709.
- 18 Izawa T. and Sudo S., Optical Fibers: Materials and Fabrication, Tokyo: KTK Scientific, 1987.
- 19 Takato N., Yasu M. and Kawachi M., Electron Lett., 1986, **22**, 321.
- 20 Rockett T. J. and Foster W. R., J. Am Ceram. Soc., 1965, **48**, 75.
- 21 Eldridge J. M. and Balk P., Trans. Metall. Soc. AIME, 1968, **242**, 539.
- 22 Tasker G. W., French W. G., Simpson J. R., Kaiser P. and Presby H. M., Apl. Opt., 1976, **17**, 1836.
- 23 Camlibel I., Pinnow D. A. and Dabby F. W., Appl. Phys. Lett., 1975, **26**, 185.
- 24 Wemple S. H., Pinnow D. A., Rich T. C., Jaeger R. E. and Van Uitert L. G., J. Appl. Phys, 1973, **44**, 5432.
- 25 Himeno A., Kobayashi M. and Terui H., Electron Lett., 1985, **21**, 1020.
- 26 Kominato T., Ohmori Y. Okazaki H. and Yasu M., Electron. Lett., 1990, **26**, 327.
- 27 Williams D. L., Ainslie B. J., Kashyap R. Campbell R. and Armitage J. R., ECOC'92, Berlin, 1992.

Chapter 4 Channel waveguide fabrication and assessment

4.1 Introduction

The previous chapters have detailed the equipment and fundamentals of the FHD process. In this chapter the reader will be given an overview of the FHD as a technique for forming planar and channel waveguides. Details of the deposition parameters, photolithographic steps and dry-etching techniques used will be presented. The assessment of the waveguides at different stages will also be described.

4.2 Planar waveguide fabrication

In general 3" silicon wafers are used for waveguide growth. A number of other different substrates can be used including quartz discs of varying diameters. Silicon wafers are of particular interest since they are inexpensive, often provide motherboards for multi-task functions, and are typically used in the silicon microelectronics industry. Silicon micromachining techniques provide passively aligned V-grooves for fibre location and silicon can provide complex optoelectronic modules comprising of electronic and optical waveguide components. Thus, silicon offers the advantages of low cost, packaged hybrid devices. The Si wafers utilised for FHD have a thermally grown 10 μm thick buffer layer of oxide to aid the wettability of the structure and to provide a necessary buffer layer for isolation from the high index silicon substrate.

4.2.1 Sample preparation

To improve yield and material quality, samples at all stages in the fabrication process are meticulously examined for cleanliness. Transfer of thermally grown samples to carriage boxes only takes place in class 100 fume cupboards. The samples received from the supplier are dispatched after a vigorous acid clean. To reduce the exposure of the substrates and hence, the risk of contamination, substrates are directly placed into the deposition chamber and do not receive any form of cleaning. It was found that this resulted in a reduction in surface defects compared to samples that had been removed for cleaning prior to depositions. Subsequent processes in the fabrication require cleaning to remove any particulate contamination.

Substrates are generally cleaned using the following well established procedure:

1. Place substrate into a beaker and rinse with opticlear. Immerse the substrate in opticlear and agitate in an ultrasonic bath for 5 minutes.
2. Dispose of the opticlear in the sink and rinse the sample in acetone. Immerse the substrate in acetone and agitate in an ultrasonic bath for 5 minutes.
3. Dispose of the acetone in the unchlorinated sump and rinse the sample in methanol. Immerse the substrate in methanol and agitate in an ultrasonic bath for 5 minutes.
4. Without extracting the sample from the beaker rinse in RO (reverse osmosis) water for 2 minutes.
5. Remove excess water from the substrate with a nitrogen blow gun and place on a 90 °C hotplate for 5 minutes to dry completely.

At all times the sample remains immersed. This cleaning procedure is adopted since opticlear is biodegradable, however it is immiscible in both water and methanol. The above process is used and strictly adhered to since each solvent is soluble in the ensuing one. A similar process is to use a water solution of Decon (1:20) followed by RO water, acetone and IPA which all placed in the ultrasonic bath for 5 minutes at each relevant stage and then blown dry and placed on a hotplate for 5 minutes.

For a more vigorous clean to remove organic and inorganic contaminants an acid bath is used. This involves both sulphuric acid (H_2SO_4) and hydrogen peroxide (H_2O_2). During this clean, safety procedures are strictly adhered to, with protective aprons, gloves and safety glasses worn. The H_2O_2 is slowly added to H_2SO_4 in small amounts and gently mixed. The temperature is constantly monitored and once 80 °C is reached the relevant sample to be cleaned is immersed in the solution for 10 minutes. The sample is removed from the solution and then flushed with large amounts of RO water. The remaining solution is disposed of in a safe and careful manner. Once the sample condition is acceptable, it is transported to the deposition laboratory for the consequent film fabrication.

4.2.2 Deposition process

In order to give reproducible deposition parameters in a safe manner and to maintain the deposition equipment, a standard process was developed. This enabled the operator to work in a safe environment, with the apparatus inspected for faults during the set-up procedure. This process is described in the following section.

Preparation

1. Clean torch in 10:1 HF solution for 10 minutes, or alternatively ultrasonic in IPA for same length of time.
2. Use Nalgene flexible tubing to connect PTFE supply gas pipes to torch and fix torch in required position.
3. If doping is to be used then prepare relevant molar solutions.
4. Ensure that chamber is cleaned thoroughly before fixing the turntable into position.
5. Boot up PC and load deposition program. Check to see if communicating to stepper motors.

Initial checks

1. Use potentiometers and digital voltmeters to set the required flow rates for halides, always ensuring that the combined total flow rate for the master line is 850 sccm.
2. Check the oil temperature circulating the jacketed Drechsel bottles is set at 20 °C to maintain the same vapour pressure.
3. Ensure that the temperature of the cabinet is greater than 20 °C to prevent hydrolysis taking place in the gas lines.
4. Check the manometer level before the deposition to make sure that there is no blockages in the halide supply line to the torch.
5. Examine the strength of the extract to determine if there is any blockages in the extract which need removing.
6. Make sure the level of the scrubber is adequate and that the pressure from the gas supply is great enough to create a fine mist to neutralise the HCl vapour produced.
7. Check the nitrogen gas supply is sufficient for the required deposition and that the pressure is 50 psi.

Deposition

1. Open small flap to the entrance of the deposition chamber and clean turntable with IPA.
2. If aerosol doping is being investigated then fill aerosol and attach to torch.
3. Open hydrogen and oxygen bottles first ensuring that the regulators are closed. Examine levels to guarantee that the gas levels are sufficient for deposition and set pressure to 20 psi.
4. For safety reasons carefully vent both the hydrogen and oxygen lines.
5. Open hydrogen gapmeter and light torch with a piezoelectric lighter. Once the flame has been struck gradually open the oxygen gapmeter and set the relevant gas flows.
6. Switch on turntable heater and set variac to 240 V.
7. Switch on cooling fan to protect stepper motor control circuitry which is positioned below the chamber.
8. Once turntable has reached optimum temperature lift small flap and load samples, ensuring that dust free gloves are worn.

Chapter 4 Channel waveguide procedures

9. Switch on halides by toggling the three supply switches simultaneously.
10. Check the manometer level for any obstructions.
12. If introducing aerosol then increase the aerosol delivery rate to the standard rate.
11. Start turntable rotating and after approximately 2 minutes once the reaction has reached equilibrium start the linear drive.
12. Monitor deposition and don't leave unattended.

Completion

1. Switch off nebuliser.
2. Turn off master flow controllers for halides.
3. Having ensured that the halides have been purged out of the system and completely burned off then carefully close hydrogen gas bottle.
4. Once the hydrogen has been cleared out of the line close the regulator.
5. Close oxygen bottle.
6. Carefully clear oxygen line and close regulator.
7. Turn off turntable heater.
8. Stop the scrubber and close the gas supply.
9. After approximately 5 minutes lift small flap and load the samples onto a carriage for consolidation in the high temperature furnace making sure that dust free gloves are worn.
10. Stop the cooling fan.
11. Remove turntable for cleaning and leave in fume cupboard.

4.2.3 Assessment of planar waveguides

Having deposited and consolidated planar waveguides, a standard set of procedures were adopted to test the quality of the waveguides, especially in respect to active devices. Prism coupling experiments¹ were performed not only to measure the refractive indices and film thicknesses, but also as a means to investigate both the in plane and out of plane scatter, which give important information about the doping uniformity. To evaluate the film thickness and to act as a figure of merit for the prism coupling a selective Pliskin etch was conducted to determine the thickness of the device². By etching different parts of the 3" wafer it was also possible to measure the thickness uniformity. Optical inspection and scanning electron micrographs were conducted to check for contamination and peculiarities. A quick method of producing channel waveguides using a sawing technique was used to perform broadband white light tests to determine rare earth doping levels. After all these initial checks it was possible to choose the best samples for more precise measurements. In this section the various techniques used to assess planar waveguides will be described and typical results presented.

Before describing the prism coupling technology a brief summary is given of the wave equations for step index 2-D waveguides (see Figure 4.1).

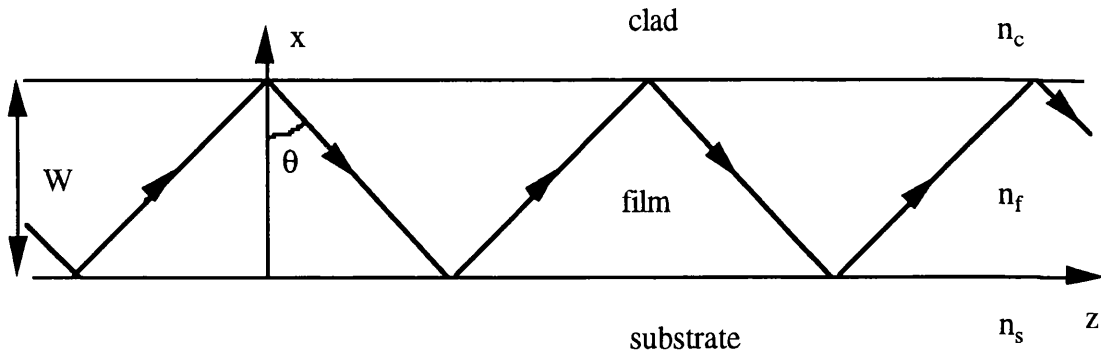


Figure 4.1 Light ray path due to total internal reflection

To support guided modes the fundamental condition that $n_f > n_c / n_s$ must be satisfied where, n_f , n_c and n_s are the respective film, clad and substrate refractive indices. This results in the light being confined to the guiding layer, n_f , and propagates in a zig-zag fashion. The actual index that the guided mode experiences is termed the effective index, N . This can be described as:

$$\beta = k_o N \quad (4.1)$$

where

$$N = n_f \sin \theta \quad (4.2)$$

where β is the propagation constant, θ is the angle of incidence at the substrate/clad-film interfaces and k_o is the free space wavevector and equals $2\pi/\lambda$, λ is the free-space wavelength.

To support a waveguide mode it is also necessary that the phase shift of the wave after two successive reflections is equal to a multiple of 2π . For the case of TE polarised light this can be expressed as

$$2k_o n_f W \cos \theta - 2\phi_s - 2\phi_c = 2m\pi \quad (4.3)$$

Where ϕ_s and ϕ_c are the phase shifts experienced on internal reflection between the film-substrate and film--clad interfaces. These can be expressed as follows

$$\phi_s = \tan^{-1} \frac{\gamma_s}{k} \quad (4.4)$$

Chapter 4 Channel waveguide procedures

$$\phi_c = \tan^{-1} \frac{\gamma_c}{k} \quad (4.5)$$

where

$$\gamma_s^2 = \beta^2 - k_o^2 n_s^2 \quad (4.6)$$

$$\gamma_c^2 = \beta^2 - k_o^2 n_c^2 \quad (4.7)$$

$$k = k_o n_f \cos \theta \quad (4.8)$$

As a result, equation (4.3) can be rewritten to give the following eigenvalue equation.

$$kW = m\pi + \tan^{-1} \frac{\gamma_c}{k} + \tan^{-1} \frac{\gamma_s}{k} \quad (4.9)$$

where $m = 0, 1, 2 \dots$ denotes the mode number and W is the waveguide thickness. Hence, if the propagation constant β and the waveguide thickness W satisfy the equation then a discrete set of modes can be supported i.e. zig-zag rays with certain incident angles can propagate as guided modes in the high index layer.

In order to use the eigenvalue equation to obtain the modal solutions for a given waveguide we rewrite equation (4.9) in a normalised form. This normalised form allows any step index structure to be easily solved. The normalised frequency V and the normalised guide index b are defined as follows

$$V = k_o W \sqrt{n_f^2 - n_c^2} \quad (4.10)$$

and

$$b = \frac{(N^2 - n_s^2)}{(n_f^2 - n_s^2)} \quad (4.11)$$

The asymmetry measure of the waveguide is defined by:

$$a = \frac{(n_s^2 - n_c^2)}{(n_f^2 - n_s^2)} \quad (4.12)$$

It can be seen that $a = 0$ for a symmetric waveguide and tends to infinity as the asymmetry increases.

Substituting the normalised values into the eigenvalue equation gives:

$$V\sqrt{1-b} = m\pi + \tan^{-1} \sqrt{\frac{b}{1-b}} + \tan^{-1} \sqrt{\frac{a+b}{1-b}} \quad (4.13)$$

Equation (4.13) can be solved numerically to produce the normalised dispersion curves³ shown in Figure 4.2. The effective index of the waveguide can be obtained from these dispersion curves when the waveguide parameters are known. Above the critical angle, defined by Snell's Law, the light is no longer confined in the guiding layer and begins to leak into the substrate. This situation is known as the cutoff of the guided mode, and is represented on Figure 4.2 when the curve crosses the V axis.

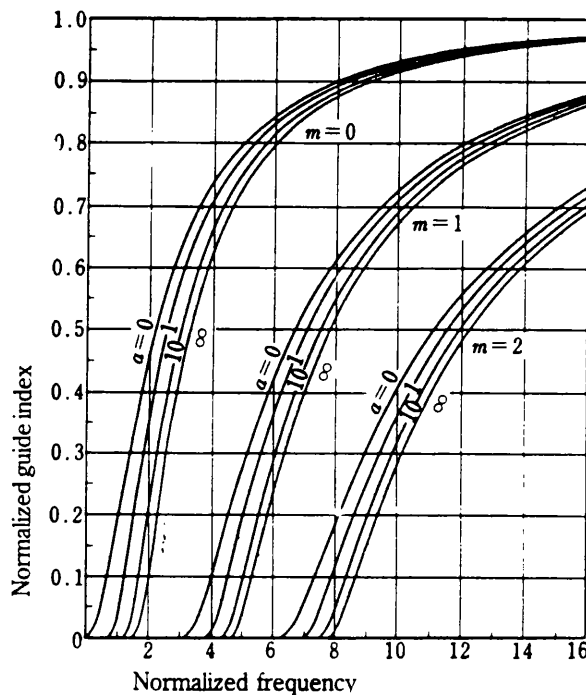


Figure 4.2 Dispersion curves of step-index planar waveguides taken from reference 3.

A similar procedure for TM modes is followed and produces the dispersion relationship illustrated in equation (4.14). Once again a discrete spectrum of guided modes plus a continuum of radiation modes are supported.

$$kW = m\pi + \tan^{-1} \left(\frac{n_f}{n_s} \right)^2 \left(\frac{\gamma_s}{k} \right) + \tan^{-1} \left(\frac{n_f}{n_c} \right)^2 \left(\frac{\gamma_c}{k} \right) \quad (4.14)$$

Although a thickness of W is measured for the waveguide the guided mode is actually confined to an effective thickness W_{eff} because it spreads somewhat into the substrate and clad. This width W_{eff} , is measured between the fictitious boundaries above and

Chapter 4 Channel waveguide procedures

below the waveguide film that are associated with the Goos-Haenchen shift. This is described as

$$W_{\text{eff}} = W + \frac{1}{\gamma_s} + \frac{1}{\gamma_c} \quad (4.15)$$

Having derived the basic dispersion characteristics it is possible to derive subsequent waveguide parameters for 2-D slab waveguides (infinite in y direction) employing the prism coupler. Referring to Figure 4.3 it is possible to set up relations for when the horizontal wave component in the prism is equal to the propagation constant of one of the guided modes. Consequently, the effective index N of a particular guide mode is described as follows

$$N = n_p \sin \left(\alpha + \sin^{-1} \left(\frac{\sin \theta}{n_p} \right) \right) \quad (4.16)$$

By evaluating the propagation constants for two or more modes it is possible to employ the dispersion relationship given in Equation (4.13) to numerically solve (iterative process) the waveguide parameters of effective thickness, refractive index and film thickness.

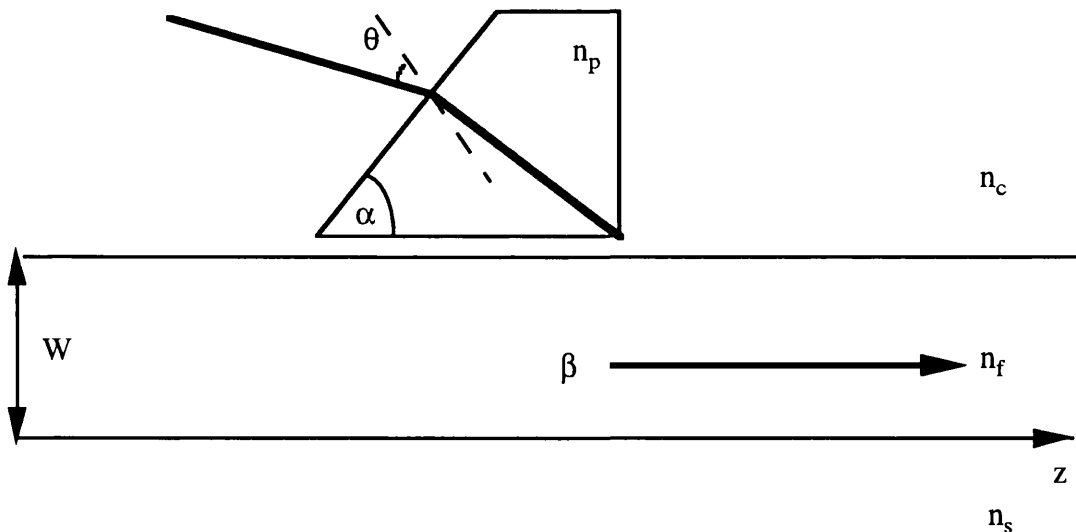


Figure 4.3 Schematic of prism coupling geometry

Prism coupling measurements were undertaken, for initial characterisation of planar waveguides. This is a simple technique which is detailed in many standard texts, hence, only a brief overview of the method is given here.

Chapter 4 Channel waveguide procedures

The standard deposition used throughout this work produces a step index waveguide as illustrated in Figure 4.1. In order to excite a guided mode, light must be coupled into the high refractive index layer. This can be achieved utilising a high-index, prism in very close proximity to the planar waveguide. A guided wave can be excited through phase matching the incident wave to the guided mode. When a laser beam strikes the base of the prism at an angle greater than the critical angle, then it undergoes total internal reflection (TIR) and the evanescent fields extends from the base of the prism into the waveguide.

As mentioned previously high-index (>1.5), high-precision prisms were used to excite the planar films. Two types of prism were used: SF15 and BaK4 Schott glasses. The SF15 had a high index of 1.694 and a prism angle of 60° , however the glass was relatively soft and susceptible to damage when being clamped on to the sample. Consequently, BaK4 Schott glass was used since it was more durable, although the index was smaller, being 1.567, and as a result required a larger prism angle of 75° . With the benefit of having a crystal shop on site it was possible to produce good prisms with accurate angles.

The TE polarised light from an He-Ne laser operating at 632.8 nm was coupled into the slab waveguides ensuring that the coupling regime was weak and that the beam width was sufficiently large for high-accuracy measurements. The refractive index and thickness of the films were measured at the point where the beam strikes the base of the prism.

To check the results from the prism coupling experiments two other techniques were used. The first method, involved removing an area of unsintered soot from the sample using a razor blade. The soot was then consolidated and the step between the two regions was measured using a Talystep, or Dek-Tak. However, a lip was often found at the point of removal owing to soot shrinkage. Also, one had to ensure complete removal of soot from the uncoated region for accurate measurements and due to the sample being processed before consolidation it was necessary to place another similar untouched substrate to compare thicknesses measured and thicknesses calculated employing the prism coupler.

A second, more ideal, solution was to use a selective etch after consolidation of the soot. This enabled the sample to be initially characterised by the prism coupler. The points at which the prism measurements were taken were then etched. A Pliskin etch was used to perform the necessary etching. This consists of 15 parts HF (49%), 10 parts HNO_3 and 300 parts H_2O . The selectivity of the etch was considerable with the

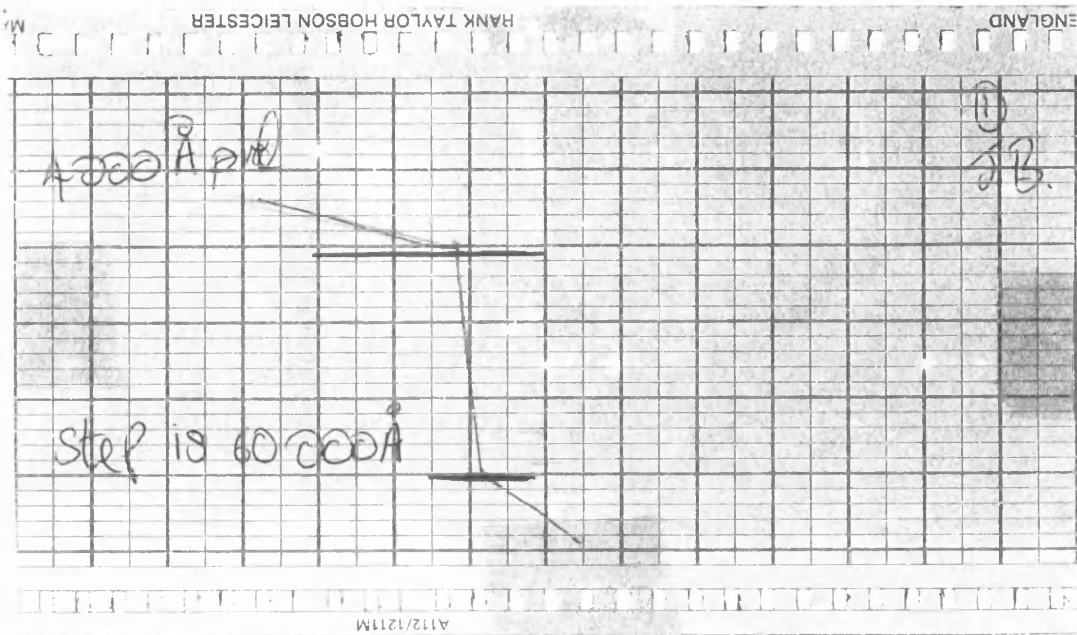


Figure 4.4 Example of a talystep measurement for Pliskin etch.

deposited SiO₂-P₂O₅ layer etch rate being 20 times faster than the thermal SiO₂ buffer. The etched pit was profiled using the Talystep or Dek-Tak. From the differences in slope of the side walls it was possible to accurately determine the etch depth. A typical talystep illustrating the nature of the etch is given in Figure 4.4.

Implementing the first technique, generally three points across the sample were measured one at the centre and one at each of the two sides. A typical talystep measurement is shown in Figure 4.5. To compare this to the prism coupler, values measured and calculated for a typical deposition are given in Table 4.1.

Position	Thickness-Talystep (µm)	Thickness-Prism Coupler (µm)	Variation (%)	Refractive Index
Left	5.9	5.72	+3.1	1.469
Centre	6.2	6.13	+1.1	1.469
Right	7.2	6.96	+3.3	1.469

Table 4.1 Comparison between prism coupler and talystep measurements.

For this particular deposition a high flow rate of POCl₃ was used and the film consolidated at a temperature of 1250 °C. It should be noted that the variation between

Chapter 4 Channel waveguide procedures

the values calculated using the prism coupling and those physically measured are accurate to approximately 3%. Also, the refractive index measured at each point correlates to a uniform index film across the sample. The variation of thickness is $\sim 17\%$ across a 3" wafer for a constant torch speed.

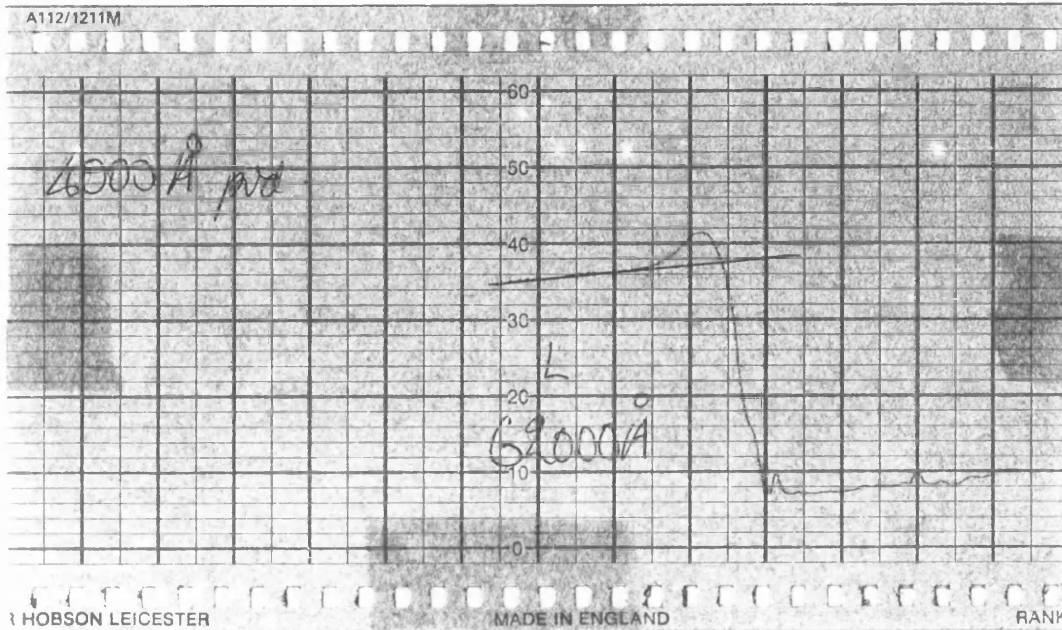


Figure 4.5 Example of a talystep measurement showing lip at scraped edge.

The Pliskin etch was used extensively offering the ability to prism couple before etching and to gauge the thickness across the complete sample instead of the centre region only. In some instances measuring only across the centre region could give spurious results as it would be possible to coincide with a band and thus, appear to give better results than actually produced.

In order to reduce the film thickness variation which arises when a constant torch speed was used, a variable traversal speed was tried. Once again a highly doped phosphorous layer was deposited and the sample consolidated under similar conditions as above. However, the torch speed was varied as a factor of $1/(\text{Radii of the turntable})$ to take into account the differences in the angular velocity. As can be seen from Table 4.2, the variation in thickness dropped dramatically to a variation of only 6%. This could still be observed by the naked eye with banding still taking place across the sample. The prism coupler once again was measured to vary only by $\sim 3\%$ in comparison to the Talystep measurements.

Position	Thickness-Talystep (μm)	Thickness-Prism Coupler (μm)	Variation (%)	Refractive Index
1	5.9	5.71	+3.3	1.467
2	6.0	5.77	+3.9	1.467
3	6.2	5.98	+3.5	1.467
4	6.3	6.09	+3.3	1.467
5	6.3	6.08	+3.5	1.467

Table 4.2 Thickness variation of a $\text{SiO}_2\text{-P}_2\text{O}_5$ film over a distance of 3".

The prism coupler also provided important information into the suitability of films for further processing, especially in the case of rare earth doping. It was able to highlight two categories of scatter:

1. Out-of-plane scattering
2. In-plane scattering

Through the guided stripe and the mode-lines it is easy to qualitatively determine the magnitude of both of these phenomenon. If the stripe was visible, indicating out of plane scatter, then at this early stage it is likely that the loss will be several decibels per centimetre, and thus, the waveguide is deemed unsuitable for further lengthy processing. Similarly, the in-plane scatter was easily estimated from the brightness and expanse of the line extending from the central spot in the m-line.

Figure 4.6 shows a sample with a high loss due to both out-of-plane scatter as demonstrated by the visible stripe and in-plane scatter from the broad divergence of the beam. Out-of-plane scatter was due to imperfections at the surface of the waveguide structure, which in this particular case was due to the rare earth doping of the waveguide. The inhomogeneous distribution of the rare earth causes the broadening of the beam and once again is a good indicator as to the solubility of the rare earth in the glass matrix. As an example Figure 4.7 depicts a sample rare earth doped where the material and process conditions have been optimised resulting in virtually no out-of-plane scatter and very weak in-plane scatter.

The waveguides produced have been step index waveguides. However it is possible to tailor the index to form graded index waveguides i.e. an index distribution

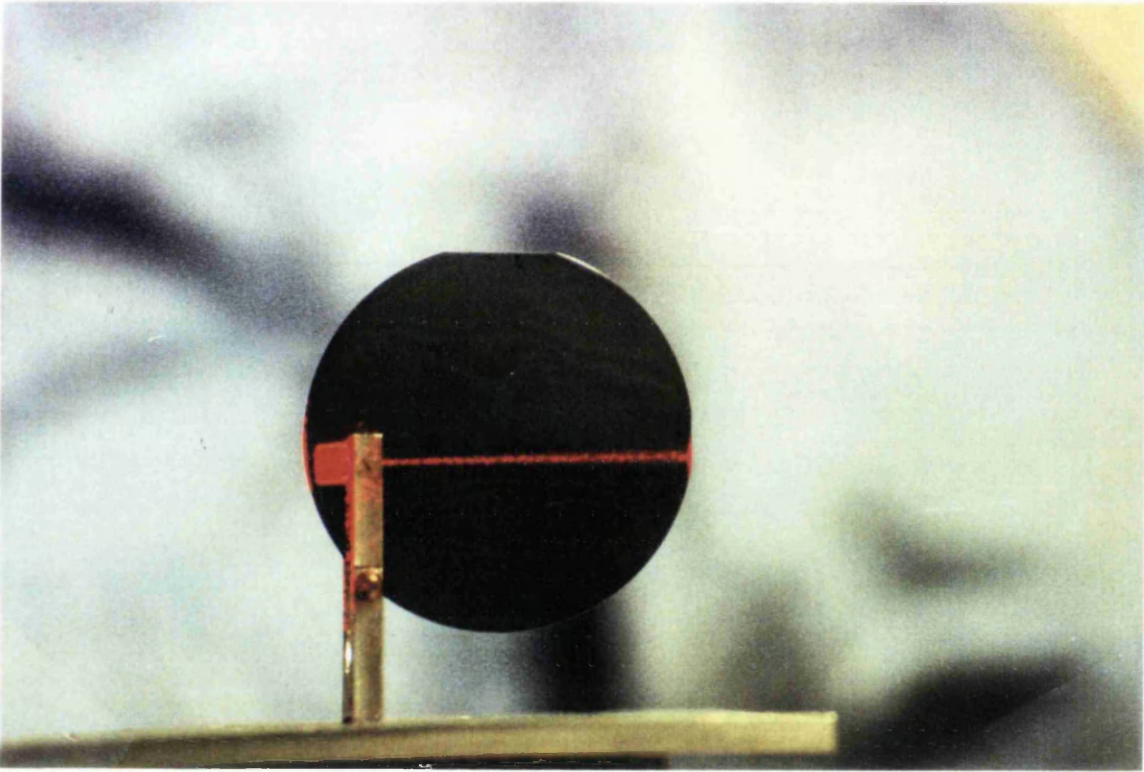


Figure 4.6 Photograph of fundamental mode propagating in Er^{3+} doped $\text{SiO}_2\text{-P}_2\text{O}_5$ layer.

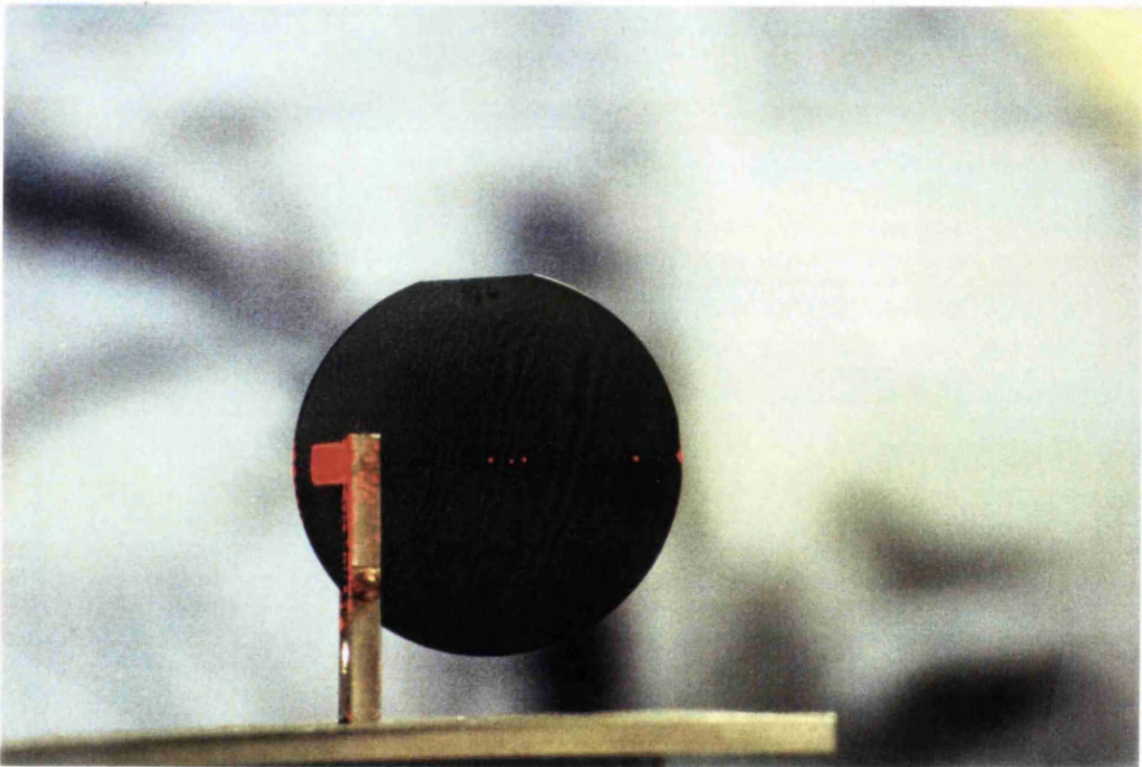


Figure 4.7 Photograph of fundamental mode propagating in Er^{3+} doped $\text{SiO}_2\text{-P}_2\text{O}_5$ layer.

Chapter 4 Channel waveguide procedures

$[n(x)]$ across the direction normal to the waveguide. As long as multimode guides are tested then it is possible to measure many effective indices N which can determine $n(x)$ based on the Wentzel-Kramers-Brillouin (WKB) method⁴.

For rare earth doped planar waveguides it was necessary to determine the doping level and doping uniformity before the photolithographic and reactive ion etching processes. Owing to the ability to define waveguides by sawing (discussed in Sections 4.5), this allowed the suitability of the waveguide to be determined before further processing was carried out.

The main method of observing waveguide quality after deposition was qualitative. However, for lossy samples, typically $> 1\text{dB/cm}$, various techniques are available, the main two being: the three prism technique⁵ and the fibre probe technique⁶ although other techniques such as the mercury drop technique⁷ can be used. The Fabry-Perot loss technique⁸ can also be used for channel waveguides.

The three prism technique, a method extended from the prism-sliding method is a technique which has been used extensively in Glasgow. The method is relatively easy and was necessary for sample evaluation. However, like the other techniques to be described, it was only used in the early days. It quickly became clear that if accurate losses could be measured, the devices were too lossy for further processing.

To implement the method, three prisms are employed: the first to couple light into the waveguide, the second a movable prism for coupling light out, and the third, a fixed prism for coupling out the remaining light. For the technique it is essential that the coupling efficiencies of the first and third prisms remain constant, ensuring that the coupling efficiencies are not altered as the 2nd prism is positioned along the wafer. As a result the output power of the guided light is independent of the coupling efficiency of the 2nd prism. The propagation loss of the planar waveguide can be subsequently found by plotting $P(z)$ as a function of distance. A least square fit to the experimental data produces a value for the propagation loss.

Another non-destructive technique is the fibre probe technique. The brightness of the guided wave streak coupled in using the prism coupler is proportional to the guide-light intensity at each point, providing the waveguide is uniform, thus enabling a figure to be deduced for propagation loss. An optical fibre maintained at the same angle and distance from the substrate detects the scattered light. The probe end is traversed along the waveguide to obtain the $\log P$ versus L plot.

Chapter 4 Channel waveguide procedures

In practice a 1 mm diameter plastic fibre with an NA of 0.47 was used as a probe and connected to a chart recorder via a Si photodetector. At each point of measurement the probe is traversed in a lateral direction across the waveguide stripe to determine the maximum intensity recorded. Lock in techniques were used to measure the powers and hence the losses were deduced.

To measure channel waveguide losses it is possible to use the cut-back method⁹. Unlike fibres, where it is a simple matter of measuring loss, this is as not as straightforward for planar samples as the sample length in comparison is very short and the effect of polishing or cleaving the sample to produce a different length can result in spurious measurements. However, the technique is very simple with a guided wave excited by end coupling and the transmitted intensity measured. As the name suggests the sample is then cut-back and the intensity measured. The transmission loss is then given by:

$$\alpha = \left| \frac{10 \log(P_1 / P_2)}{(L_1 / L_2)} \right| \quad (4.17)$$

where L_1 , L_2 and P_1 , P_2 are the lengths and transmittances for before and after cutting, respectively. The coupling conditions can not be guaranteed to be constant especially as the process should be iterated for accurate values. Another disadvantage is that it is a destructive method. For measurement of channel waveguides a fibre based procedure is adopted and detailed in Section 4.6.

For the techniques employed the processes although simple and non-destructive were highly time consuming as each sample required point by point measurements. As with most measurement systems, the greater the number of points used the better the accuracy of the method, consequently it was not uncommon for 20 measurements to be taken over a distance of 4 cm. The techniques also relied on continuous conditions with measurements having to be made where no isolated scattering centres were present.

4.3 Photolithography

Photolithography, a technique adapted from the microelectronics industry to optical integrated circuits (OICs), provides a means of defining optical waveguide patterns for subsequent etching¹⁰. The technique uses an ultraviolet photosensitive polymer. Depending on the polymer, known as photoresist, the pattern of the exposed region either remains, or disappears, after development. The former is known as a negative resist and the latter known as a positive resist. To define the pattern onto the resist a photomask which contains the waveguide pattern is placed onto the sample, the substrate is then exposed to the ultraviolet light and the sample is placed in a solution to develop the image. The processes developed in this work, allow structures down to $\sim 1 \mu\text{m}$ to be resolved. For sub-micron devices a direct write regime involving an electron-beam writer was used, this is detailed in Chapter 6.

The qualities necessary for an acceptable resist are: resistance against the etching, sensitivity, resolution, coating uniformity and adhesion to the substrate. Most of the current work used positive resist, thus, the regions which were exposed to the UV radiation were removed after development.

The masks used to define the waveguide pattern were either ferric, or chrome. High quality masks were produced by an electron beam writer, unlike the past when good quality masks were prepared by photoreducing patterns. The masks in general were light field indicating that the patterns were defined by the opaque regions i.e. the metal lines. Various mask designs were produced some involving straight waveguides with varying widths and more intricate designs based on spiral designs to produce waveguides which were over 30 cm in length, for future Er doped amplifier structures. Other masks designed were couplers (1x2, 1x3, MMI), Mach-Zehnders and ring resonators.

The standard photolithographic process was as follows. Primer was spun onto the sample, to aid adhesion and to prevent uneven coating which would result in poor contact between the resist and mask. The resist was then deposited on to the sample using a syringe with $0.3 \mu\text{m}$ filter and spun at 3000 rpm to produce an even coating. The sample was then pre-baked at 90°C for thirty minutes to completely vaporise any remaining solvent and enhance adhesion to film. Exposure of the samples was carried out using either a contact printer or more preferably a Hybrid Technology Group (HTG) mask aligner. Contact printing ensures a hard contact between the resist and mask, eliminating diffraction effects and thus ensuring a good reproduction of the

After development, the samples were rigorously tested for correct exposure and development. Markers, of sizes 1- 4 μm , were designed in to each mask and analysed either under an optical microscope or by use of an SEM.

Etching techniques were employed to reproduce the waveguide pattern into the deposited film. Depending on the etch parameters used, either a direct method, or a lift-off process, was used to define the waveguides. The two techniques are illustrated in Figure 4.8. The direct method, described earlier, is the simplest, with the resist pattern providing the mask for etching. When deeper etch depths, or more rigorous etches, were required the lift-off process was used. This involved a metal mask being deposited onto the resist and the unmasked waveguide areas. Prior to evaporating the metal it was found to be advantageous to carry out an O_2 RIE for 1 minute, to remove any residual resist left in the unmasked areas. The disadvantage of this was that part of the resist was also partially removed. By immersing the sample in acetone the remaining resist was removed along with the metal layer on its top. This left only the metal pattern on the sample. A typical process used involves a light field mask with a special type of resist known as reversal resist¹¹. Typical parameters are given in Table 4.4.

Resist primer	Hexamethyl disilazine (HMDS)
Spin speed and time	4000 rpm for 30 seconds
Photoresist	AZ-5214E
Spin speed and time	4000 rpm for 30 seconds
Photoresist thickness	1.2 μm
Soft bake temperature and time	90 $^\circ\text{C}$ for 10 minutes
Exposure time - Mask aligner	7 seconds
Reverse bake temperature and time	125 $^\circ\text{C}$ for 10 minutes
Flood exposure - Mask aligner	90 seconds
Developer	1:1 AZ 312 MIF Developer:RO water
Development time	75 seconds
Metal mask	NiCr
Metal thickness	2000 Å
Lift-off	Immerse in acetone

Table 4.4 Standard process for reversal photoresist patterning.

To remove the remaining photoresist, or metal mask, after etching, samples were placed either in an acid bath, described in Section 4.2.1, or in a chrome etch (4 parts

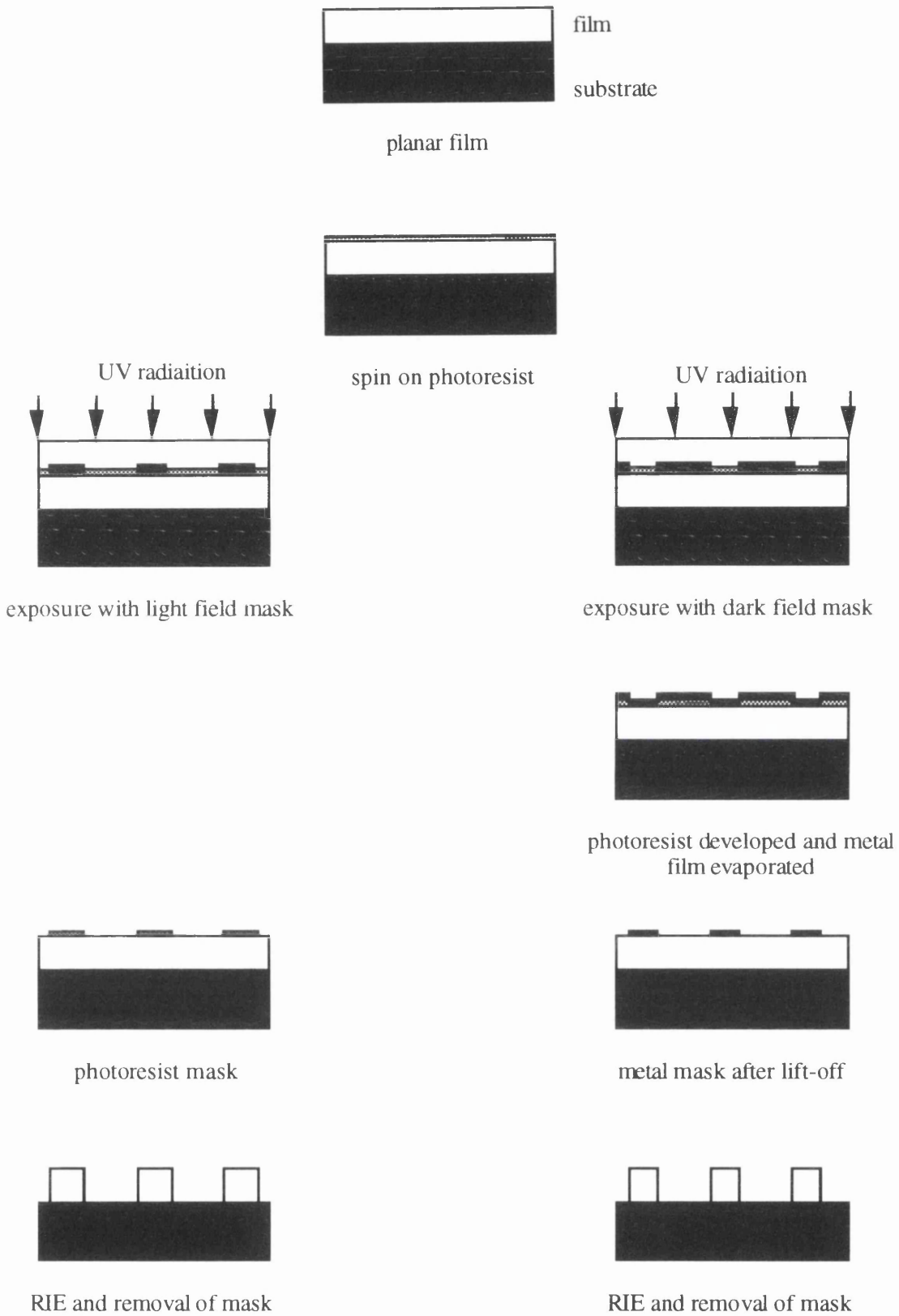


Figure 4.8 Photolithographic process using positive photoresist with light (left process) and dark (right process) field masks.

Chapter 4 Channel waveguide procedures

HCl (30% concentration) and one part RO water), respectively. In both cases the masks were removed in the order of minutes.

Care had to be taken when depositing the metal for lift-off. It was found that for films of NiCr with thicknesses greater than 2000 Å the metal cracked. Two possible problems were either heat transfer during evaporation was causing the resist to reflow, or only a certain thickness of metal could be tolerated before internal stress induced cracking. To help prevent any problem associated with resist flow during the metal deposition a 15 minute chlorobenzene soak was used. This is a standard technique for improving lift-off and was used to create a harder layer of resist at the surface.

The following tests were conducted (Table 4.5), all samples were coated with S1400-31 photoresist.

Mask	Thickness	Additional information	Surface quality	Lift-off
NiCr	2000 Å		cracked	N.A.
NiCr	2000 Å	Chlorobenzene soak	cracked	N.A.
NiCr	100 Å		good	good
NiCr	500 Å		good	good
Ti/ Ni	150 Å / 600 Å (3x)		good	poor
NiCr	500 Å (4x)		cracked	N.A.
Ti/ Ni	150 Å / 600 Å (3x)	Chlorobenzene soak	good	poor

Table 4.5 Various metal depositions.

From these studies, it became apparent that there was a critical thickness at which point the NiCr began to crack. Unfortunately, this was below the 2000 Å necessary for the large etch depths required in this work. To overcome the stress problems, alternate Ti/ Ni layers were deposited. This allowed thick films to be deposited, however, when lift-off was attempted the metal tended to peel completely off due to poor adhesion.

A solution to the above problem was found to be the evaporation of 2000 Å NiCr onto the silica film. Resist was spun on to the metal and the resist was exposed and developed. Using the resist as a mask, the NiCr was wet etched and the remaining resist removed by immersing in acetone. This was found to give adequate results with the 2 μm markers easily distinguished. A schematic of the process is illustrated in Figure 4.9 and an SEM of the metal mask given in Figure 4.10.

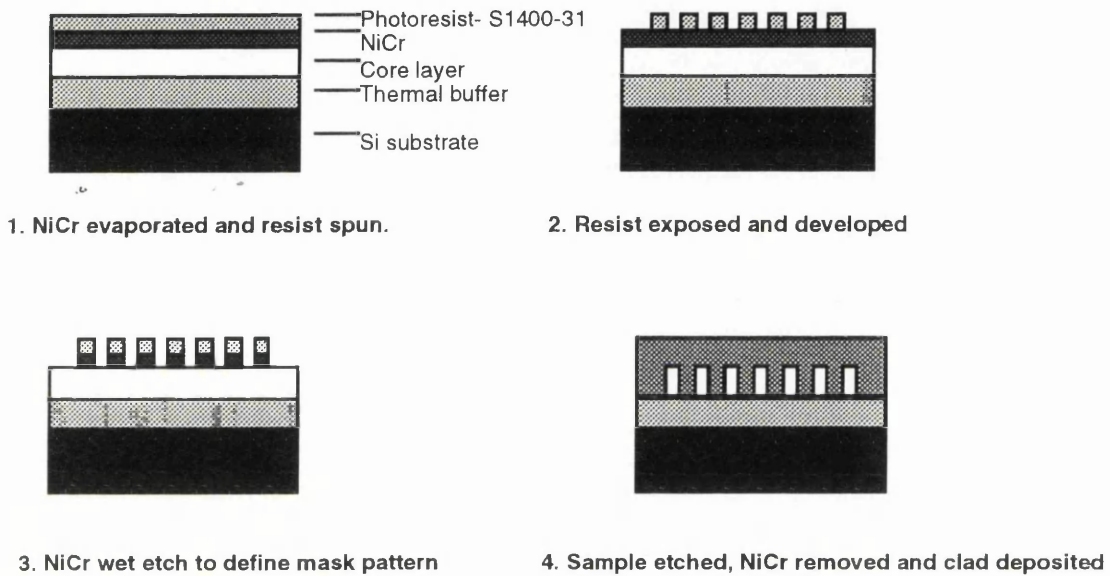


Figure 4.9 Schematic diagram of photolithographic process for metal mask.

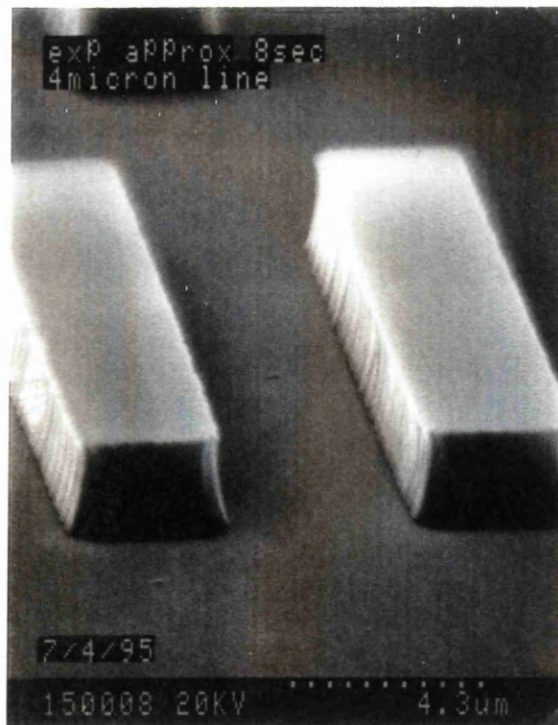


Figure 4.10 SEM photograph of NiCr metal mask and resist.

4.4 Reactive Ion Etching (RIE)

The previous section described the processes to produce replicas of circuit features on the planar sample. To transfer the pattern into the planar waveguide the unmasked region is selectively removed by either dry or wet etching.

Reactive ion etching (RIE) is a form of dry etching grouped into the glow discharge methods¹². Other related techniques include reactive gas plasma and inert gas plasma etching. The other major form of dry etching is based on ion beam etching, this is more of a physical process. Typical processes are ion milling, chemical assisted ion milling and reactive ion beam etching. It is therefore, probably easier to think of RIE as being a hybrid of the glow discharge and ion beam techniques.

Plasma etching has had a rapid development since its beginning in the early 1970s¹³. This was stimulated by its application to the manufacture of microelectronic devices, with the ability to mass replicate tightly controlled, micron sized features in a variety of materials, the most significant material being Si. The basic reasons for the rapid development of plasma etching include: anisotropic etching, less consumption of raw materials (cost and environmental impact, although some may debate this point as CFCs are released), clean process taking place in a vacuum, compatible with automation and precise pattern transfer.

The simplest plasma reactors consist of two parallel plate electrodes in a low pressure (typically ranging from 0.01 to 1 Torr) chamber. When a high frequency voltage is applied between the electrodes, current flows forming a plasma, which emits a characteristic glow. Reactive radicals (atoms with incomplete bonding) are generated in this electrical discharge. The electrons collide with neutral etch gas molecules to form the important species in plasma etching. The sample to be etched is placed on the driven electrode and exposed to both neutral and charged species. Some of these species combine with the substrate and form volatile products which evaporate and etch the sample.

In formal terms there are equal numbers of positive and negative charged particles in a plasma, but since the electrons are more mobile than the heavier ions they diffuse to the substrate electrode faster and charge it negatively, leaving the plasma centre positive. A boundary layer known as a 'sheath' is set up between the plasma and electrodes. Within the plasma the ion motion is random, however, when a positive ion drifts to the

sheath boundary, the perpendicular electric field accelerates it towards the wall and substrate surfaces to initiate etching.

A Plasma Technology μp 80 machine has been used in the following research. The configuration of the machine is such that the sample is placed on an electrode with a smaller area so that most of the applied voltage is dropped across the electrode. This is illustrated in Figure 4.11.

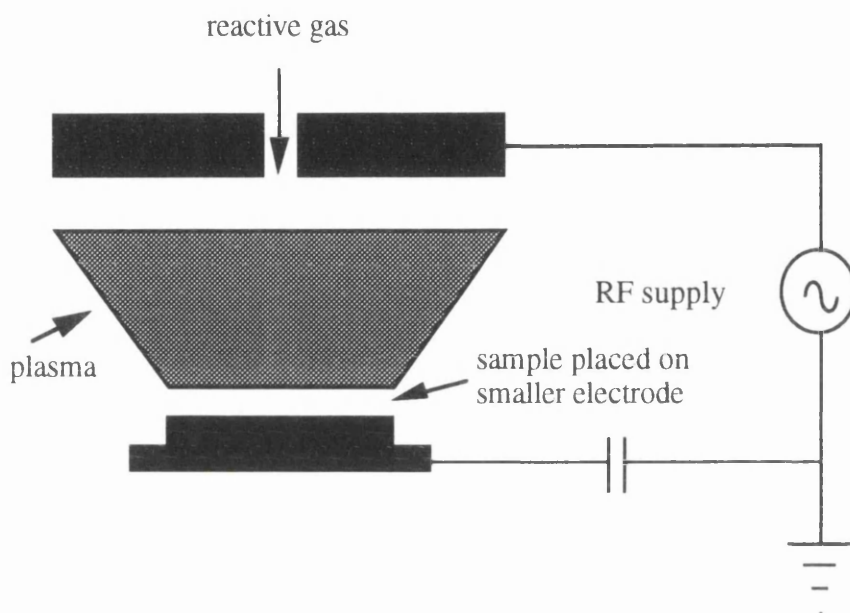


Figure 4.11 Schematic diagram of RIE chamber.

Several different etching processes were investigated during the course of the work. To be practical an etching process must be relatively fast and have good selectivity between the mask and the material being etched. In addition the process should be anisotropic, resulting in vertical sidewalls and result in minimum surface damage. For this research particular problems were encountered for rare earth doped films, due to the non-volatility of the rare earths. This had the undesirable effect of producing surface roughness in the form of rare earth fluoride compounds and micromasking. The redeposition of the rare earth was observed to be in the order of $0.1\ \mu\text{m}$. However, for nonhomogeneous distributions, observed in early aerosol doping the scale was often much larger (described in Chapter 5) as shown in Figure 4.12.

Surface roughness has the undesirable effect of increasing propagation losses. Two indirect methods were devised to reduce the optical field interacting with the imperfections at the sidewalls. Samples were over etched, so that all of the film and $\sim 2\ \mu\text{m}$ of the thermal oxide layer were removed. This increased the separation between

the rare earth redeposition and waveguide core. Samples were also reflowed to smooth the sidewalls. This involved samples being placed in a consolidation furnace at a temperature to soften the glass. The effects of surface tension resulted in the waveguide walls being smoothed. However, a significant problem for rare earth doped silica waveguides was that increased thermal exposure (discussed in Chapter 5) has the detrimental effect of reducing the fluorescence lifetime and consequently the efficiency of devices¹⁴. It was also observed for rare earth doped channel waveguides that as samples were reflowed surface tension of the glass functioned to round the waveguide cross section which fused with the redeposited material creating structures as illustrated in Figure 4.13.

In the following sections the major etching processes investigated during the course of this project will be described. The advantages and disadvantages of each will be outlined.

4.4.1 CHF₃ etch

Throughout the duration of these studies most structures were defined using a low flowrate, low pressure, high DC bias, CHF₃ etch. The advantages of this process were the reduced etch wall roughness, anisotropy (~5° from the vertical), etch selectivity between film and mask and reduced non-volatile rare earth products. This is a direct consequence of the larger mean free path for plasma collisions which results in a more physical etching mechanism, similar to the ion beam etching discussed in the introduction. The nature of the etch also allowed photoresist to be used as a mask material with maximum etch depths of 9.2 μm possible for photoresist thicknesses of 2.1 μm i.e. etching ratio of > 4:1. Figure 4.14 gives an example of a sample etched employing the CHF₃ etch. From the figure it can be seen that the sidewalls are almost vertical and that there is very little surface roughness. However, it is evident that trenching has taken place which is a result of ions reflecting off the base of the waveguide.

Another result of this process is etch rates of 2.1 μm/hour as low fluoride:carbon ratios result in low etch rates¹⁵. The low fluoride:carbon ratio also increases polymer redeposition owing to the reduced F atoms ability to volatilise the Si. Therefore, to reduce polymer redeposition it was necessary to interrupt the etch after 50 minutes to clean the chamber employing both IPA solution followed by a low pressure O₂ RIE. Taking into account the necessary procedure of pumping the chamber down to base pressure then typically, to etch a standard device took almost two days. One of the



Figure 4.12 SEM photograph of an etched $\text{SiO}_2\text{-P}_2\text{O}_5$ waveguide with a nonhomogeneous distribution of rare earth dopant.

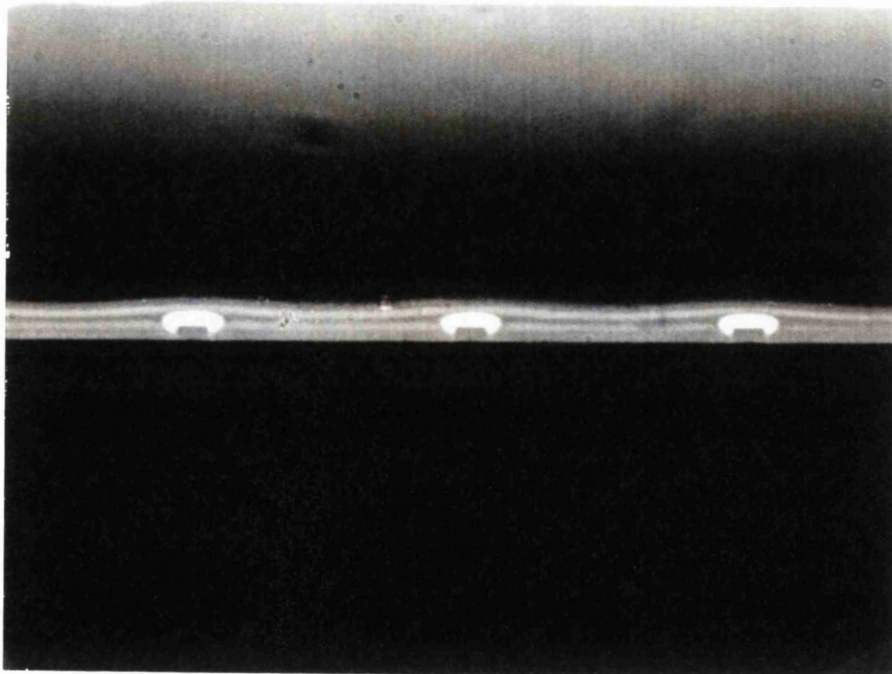


Figure 4.13 Photograph of cross-section view of rare earth doped $\text{SiO}_2\text{-P}_2\text{O}_5$ waveguide.



Figure 4.14 SEM of RIE of $\text{SiO}_2\text{-P}_2\text{O}_5$ film using CHF_3 etch.

objectives of the project was to improve the sample yield and although this process provided good results it was a 'bottleneck' to device fabrication.

The maximum flowrate available on the μP 80 machine for CHF_3 was 45 sccm. In an attempt to increase the etch rate, etch tests were conducted with the pressure and DC bias increased to 25 mT and 610 V respectively. The increase in pressure results in a lower dark space near the driven electrode and consequently reduced etch directionality. The RF power was thus increased to 250 W compared to the 100 W typically employed which counteracts the reduced etch directionality for increased pressures.

The high CHF_3 etch rate as expected caused much more polymer redeposition. So much so that samples were rendered useless when employing a resist mask. Metal masks as discussed in the previous section (Section 4.3) were used and etch rates as great as $5.4 \mu\text{m}/\text{hour}$ were measured. The etch quality was also good and comparable to the low pressure.

4.4.2 $\text{C}_2\text{F}_6 + \text{O}_2$ etch

As mentioned previously for larger etch rates it is necessary to increase the fluoride to carbon ratio. This is possible by adding O_2 to the plasma which also attacks the

polymer redeposition and photoresist mask material. Etch tests were conducted for C_2F_6 plus O_2 with metal masks. The relevant parameters are detailed in Table 4.6. As seen from the table for this high power process the etch was quite physical in nature even sputtering the metal off. From the parameters tried it was evident that a much more robust mask would be necessary since there was not much etch selectivity between film and mask material. The maximum thickness only being $3.8 \mu m$ before complete mask removal.

From previous work the etch rate was measured to be $6 \mu m/hour^{16}$ for reduced powers of 100 W. The etch quality was found to be very good. However, when rare earth doped material was etched the etch rate decreased to $2 \mu m/hour$.

4.4.3 $CHF_3 + C_2F_6$ etch

From results based on recipes used by Dr G. D. Maxwell at BT Laboratories a CHF_3 etch with the addition of C_2F_6 was investigated in the latter period of these studies. Once again the parameters are detailed in Table 4.6. Owing to the relatively high flow rates, the pressure was high as were both the RF power and DC bias.

The important advantage of this method is that the etch rate is $7.8 \mu m/hour$. Providing 2000 \AA of NiCr can be deposited then samples can be etched $8 \mu m$ in a much reduced time compared to the CHF_3 etch. The etch quality of the waveguides is very good as illustrated in Figure 4.15. Owing to time constraints, however, it was not possible to determine whether there was an improvement in propagation losses for samples etched in $CHF_3 + C_2F_6$ compared to low pressure CHF_3 etches, especially for rare earth doped samples. It is therefore the authors opinion that a more complete investigation into etching of rare earth doped silica is still to be carried out.

A summary of the characteristics of the various etch processes are presented in Table 4.6.

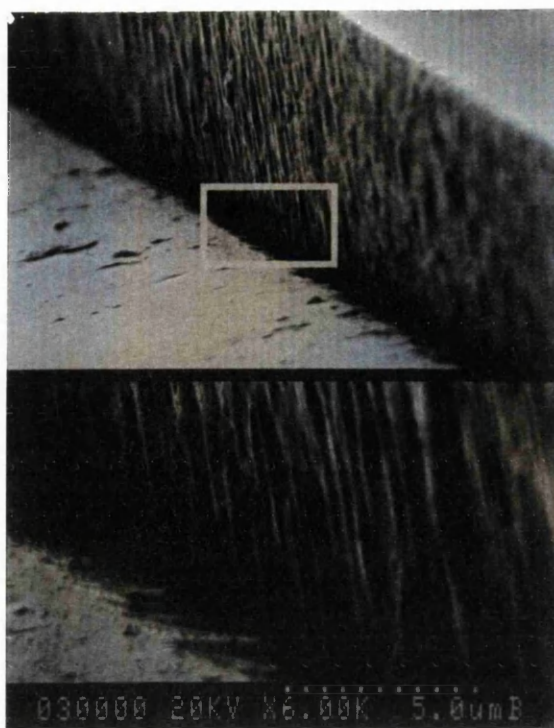


Figure 4.15 SEM of RIE of SiO₂-P₂O₅ film using CHF₃/ C₂F₆ etch.

	CHF ₃ / C ₂ F ₆	CHF ₃	CHF ₃	C ₂ F ₆ / O ₂
Flow rate (sccm)	45 24	45	8	24 15
Pressure (mT)	32	25	8	23
Power (W)	250	250	100	250
d.c. bias (-V)	580	610	510	610
masks				
S1400-31 (Å)	24000	24000	24000	24000
NiCr (Å)	1500	1500	N/A	1500
Chrome (Å)	1500	1500	N/A	1500
Etch rate (µm/hr)	7.8	5.4	2.1	3.8 (minimum)
Mask etch rate				
S1400-31 (Å/hr)	Polymer	Polymer	5800	N/A*
NiCr (Å/hr)	1800	1100	N/A	N/A*
Chrome (Å/hr)	2100	1300	N/A	N/A*

Table 4.6 Various etch parameters for SiO₂-P₂O₅ films investigated.

* the masks were all completely removed within 30 minutes. However, double the etch depth was measured for the metal masks in comparison to the resist mask.

4.5 Waveguide cutting and polishing processes

To be able to test the etched devices it is necessary to efficiently couple light into the waveguides by end-fire, or fibre butt-coupling. This involves the waveguides being cut perpendicular to the waveguide axis before being polished to remove any chips, scratches and roll-off at the edges. Furthermore to produce Fabry-Perot laser cavities for rare earth doped silica it is essential that the waveguides are polished normal to the waveguides with only small facet angles being able to be tolerated¹⁷.

The lengthy process involves the planar sample being cut, using a circular diamond saw on a Loadpoint machine. It is interesting to note that samples could not be cleaved along the crystal axis due to dislocations introduced in the Si crystals during the high temperature consolidation (discussed in Chapter 3). Generally the 3" wafer were cut into rectangular pieces with a reference side denoted. Following this waveguides were defined and placed in parallel with the reference edge. A special glass carrier rod as illustrated in Figure 4.16 was devised and enabled the reference edge to lie against the raised carrier rod edge. By employing Shellac the sample was bonded up-side down to prevent chipping during the polishing process and the Shellac filled in the gaps between the ridges. The carrier rod was then placed in a holder for a Logitech polishing ring. Once again this was designed to run parallel with the reference edge. It should be noted that the completed polished waveguide edges were measured to be within 0.25° of the normal.

The polishing itself involved a three stage process. A roughing down, employing $100\ \mu\text{m}$ silicon carbide powder was followed by a semi-polish using $3\ \mu\text{m}$ aluminium oxide powder. The sample was finally polished in Syton W15, a colloidal silica solution.

The cutting and polishing processes were rather lengthy, typically taking a week. Thus, the Loadpoint cutting machine was adapted to allow accurate and good quality cutting. The diamond saws were replaced with $100\ \mu\text{m}$ thick resinoid blades impregnated with 3000 grit diamonds. This effectively produced polished grade facets. However, for unclad waveguides often due to stress the waveguides would break from the edges. This was not the case for clad waveguides where the clad effectively reduced the strain on the channels.

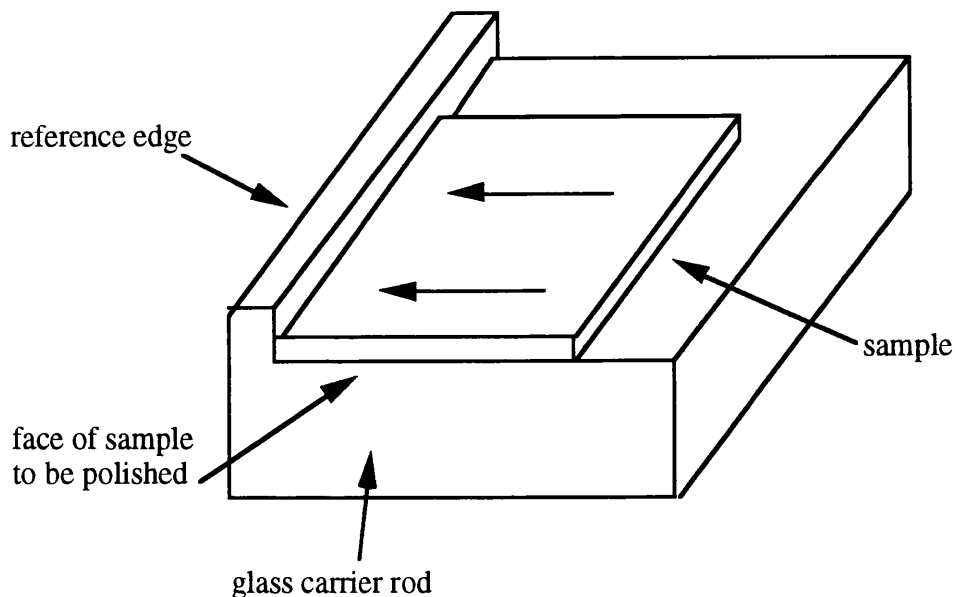


Figure 4.16 Glass carrier rod design for polishing of samples.

To produce waveguides normal to the edges a microscope, with a cross-wire lens was installed, and a rotating mount polished flat was devised. Thus, the following procedure was developed to produce accurate cuts. First a 'scrap' piece was cut and the cross-wire carefully aligned to the cut. The sample to be cut was then inspected under the microscope and the channel waveguides lined up parallel to the cross-wire. The turntable then allowed the waveguides to be rotated by 90^0 and to be cut in the desired position i.e. normal to the waveguides. The system is extremely user dependent but with careful alignment typical measurements given in Table 4.7 were obtained. For these measurements samples were cut into $2 \times 2 \text{ cm}^2$ square pieces. An edge was chosen

Sample identification	Deviation from normal relative to 1st edge (degrees)		
	1st edge	2nd edge	3rd edge
101	0.03	0.21	0.22
102	0.13	0.09	0.06
103	0.06	0.03	0.13
104	0.06	0.13	0.04
105	0.02	0.11	0.04
106	0.11	0.12	0.06

Table 4.7 Measurements of waveguide sawing accuracy.

and the other 3 edges measured in relation to it using a spectrometer, resolved to thirty seconds. This process thus allowed devices to be produced within the space of a few hours. Another advantage is that samples could be clad before cutting. This is important as devices which had already been cut before depositing a cladding layer would suffer from soot shrinkage and peel from the edges, thus requiring a further cutting and polishing process.

The adaptability of the system was further proven with ridges of between 25 and 100 μm width and 5 cm in length being able to be cut as shown in Figure 4.17 This is discussed in more detail in Section 5.2.3. for quick assessment of rare earth doped waveguides.



Figure 4.17 SEM of ridge waveguides formed by sawing.

4.6 Channel waveguide loss measurements

The chapter has shown in some detail all the necessary requirements for the formation of silica channel waveguides. The optical inspection of planar samples using the prism coupler, the subsequent photolithographic and reactive ion etching techniques for channel waveguide production and finally, the cutting of the clad channel waveguides for end-firing, or fibre-butt, coupling.

In order to produce waveguide lasers it was essential that low loss waveguides could be produced. This is essential if low threshold and high slope efficiency are to be demonstrated. In order to assess the losses of the channel waveguides an optical loss kit was set up, as illustrated in Figure 4.18.

The system allowed insertion losses to be measured at the wavelengths 632.8 nm, 1317 nm and 1553 nm. Spectral measurements could also be performed using the white light source. Two single mode optical fibre-pigtailed temperature controlled laser diodes were the sources at the infra-red wavelengths and a stabilised He-Ne laser end-fire coupled into a standard single mode fibre provided the red measurement. The laser diodes were internally modulated whilst the He-Ne was mechanically chopped to allow lock-in methods for detection. Standard fibre connectors were used so that the devices could be aligned in the visible and then easily switched to the infra-red. At the output, stages were able to be exchanged between fibre for power detection and objective lens to allow modal observation on a infra-red sensitive camera.

To improve coupling efficiencies and reduce Fresnel reflections the end of the input single mode fibre was coated in index matching fluid and brought into contact with the device. The device was coupled at 632.8 nm with an optical microscope above the device enabling quick alignment with the stages possessing differential and piezoelectric translation adjustment. At the output a multimode fibre coated with index matching fluid collected the light output. This was detected by a silicon photodetector and displayed on a lock-in amplifier. The fibres were adjusted at both input and output employing the piezoelectric adjustments to maximise the throughput. Subsequently, it was a simple matter to switch to either the 1.3 μm or 1.5 μm source.

For the long wavelength sources a 3 dB coupler was connected such that one output was butt-coupled to the waveguide device and the other port was connected to a Ge detector for a reference value. The output from the device was connected to a Ge photodetector. Both the Ge detector signals were subsequently pre-amplified and measured on the lock-in amplifiers.

To deduce insertion losses the devices were removed and the throughput was detected for fibre to fibre measurements. Table 4.8 gives an example of loss measurements at 632.8 nm for 5.8 cm long Nd^{3+} doped silica waveguides with dimensions of $12 \times 8 \mu\text{m}^2$. Of interest is that although this was a good wafer with very low insertion losses the problem of scattering centres is highlighted for the waveguide that has an insertion loss of 8.9 dB, which is four times greater than the typical measurements.

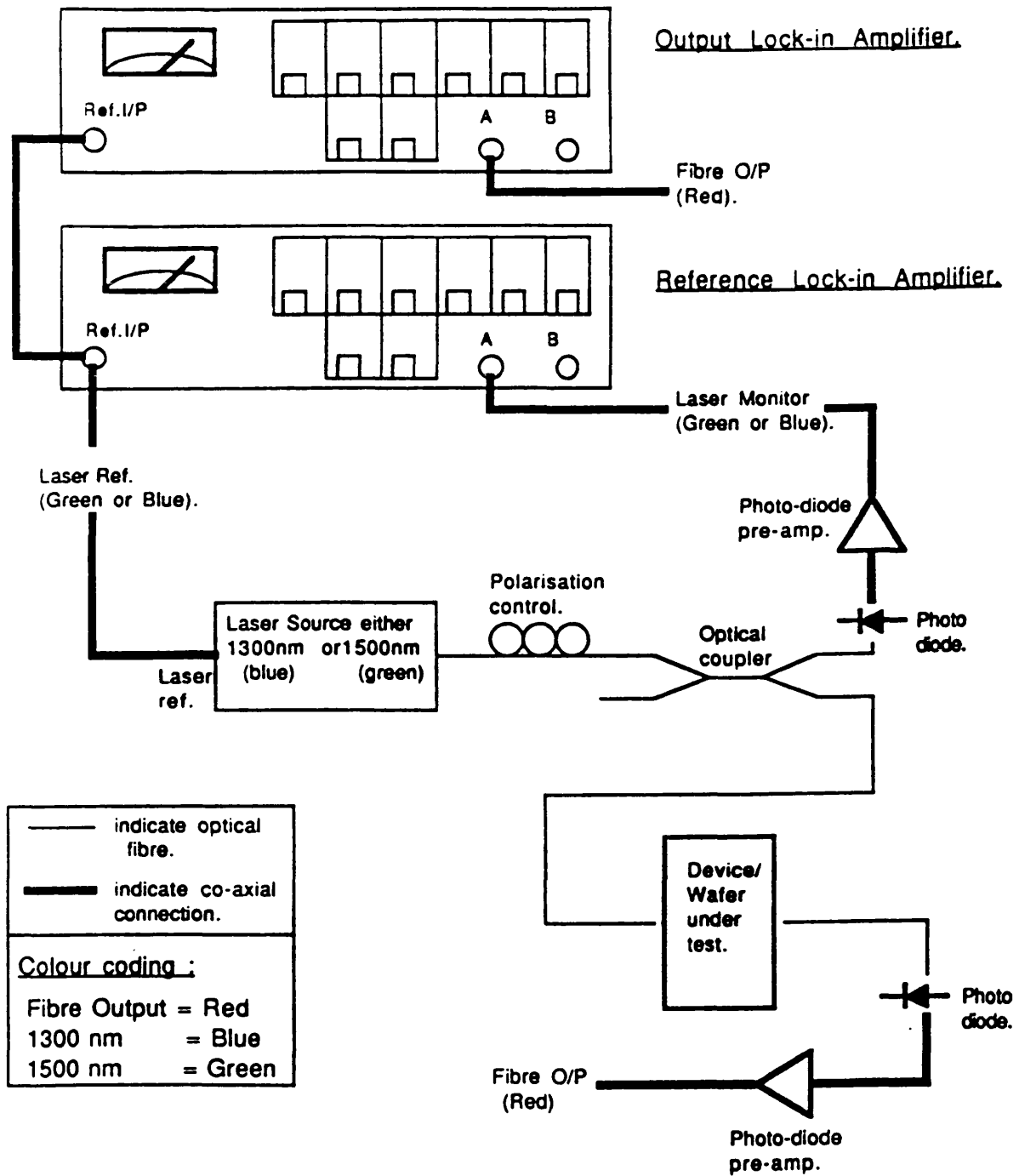


Figure 4.18 Loss measurement kit to measure ridge waveguide losses.

This was easily detected by the naked eye with a large scattering centre being encountered.

Sample 395 (12x8 μm^2)	Insertion loss for 6 cm long waveguides (dB)
W1	1.77
W2	1.77
W3	1.26
W4	1.5
W5	1.84
W6	8.09
W7	1.58
W8	2.23
W9	2.31
W10	1.84

Table 4.8

To measure propagation losses two methods could have been investigated. The first would involve the output fibre being changed from a multimode to a single mode fibre. The increase in insertion loss would then detail the loss due to the single mode coupling and thus the propagation loss. The second would involve the destructive method of cut-back which has already been discussed in Section 4.2.3. It is the authors opinion that both methods could result in spurious measurements, be quite time consuming and that the results witnessed for insertion losses were a more than accurate technique to determine channel waveguide suitability.

4.7 Summary

Microfabrication techniques as well as the resulting optical inspection techniques for silica waveguides have been outlined. Fabrication techniques have been studied with the emphasis placed on providing higher yield and increased throughput processes whilst at the same time not compromising the waveguides properties. To that end optical inspection of planar waveguides is a swift qualitative technique. RIE has been described and methods detailed for higher etch rates. Polishing of waveguides has been replaced with an extremely fast cutting method, providing facets with polished finishes. Channel waveguide inspection employing the fibre measurement kit has consequently

Chapter 4 Channel waveguide procedures

shown that by following the methods described, devices can be produced with low insertion losses at a fraction of the time.

References

- 1 Tien P. K. and Ulrich R., J. Opt. Soc. Am., 1970, **60**, 1325.
- 2 Pliskin W. A. and Gnall R. P., J. Electrochem. Soc., 1964, **111**, 872.
- 3 Lee D. L., Electromagnetic Principles of Integrated Optics, John Wiley and Sons, Inc., 1986.
- 4 Nishihara H., Haruna M. and Suhara T., Optical Integrated Circuits, McGraw-Hill, 1989.
- 5 Won Y., Jaussaud P. C. and Chartier G. H., Appl. Phys. Lett., 1980, **37**, 269.
- 6 Nourshargh N., Starr E. M., Fox N. I. and Jones S. G., Electron. Lett., 1985, **21**, 818.
- 7 Jackel J. L. and Veselka J. J., Appl. Opt., 1984, **23**, 197.
- 8 Jenkins F. A. and White H. E., Fundamentals of Optics, McGraw-Hill.
- 9 Kawachi M., Yasu M. and Ecadhiro T., Electron Lett., 1983, **19**, 583.
- 10 Sze S. M., Semiconductor Devices, John Wiley and Sons, Inc., 1985.
- 11 Reuhman-Huisken M. E., Mutsaers C. M. J., Vollenbroeck F. A. and Moonen J. A. H. M., Microelectron. Eng., 1989, **9**, 551.
- 12 Manos D. M. and Flamm D. L., Plasma Etching An Introduction, Academic Press, Inc., 1989.
- 13 Irving S. M., Solid State Techn., 1971, **14**, 47.
- 14 Bonar J. R. and Aitchison J. S., to be submitted for publication in Appl. Phys. Lett.

Chapter 4 Channel waveguide procedures

- 15 Coburn J. W., Short Course 23, SPIE, San Jose, 1990.
- 16 Bebbington J. A., PhD Thesis, University of Glasgow, 1993.
- 17 Marcuse D., J. Lightwave Techn., 1989, 7, 336.

Chapter 5 Assessment of techniques for rare earth doping

5.1 Introduction

Rare earth doping of various materials has been the subject of a great deal of recent research. The first results were reported on the doping of neodymium into bulk glasses and crystals for applications in solid state lasers¹⁻². This took place in the early 60's. However, the lower threshold and better thermal conductivity of crystals, such as YAG, made it the preferred material for CW laser operation.

The rare earth neodymium has received more attention than the other rare earths. It was discovered early on, that operation at 1.06 μm was readily achievable. To this day Nd:YAG lasers are a common feature in laser laboratories having wide applications in fundamental and applied research.

The first amplification of 1.06 μm light in a Nd^{3+} doped fibre was demonstrated by Koester and Snitzer³. The fibre was 1m long, with a core diameter of 10 μm . It was not until 1974 that Stone and Burrus observed a Nd^{3+} doped fibre CW laser pumped by a GaAs diode, thus demonstrating a compact and practical source⁴.

Development of fibre fabrication techniques in the 70's resulted in high purity, single mode fibres with low propagation losses. However, research into rare earth doped fibres abated until researchers at Southampton University fabricated the first single mode silica fibre doped with rare earth ions⁵, using an extension of the MCVD technique (described in Chapter 2). There are many advantages of using a fibre geometry for the demonstration of amplification and lasing. Long lengths of active material can be used as a low loss laser, resulting in low threshold and high efficiency. The fibre has obvious compatibility with existing telecommunications fibre.

In recent years the role of erbium doped silica fibre has become important because of its emission at 1.55 μm in the low-loss telecommunications window⁶. In addition, the pump bands at 980 and 1480 nm allow semiconductor lasers to be used as pump sources⁷. Much of the 'knock-on' effect has been to create more awareness in passive and active integrated structures. Materials such as glass, lithium niobate, polymers and

various crystals are presently in vogue for integrated devices in telecommunication systems, as well as being incorporated into other functions such as sensors.

5.2 Rare earth doped fibres

Before reviewing the standard techniques for incorporating rare earth ions into silica fibres, it is necessary to consider the electronic structure of free rare earth ions and the consequences when the ions are embedded in a host glass i.e. when they interact with a crystal field. Free rare earth ions exist with the same outer electronic configuration of $5s^2 5p^6 6s^2$ plus a varying number of electrons in the inner 4f shell. It is the partially filled 4f shell that is responsible for the optical properties. However, normally, the rare earths exist as triply oxidised ions (+3 state)⁸. In the first two steps of ionisation the 6s electrons are removed and the third ionisation removes one of the 4f electrons.

When a rare earth ion is incorporated into a glass it is subjected to electric fields, due to the ligand field of the host. The ions however are partially shielded as they are found inside the $5s^2$ and $5p^6$ shells. This has two important consequences. Firstly, the $2J+1$ fold degeneracy of the $2S+1L_J$ level is broken into a number of Stark levels. The exact number being dependent on the symmetry of the host, with the full number being observed in glass. Secondly, and probably of more importance is that the inversion symmetry of the local environment of the ions is broken, permitting electric dipole transitions between the energy levels. The result is that broad absorption and fluorescence spectra of the rare earth ions are witnessed in silica hosts (illustrated in Section 5.3.1) due to the Stark levels which are both homogeneously and inhomogeneously broadened. This is due to the fact that glasses have an amorphous structure resulting in each rare earth ion seeing a different electric field.

Chapter 2 described the various techniques for fibre manufacture. As mentioned all the techniques are a variation of the MCVD process, however, no indication was given into the methods to incorporate rare earth ions into the core of silica fibres. It should be noted that fluoride fibres although not mentioned have made a considerable impact providing an important alternative glass host to silica especially in the $1.3 \mu\text{m}$ telecoms window. The interested reader is referred to various references in regard to manufacture and optical properties^{9,10,11}.

5.2.1 Solution doping

Stone and Burrus first demonstrated solution doping of rare earth ions using the MCVD technique¹². The first stage in the process involves the core being deposited on the clad

glass layer at a lower temperature to prevent complete fusing of the glass. Consequently, a partially sintered, porous layer is formed. An alcohol, or aqueous, solution of the rare earth chloride, or nitrate, is poured into the preform and allowed to soak into the partially fused preform. It is then necessary to dry out the tube to remove OH⁻ impurities and finally consolidate the preform in the normal manner. It is a simple manner to tailor the rare earth concentration by either varying the dopant solution strength or the immersion time¹³.

A similar process may be used in conjunction with the VAD process, although sometimes it is termed as 'molecular stuffing'¹⁴. In this instance the core boule, often referred to as the 'seed' rod, is partially fused and immersed in an alcoholic solution of rare earth chloride. The rod is subsequently dehydrated, fully consolidated and overlaid before being pulled into a fibre.

5.2.2 Volatile halide methods

It is also possible to use gas phase techniques to fabricate doped fibres⁵. These methods require heating of the rare earth chlorides since they have a very low vapour pressure. Various techniques have been used in conjunction with the MCVD process to introduce the rare earth into the reaction¹⁵⁻¹⁶. Commonly, rare earth compounds are melted on to the walls of a dopant carrier chamber, situated upstream of the silica tube where the deposition takes place (a similar technique is the Frit method¹⁷). The chamber is warmed to approximately 1000 °C to produce a vapour which is carried into the reaction zone along with the main reactants. Slight variations to this technique are to use rare earth halide crystals or an impregnated silica sponge, as the dopant source.

The OVD process employs a volatile organometallic precursor¹⁸. The vapour is transported to the OVD burner for oxidation and deposition. This is a more expensive technique requiring complex precursors and accurate temperature control of the delivery lines to avoid condensation.

The VAD process again involves having a partially fused boule subjected to a rare earth vapour¹⁹. The boule is placed in a consolidation furnace at temperatures above 800 °C. The rare earth crystals are melted and the released vapour diffuses in to the pores of the boule. The boule is subsequently fused and drawn to produce a rare earth doped fibre.

5.2.3 Aerosol doping

Aerosol doping is a technique that has not been widely researched. However, the method was patented as early as early as 1982 by researchers at NTT²⁰⁻²¹. Much of the research into MCVD, VAD and OVD technologies employing aerosol doping has taken place at Brown University²²⁻²³.

Essentially an aqueous solution of the rare earth chloride is nebulised employing a transducer and swept into the reaction zone, ensuring that condensation of the rare earth chloride does not take place, using oxygen as the carrier gas. Once in the reaction zone the temperature of 1200 °C evaporates the water to leave a submicron particle of rare earth which is oxidised and directly incorporated in to the partially fused core layer. A more specialised technique is to employ a readily nebulised solution which incorporates all the components of the glass into an input feed along with the glass forming material. This can be achieved using tetraethylorthosilicate (TEOS) which is a suitable solvent for the rare earths. As a result microcrystalline structures formed from the possibility of phase separation within the glass structure are avoided.

A multi-conduit burner incorporating an extra port can be used for both the OVD and VAD techniques. The extra port feeds the aerosol into the reaction with an inert gas employed to both nebulise the rare earth solution and to provide means of transporting the nebulised solution.

5.2.4 Rod-in-tube method

The most basic technique, although not as common as the techniques described, is the rod-in-tube method²⁴. This involves commercially available bulk laser glasses being sleeved in a tube of lower index glass and pulled down to form a fibre. The most important prerequisite is that the same thermal expansion is chosen for both glasses.

5.3 Rare earth doping of planar waveguides

There are a number of important differences between the fabrication of silica fibres and silica planar samples. The main difference is the physical constraint imposed for feasible planar fabrication. The maximum substrate size reported has been 5 inch silica wafers processed by NTT²⁵. Employing FHD and RIE, waveguide patterns which spiral in and out have been produced with lengths of 10 m and propagation losses of

1.7 dB²⁶. A very important future development for these passive devices is the formation of delay lines.

Planar samples require a suitable substrate, typically silicon, which means that processing cannot take place at such high temperatures as for fibre fabrication. The maximum sintering temperature is limited to ~1400 °C, above this value the substrate buckles and cracks. This is of particular importance for rare earth doping where high temperature processing is important to minimise scatter and maintain a long lifetime. The drawing of fibres also reduces any imperfections in the fibre preform such that propagation losses are expressed in units of dB/km compared to dB/cm for planar devices. The main basis for this study has involved the adaptation to a planar format of both the solution and aerosol doping techniques.

Other techniques developed for doping of planar waveguides on silicon substrates are plasma enhanced chemical vapour deposition (PECVD)²⁷, electron beam vapour deposition (EBVD)²⁸, implantation of MeV Er³⁺ ions²⁹⁻³⁰ and sputter deposition techniques^{31,32,33}. Probably, the most exciting advances in the methods mentioned above has been the extremely high Er³⁺ doped concentration waveguide amplifier fabricated by researchers at AT&T. The amplifiers were made by RF-sputter deposition of transparent Er³⁺ doped soda lime glasses on oxidised silicon wafers and were able to produce a gain per unit length of 3.3 dB/cm³⁴.

Ion exchange in glasses has also been shown to produce successful rare earth doped planar devices³⁵⁻³⁶ Malone et al were able to achieve laser oscillation at 906, 1057 and 1358 nm in the same Nd³⁺ doped glass³⁷. Other novel designs have been fabricated to produce Y-branch waveguide lasers and amplifiers³⁸ and monolithic integrated Q-switched lasers³⁹.

LiNbO₃ and other crystals are also of great interest^{40,41,42,43,44,45,46}. This is due to the versatility of LiNbO₃ which possesses a large nonlinear effect, not to mention electro-optic and acousto-optic effects. Other crystals such as YAG, LiTaO₃, Ti:Al₂O₃ and Cr doped garnets could also provide suitable integrated waveguide lasers.

Polymer waveguides are structures which have been fabricated on various substrates to provide cheap and reliable means of performing passive functions for network systems. They are compatible with silica fibres and relatively environmental resistant. Many devices have been fabricated including a Nd³⁺ doped graded-index polymer waveguide amplifier⁴⁷. This exhibited a gain of 8.5 dB over 2.2 cm at 1.06 μm.

5.3.1 Solution doping

Solution doping is a technique that has been developed from fibre manufacture. A great deal of success has been achieved at NTT laboratories by employing this technique. Since the first report of a neodymium doped silica waveguide laser in 1989⁴⁸, the group have progressed to demonstrate various Er doped waveguide lasers and amplifiers^{49,50,51,52}. They were able to report an Er doped amplifier, integrated with a WDM coupler, which produced a high gain of 27 dB and a low noise figure of 5 dB⁵³. Other significant accomplishments were a single-frequency Er³⁺ doped waveguide laser with integrated photo-imprinted Bragg reflectors⁵⁴ and tunable Y-branched waveguide lasers⁵⁵.

This technique has been implemented using the standard process depicted in Figure 5.1. It involves the deposited soot being partially sintered. The porous soot is then immersed in an aqueous or alcohol solution of the rare earth chloride. The sample is then carefully dried and completely sintered. Various dopants have been incorporated during the research including Nd, Er, Eu, Yb and Al.

To produce a low loss rare earth doped planar sample it was vitally important that conditions were found where the dopant could be incorporated into the glass matrix in a reliable and uniform manner. To change the dopant level the immersion time was kept constant and the solution strength varied. For the sake of reproducibility, the partial fusion tests took place for a constant time of 10 minutes. Tests were conducted for temperatures of 900 to 1000 °C for deposition parameters of 150 sccm SiCl₄, 180 sccm PCl₃ and 480 sccm POCl₃. For 900 °C the structure was too weak, with the delicate glass matrix being damaged when immersed in the solution. At the other end of the scale when the samples were fused at 1000 °C the glass was found to be too fused with the glass close to consolidation and more susceptible to isolated doping centres. This would result in uneven doping and increased ion-ion interactions as well as increased number of scattering centres. The ideal structure was found at 925 °C where the glass had formed a skeleton structure. This involves the low density glass forming necks between adjoining particles. As a result an open but strong structure was produced providing a large surface area on which the dopant solution could be adsorbed. Figures 5.2a-e illustrate SEM photographs of some of the glass structures. However, to minimise the scatter of the guides it was necessary to carefully dry the samples after immersion. Samples were placed on a spinner for 30 seconds increasing the speed gradually to 3000 rpm and placed on a hot plate for five minutes. The samples were then placed in an electric furnace for complete consolidation.

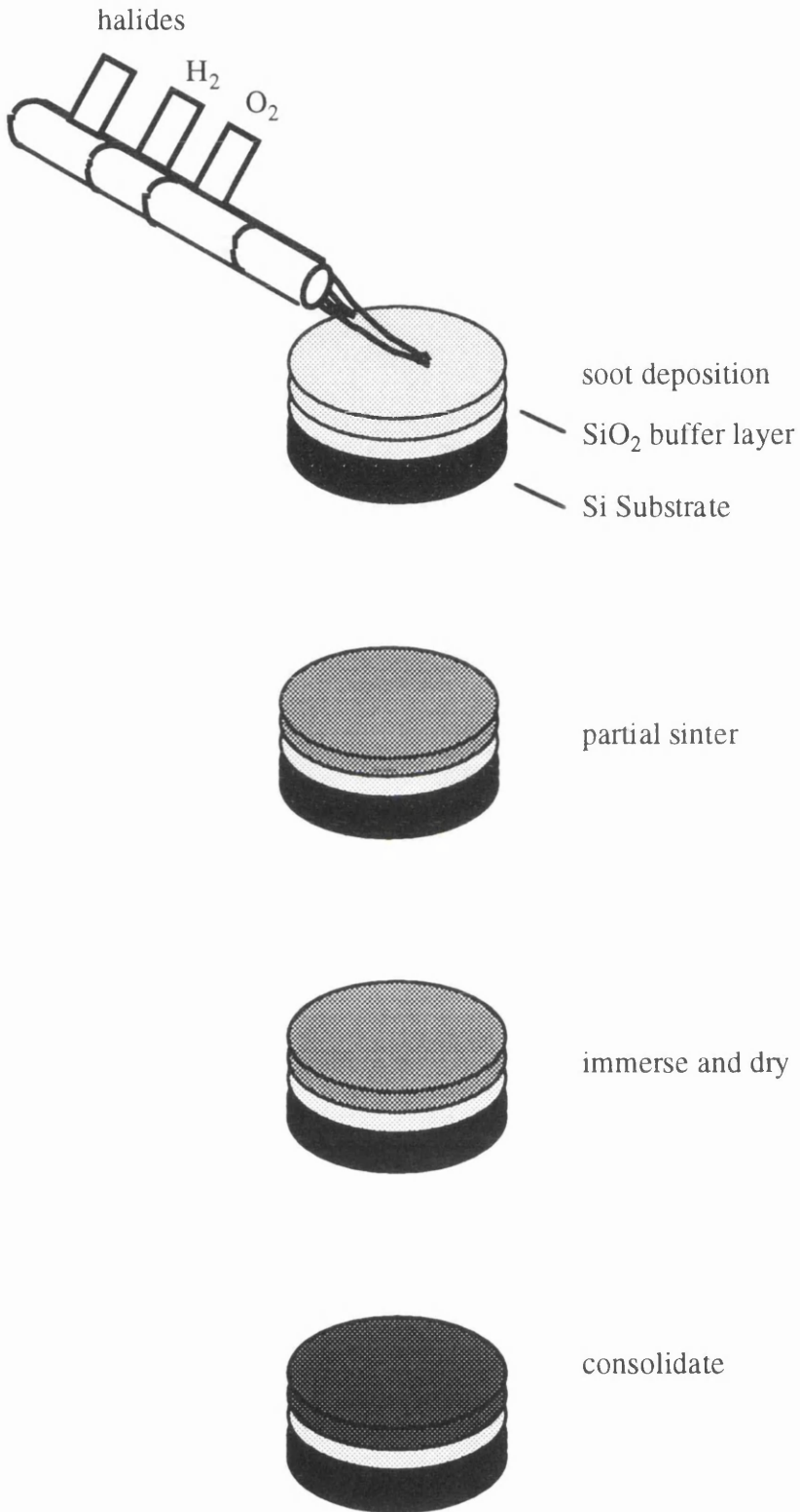


Figure 5.1 Solution doping technique for FHD.



Figure 5.2a SEM photograph of SiO₂-P₂O₅ film fused at 900 °C for 10 minutes.

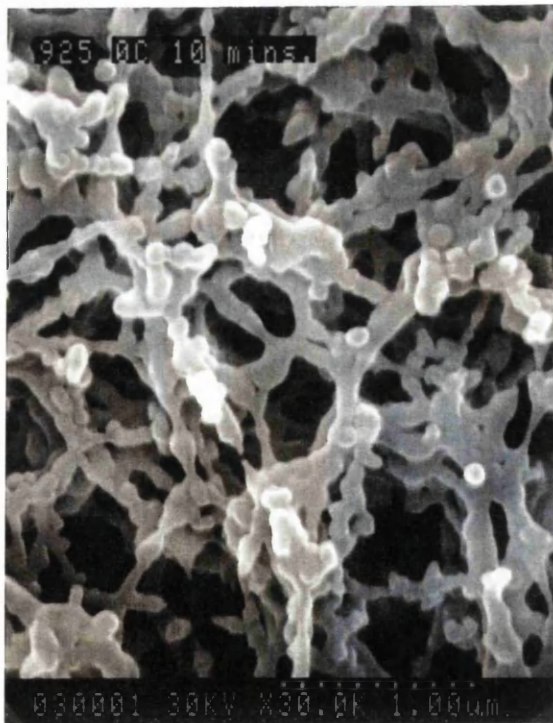


Figure 5.2b SEM photograph of SiO₂-P₂O₅ film fused at 925 °C for 10 minutes.

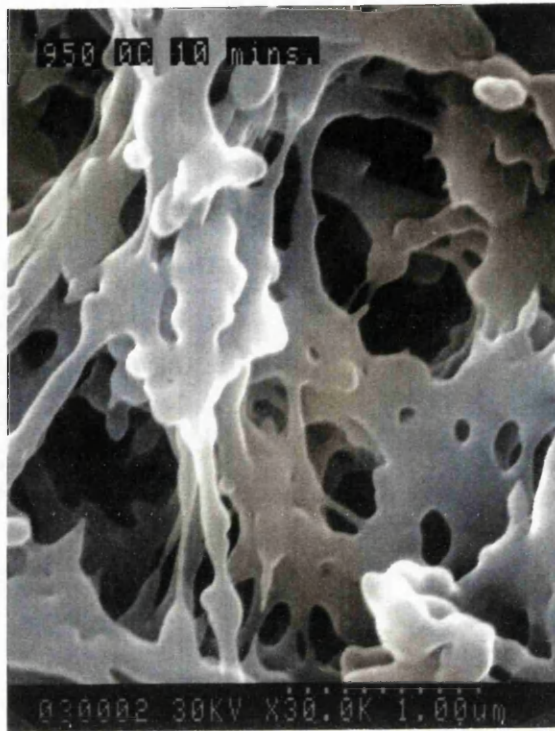


Figure 5.2c SEM photograph of SiO₂-P₂O₅ film fused at 950 °C for 10 minutes.

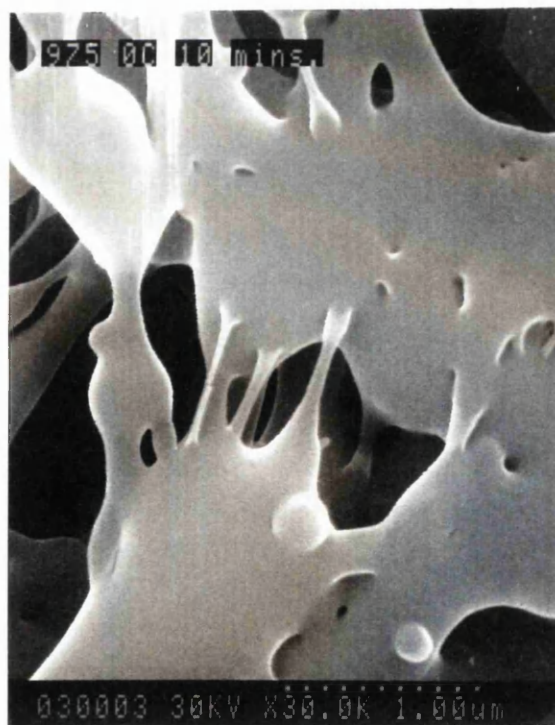


Figure 5.2d SEM photograph of SiO₂-P₂O₅ film fused at 975 °C for 10 minutes.

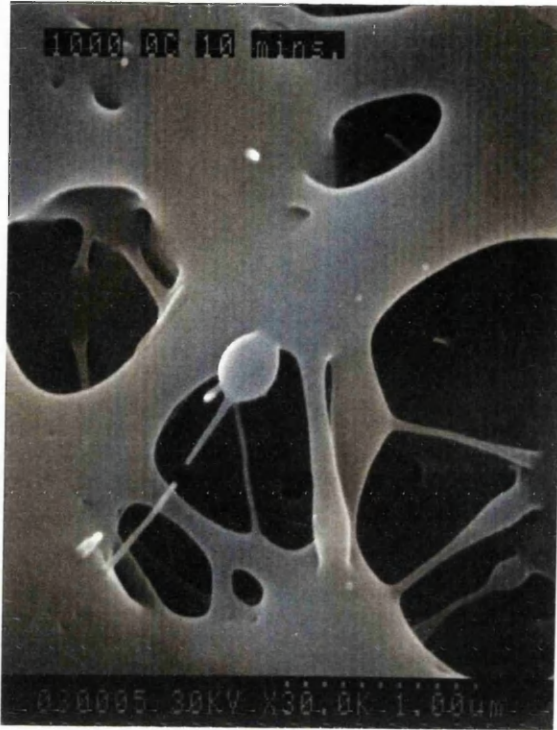


Figure 5.2e SEM photograph of SiO₂-P₂O₅ film fused at 1000 °C for 10 minutes.

5.3.2 Aerosol doping

Aerosol doping on a planar format has not been reported by any other group. However, Tumminelli and co-workers did produce a Nd:glass laser by flame hydrolysis deposition using chelates⁵⁶. The Nd³⁺ was introduced into the reaction by vapour phase transport of neodymium chelate of 2, 2, 6, 6-tetramethyl-3, 5-heptanedione [Nd(thd)₃]. Al³⁺ was employed as a codopant to raise the core refractive index and to act as a homogenising agent. To provide enough dopants two source columns were arranged to be individually heated. The delivery lines to the torch were also heated to prevent condensation and helium was used as the carrier gas. The burner itself was used to consolidate the deposited soot. Interestingly guides were formed by milling regions of the film with a dicing saw producing guides of approximately 7 μm x 26 μm and 8 μm x 32 μm. With this crude technique of ridge waveguide fabrication a threshold of 143 mW and a slope efficiency of 2.1 % was measured.

The aerosol doping technique is a much simpler technique than the vapour phase transport scheme⁵⁷. The dopants are readily available and inexpensive compared to the chelates. A significant advantage is that the doping is carried out at a macroscopic level such that it promotes homogeneous distribution of the rare earth ions.

Chapter 5 Assessment of techniques for rare earth doping

A schematic of the deposition technique is shown in Figure 5.3. The dopant is incorporated directly, avoiding the extra steps of partially sintering and immersion in the dopant solution. The only variation in the system is the incorporation of an extra port on the torch for the aerosol inlet. Various torch designs were investigated during the course of this work⁵⁸, Chapter 3 depicts some of the designs.

A PVC pneumatic atomiser, shown in Figure 5.4, was employed to atomise the solution using zero grade N₂ gas which also transported the aerosol droplets to the torch. To prevent the rare earth condensing before the reaction zone it was necessary to design the torch such that the gas flow was unobstructed with a shallow port inlet and no drastic decrease in the inlet volume. When the aerosol enters the reaction zone the water evaporates to leave a sub-micron particle of rare earth chloride which is subsequently oxidised in the non-stoichiometric flame.

The flow rate of the N₂ was maintained at 3 l/minute providing a delivery rate of 0.15 ml/minute whilst not compromising the shape of the flame. It was found that increasing the flow rate led to a turbulent flame and consequently, nonuniformity of the deposited film. To alter the doping concentration aqueous solutions of the rare earth salt were varied, generally between 0.1 to 1 M solution strength. Visually the rare earth could be observed entering the flame as the flame changed colour to violet and green for Er³⁺ and Nd³⁺ respectively.

When the aerosol was introduced to the burner, it resulted in the flame being cooler, inhibiting hydrolysis and consequently both the index and thickness were lower. In general it was found that the index decreased by approximately 10 % and the thickness reduced by about 15 %.

5.3.3 Optical properties of rare earth doped waveguides

The steps necessary to deduce doping levels, losses and doping homogeneity involved a systematic procedure of tests. The rare earths neodymium and erbium were the main focus of attention for waveguide laser fabrication. The prism coupler was the initial test to deduce refractive indices and scattering losses.

It is well known that to create a more soluble network for rare earth ions, a high phosphorous content glass should be used⁵⁹. Thus, layers which were low in phosphorous content had a reduced index and displayed high scattering losses. For the particular case of solution doping, problems in the drying process could be observed by scattering at the edges of the wafer due to residue rare earth.

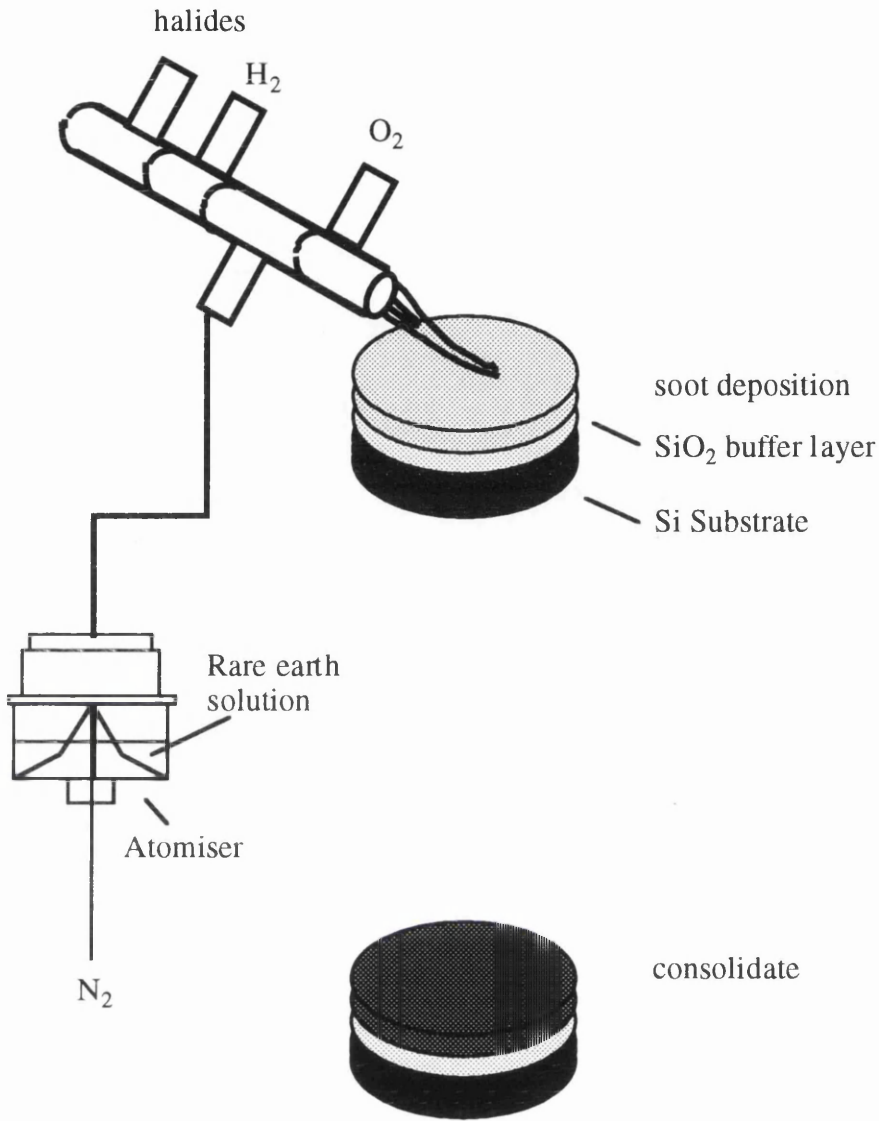


Figure 5.3 Aerosol doping technique for FHD.

Absorption measurements to find out the doping levels of the rare earth devices were conducted. Employing the fibre loss kit described in Chapter 4, a fibre connected white light source was coupled into long channel waveguides. For speed of assessment approximately 30 μm ridges were formed by cutting ridges with a resinoid saw. The resultant spectrum was measured on a spectrum analyser. Both the input and output fibres were multimode. Figures 5.5 and 5.6 are typical spectra for the Nd^{3+} $^4\text{I}_{9/2}$ - $^4\text{F}_{7/2}$ $^4\text{I}_{9/2}$ - $^4\text{F}_{5/2}$ and $^4\text{I}_{9/2}$ - $^4\text{F}_{3/2}$ transitions and the Er^{3+} $^4\text{I}_{15/2}$ - $^4\text{I}_{13/2}$ transition respectively.

To optimise pumping conditions for a waveguide laser it is important that both the peak absorption wavelength and the doping level are known. The white light transmission spectrum measured by the spectrum analyser allows this. The doping levels are measured by correlating data from the absorption peaks in the transmission spectra to

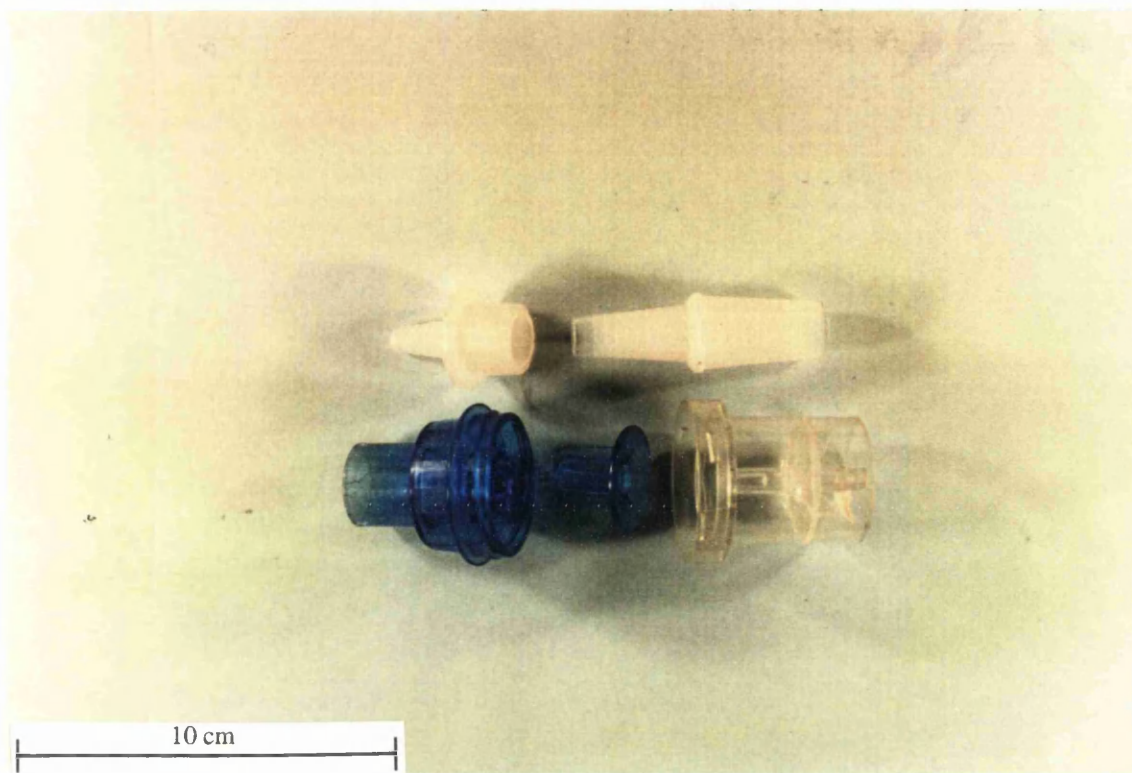


Figure 5.4 Photograph of PVC pneumatic atomiser.

extinction coefficients of $5 \text{ dBcm}^{-1}\text{wt.}\%^{-1}$ for the $\text{Nd}^{3+} \text{ } ^4\text{I}_{9/2} \text{--} ^4\text{F}_{5/2}$ (804 nm) and $2.2 \text{ dBcm}^{-1}\text{wt.}\%^{-1}$ for the $\text{Er}^{3+} \text{ } ^4\text{I}_{15/2} \text{--} ^4\text{I}_{13/2}$ (1535 nm) transition detailed in published reports⁶⁰. Figure 5.7 illustrates superimposed Er^{3+} absorption measurements for varying concentrations of aerosol doped samples with a N_2 flow rate of 3 l/min.. As result, Table 5.1 shows the doping levels measured for 6.5 cm long waveguides, cut to a width of approximately $20 \mu\text{m}$. Points to note from the table are that the doping levels do not quite vary linearly (experimental error), Er^{3+} doping levels saturate for solution strengths greater than 1 M and the use of Al^{3+} inhibits the Er^{3+} doping level, by competing with the Er^{3+} for host sites, especially for the heavier doped samples. It was also found that Al^{3+} dilutes the Er^{3+} concentration for solution doping⁶¹. The addition of alumina is known to broaden the transition and reduce the peak cross-sections for absorption and emission⁷. Thus, it can be seen from Figure 5.7 that the spectral shape remains similar for all the waveguides indicating that the drop in peak absorption is not accompanied by a broadening of the spectra. Thus, the drop in Er_2O_3 concentration is not due to a change in cross-section. Figure 5.8 is also shown for the sample aerosol doped with 2 M Er^{3+} for a larger waveguide range to highlight the $\text{Er}^{3+} \text{ } ^4\text{I}_{15/2} \text{--} ^4\text{I}_{11/2}$ (980 nm) transition employed for pumping devices.

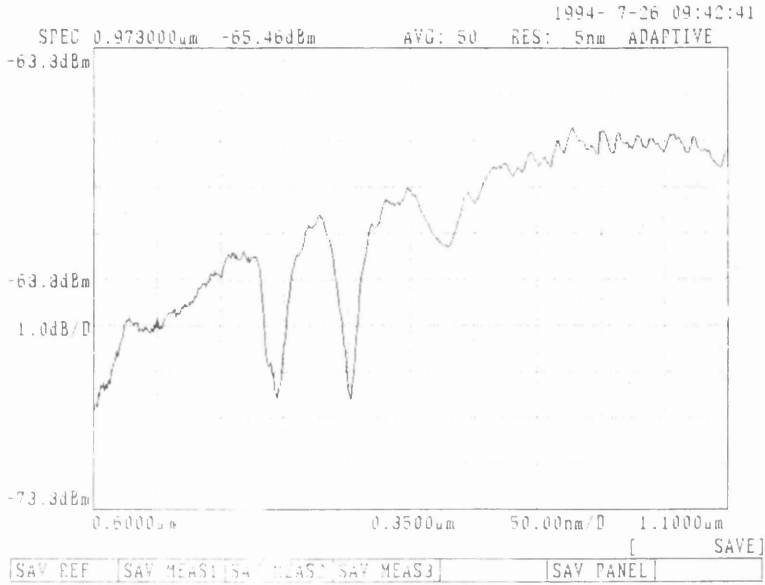


Figure 5.5 Absorption spectrum for the Nd³⁺ ⁴I_{9/2}-⁴F_{7/2}, ⁴I_{9/2}-⁴F_{5/2} and ⁴I_{9/2}-⁴F_{3/2} transitions.

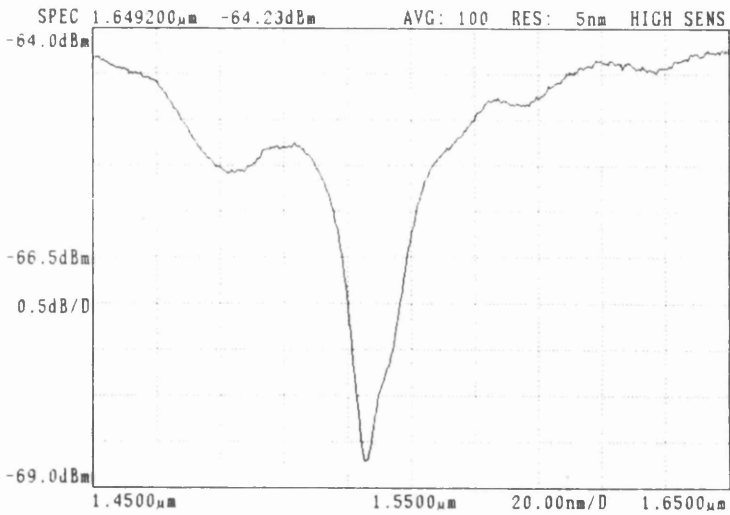


Figure 5.6 Absorption spectrum for the Er³⁺ ⁴I_{15/2}-⁴I_{13/2} transition.

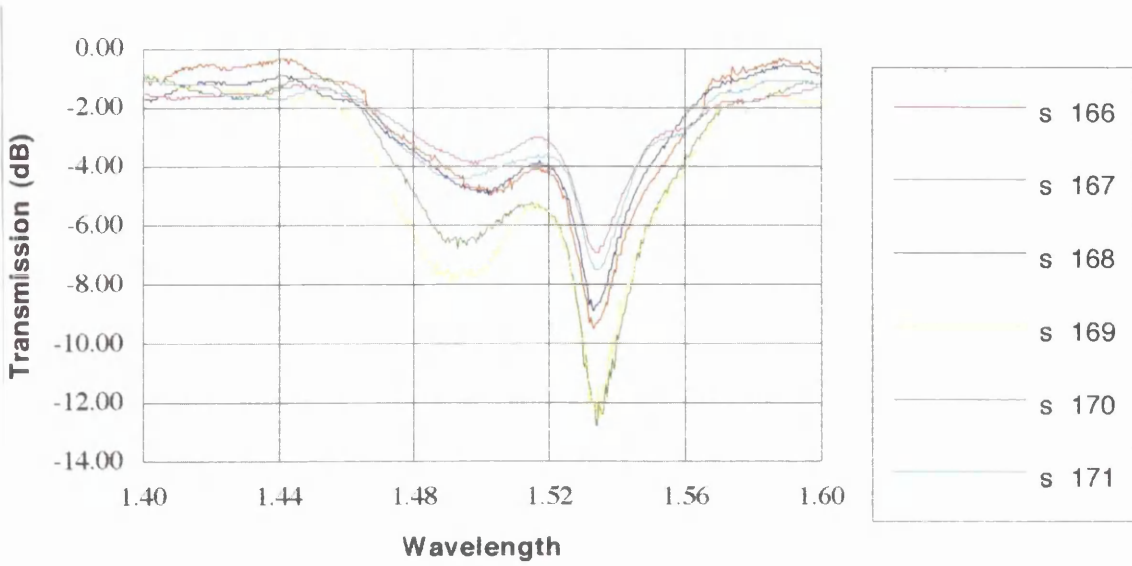


Figure 5.7 Absorption spectrum of Er³⁺ doped SiO₂-P₂O₅ waveguides.

Sample	Concentration	Absorption (dB/cm)	wt. %
166	2 M Er/ 0.4 M Al	1.2	0.54
167	2 M Er	1.7	0.77
168	1 M Er/ 0.4 M Al	1.2	0.54
169	1 M Er	1.6	0.72
170	0.5 M Er/ 0.4 M Al	0.8	0.36
171	0.5 M Er	0.95	0.43

Table 5.1 Doping levels of Er³⁺ doped SiO₂-P₂O₅ waveguides.

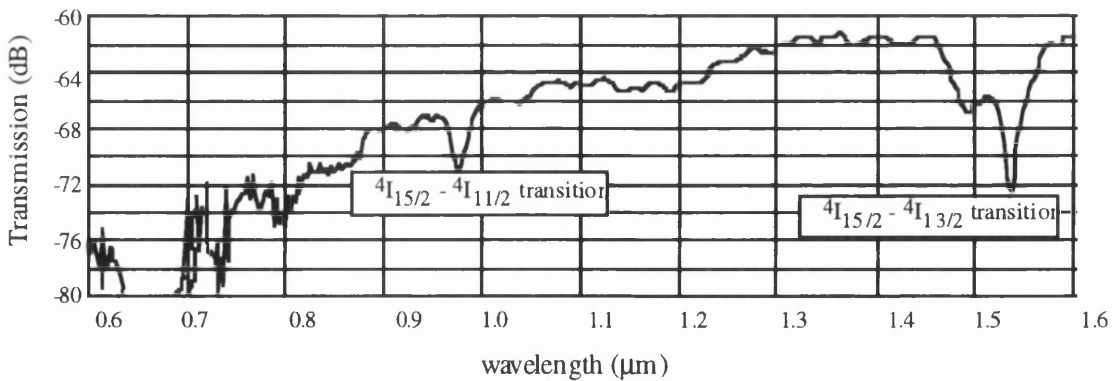


Figure 5.8 Absorption spectrum for Er³⁺ doped SiO₂-P₂O₅ film.

Chapter 5 Assessment of techniques for rare earth doping

A similar procedure was conducted to measure the doping levels for solution doped samples. Samples were partially sintered at 925 °C for 10 minutes in an absolute alcohol solution of solution strengths varying between 0.05 and 0.04 M. Note that the solution strengths are more than one order of magnitude lower than that used for aerosol doping. The results are given in Table 5.2.

Sample	Concentration	Absorption (dB/cm)	wt %
102/ 1	0.005 M Er	0.6	0.27
102/ 2	0.01 M Er	1.1	0.5
102/ 3	0.02 M Er	1.45	0.66
102/ 4	0.04 M Er	2.45	1.1

Table 5.2 Doping levels of Er³⁺ doped SiO₂-P₂O₅ waveguides.

The important features to note from Table 5.2 are that higher doping levels could be incorporated into the partially fused glass matrix using the solution doping technique than compared to the aerosol technique. The doping level increases with increasing solution strengths, although once again not in a linear manner. The maximum level of dopant was found to be approximately 1 wt% and when codoping with Al³⁺, although not tabulated, a decrease in Er³⁺ level was witnessed.

The apparent difference in doping levels between the solution and aerosol techniques are more to do with the rare earth delivery system. The aerosol is not able to give a larger supply with increased rare earth solutions unless either the flow rate to the aerosol is increased or the deposition parameters are altered. Increasing the nebuliser flow rate to greater than 3 l/minute, unfortunately results in a turbulent flame. The halide parameters to the torch could be altered to produce thinner films per traversal with the same aerosol delivery. This in theory should permit larger doping levels, however, no measurements were made to find the maximum doping level possible, since from previous work a doping level of 0.5 wt% was adequate for the devices under consideration. Also, the halide flow rates were optimised so that reproducible, doped, films were fabricated with a deposition rate of 1 µm per traversal.

Fluorescence measurements were undertaken for Nd³⁺ and Er³⁺ samples produced using both solution and aerosol techniques. The 514 nm line from an argon ion laser was 'end-fire' launched into sawn waveguides (described earlier). The resultant spectra was measured on an Advantest spectrum analyser.

Figure 5.9 to 5.12 illustrates fluorescence spectra of Nd^{3+} and Er^{3+} doped samples employing both aerosol and solution techniques. For Nd^{3+} the fluorescence spectra from the metastable ${}^4\text{F}_{3/2}$ to the ${}^4\text{I}_{11/2}$ (1051 nm) energy level as well as the ${}^4\text{I}_{9/2}$ (874 nm) and ${}^4\text{I}_{13/2}$ (1320 nm) energy levels are given. The fluorescence spectra of the Er^{3+} ${}^4\text{I}_{13/2}$ to ${}^4\text{I}_{15/2}$ is also detailed.

Irrespective of doping levels of rare earth, or doping techniques, the spectra observed were identical with both the full width maximum (FWHM) and the emission peak being similar. However, doping with P_2O_5 resulted in the emission peaks moving to shorter wavelengths and a narrowing of the emission bands compared to the pure silica host⁶². This is most apparent for Er^{3+} doped pure silica which exhibits two emission peaks at 1.535 μm and 1.552 μm . This is to be expected since the P_2O_5 codopant concentration is typically 20 wt%.

Codoping with Al^{3+} creates Al-O⁻ groups which partially coordinate the triply ionised rare earth⁶³. The aluminium ion concentration for the devices fabricated was measured to be only 0.04 wt%. Figure 5.13 illustrates the fluorescence spectra for the ${}^4\text{F}_{3/2}$ to the ${}^4\text{I}_{11/2}$ transition of Nd^{3+} . The salient features to note are that the FWHM has increased to 24 nm and that the emission peak is at the shorter wavelength of 1051 nm. Typical values for FWHM are 20 nm and emission peak at 1054 nm. This change in spectral response is also borne out with the ${}^4\text{I}_{9/2}$ - ${}^4\text{F}_{5/2}$ absorption peak moving to the shorter wavelength of 802 nm compared to the typical absorption band of 804 nm for phosphorous doped samples without Al^{3+} . Of particular interest is that no such features were observed when solution doping. This would tend to support the theory that the aluminium ions, although only a small amount, are incorporated into the glass matrix in a more homogeneous manner, being able to change the fluorescence spectra. No change in spectral response was measured for samples solution doped with aluminium concentrations of up to 2 wt%⁶⁴.

Fluorescence lifetime measurements were undertaken to highlight ion-ion interactions, such as quenching and up-conversion. This is an essential part of the optical assessment as any decrease in the effective lifetime of the upper lasing level decreases the internal quantum efficiency of oscillators and amplifiers. Consequently, information can be deduced to the solubility and doping uniformity of the rare earth in the host glass. Much of the work concentrated on Er^{3+} systems owing to its longer fluorescence lifetime (~10 ms for fibres) in comparison to the Nd^{3+} system.

Chapter 5 Assessment of techniques for rare earth doping

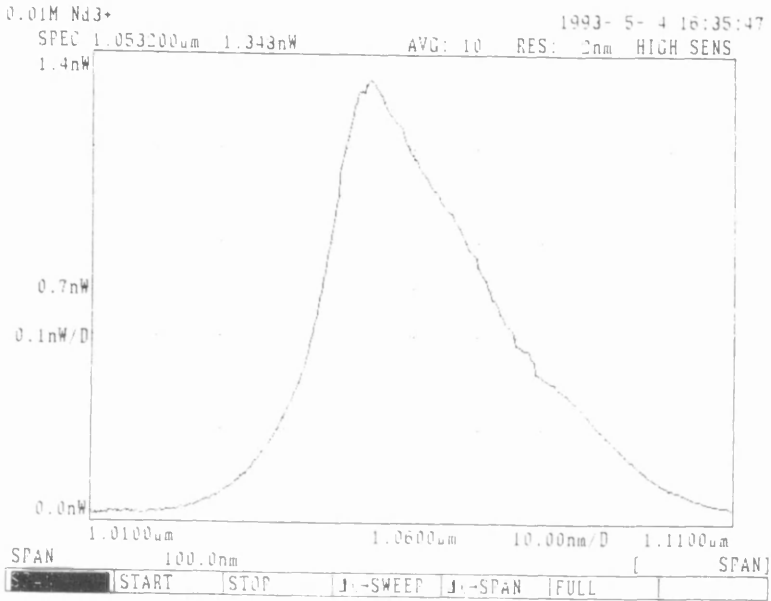


Figure 5.9 Fluorescence spectrum for the $\text{Nd}^{3+} 4\text{F}_{3/2}-4\text{I}_{11/2}$ transition.

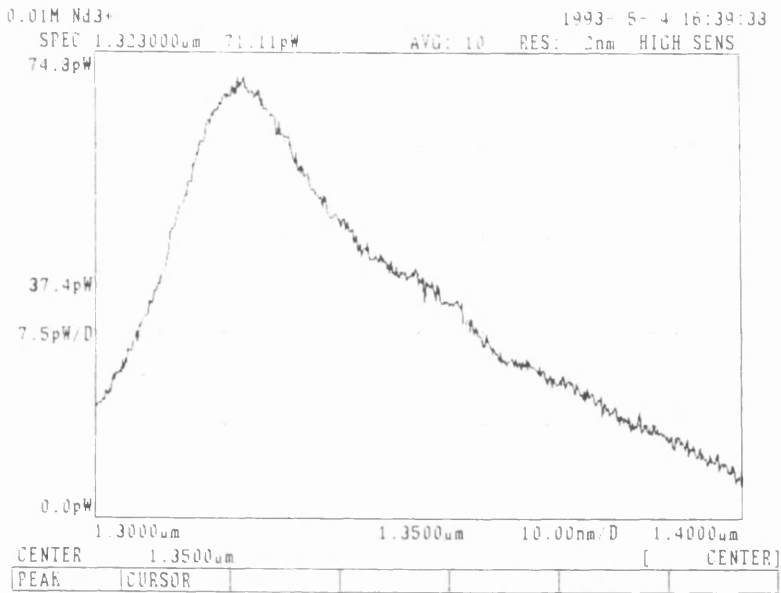


Figure 5.10 Fluorescence spectrum for the $\text{Nd}^{3+} 4\text{F}_{3/2}-4\text{I}_{9/2}$ transition.

Chapter 5 Assessment of techniques for rare earth doping

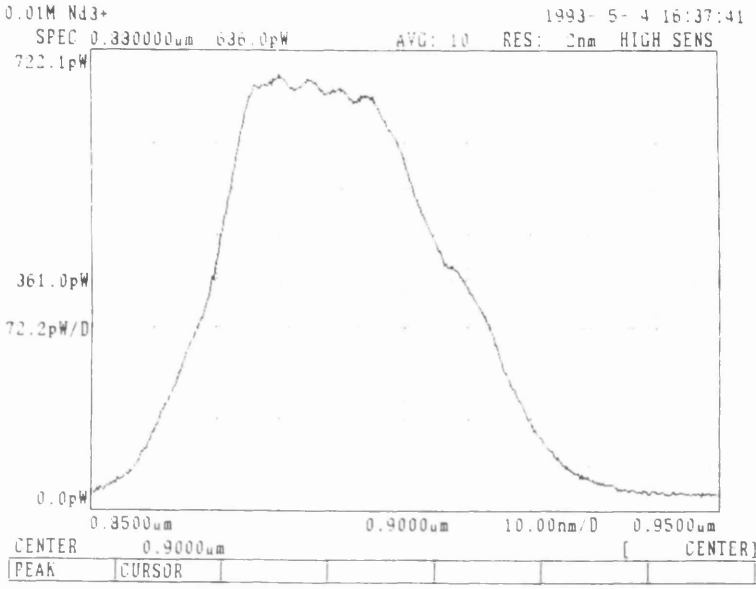


Figure 5.11 Fluorescence spectrum for the Nd³⁺ ⁴F_{3/2}-⁴I_{13/2} transition.

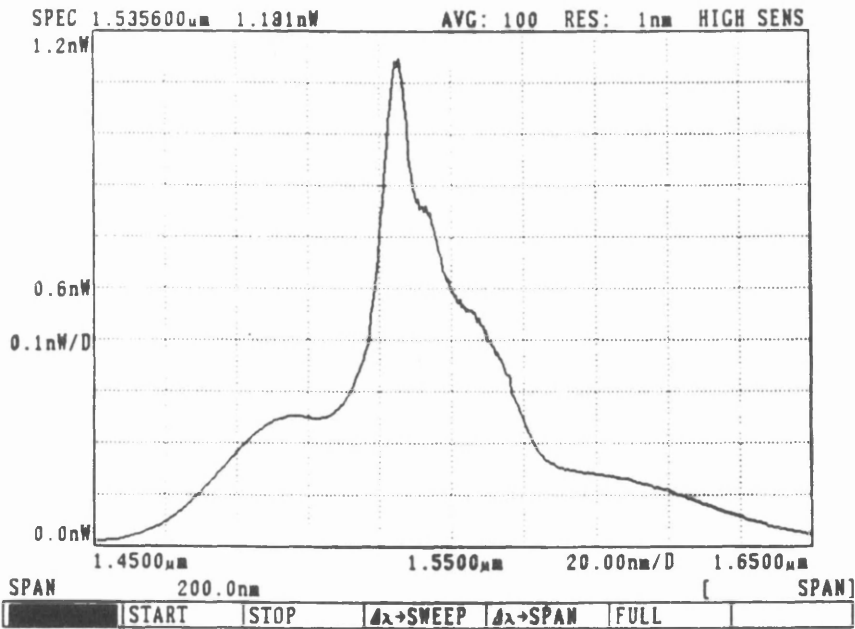


Figure 5.12 Fluorescence spectrum for the Er³⁺ ⁴I_{13/2}-⁴I_{15/2} transition.

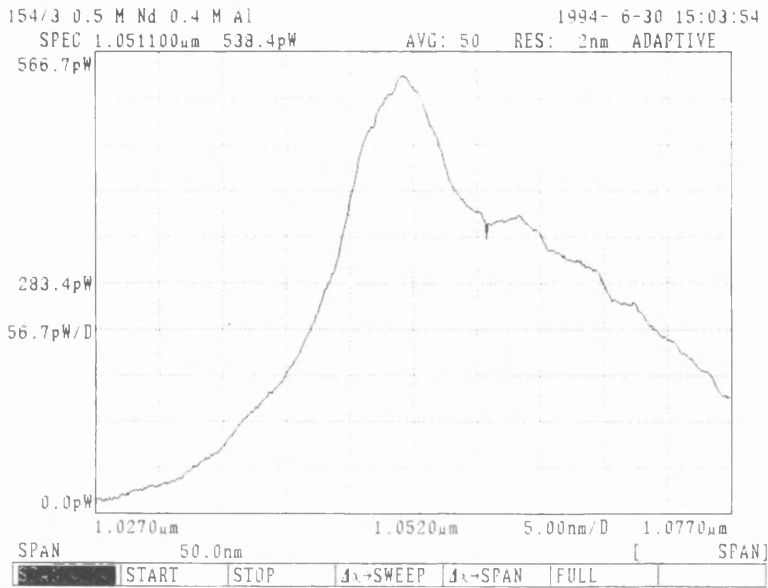


Figure 5.13 Fluorescence spectrum for the $\text{Nd}^{3+} \ ^4\text{F}_{3/2} \text{-} \ ^4\text{I}_{11/2}$ transition for a Nd/ Al aerosol doped sample.

Energy level diagrams are illustrated in Figure 5.14 for neodymium and erbium. Within each diagram ion-ion interaction processes are highlighted. The likelihood of these processes is increased due to the high doping levels required for short length planar samples with the probability depending on the ion separation to the sixth power⁶⁵.

Concentration quenching particularly effects Nd^{3+} . This process involves two neighbouring ions, one in the ground state, $\ ^4\text{I}_{9/2}$ and the other in the excited state, $\ ^4\text{F}_{3/2}$ undergoing a radiationless transition to both end up in the $\ ^4\text{I}_{15/2}$ level where they quickly relax to the ground state. Consequently, this mechanism depopulates the upper lasing level and so increases threshold. This results in a departure from the exponential decay, which is independent of the pump power since only one ion is required for the cross relaxation.

The Er^{3+} system on the other hand suffers from the ion-ion interactions based on cooperative upconversion. In contrast to Nd^{3+} , this mechanism involves two adjacent ions being initially in the excited $\ ^4\text{I}_{13/2}$ level, and the subsequent energy transfer promotes one ion the ground state $\ ^4\text{I}_{15/2}$, and the other to a higher state $\ ^4\text{I}_{9/2}$. Most ions in the $\ ^4\text{I}_{9/2}$ state quickly relax to the metastable state $\ ^4\text{I}_{13/2}$, such that the net result is the

loss of one excitation in the ${}^4I_{13/2}$. Since the mechanism requires two excited interacting ions the process is dependent on pump power and results in non-exponential decay curves for increased pump powers.

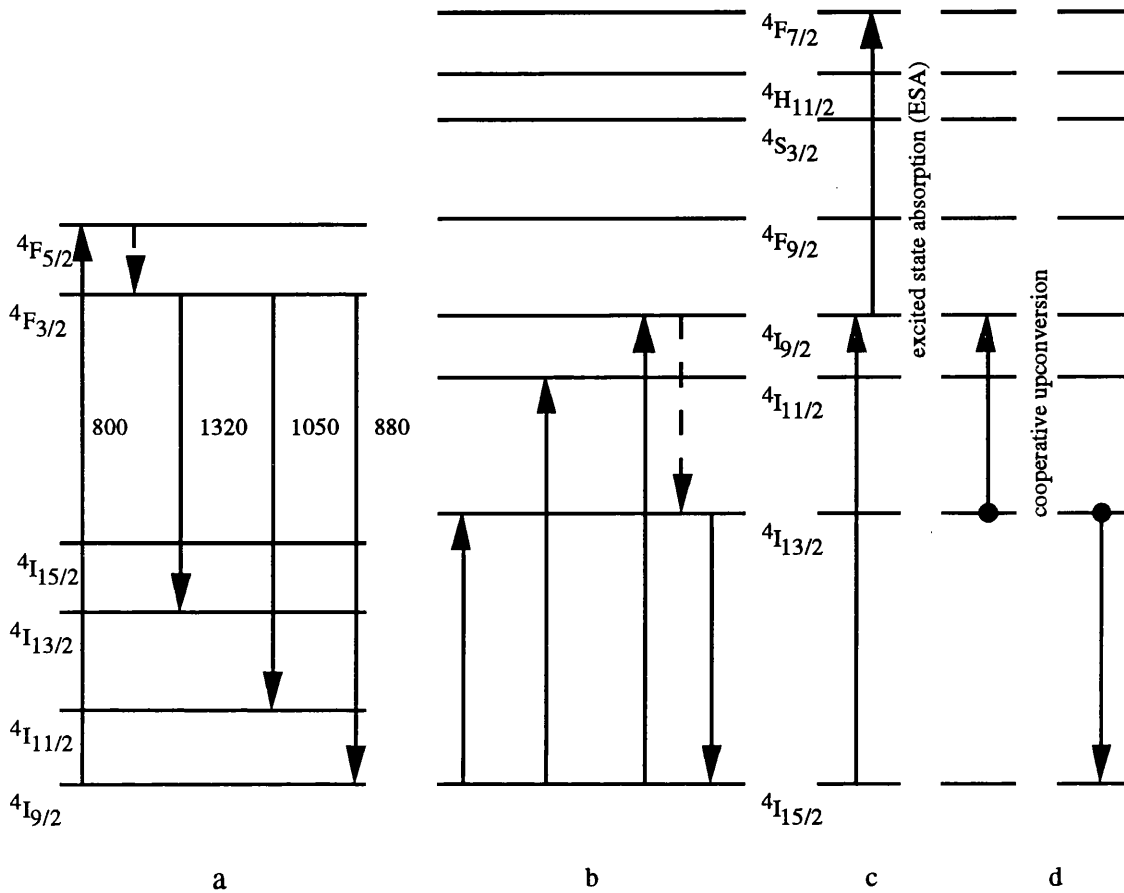


Figure 5.14 Optical transitions and simplified energy level diagrams for Nd^{3+} (a) and Er^{3+} (b). The Er^{3+} cooperative upconversion (c) and ESA (d) processes are shown.

Various studies have been conducted to monitor the effects of clustering on the performance of fibre amplifiers. Increasing the Er^{3+} concentration in pure silica fibres was found to be detrimental, with the pump threshold for obtaining net gain at 1530 nm increasing from 12 mW to 35 mW for 77 ppm and 970 ppm doping concentration respectively⁶⁶. The addition of Al_2O_3 to the silica, reduced the clustering and as a result doping concentrations of 1000 ppm could be tolerated without a decrease in efficiency⁶⁷. Further evidence of a cooperative upconversion mechanism was confirmed from time dependence studies in highly doped (2wt.%) Er:Al/P-silica fibre⁶⁵. Strong excitation from a colour-centre laser at 1500 nm resulted in detection of emission at 800 nm from the ${}^4I_{9/2}$ level. The upconverted fluorescence exhibited the same decay kinetics as the square of the 1550 nm fluorescence from the ${}^4I_{15/2}$. This is expected due to the prerequisite of having two adjacent ions simultaneously in their excited states. The presence of clustering in Nd^{3+} doped silica has also been measured.

disappeared with the addition of relative small amounts of aluminium or phosphorous into the glass matrix⁶³.

To measure the effects of ion-ion interactions experiments were conducted at BT Laboratories to measure fluorescent lifetimes for the Er³⁺ system. Sawn waveguides of widths approximately 15 μm were tested. A schematic of the experimental set-up is given in Figure 5.15.

Initial experiments involved using a modulated AlGaAs laser as the excitation source. However, even when using a laser array the maximum amount of power which was incident to the waveguides was approximately 100 mW. As mentioned, the cooperative upconversion in the Er³⁺ system is dependent on pump power, hence a more powerful source was required. A Ti:sapphire laser tuned to 980 nm was thus chosen as a suitable pump source. To maintain a stable output, the argon ion laser pumping the Ti:sapphire was operated at maximum power and an attenuator was used to vary the Ti:sapphire power incident onto the sample. A wavemeter was also employed to monitor the excitation wavelength. The beam was mechanically chopped at a rate of 500 Hz, with a pulse rise and fall time on the order of 100 nanoseconds, to allow analysis of the initial fast decay mechanism. The light was coupled into a WDM coupler. One output was incident at the waveguide whilst at the other output port of the WDM, the power was monitored. This enabled the power output of the fibre incident to the waveguide to be calibrated. The maximum power measured at the output of the fibre was observed to be 330 mW. Index matching fluid was used to increase the coupling efficiency between the fibre and waveguides. The resultant fluorescence was detected transversely to the waveguide using a Ge photodiode, with a Si filter inserted to remove the unwanted scattered pump. The detector was able to be placed close to the input of the waveguides such that only highly excited regions were studied alleviating the problems of reabsorption, which take place for highly doped Er³⁺ structures. The process also diminishes the problems of unwanted pump levels which could saturate the detected signal. Unlike fibres it was not necessary to damage the facets of the waveguides to prevent the build up of amplified spontaneous emission. The subsequent fluorescence decay curves were stored on a Tektronix 7854 digital oscilloscope for further signal analysis. The overall response of the system was found to be approximately 1 μs .

Lifetimes of upconverted excited levels in Er³⁺ systems have been reported to lie between 1 and 10 μs ⁶⁸. Thus, it was felt that the detection system described was suitable for fluorescence lifetime measurements. The decay curves measured were stored on the digital sampling oscilloscope allowing examination of the natural logarithm and the differential of the natural logarithm. This facilitated analysis of the

logarithm and the differential of the natural logarithm. This facilitated analysis of the signal to determine any departure from the expected exponentiality and the instantaneous decay rate at any time during the decay process. Figures 5.16 and 5.17 are examples of the process with the last trace highlighting the fast decay component witnessed. This fast decay component is due to cooperative upconversion.

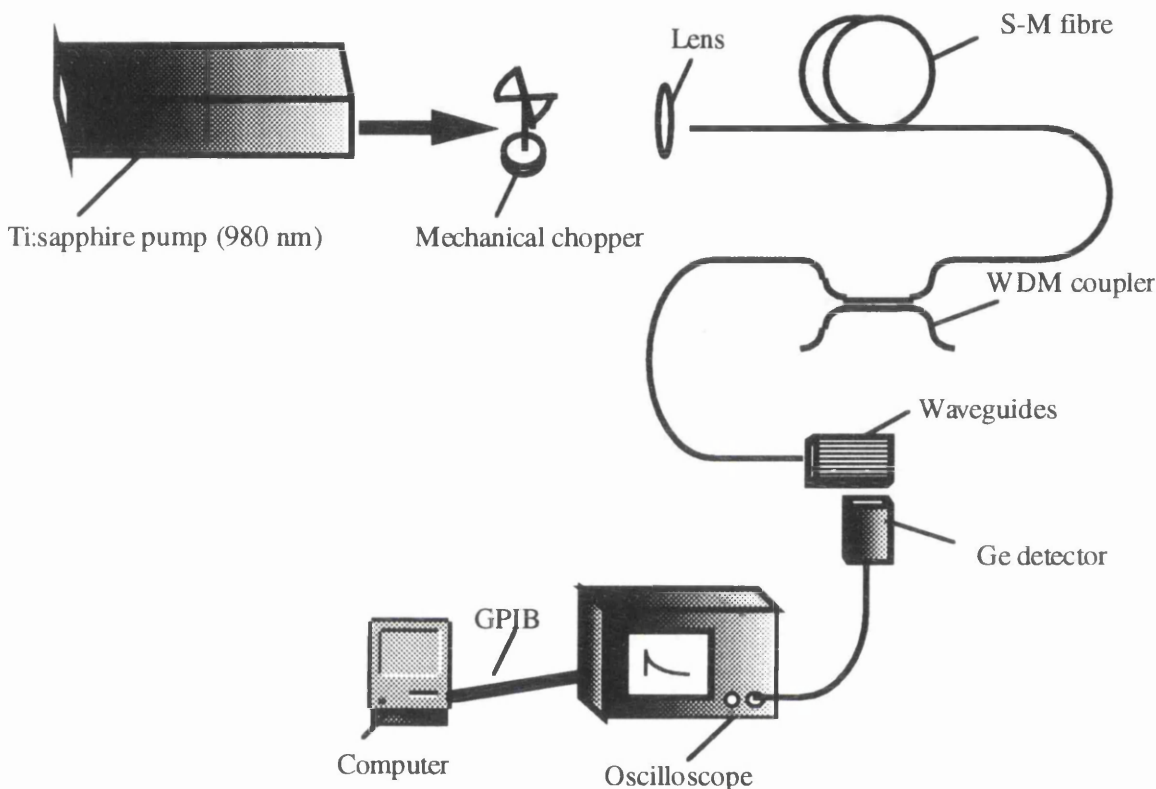


Figure 5.15 Experimental set-up for measuring fluorescence lifetimes.

To understand the Nd^{3+} system better, experiments were also conducted to measure the fluorescence lifetime for Nd^{3+} in planar silica samples. The typical lifetimes for lightly doped Nd^{3+} doped silica fibres are $500 \mu\text{s}$ ⁶⁹, whilst a nonuniform distribution of Nd^{3+} in planar silica samples was measured to have a lifetime of $250 \mu\text{s}$ ⁷⁰. The experimental set-up is similar to Figure 5.15.

An argon ion laser operating at 514 nm was used as the pump source. The beam was focused using a x20 lens and a mechanical chopper placed at the focus. The resulting chopped beam was collimated using a second identical lens. The beam incident on the chopper was placed as close to the outside edge of the chopper as possible, such that the theoretical fall and rise time of the beam pulse was calculated to be in the order of 0.5 ns. The collimated beam was end-fired into samples with waveguide widths of approximately $15 \mu\text{m}$. The maximum power incident was 600 mW. For neodymium a fast Si detector was used. To avoid saturating the detector with pump light, two filters

were placed in front of the detector. The transmission above 850 nm was 0.9 whilst below 850 nm the transmission was -60 dB. This was a necessary step as the Si detector was sensitive at the pump wavelength. The detected signal was sampled with a 400 MHz digital oscilloscope. Unfortunately, facilities were not available to allow signal analysis to investigate fast decay mechanisms. As a result the lifetime was determined by measuring the time taken for the signal to decay to the 1/e value of its peak value.

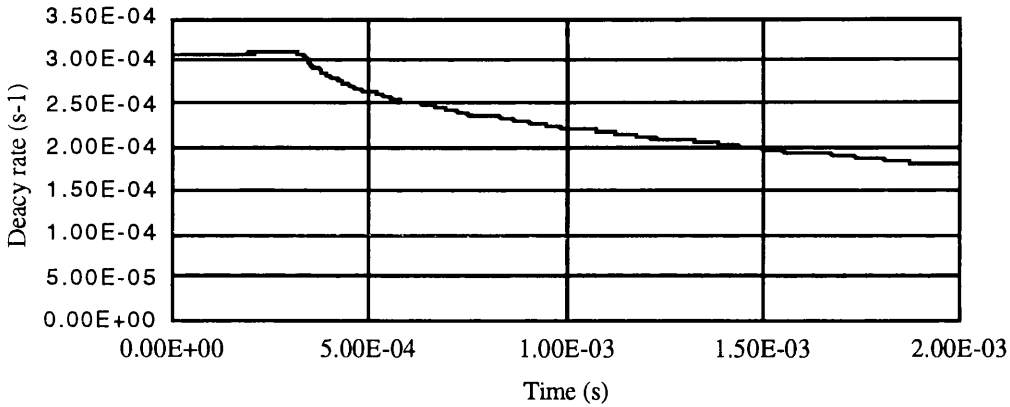


Figure 5.16 Fluorescent decay curve for an Er^{3+} doped $\text{SiO}_2\text{-P}_2\text{O}_5$ film.

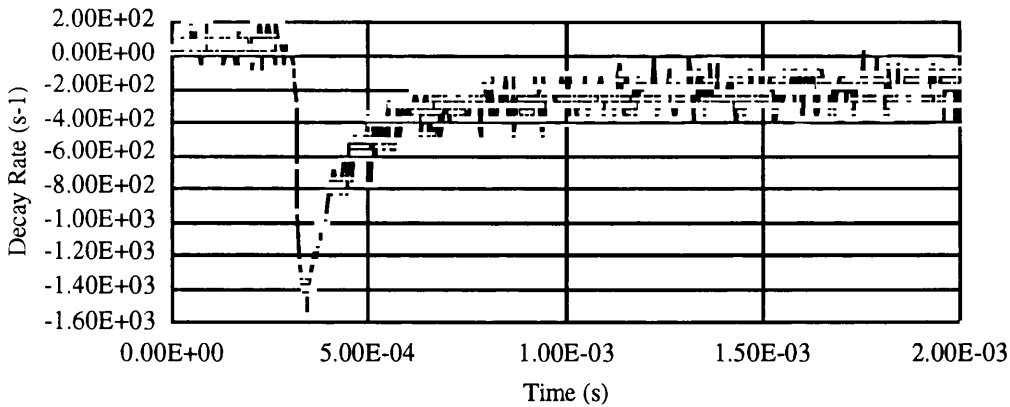


Figure 5.17 Differential of the natural logarithm of the decay curve for an Er^{3+} doped $\text{SiO}_2\text{-P}_2\text{O}_5$ film.

Measurements were undertaken and typical lifetimes measured were in the order of 300 μs . Figure 5.18 is a typical lifetime trace with the 1/e point occurring at 312 μs . However, the pulses incident to the waveguides were measured and found to have a fall and rise time of 6 μs . The overall response of the system should have been able to

resolve the pulse easily. To improve the response of the detector the load of 1 M Ω at the oscilloscope was replaced with terminal loads of 10 k Ω and 50 Ω . However, no significant change was witnessed in the response. It was the authors opinion that the lensing at the chopper was causing diffraction such that it was masking the pulse. To prevent this phenomenon it would be necessary to insert a spatial filter. However, the waveguide itself would act as a spatial filter 'cleaning' up the incident pulse such that the measurements witnessed were realistic values and thus, a value of $\sim 310 \mu\text{s}$ could be attributed to the slow decay component for the Nd³⁺ doped planar samples.

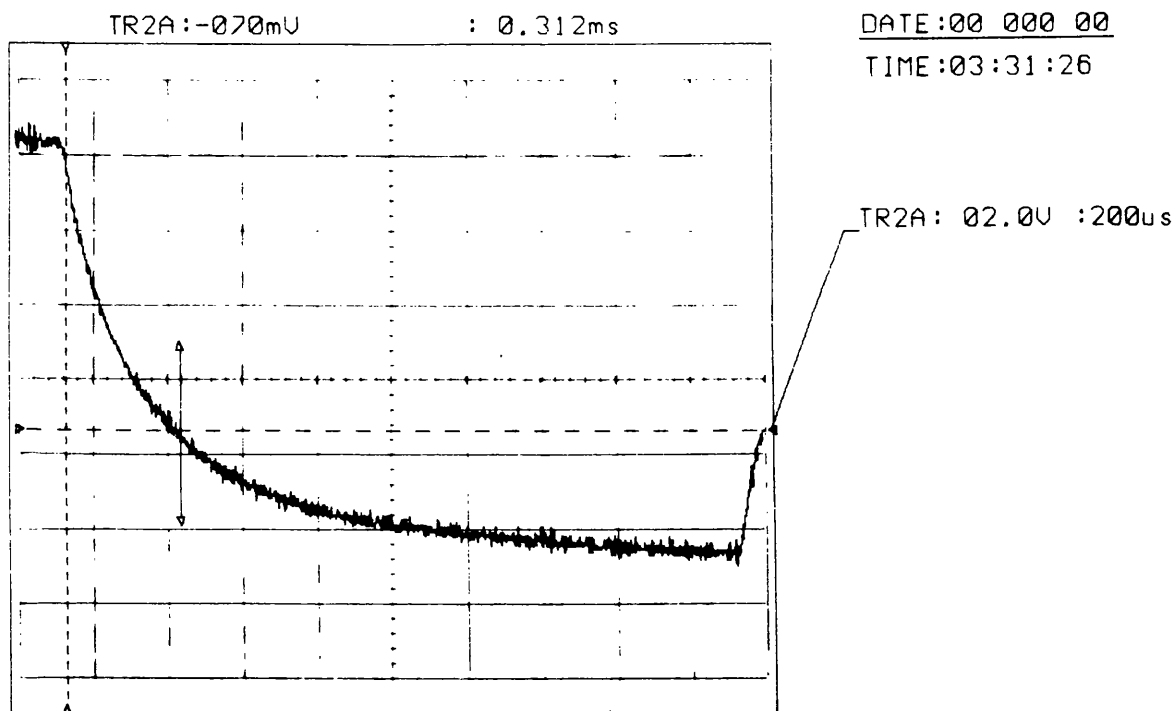


Figure 5.18 Fluorescent decay curve for a Nd³⁺ doped SiO₂-P₂O₅ film.

The techniques described were adequate to measure the fluorescence lifetimes and taking the differential of the natural log of the decay trends could be observed for doping regimes. However, no experiments had been conducted to try and measure the clustering concentration. Consequently, an experiment was devised based on fibre work by Quimby et al⁷¹. The experimental set-up was modified from Figure 5.15. Er³⁺ doped samples were pumped at 980 nm with light from a tunable Ti:sapphire laser. The transmitted pump power was detected at the output. Three multimode fibres bundled together were used to measure the green and infra-red fluorescence at 90° employing a photomultiplier tube and Ge detector respectively. A fibre connected filter was used to remove unwanted residual pump light for the infra-red measurement.

To model the clustering the following analysis was derived assuming a single-ion scheme. Pump light excites the $^4I_{11/2}$ and $^4F_{7/2}$ level through ground state absorption (GSA) and excited state absorption (ESA), respectively. The ions in the $^4F_{7/2}$ quickly relax to the metastable $^4S_{3/2}$ level resulting in green fluorescence to the ground state. Thus, it can be written that the green fluorescence varies with pump power as

$$\text{Green}_{\text{flu}} \propto N_3 \frac{P}{h\nu_p} \sigma_{\text{esa}} \tau_4 \quad (5.1)$$

where P is the pump power, $h\nu_p$ is the pump photon energy, σ_{esa} is the ESA cross section, τ_i is the lifetime of level i and N_i is the population of level i. The infra-red fluorescence at 1530 nm from the $^4I_{13/2}$ level which is measured in the experimental set-up, can be modelled. The IR fluorescence from level 2 varies with pump power in the same way as the population of level 3 such that

$$N_3 = N_2 \frac{\tau_3}{\tau_2} \propto \text{IR}_{\text{flu}} \quad (5.2)$$

From the analysis it is thus expected that for the single ion scheme, green upconverted fluorescence divided by the pump should be proportional to the IR fluorescence:

$$\frac{\text{Green}_{\text{flu}}}{P} \propto \text{IR}_{\text{flu}} \quad (5.3)$$

Thus, employing the experimental set-up described when plotting the $\text{Green}_{\text{flu}}/P$ against the IR_{flu} a straight line would be expected as they should be directly proportional. The published material found that there was an additional component to the Green fluorescence for all tested fibres with a much higher saturation power, suggesting the onset of clustering. i.e. at high pump levels ions are still being transferred to the $^4I_{11/2}$ level but instead of undergoing non-radiative decays to the metastable level $^4I_{13/2}$ they are instead being promoted to higher levels by pump ESA which requires much more power before saturating.

The authors concluded that to explain the anomalous pump-power dependence of the 980 nm ESA, clusters should be considered. The clusters consisted of a number of ions per cluster which could transfer energy within the cluster but could not react with different cluster groups. Consequently, the following relationships were given for steady state pumping conditions

SINGLE IONS

$$N_3 = \frac{(1-k)NW_P\tau_3}{1+W_P\tau_2}$$

$$N_2 = \frac{(1-k)NW_P\tau_2}{1+W_P\tau_2}$$

CLUSTERED IONS

$$N_3 = \frac{kNW_P\tau_3}{1+W_P(\tau_3+\tau_x)} \quad (5.4)$$

$$N_2 = \frac{kNW_P\tau_x}{1+W_P(\tau_3+\tau_x)} \quad (5.5)$$

Where W_P is the pump rate, N is the total number of Er^{3+} ions per unit volume. k is termed as the fraction of clustered ions whilst τ_x is the upconversion transfer time.

From the measured data the authors were able to fit the data to give an indication of the cluster concentration and the upconversion transfer time.

The experiment was conducted at BT Laboratories for Er^{3+} samples over a waveguide length of 1 cm such that the power measured at the output could be assumed to be the power the ions were subjected to. The technique was successful in measuring the pump and IR components. Unfortunately, the Green fluorescence was not able to be detected using the photomultiplier tube owing to the small signal intensities. Index matching fluid was placed on top of the waveguide and the fibre bundle placed in contact with the fluid to increase the coupling efficiency. This was still not adequate as the PMT was still not able to resolve any signal. A solution to the process was to employ a large area light pipe. As a result, at the point of writing, a fibre bundle consisting of 100 multimode fibres is being fabricated at BT Laboratories Crystal Workshop to facilitate the need for a larger detection area.

Until the samples are subjected to the quantitative characterisation experiment and the measured values are fitted to the cluster model, it will not be possible to determine the number of clustered ions. However, it should be noted that the fluorescence lifetime measurements described do allow trends to be observed for ion-ion interactions. As a result, conditions can still be set to reduce the fast decay components and thus conditions ascertained for increased amplifier efficiency.

5.3.4 Electron microprobe

Before analysing the experimental results for fluorescent lifetimes, it was felt necessary to determine the doping levels using an electron microprobe and to compare these

values to those determined from extinction coefficients⁶⁰. Thus, an accurate picture of the lifetime variations as a function of the doping level could be built up. Microprobe analysis had the added advantage of being able to analyse various areas of the sample for doping homogeneity.

Analysis was undertaken at the Department of Geology, Edinburgh University. Kind thanks are extended to both Dr S. Kearns and Dr P. Hill for the provision of the facilities, the helpfulness in the measurements undertaken and the brief overview to the workings of the electron microprobe .

Figure 5.19 is a basic schematic diagram of the electron microprobe. The particular probe used for this investigation was a Cameca-Camebax microbeam. The basic operation of the probe involves electron bombardment of the material. Consequently, X-rays are generated in the sample under test. From the wavelength and intensities of the lines in the X-ray spectrum the elements present may be identified and their concentrations estimated. An example of a resultant X-ray spectrum from a phosphosilicate core layer doped with both Er^{3+} and Al^{3+} is shown in Figure 5.20. The advantage of this technique compared to others is that chemical analysis can be obtained on very small selective areas by the use of a finely focused beam which typically operates in the 1-20 keV range. In the particular case in Edinburgh the spot size was $5 \mu\text{m}^2$ defocused, penetrating to a depth of $5 \mu\text{m}$

For quantitative analysis the intensities of the X-ray lines from the sample were compared to those from standard samples of known composition. Some of the samples used to determine Si, P, Al and Er were mineral wollastonite (CaSiO_3), mineral apatite ($\text{Ca}_5(\text{PO}_4)_3$), synthetic sapphire (Al_2O_3) and silicate glass doped with 18.99 wt% erbium respectively. 'Matrix corrections' were taken into account for instrumental corrections and correction for background intensities.

The Camebax had the facilities for scanning the beam in a raster manner. Consequently, 'dark' and 'light' regions could be identified for an aerosol Er^{3+} doped sample fabricated employing the old design of torch, discussed later. The strength of the aerosol solution was 1 M/ 0.4 M Er/ Al respectively. The expected doping level for the Er^{3+} ions was ~0.5 wt% . The measured values located around the samples are given in Table 5.3, all measurements are given in wt% and are accurate to 100 parts in 10^6 . This unit can be slightly misleading as to the apparent large difference in wt% between Er_2O_3 and Al_2O_3 . However this is to do with the molecular weight of Er_2O_3 being over three times that of Al_2O_3 . The average elemental Er doping level corresponds to approximately 0.25 wt% for this structure. Performing an absorption measurement on

the same device resulted in a doping level of 0.17 wt%. The discrepancies in doping level measurements was deemed to be because of the erratic doping levels throughout the structure, owing to the torch design.

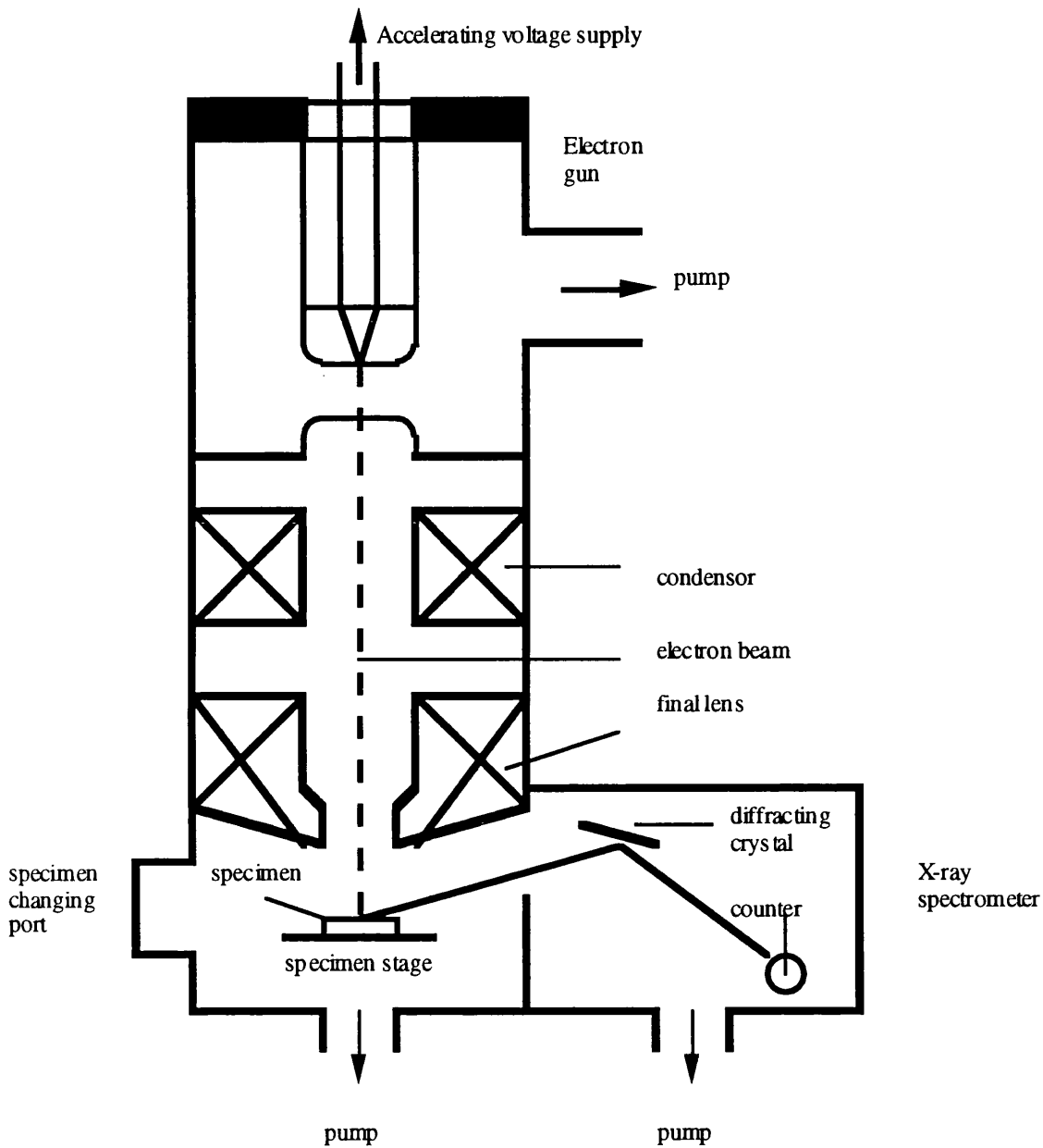


Figure 5.19 Schematic diagram of microprobe.

From Table 5.3 there are a few salient points. Firstly the SiO_2 and P_2O_5 levels agree with those predicted by theory (Chapter 3). Importantly the standard deviation for the Er_2O_3 level is high illustrating, large variations in concentration. This inhomogeneous doping is due to the build up of rare earth conglomerates as discussed in the subsequent paragraphs. It was even noted that by carefully scanning the samples for high intensity areas that a region with a doping level of 3 wt% was found. The same trend was

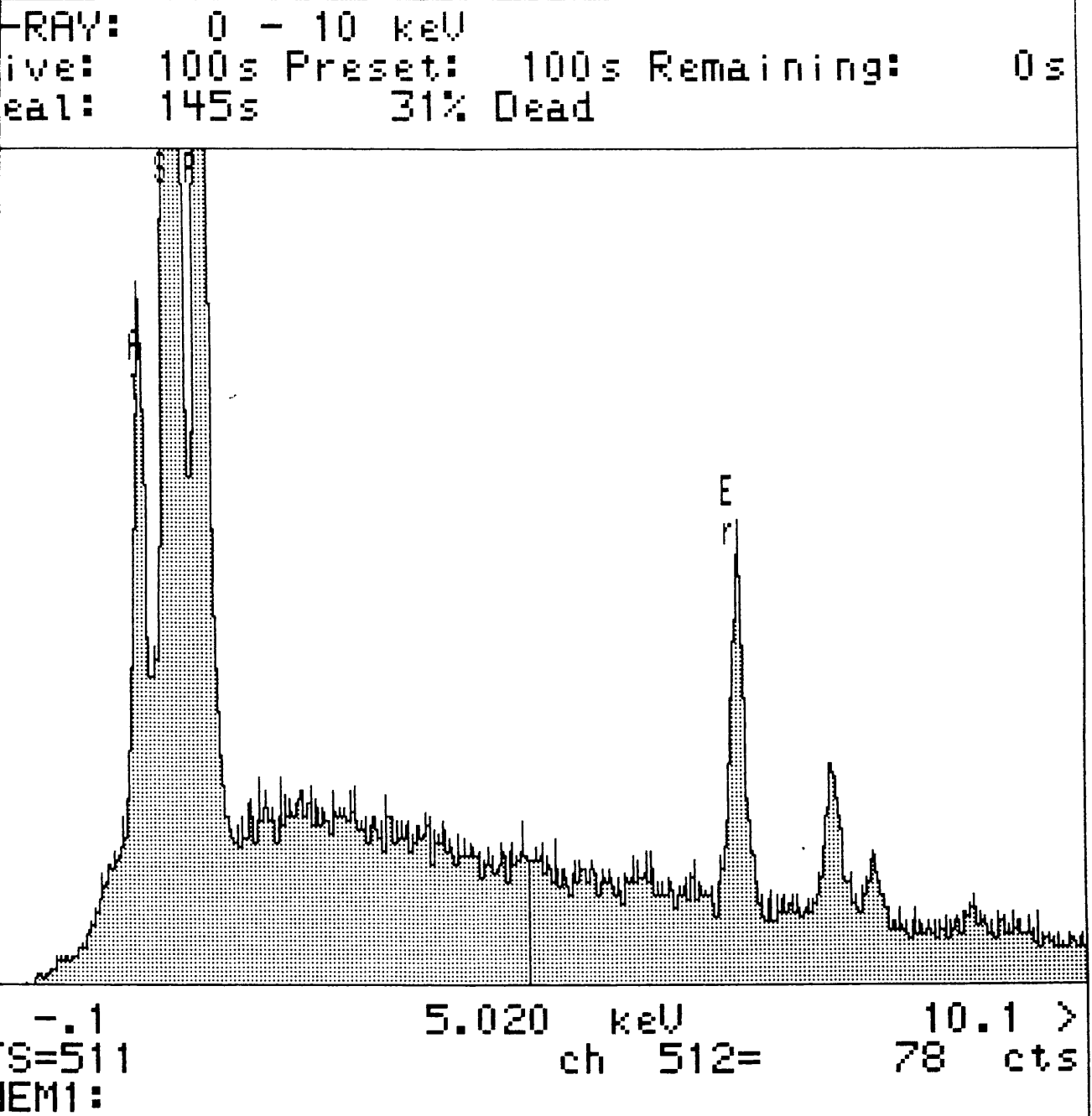


Figure 5.20 X-ray spectrum from an aerosol Er/ Al doped $\text{SiO}_2\text{-P}_2\text{O}_5$ film.

witnessed for Al_2O_3 with the higher levels situated in the same regions as the Er_2O_3 concentration. This has the potential advantage of aiding fluorescence lifetimes as Al^{3+} forces more non-bridging oxygen ions. Another possible dopant which has been investigated in short erbium doped fibres for reducing ion-ion interactions is the rare earth La^{3+} ⁷². The La^{3+} ions do not prevent clustering but they lower the probability of Er^{3+} ions being close to each other such that there is less likelihood of a fast cross

relaxation occurring between the Er^{3+} ions, since La^{3+} have no absorption features at the wavelengths discussed. Yb^{3+} which was investigated to sensitise fibres is another possibility as it is immune to upconversion (only two levels) and would increase the separation between ions. Ga^{3+} is another likely codopant to coordinate the Er^{3+} ions. However, due to time constraints these were not investigated.

	SiO_2	Al_2O_3	Er_2O_3	P_2O_5	Total
1	76.23	0.11	1.37	22.35	100.06
2	77.34	0.04	0.35	21.87	99.60
3	77.22	0.06	0.32	21.29	99.6
4	76.12	0.11	1.00	21.03	98.26
5	76.20	0.10	1.08	22.16	99.54
6	76.74	0.05	0.41	22.09	99.29
7	77.41	0.06	0.40	22.21	100.08
8	78.39	0.05	0.50	20.76	99.70
9	77.36	0.07	0.73	20.98	99.14
10	77.28	0.10	0.95	21.26	99.59
Mean	77.03	0.08	0.71	21.60	99.42
S.D.	0.71	0.03	0.37	0.60	0.55
Max.	78.39	0.11	1.37	22.35	100.08
Min.	76.12	0.04	0.32	20.76	98.26

Table 5.3 Results from microprobe analysis of aerosol Er/ Al doped $\text{SiO}_2\text{-P}_2\text{O}_5$ films.

As discussed throughout the report, to fabricate efficient Er-doped devices it is necessary for the dopant to be homogeneously distributed, thereby eradicating both scatter losses⁵⁹ and ion-ion interactions⁷³. Therefore, devices were tested for scatter losses and fluorescence lifetimes. The following sections detail results from a small number of samples tested during the work, with the aim of highlighting the typical results and trends.

5.3.5 Lifetime results

Aerosol doped $\text{SiO}_2\text{-P}_2\text{O}_5$ glass waveguides were formed on a 10 μm thick SiO_2 buffer layer.. The composition of the core glass formed was (in wt%): SiO_2 : P_2O_5 78.3: 21.1 (Table 5.3). ErCl_3 is incorporated into the silica during the deposition as previously described.

A burner incorporating an extra port was specially designed to prevent the condensing of the rare earth chloride. The resulting structures were fully fused in a high temperature furnace. Figure 5.21 shows an SEM of a rare earth doped etched structure. For fluorescence lifetime measurements channel waveguides were sawn with dimensions $\sim 15 \times 6 \mu\text{m}^2$ using a wafer dicing saw which also produced quality waveguide facets for end-fire coupling.

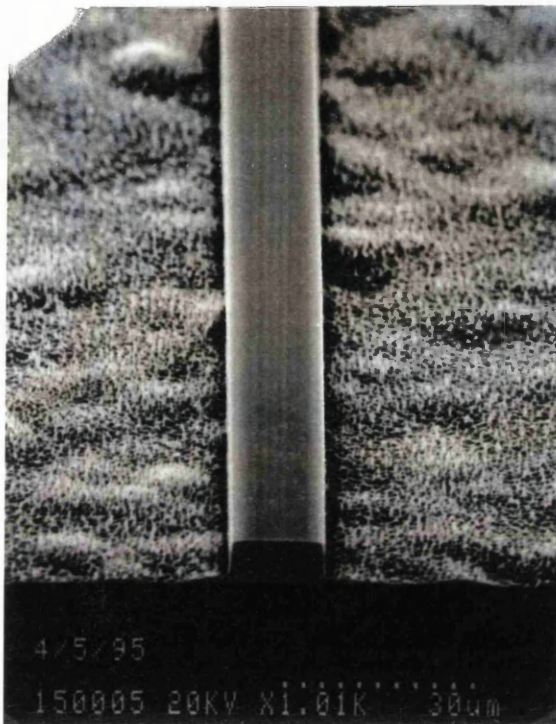


Figure 5.21 SEM photograph of an etched doped silica waveguide.

Scatter losses were investigated by prism coupling TE polarised light from a 4.8 mW He-Ne 632.8 nm laser into planar waveguides. For efficient Er-doped devices, it is extremely important that the out of plane scatter is negligible.

Results showed that irrespective of doping level above approximately 0.15 wt% scatter was much more pronounced for lower fusing temperatures. This is illustrated in Figures 4.6 and 4.7 of Chapter 4, where two samples doped with 0.36 wt% are compared. In Figure 4.6 the sample was fused at 1250 °C (sample 146) whilst the sample in Figure 4.7 (sample 154) was fused at 1375 °C. It can be clearly seen that sample 146 has a propagation loss of ~ 2 dB/cm whereas for sample 154 this has been reduced to below 0.5 dB/cm. Increasing the temperature above 1375 °C resulted in catastrophic breakdown of the wafer with implosions along faults in the Si crystal

planes and ultimately complete deformation of the Si wafers rendering them useless (Chapter 3 highlights this in more detail). Initially, large scattering centres were also observed in samples fabricated with the standard oxy-hydrogen burner owing to the complex aerosol delivery system. It should also be pointed out that there is more in plane scatter than observed for passive $\text{SiO}_2\text{-P}_2\text{O}_5$ films indicating mode conversion is taking place. With this preliminary experiment it was possible to deduce suitable samples for lifetime tests as there was no need for further measurements when samples exhibited high losses. High temperatures have also been shown to improve fluorescence lifetimes in fibre studies.

Ridge waveguides were formed by sawing and absorption data measured. An Advantest white light source was used to fibre couple into the sawn waveguides. The resulting output spectrum was collected and measured on an Anritsu spectrum analyser. By measuring the depth of the absorption features, Er^{3+} doping levels could be deduced⁶⁰ and the results for a range of samples are detailed in Table 5.4.

Fluorescence decay measurements were made using the experimental set-up shown in Figure 5.15. A Ti:sapphire producing pump powers of ~ 330 mW at the output of a single-mode fibre was used to excite the waveguides. Index matching fluid was used to increase the coupling efficiency so that the samples were all investigated under similar high pump power conditions. This is important since spontaneous emission lifetimes decrease with high pump powers. Differentials of the natural logarithm were measured, to highlight any small departures from an exponential decay and thus indicate the presence of ion-ion interactions. All samples were initially fused at 1375 °C, and lifetimes measured as a function of Er^{3+} concentration, aluminium co-doping and post thermal treatment. The latter consideration was necessary for cladding purposes.

Initial tests used samples produced with a standard torch design, where the burner had traversed the sample 6 times to produce film thicknesses of 6 μm . Samples were fabricated with varying ErCl_3 solutions of 0.25 M, 0.5 M and 1 M. The fast decay component was measured only to be ~ 1.7 ms for all samples. However, due to the ErCl_3 within the torch condensing, the maximum amount of Er^{3+} incorporated was only 0.17 wt%. This was also borne out in the fluorescence lifetime set-up when the samples were pumped at 980 nm as pump ESA resulted in very weak nonuniform green fluorescence being observed⁶⁸. The $^4\text{S}_{3/2}$ level is populated and produces fluorescence when the ions radiatively decay to the $^4\text{I}_{15/2}$ ground level.

A radical redesign of the torch was undertaken and produced doping levels of up to 0.72 wt% for 1M ErCl_3 solutions. It is worth pointing out that the Er^{3+} concentration

Torch	Doping level (M)	Er ³⁺ concentration (wt%)	Post anneal (° C)	Fast decay component (ms)
standard	0.25 Er	0.12		1.7
standard	0.5 Er	0.17		1.7
standard	1 Er	0.17		1.7
modified	0.5 Er	0.43		0.67
modified	1 Er	0.72		0.4
modified	1 Er / 0.4 Al	0.56		0.96
modified	1 Er / 0.4 Al	0.56	850-1200 (1hr)	0.58
modified	1 Er / 0.4 Al	0.56	1200 (1 hr)	0.6
modified	1 Er / 0.4 Al	0.56	1200 (2hr)	0.56

Table 5.4 Er³⁺ doping concentration and fast decay component measurements.

could easily be increased by tailoring the halide deposition to produce only 0.5 μm per traversal. Fluorescence lifetime measurements of the differential of the natural log for ErCl₃ solutions of 0.5 M and 1.0 M plus a 1.0 M co-doped with 0.4 M Al(NO₃)₃ are given in Figure 5.22. The slow decay component from the dispersed Er³⁺ ions is typically 5 ms whilst the fast decay component becomes more pronounced for increased dopant being ~0.67 ms and ~0.4 ms for the 0.5 M and 1.0 M respectively. This is to be expected as the heavier doped sample is more susceptible to microclustering. The sample co-doped with Al³⁺ showed the best fast decay component of 0.91 ms, an initial decay rate which is ~5 times higher than the final rate of the slow decay component. This is due to the co-ordination of more non-bridging oxygen ions which screen the Er ions from their large cationic field strengths⁶³. Electron microbeam analysis indicated an Al ion concentration of 0.04 wt% using a Camebax Microbeam. Pump ESA was still in evidence though, with a weak uniform green stripe observed along the guide. The solubility for Al(NO₃)₃ in cold water is 63.7 grams/100 cc, thus it was difficult to dissolve solutions stronger than 0.4 M. However, for etching of channel waveguides this did not decrease the etching rate to unacceptable levels as is the case for highly solution codoped Al(NO₃)₃ samples which result in mask break-down due to underetching⁶⁴.

Having, determined suitable material and temperature parameters for the core structure tests were carried out to investigate the fast decay component as a function of post annealing. These temperatures were based on suitable values for cladding conditions. The first condition involved ramping the temperature from 850 °C to 1200 °C and dwelling for one hour whilst the other two involved plunging the sample at 1200 °C and dwelling for one and two hours as illustrated in Figure 5.23. This resulted in a fast decay component of ~0.6 ms for all the samples. Thus the Er³⁺ ions do not undergo serious ion-ion interactions from post annealing with the major influences being the initial time duration and fusing temperature as well as the doping regime.

In conclusion the major factors which determine both scatter loss and the fast decay component for aerosol doped samples are primarily the initial fusing conditions. It was discovered that the higher the temperature and the shorter the time duration the better the results with decreased initial decay rates and reduced out of plane scatter. Post annealing did not drastically effect the fast decay component as it is believed that the co-ordination conditions for the rare earth is more pronounced during the initial soot collapse, with the rare earth having more favourable conditions for clustering. Codoping with a very small wt% of aluminium reduced the fast decay component without seriously reducing the etch rate or the etch quality. Thus, the rare earth ions are seen to disperse well and improve the laser conditions for a planar device.

The lifetimes of solution doped samples were also investigated. Dr G. D. Maxwell at BT Laboratories is acknowledged for his help and collaboration in regards to solution doped material.

The time resolved excited state fluorescence measurements were measured in the same manner as described earlier. Much of the same trends were witnessed, although other co-dopants were investigated. Increasing the Er³⁺ level resulted in an increase of the concentration quenching effect as did increased thermal exposure. To reduce the effect, Al³⁺, Ga³⁺ and Ca²⁺ were employed as co-dopants. The Ca²⁺ co-dopant was investigated due to the RF-deposition work conducted by AT&T workers. The RF-sputtering deposition technique of Er³⁺ doped soda lime glass (SiO₂-Na₂O-CaO) was able to incorporate extremely high concentrations of Er³⁺ but still achieve a long lifetime of up to 12 ms³³.

Compared to aerosol doping larger amounts of dopant were incorporated for weaker solution strengths. Typically, the maximum erbium solution strength was 0.04 M providing a doping level of 1.1 wt%. The Al³⁺, Ga³⁺ and Ca²⁺ co-dopant solution

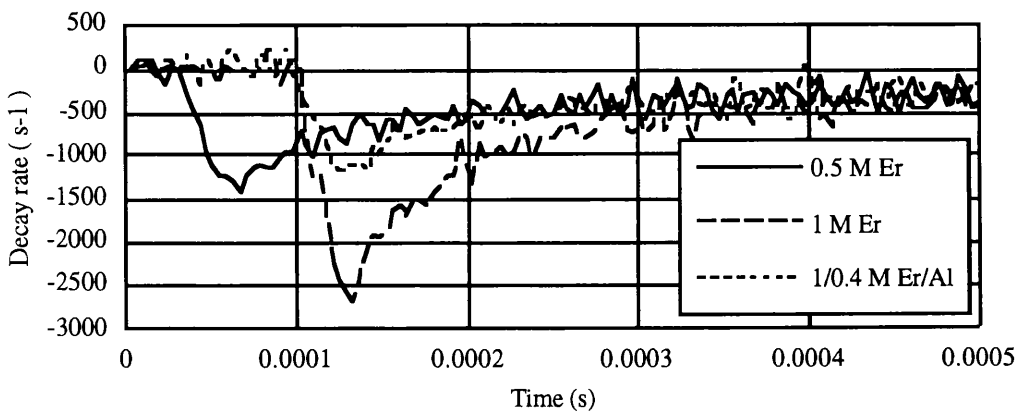


Figure 5.22 Differential of the natural log for varying Er doping conditions.

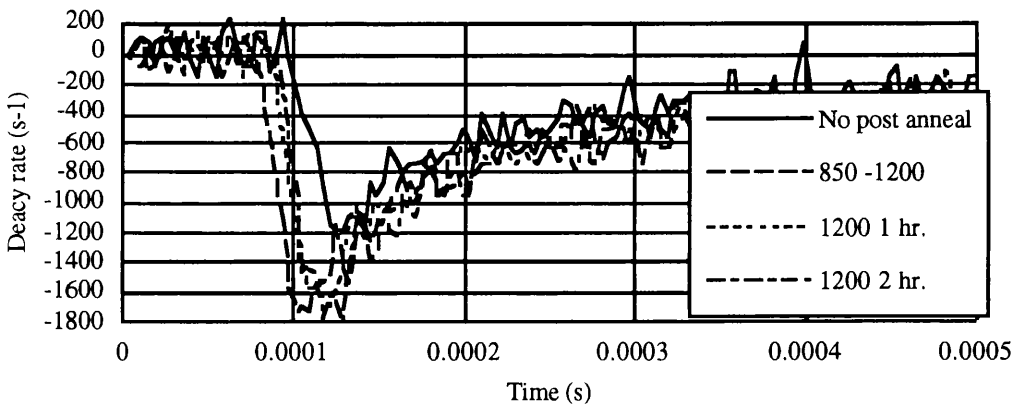


Figure 5.23 Differential of the natural log for varying post anneal conditions.

strengths were generally an order of magnitude greater than that of Er^{3+} . For a solution strength of 0.4 M aluminium the amount incorporated was approximately 1 wt%. It was also found that co-doping resulted in a reduction in the Er^{3+} level.

The co-dopants were all observed to greatly reduce the fast initial decay component. Unlike, the aerosol technique though the spectral response of the system was dominated by the effect of the P_2O_5 co-dopant with no observable broadening or narrowing in the width of the absorption for the other co-dopants. Another feature was the much reduced etch rates especially for the Al^{3+} co-doped system. Doping with an Al^{3+} level of 1 wt% resulted in an etch rate reduction of greater than four times. The other co-dopants with a doping level of 1 wt% were seen to reduce the etch rate by

approximately one half, which was still sufficient though to etch waveguides before mask breakdown.

At the point of writing it is still not certain which technique results in the least amount of clustered rare earth ions. Until, ESA experiments are conducted and the measured values are fitted to the cluster model technique it will not be possible to determine the better of the two doping regimes. However, both techniques do exhibit similar characteristics and are in nature simple techniques.

5.3.6 Nd³⁺ doped planar waveguide lasers

Nd³⁺ solution doped waveguides were fabricated whilst visiting BT Laboratories. The phosphorous level of the deposited soot was chosen to be high as possible. Subsequently the soot was partially fused and immersed into an alcohol solution of NdCl₃. After drying the porous structure was fully fused to consolidate the Nd³⁺ doped SiO₂-P₂O₅ glass. Using standard photolithographic techniques and a C₂F₆/ CHF₃ reactive ion etch (RIE) 12 x 8 μm² waveguide ridges were formed. The RIE process was based on a 'fast' etch devised for passive devices at BT laboratories. A 20 μm thick SiO₂-P₂O₅-B₂O₃ cladding layer with a refractive index matched to that of the buffer layer was then formed by F.H.D.. This resulted in an index difference of 0.87 % between the core and cladding. The final device was cut to a length of 5.9 cm, with the waveguides not undergoing the slow process of polishing.

Initial measurements for Nd³⁺ absorption and insertion losses were conducted to evaluate the samples suitability for laser oscillation. Absorption measurements were undertaken using a white light source and an Advantest optical spectrum analyser, the resulting loss spectrum of a 12 μm wide channel waveguide is illustrated in Figure 5.23. The absorption at 804 nm corresponds to the Nd³⁺ ⁴I_{9/2}-⁴F_{5/2} transition and a doping level of 0.38 wt.%. Insertion losses were measured at point wavelengths using a fibre to fibre arrangement. Piezo controllers and lock-in amplifiers were used to maximise the throughput of input and output fibres at 632.8 nm and 1317 nm. The fibres were then drawn apart and the waveguides inserted. Once again the throughput was maximised and the insertion losses deduced. This produced insertion losses of 1.7 dB and 0.84 dB for 632.8 nm and 1317 nm respectively.

Fluorescent spectra were obtained by 'end-firing' 514 nm light from an argon ion laser into the waveguide and recording the output on a spectrum analyser. Figure 5.24 shows the Nd³⁺ ⁴F_{3/2}-⁴I_{11/2} transition. The emission peak was centred at 1.0544 μm

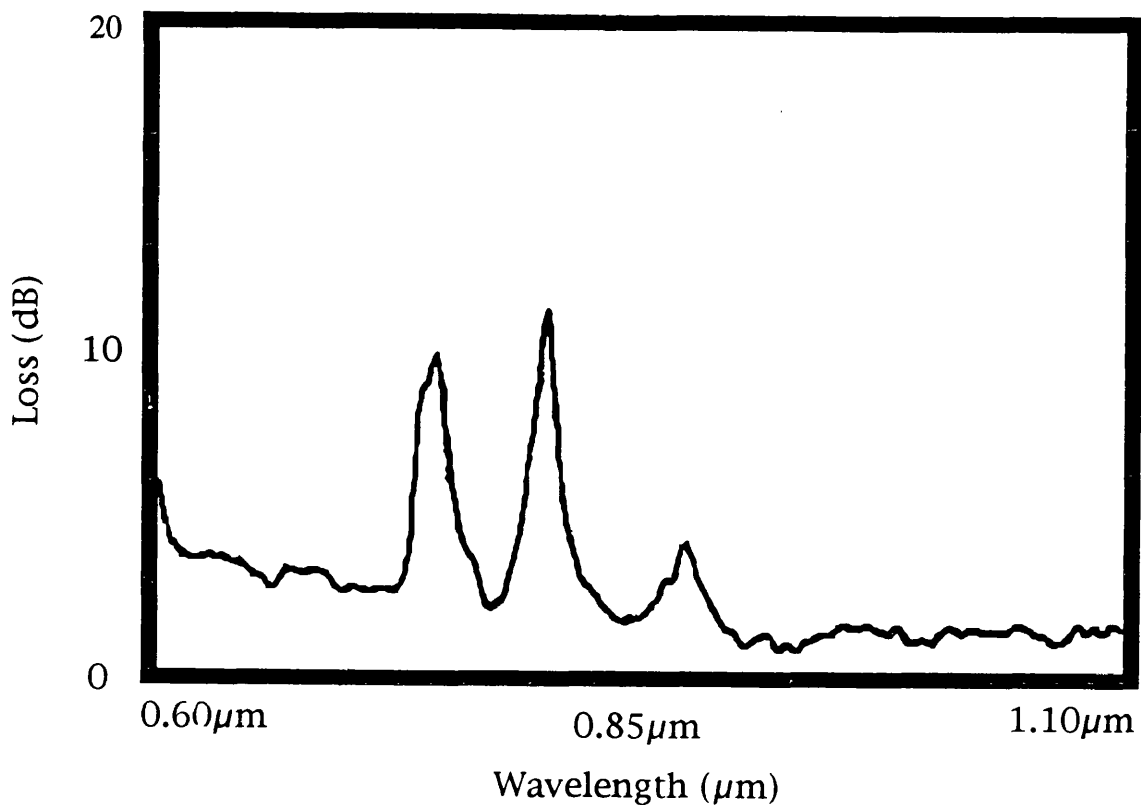


Figure 5.23 Loss spectrum of Nd³⁺ doped silica waveguide fabricated by solution doping.

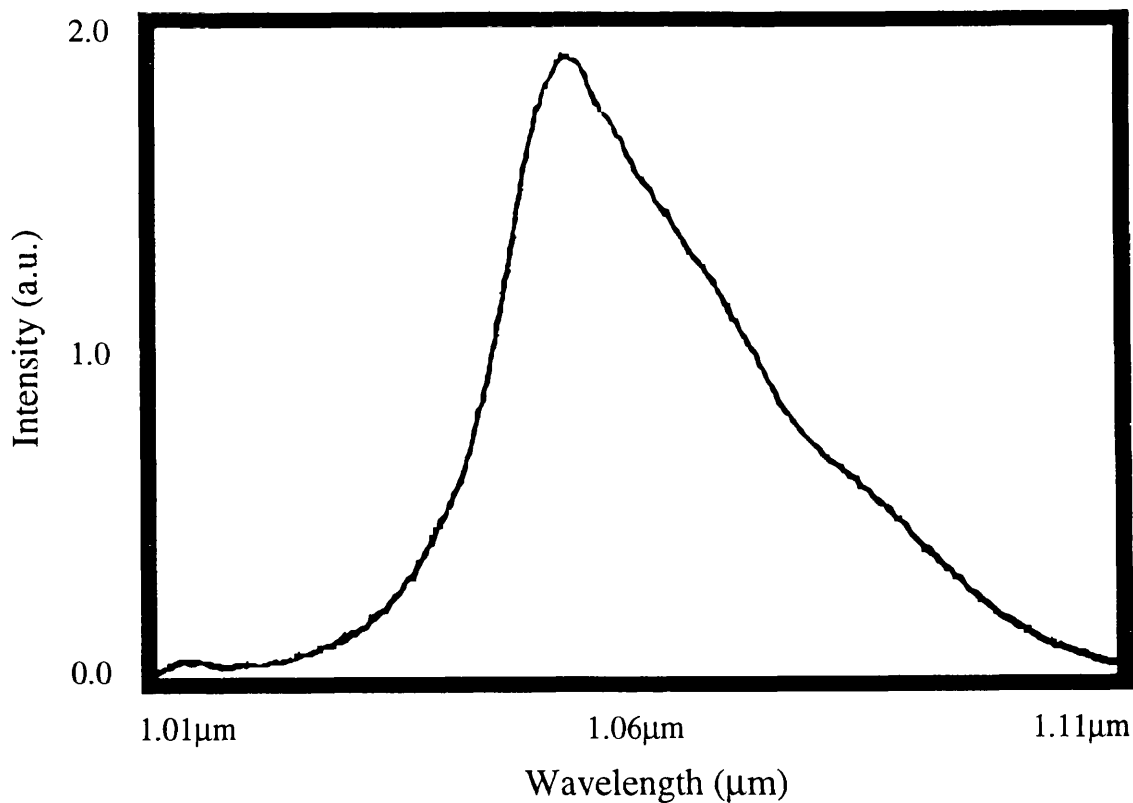


Figure 5.24 Fluorescence spectrum of Nd³⁺ doped silica waveguide fabricated by solution doping.

with a F.W.H.M. of 20 nm which is in good agreement with the heavily doped phosphorous silica glass.

A laser cavity was formed by butting dielectric coated mirrors onto the waveguide ends, with index matching liquid. Pressing of the 2 mm thick mirrors against the ends of the 1 mm thick substrate was quite a precarious method and not exactly ideal. To aid the process special mounts were designed to allow attachment of the substrate to the mount. They were also able to support the mirrors such that the centre of the mirror coincided with the waveguides under test and could be pressed quite firmly against the end. A more ideal solution would be to coat the waveguide ends with dielectric reflection mirrors. The input mirror had a high reflectivity (99.9 %) at the lasing wavelength and high transmission (90 %) at the pump wavelength. The output mirror had $R = 95 \%$ at the lasing wavelength and $T = 95 \%$ at pump. Optical pumping was performed by a Ti:sapphire laser tuned to the main Nd^{3+} absorption line of 804 nm. The pump light was end-fire coupled into the waveguides using a x10 microscope objective. The objective was coated for high transmission at the pump wavelength and AR coated for the lasing wavelength. The resulting output was filtered to remove the residual pump and a beam splitter was used to allow simultaneous measurement of the spectra and output power. An Advantest Spectrum analyser was used to measure the spectra characteristics and a Ge detector to calibrate the output power levels.

A typical lasing spectrum for the $12 \times 8 \mu\text{m}$ is illustrated in Figure 5.25. For this particular Nd^{3+} doped silica sample multi-mode oscillation took place. The F.W.H.M. was measured to be 0.3 nm at $1.0529 \mu\text{m}$ and 0.2 nm at the $1.0558 \mu\text{m}$ peak. The lasing threshold was 20 mW of absorbed pump power and the slope efficiency was recorded to be 2.6 % (Figure 5.26). To measure the absorbed pump power the Ti:sapphire was tuned to a wavelength which exhibited no absorption (typically 848 nm). The transmitted power was then compared to the transmitted power at 804 nm. Thus, for a threshold of 20 mW the actual incident power to the objective microscope was 220 mW. Figure 5.27 is included to illustrate the spectrum at threshold. Output powers of over 1 mW were measured for this particular doping concentration⁷⁴.

CW oscillation of the Nd^{3+} doped sample was maintained for a complete day (~ six hours) without any deterioration in output power, or variation in peak wavelength, indicating the lack of thermal problems. The measured slope efficiency is greater than previously reported results and the threshold is also lower. Reasons for the improvement in device parameters is the lower propagation losses and the possible longer fluorescence lifetimes.

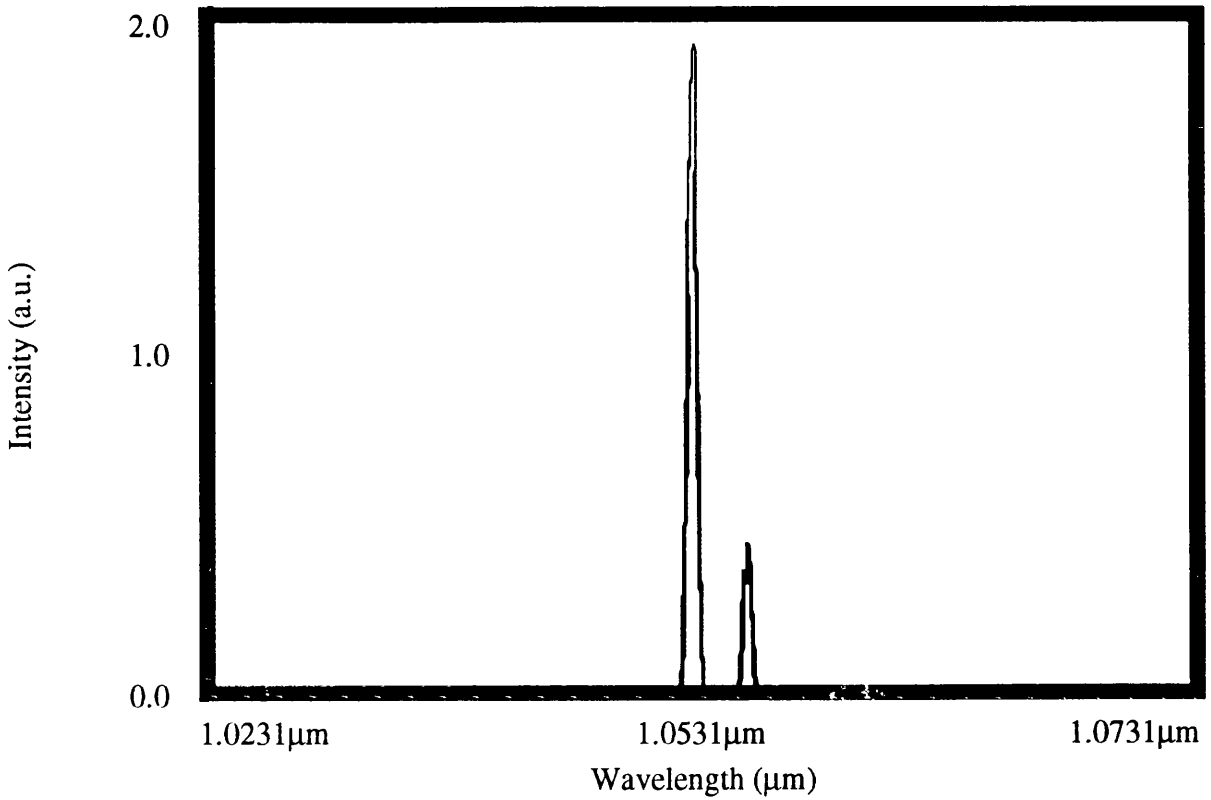


Figure 5.25 Lasing spectrum of Nd^{3+} doped silica waveguide fabricated by solution doping.

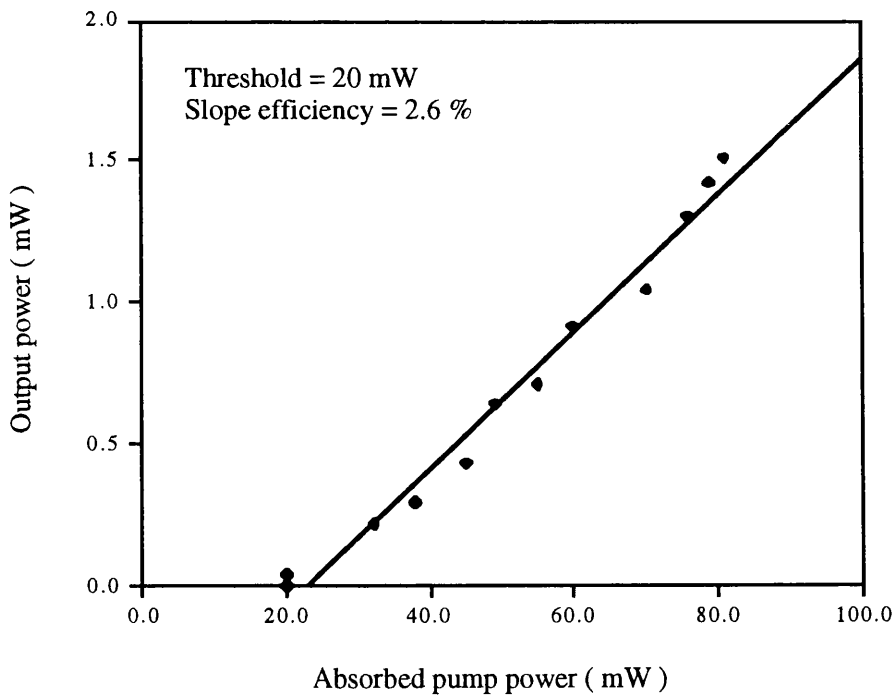


Figure 5.26 Slope efficiency of Nd^{3+} doped silica waveguide fabricated by solution doping.

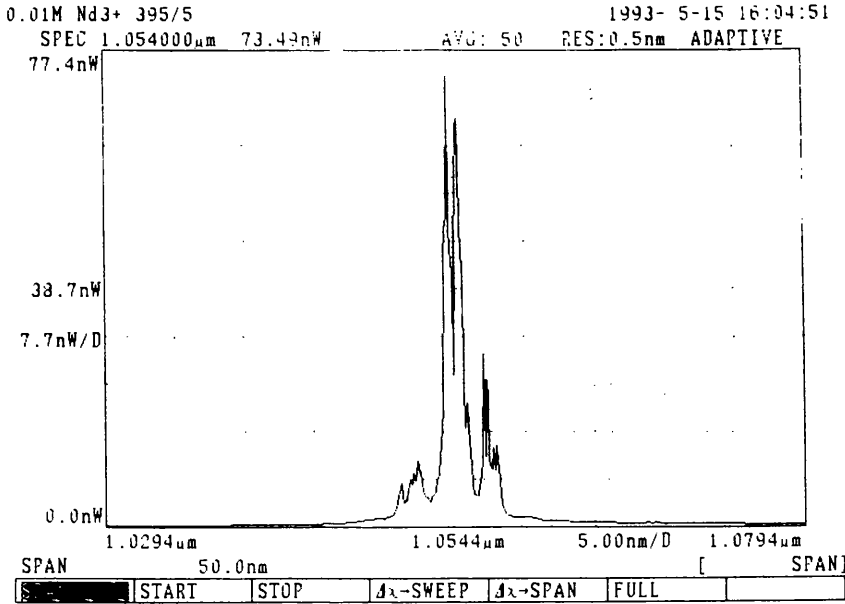


Figure 5.27 Lasing spectrum at threshold of Nd³⁺ doped silica waveguide fabricated by solution doping.

A mathematical analysis based on the Rigrod method⁷⁵ was carried out to determine the optimum output power extraction efficiency as a function of the output pump mirror reflectance. The analysis assumes a homogeneously saturable gain with no distributed losses. Figure 5.28 illustrates the left and right-travelling intensities in a laser with a larger output coupling. After a brief analysis it can be shown that the intensity striking the output coupler is

$$I_2 = \frac{1}{(1 + r_2 / r_1)(1 - r_1 r_2)} \left[2\alpha_{mo} L - \ln \left(\frac{1}{r_1 r_2} \right) \right] \quad (5.6)$$

where α_{mo} is the unsaturated gain coefficient, L is the length of the medium and r_1 and r_2 are the square root of the input and output mirror reflectances at the lasing wavelength, respectively. It can thus be written that the output intensity, assuming that any finite reflectivity at the other mirror represents unavoidable loss, is

$$I_{out} = T_2 I_2 = \frac{T_2 I_{sat}}{(1 + r_2 / r_1)(1 - r_1 r_2)} \left[\ln G_o - \ln \left(\frac{1}{r_1 r_2} \right) \right] \quad (5.7)$$

where G_o is the small signal gain and is equivalent to $\exp(2\alpha_{mo}L)$ and I_{sat} is the saturation intensity. The maximum intensity which can be extracted from the laser medium is

$$I_{avail} = 2\alpha_{mo}I_{sat}L \quad (5.8)$$

such that the power-extraction efficiency can be written as

$$\eta \equiv \frac{I_{out}}{I_{avail}} = \frac{T_2}{(1+r_2/r_1)(1-r_1r_2)} \left[1 + \frac{\ln r_1 r_2}{\ln G_o} \right] \quad (5.9)$$

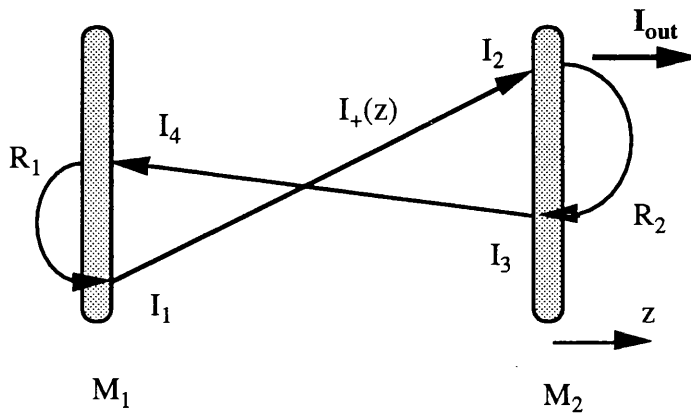


Figure 5.28 Schematic of laser cavity with large output coupling.

Since the analysis depends on no distributed losses, it was felt sufficient to incorporate the small losses as part of the left-hand mirror reflectivity. Thus, Figure 5.29 illustrates the device with no loss ($R_1 = 99\%$) and $R_1 = 95\%$ for a small distributed loss.

As is the case for the system under consideration the gain is relatively low and hence the output coupling is much more critical for optimum output power. The optimum was calculated to be in the region of 80 % reflection. Figure 5.29 illustrates this point. A dielectric coated mirror with a reflectance of 80 % was butted to the waveguide output end, producing a slope efficiency of 10 % but at the cost of an increased lasing threshold of 35 mW absorbed pump power⁷⁶. The experimentally measured output power from this laser is shown in Figure 5.30, as a function of the absorbed pump power. A dielectric mirror with an output mirror reflectance of 90 % was also tested and found to have a threshold of 25 mW and a slope efficiency of 6.1 % (Figure 5.31).

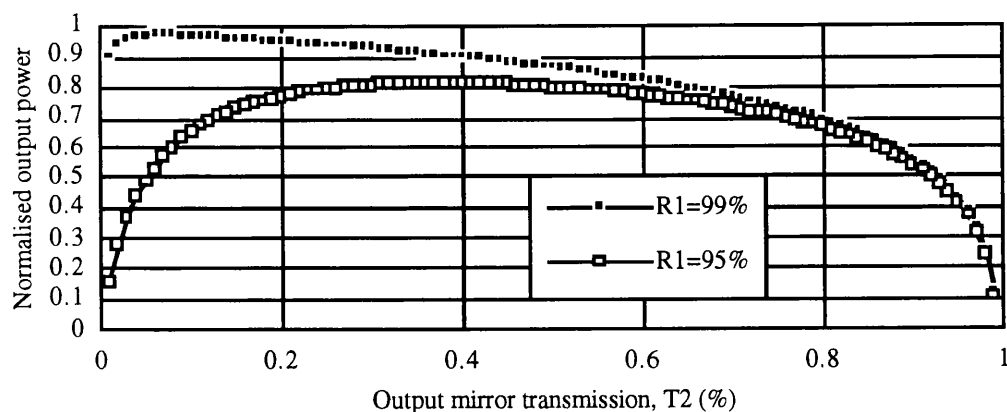


Figure 5.29 Rigrod analysis for Nd^{3+} doped silica waveguide laser.

A subsequent solution doped sample with a doping level of 0.5 wt% was also able to achieve CW laser oscillation. Powers greater than 2 mW were output but unfortunately this was limited by the maximum power available. Unfortunately, incident powers greater than 450 mW were necessary for threshold and the maximum power available from the Ti:sapphire at 804 nm was 550 mW. Consequently, measurements were not readily available especially with the unsatisfactory mirror arrangement, although Figure 5.32 details the measured spectrum.

Nd^{3+} aerosol doped planar waveguides were formed using the specially designed four port oxy-hydrogen torch⁷⁷. Transport of the Nd/ Al aqueous solution to the burner was possible using a suitable PVC pneumatic atomiser and N_2 gas. Al^{3+} was used as a co-dopant as it resulted in a reduction in the fast decay component of the fluorescence decay. The rare earth concentration was dependent both on the strength of the solution and the transport gas flow rate. The torch was designed to avoid the possibility of gravitational settling and hence, condensation of the rare earth, as discussed earlier. The low density soot was then fully fused in a high temperature electric furnace to produce a low loss doped silica waveguide. Ridge waveguides ($25 \times 7 \mu\text{m}^2$) were formed using standard photolithographic techniques and a CHF_3 RIE. A $20 \mu\text{m}$ thick $\text{SiO}_2\text{-P}_2\text{O}_5\text{-B}_2\text{O}_3$ cladding layer, index matched to the buffer was then formed by a second step FHD. The index difference between the core and cladding was 1.2 % and the final device was sawn to a length of 4.5 cm.

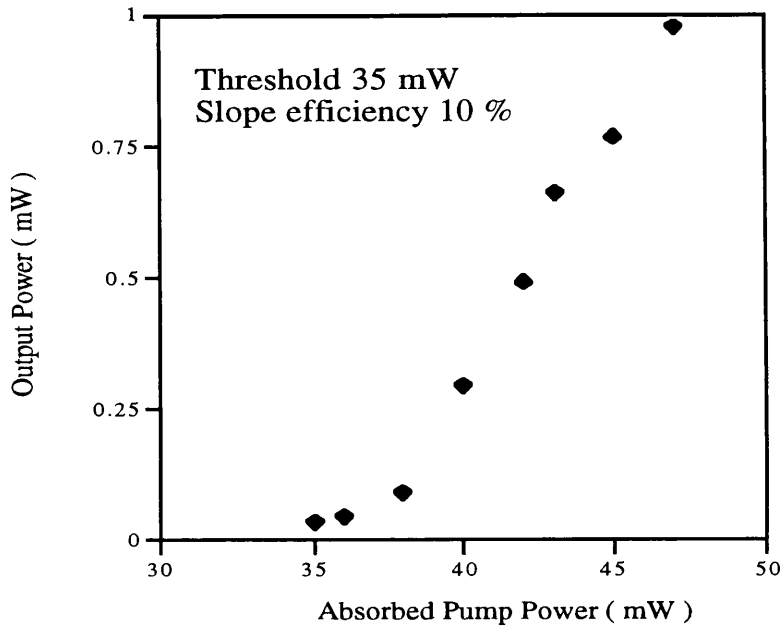


Figure 5.30 Slope efficiency of Nd^{3+} doped silica waveguide fabricated by solution doping for an output mirror reflectance of 80 % at the lasing wavelength.

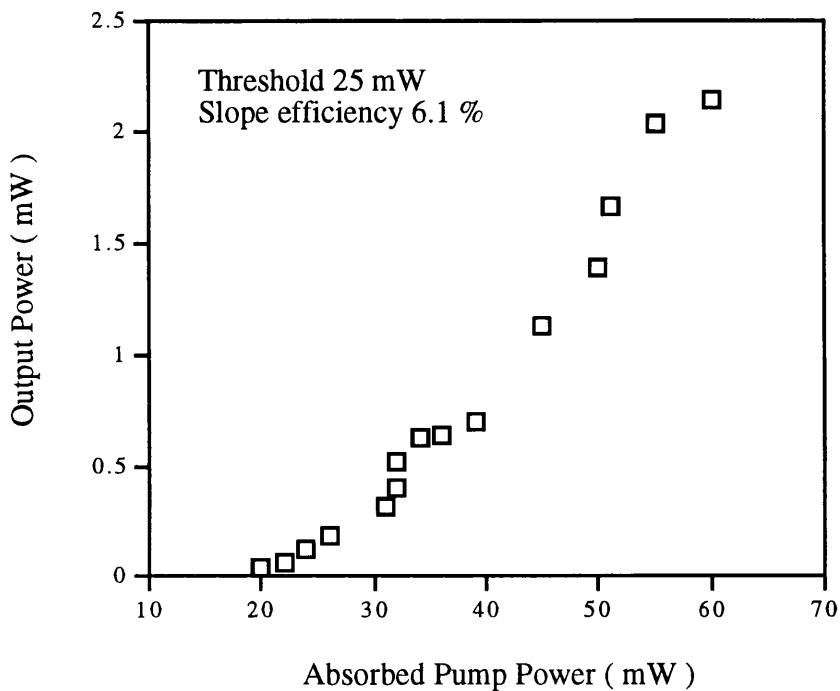


Figure 5.31 Slope efficiency of Nd^{3+} doped silica waveguide fabricated by solution doping for an output mirror reflectance of 90 % at the lasing wavelength.

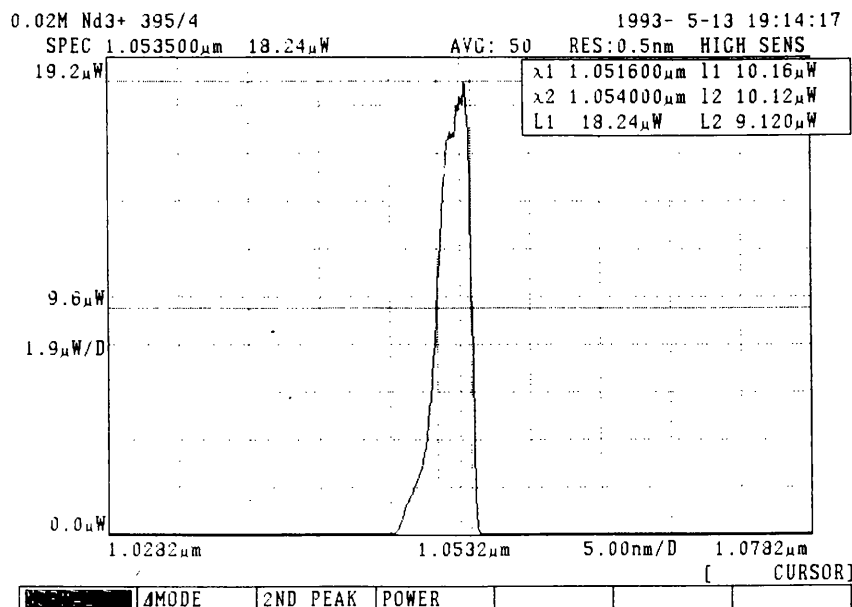


Figure 5.32 Lasing spectrum of Nd³⁺ doped silica waveguide fabricated by solution doping with a doping level of 0.5 wt%.

To evaluate the suitability of the waveguides the exact same processes were conducted as for the solution doped laser. Propagation loss and Nd³⁺ absorption measurements were undertaken. Figure 5.33 shows the loss spectrum for the 25 x 7 μm² buried channel waveguide measured using a fibre connected white light source and an optical spectrum analyser. The Nd³⁺ ion concentration was estimated to be 0.25 wt % using the Nd³⁺ ⁴I_{9/2} - ⁴F_{5/2} absorption at 802 nm. This was confirmed by electron microprobe analysis implementing a Camebax Microbeam, which indicated an ion concentration of approximately 0.21 wt % for Nd and 0.04 wt % for Al. Point wavelength sources at 632.8 nm and 1317 nm were used to measure insertion losses. Piezo controllers and lock-in amplifiers were used to maximise the throughput. The throughput was then maximised with the sample in place producing insertion losses of 3.2 dB and 1.8 dB at 632.8 nm and 1317 nm respectively. The loss was higher than that of the comparable solution doped samples detailed earlier. The most likely reasons for this were due to the combined effect of decreased coupling efficiency for the highly multimode waveguide and phosphorous out diffusion from the core⁵⁹. Cladding conditions for the samples were not as good as the solution doped devices resulting in some slab guidance.

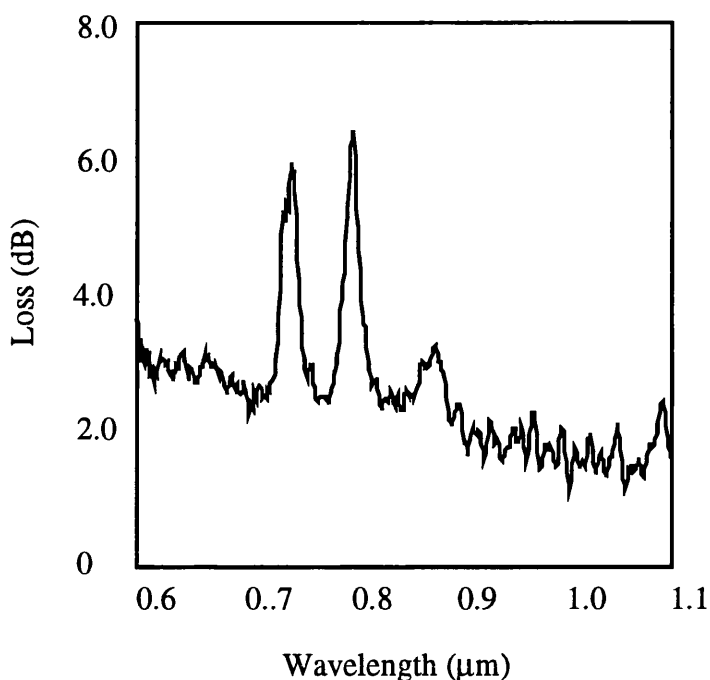


Figure 5.33 Loss spectrum of Nd³⁺ doped silica waveguide fabricated by aerosol doping.

An argon ion laser tuned to 514 nm was 'end-fire' coupled into the waveguide and the fluorescence spectrum was recorded on a spectrum analyser. The Nd³⁺ ⁴F_{3/2} - ⁴I_{11/2} transition produced an emission peak centred at 1.0513 μm with a FWHM of 25 nm, the FWHM being broader than that observed for non Al³⁺-doped samples.

To form a laser cavity dielectric coated mirrors were butted to the end of the waveguides with index matching fluid to suppress unwanted Fabry-Perot modes and increase the coupling coefficient. The input mirror had a high reflectivity (99.9 %) at the lasing wavelength and high transmission (90 %) at the pump wavelength. The reflectivity of the output mirror at the lasing and pump wavelength were 95 % and 5 % respectively. An argon ion laser pumped a Ti:sapphire laser, tuned to 802 nm was used to optically pump the waveguide cavity. High pass filters were placed at the output to remove residual pump light and a beam splitter inserted to measure the spectra and output simultaneously.

An example of the lasing spectra measured is shown in Figure 5.34. The FWHM was measured to be 0.3 nm at 1.0525 μm. The lasing threshold was 22 mW of absorbed pump power and the slope efficiency was recorded to be 2.5 % (Figure 5.35). The absorbed pump power was measured in the same fashion as the solution doped device with incident powers greater than 200 mW necessary to reach threshold. It is believed

that the threshold and slope efficiency will be improved as the deposition parameters are optimised for the aerosol reaction, and with smaller waveguides due to the increased transfer rate of the pumping energy . Also, the power-extraction efficiency is still to be determined and tested in the same way as the solution doped samples but it is envisaged that optimising the output coupler configuration will result in increased efficiencies.

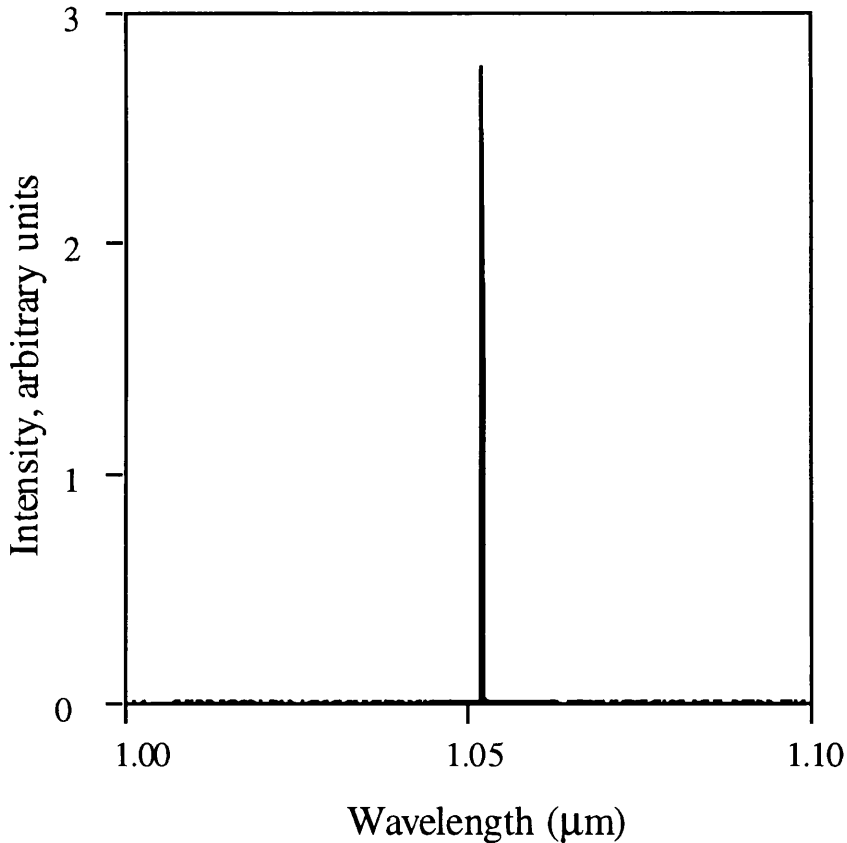


Figure 5.34 Lasing spectrum of Nd³⁺ doped silica waveguide fabricated by aerosol doping.

As a result of aiming to produce the first Nd³⁺ doped aerosol laser, the waveguide dimensions were chosen to be large to decrease scattering losses. Results presented are promising with reasonable results observed for the threshold and slope efficiency. The process is still to be refined due to a change in dynamics for the reaction, however, it is believed that this single step process offers homogeneously distributed doping which can be easily confined to both vertical and regional areas. The doping is carried out at a macroscopic level such that the doping level is less susceptible to localised doping. The system is also relatively inexpensive and less time consuming than the solution doping technique. It is the authors opinion that the doping method is a good alternative to solution doping, although it is still to be proven which is superior.

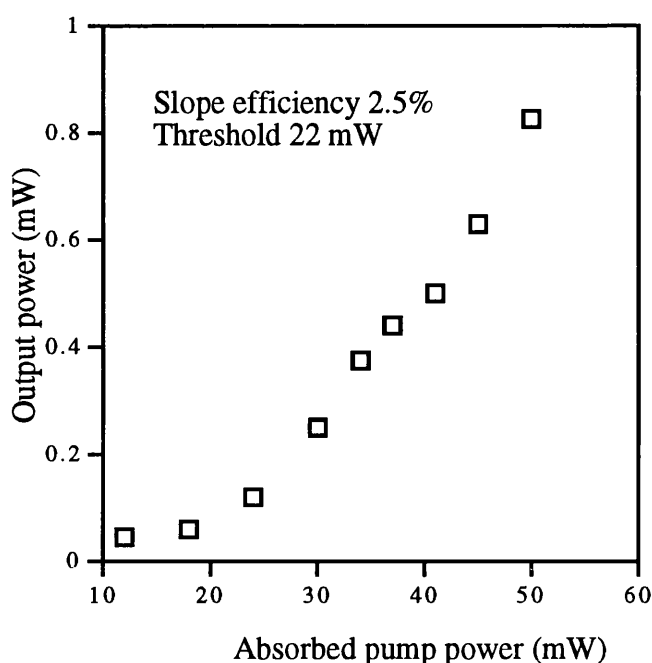


Figure 5.35 Slope efficiency of Nd^{3+} doped silica waveguide fabricated by aerosol doping.

5.3.7 Er^{3+} doped planar waveguide laser

Much of the work throughout the duration of the studies was based on the Nd^{3+} system. The main basis for this was the limited resources for suitable high pump power sources at 980 nm and 1480 nm within the department necessary for measuring Er^{3+} . However, Dr C. M. Sotomayor Torres is to be thanked for allowing the use of a high power argon ion laser. As a result, time was gained to measure Er^{3+} doped silica waveguides, as the Ti:sapphire laser was subsequently able to produce powers as great as 1 W at 980 nm.

As a result Er^{3+} doped samples produced by Dr G. D. Maxwell at BT Laboratories were able to be tested for CW oscillation employing the high phosphorous content glass. An incomplete analysis of the sample was undertaken with some of the waveguide analysis taking place at BT Laboratories.

A long path length coil based on a spiral design 33 cm long was fabricated with waveguide dimensions of $8 \times 16 \mu\text{m}^2$. The Er^{3+} doping level was 0.3 wt% and the insertion loss was measured to be 9.2 dB at 1.3 μm . Subsequently, a 20 μm thick

$\text{SiO}_2\text{-P}_2\text{O}_5\text{-B}_2\text{O}_3$ cladding layer with a refractive index matched to that of the buffer layer was then formed by FHD.

Two techniques to form a laser cavity were set-up. The first involved a fibre arrangement to try and reduce the problems encountered by butting dielectric coated mirrors against the waveguides. Figure 5.36 is the experimental set-up. A 1x2 splitter at 980 nm was used to pump the device at both ends. This was due to the waveguide length, to reduce possible reabsorption effects. Two WDMs were employed to provide a means of fibre launching the pump power. Index matching fluid was applied to the end of the fibres to improve coupling and reduce any unwanted Fresnel reflections. The cross ports had specially made mounts to attach the fibre firmly against the dielectric mirrors to form a coupled cavity. Unfortunately, the 1x2 splitter exhibited losses greater than 3 dB such that lasing was unattainable.

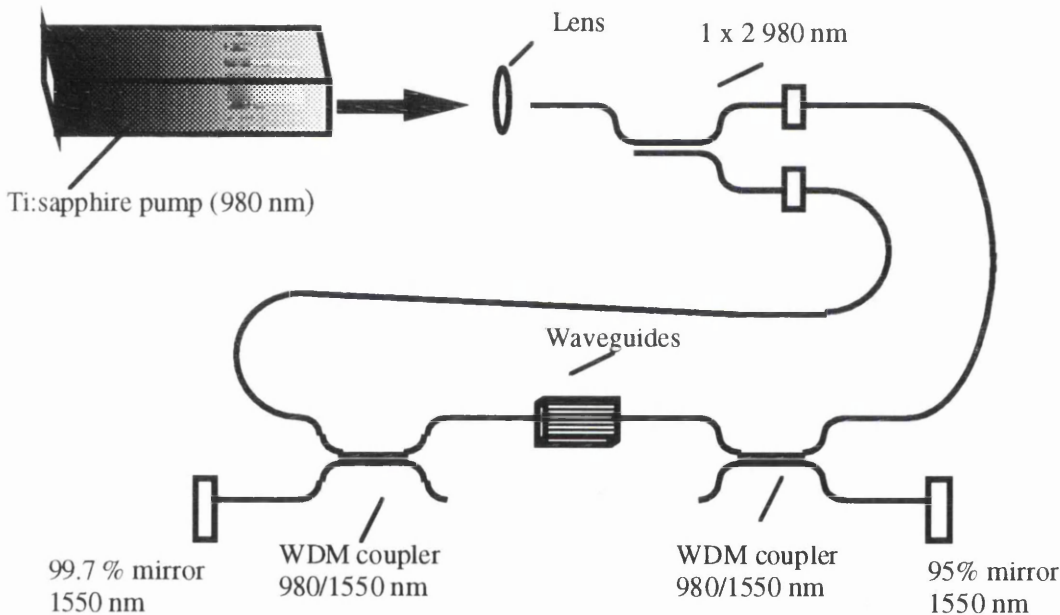


Figure 5.36 Experimental set-up for forming laser cavity.

By directly butting directly coated mirrors to the end of the doped waveguides it was possible for lasing action to take place at $1.534 \mu\text{m}$, the peak wavelength of the absorption, with a FWHM of 0.2 nm (Figure 5.37). To achieve lasing action high reflectivity mirrors (99.7 % at $1.55 \mu\text{m}$) were necessary. As a result, the threshold was measured to be only 23 mW but at the expense of the slope efficiency of 0.04 %. Figure 5.38 illustrates the values measured. However, the unsuitability of the experimental arrangement was highlighted when lasing action was briefly witnessed for a 95 % output mirror and could not be repeated.

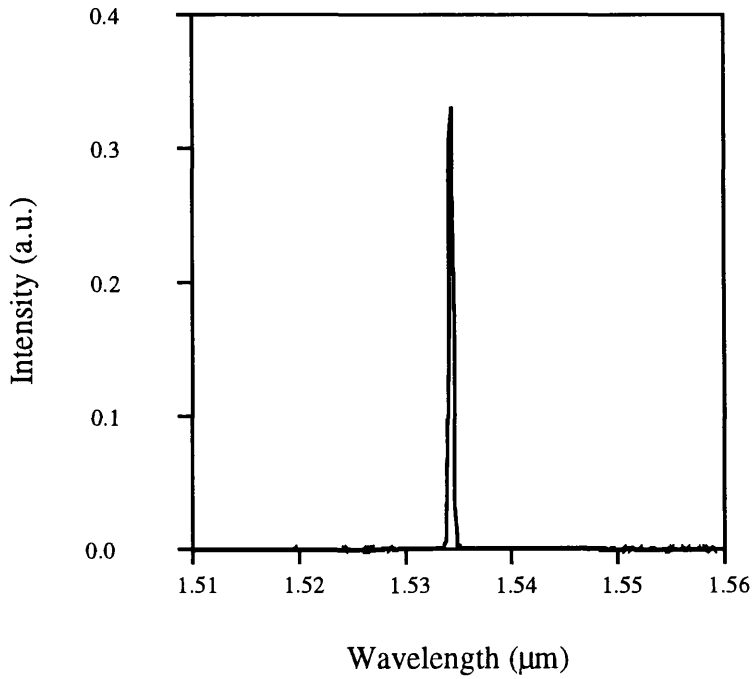


Figure 5.37 Lasing spectrum of Er^{3+} doped silica waveguide fabricated by solution doping.

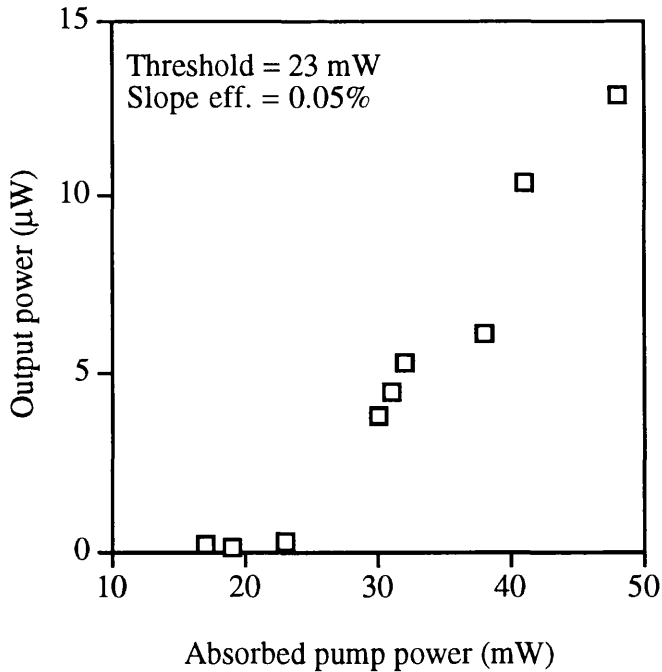


Figure 5.38 Slope efficiency of Er^{3+} doped silica waveguide fabricated by solution doping

In conclusion lasing was witnessed for a long path length coil. Researchers at NTT observed lasing for higher doped waveguides with a reduced waveguide length⁴⁹. The lasing wavelength however took place further out at 1.6 μm due to reabsorption effects at the peak of the fluorescence.

5.4 Conclusions

Rare earth doping of $\text{SiO}_2\text{-P}_2\text{O}_5$ films was achieved using the solution and aerosol doping techniques. Both techniques exhibited similar characteristics. The propagation loss due to volume scattering was found to be a function of the thermal processing and dopant concentration. Increasing the processing temperature to 1375 $^\circ\text{C}$ and decreasing the thermal exposure to 15 minutes the propagation loss decreased dramatically to below 0.5 dB/cm. In fact, the insertion loss of a 6 cm long channel waveguide was measured to be as low as 1.5 dB at 632.8 nm.

The doping homogeneity of the rare earth ions was investigated. Trends measured for both techniques were similar. Increasing the dopant concentration and reducing the processing temperature resulted in a more pronounced fast decay component. Alumina co-doping resulted in a reduction in ion-ion interactions for both techniques. However, the aerosol technique resulted in a reduction in the fast decay component for very small alumina levels compared to the solution doping. In relation to the doping homogeneity the analysis detailed was not quantitative and it is still not possible to determine the superior doping technique.

Using the two techniques Nd^{3+} doped silica waveguide lasers were fabricated. It would have been more beneficial to have fabricated similar devices to make a direct comparison. This was due to the fact, that to produce the first Nd^{3+} doped aerosol laser, waveguides with large dimensions were fabricated. However, the solution doped waveguide structure does tend to support a better technique as the smaller waveguide dimensions and larger Nd^{3+} ion concentration still result in a lower loss structure. However, when comparing the respective slope efficiencies, the solution device is 2.6% and the aerosol device is 2.5%. This suggests that the aerosol doping homogeneity is better as Nd^{3+} ion-ion interactions depopulate the upper level and consequently increase the threshold. However, although it is still not possible to determine the best technique, aerosol doping does offer an inexpensive and fast alternative to solution doping.

References

- 1 Johnson L. F. and Nassau K., Proc. IRE, 1961, **49**, 1704.
- 2 Snitzer E., Phys. Rev. Lett., 1961, **7**, 444.
- 3 Koester C. J. and Snitzer E., Appl. Opt., 1964, **3**, 1182.
- 4 Stone J. and Burrus C. A., Appl. Opt., 1974, **13**, 1256.
- 5 Poole S. B., Payne D. N. and Fermann F. E., Electron. Lett., 1985, **21**, 737.
- 6 Mears R. J., Reekie R., Jauncey I. M. and Payne D. N., Electron. Lett., 1987, **23**, 1026.
- 7 France P. W., Optical Fibre Lasers and Amplifiers, Blackie Publishers, 1991.
- 8 Patek K., Glass Lasers, Butterworth and Co. Ltd., London, 1970.
- 9 Brierley M. C. and France P. W., Electron. Lett., 1987, **23**, 815.
- 10 Grubb S. G. and Eden J. G., Short Course 101, CLEO'94, Anaheim, 1994.
- 11 Spirit D. M., Walker G. R., France P. W., Carter S. F. and Szebesta D., Electron. Lett., 1990, **26**, 1218.
- 12 Stone J. and Burrus C. A., Appl. Phys. Lett., 1973, **23**, 388.
- 13 Townsend J. E., Poole S. B. and Payne D. N., Electron. Lett., 1987, **23**, 388.
- 14 Gozen T., Kikukawa Y., Yoshida M., Tanaka H. and Shintani T., Proc. Optical Fibre for Comm., New Orleans, 1988.
- 15 Ainslie B. J., Craig S. P. and Davey S. T., Mater. Lett., 1987, **5**, 143.
- 16 MacChesney J. B. and Simpson J. R., Proc. Optical Fibre for Comm., San Diego, 1985.

Chapter 5 Assessment of techniques for rare earth doping

- 17 Ainslie B. J., Craig S. P. and Davey S. T., *J. Lightwave Techn.*, 1988, **6**, 287.
- 18 Thompson D. A., Bocko P. L. and Ganon J. R., *Proc. Fibre Optics in Adverse Environments (II)*, SPIE, 1984, **506**, 170.
- 19 Shimizu M., Hanawa F., Suda H. and Horiguchi M., *Jpn. J. Appl. Phys.*, 1989, **28**, 476.
- 20 Takahashi S., Sanada K., Inanda K. and Fakuda O., *United States Patent*, no. 4, 336, 049, Jun. 22, 1982.
- 21 Takahashi S., Sanada K., Inanda K. and Fakuda O., *United States Patent*, no. 4, 338, 098, Jun. 14, 1983.
- 22 Morse T. F., Reinhart L., Kilian A., Risen W. Jr., and Cipolla J. W. Jr., *SPIE Fibre Laser Sources and Amplifiers*, 1989, **1171**, 72.
- 23 Morse T. F., Kilian A. and Reinhart L., *J. Non-Cryst. Solids*, 1991, **129**, 93.
- 24 Amano S., Yamashita T., Tajima H., Masuda I. and Izumitani T., *European Conf. on Optical Comm.*, Helsinki, 1987.
- 25 Hibino Y., Okazaki H., Hida Y. and Ohmori Y., *Electron Lett.*, 1993, **29**, 1847.
- 26 Hida Y., Hibino Y., Okazaki H. and Ohmori Y., *Proc. IPR*, Dana Point, 1995.
- 27 Shuto K., Hattori K., Kitagawa T., Ohmori Y. and Horiguchi M., *Electron. Lett.*, 1993, **29**, 139.
- 28 Nakazawa M. and Kimura Y., *Electron. Lett.*, 1992, **28**, 2054.
- 29 Polman A., Jacobson D. C., Poate J. M. and Arnold G. W., *Nucl. Instrum. Methods*, 1991, **B 59/60**, 3430.

Chapter 5 Assessment of techniques for rare earth doping

- 30 Polman A., Jacobson D. C., Eaglesham D. J., Kistler R. C. and Poate J. M., *J. Appl. Phys.*, 1990, **70**, 3778.
- 31 Yajima H., Kawase S. and Sekimoto Y., *Appl. Phys. Lett.*, 1972, **21**, 407.
- 32 Schumulovich J., Wong A., Wong Y. H., Becker P. C., Bruce A. J. and Adar R., *Electron Lett.*, 1992, **28**, 1181.
- 33 Nykolak G., Becker P. C., Schumulovich J., Wong Y. H., DiGiovanni D. J. and Bruce A. J., *IEEE Photon. Techn.*, 1993, **5**, 1014.
- 34 Nykolak G., Haner M., Becker P. C., Schumulovich J. and Wong Y. H., *IEEE Photon. Techn.*, 1993, **5**, 1185.
- 35 Ramaswamy R. V. and Srivastava R., *J. Lightwave Techn.*, 1988, **6**, 984.
- 36 Mwarania E. K., Reekie L. Wang J. and Wilkinson J. S., *Electron Lett.*, 1990, **26**, 1317.
- 37 Malone K. J., Sanford N. A. and Hayden J. S., *Electron Lett.*, 1993, **29**, 691.
- 38 Sanford N. A., Malone K. J., Larson D. R. and Hickernell R. K., *Opt. Lett.*, 1991, **16**, 1168.
- 39 Mwarania E. K., Murphy D. M., Hempstead M., Reekie L. and Wilkinson J. S., *IEEE Photon. Techn.*, 1992, **4**, 235.
- 40 Lallier E., Pocholle J. P., Papuchon M., de Micheli M. P., Li M. J., Qing He, Ostrowsky D. B., Grezes-Besset C. and Pelletier E., *IEEE J. Quantum Electron.*, 1991, **27**, 618.
- 41 Hempstead M., Wilkinson J. S. and Reekie L., *IEEE Photon. Techn.*, 1992, **4**, 852.
- 42 MacKinnon N., Norrie C. J. and Sinclair B. D., *J. Opt. Soc. Am. B*, 1994, **11**, 519.

- 43 Brinkmann R., Sohler W. and Suche H., *Electron. Lett.*, 1991, **27**, 415.
- 44 Amin J., Hempstead M., Román J. and Wilkinson J. S., *Optics Lett.*, 1994, **19**, 1541.
- 45 Chandler P. J., Field S. J., Hanna D. C., Shepherd D. P., Townsend P. D., Tropper A. C. and Zhang I., *Electron. Lett.*, 1989, **25**, 985.
- 46 Zhou F., De La Rue R. M., Ironside C. N., Han T. P. J., Henderson B. and Ferguson A. I., *Electron Lett.*, 1992, **28**, 2041.
- 47 Chen R. T., Lee M., Natarajan S., Lin C., Ho Z. Z. and Robinson D., *IEEE Photon. Tech. Lett.*, 1993, **5**, 1328.
- 48 Hibino Y., Kitagawa T., Shimizu M., Hanawa F. and Sugita A., *IEEE Photon. Techn. Lett.*, 1989, **1**, 349.
- 49 Kitagawa T., Hattori K., Shimizu M. Ohmori Y. and Kobayashi M., *Electron. Lett.*, 1991, **27**, 334.
- 50 Hattori K. and Kitagawa T., *IEEE Photon. Techn. Lett.*, 1992, **4**, 973.
- 51 Kitagawa T., Hattori K., Hibino Y., Ohmori Y. and Kobayashi M., *Proc. ECOC'92, Berlin, 1992*, 907.
- 52 Kawanishi S., Hattori K., Takahara H., Oguma M., Kamatani O. and Hibino Y., *Electron Lett.*, 1995, **31**, 363.
- 53 Hattori K., Kitagawa T., Oguma M., Ohmori Y. and Horiguchi M., *Electron Lett.*, 1994, **30**, 856.
- 54 Kitagawa T., Bilodeau F., Malo B., Thériault S., Albert J., Jihson D. C., Hill K. O., Hattori K. and Hibino Y., *Electron. Lett.*, 1994, **30**, 1311.
- 55 Oguma M., Kitagawa T., Hattori K. and Horiguchi M., *IEEE Photon. Techn. Lett.*, 1994, **6**, 586.

Chapter 5 Assessment of techniques for rare earth doping

- 56 Tumminelli R., Hakimi F. and Haavisto J., *Opt. Lett.*, 1991, **16**, 1098.
- 57 Bebbington J.A., G.Barbarossa, Bonar J.R. and Aitchison J.S., *Appl. Phys. Lett.*, 1993, **62**, 337.
- 58 Bonar J.R., Bebbington J.A., Aitchison J.S., Maxwell G.D and Ainslie B.J., *Proc. IEE - 'Planar Silicon Hybrid Optoelectronics'*, London, 1994.
- 59 Kitagawa T., Hattori K., Hibino Y. and Ohmori Y., *J. Lightwave Techn.*, 1994, **12**, 436.
- 60 Ainslie B. J., Armitage J. R., Craig S. P. and Wakefield B., *Mater. Lett.*, 1988, **6**, 139.
- 61 Bonar J. R. and Aitchison J. S., to be submitted for publication in *Appl. Phys. Lett.*
- 62 Hattori T., Hattori K., Shimizu M., Ohmori Y. and Kobayashi M., *Electron. Lett.*, 1985, **27**, 334.
- 63 Arai K., Namikawa H., Kumata K. and Honda T., *J. Appl. Phys.*, 1986, **59**, 3430.
- 64 Dai G., Internal BT Report, 1995.
- 65 Ainslie B. J., Craig-Ryan S. P., Davey S. T., Armitage J. R., Atkins C. G., Massicott J. F. and Wyatt R., *IEE Proc., Pt. J*, 1990, **137**, 205.
- 66 Shimizu M., Yamada M., Horiguchi M. and Sugita E., *IEEE Photon. Techn. Lett.*, 1990, **2**, 43.
- 67 Laming R. I., Townsend J. E., Payne D. N., Meli F., Grasso G. and Tarbox E. J., *IEEE Photon. Techn. Lett.*, 1990, **3**, 253.
- 68 Thøgersen J., Bjerre N. and Mark J., *Optics Lett.*, 1993, **18**, 197.

Chapter 5 Assessment of techniques for rare earth doping

- 69 Ainslie B. J., Craig S. P., Davey S. T., Barber D. J., Taylor J. R. and Gomes A. S. L., J. Mater. Sci. Lett., 1987, **6**, 1361.
- 70 Hattori K., Kitagawa T. Ohmori Y. and Kobayashi M., IEEE Photon. Techn. Lett., 1991, **3**, 882.
- 71 Quimby R. S., Miniscalco W. J. and Thompson B., SPIE Fiber Laser Sources and Amplifiers V, 1993, **2073**.
- 72 Pálsdóttir B. and Larsen C. C., Proc. ECOC'93, 1993, 181.
- 73 Wyatt R., SPIE, 1989, **1171**, 54.
- 74 Bonar J.R., Bebbington J.A., Aitchison J.S., Maxwell G.D and Ainslie B.J., Electron. Lett., 1994, **30**, 229.
- 75 Rigrod W. W., J. Quantum Electron., 1978, **14**, 377.
- 76 Bonar J.R., Bebbington J.A., Aitchison J.S., Maxwell G.D and Ainslie B.J., Proc. CLEO, Anaheim, 1994.
- 77 Bonar J.R., Bebbington J.A., Aitchison J.S., Maxwell G.D and Ainslie B.J., Electron. Lett., 1995, **31**, 99.

Chapter 6 Monolithic integration for future rare earth doped silica waveguide devices

6.1 Introduction

A myriad of passive and active devices have been produced employing silica-on-silicon waveguide technology¹. Of particular importance is the integration of passive and active components on the same substrate to permit monolithic integration. This would permit devices such as transparent 1xN splitters to be fabricated.

6.2 Grating devices

6.2.1 Introduction

The formation of grating structures on thin film waveguides has various applications such as waveguide coupling, feedback mechanisms for lasers, filters etc. In this report both evanescent field coupling with a prism and end-fire coupling have been used to couple light into and out of silica waveguides. Diffraction gratings fabricated on the waveguide can also be used to couple light into the guide with the advantage that they are simple, reproducible and permanent couplers. The diffraction coupler is also resistant to vibrations and thermal effects making it a suitable candidate for batch processing of optical integrated circuits.

Chapter 5 reported results for waveguide lasers. A major drawback in fabricating the devices was the method of providing feedback using external dielectric mirrors. The mirrors were extremely sensitive to vibration and misalignment, moreover if external reflectors are present then this results in making integration extremely difficult. The laser structures also had to be carefully sawn, or polished, to ensure they were normal to the guides for peak reflectivity.

Gratings can be used to form Bragg reflectors which provide the necessary feedback for laser action. Such gratings are insensitive to vibrations and expedite the formation of monolithic integrated waveguide lasers. Such gratings also provide wavelength control, single longitudinal mode lasers which would be important for wavelength division multiplexing (WDM) optical communication systems. Another possibility for WDM systems, demonstrated in Er^{3+} doped fibre amplifiers, is to incorporate a grating structure into the fibre to smooth the gain spectrum and saturation characteristics². The integrated planar form would have the physical advantages of being more rugged and stable with the centre wavelength and strength of the filter precisely defined in relation to the fibre equivalent. Semiconductor external cavity lasers have also been fabricated by using a grating on a planar silica waveguide as the feedback element. The waveguide grating, locks-up the semiconductor laser providing the various advantages already mentioned³.

To fabricate gratings two methods have been investigated namely: holographic⁴ and direct writing. Surface gratings with grating amplitudes less than that of the grating period were fabricated, permanent structures were then formed by RIE. Instead of etching gratings into the waveguide core it was decided to etch the waveguides into the thermal oxide substrate. As mentioned in Chapter 3, the surface tension of the soot deposited by FHD has a low viscosity, such that when the soot is sintered the surface area of the core is minimised. Consequently, the core layer is planarised and the grating structures are covered. The minor variation in thickness of the deposited soot was also a consideration for reproducing fine structures. Dopant diffusion created by the heat in the cladding process was another constraint in grating fabrication⁵. To overcome the waveguide deformation and dopant diffusion it is possible to form clad waveguides then form surface relief gratings. This is achieved by etching the overcladding to expose the core surface. The grating is then formed on the uncovered area using e-beam exposure and RIE.

Feedback for a laser is provided via backward Bragg scattering from periodic perturbations of the refractive index. The Bragg condition is satisfied when $\Lambda = \lambda_g/2$, where Λ is the grating period and λ_g is the launched wavelength into the waveguide.

To model the Bragg gratings, studies were based on the coupled wave theory of Kogelnik⁶. For these studies it was assumed that the amplitude of the grating corrugations (h) was small compared to Λ . The reflected light induced by such gratings is dependent on both the length of the grating L , and the coupling coefficient κ

between the incident and reflected waves. The coupling coefficient κ for TE waves is given by:

$$\kappa = \frac{\pi h (n_f^2 - n_s^2) E_c^2}{2\lambda N \int_{-\infty}^{\infty} E_y^2 dx} \quad (6.1)$$

where N is the effective guide index, n_f and n_s the refractive indices of the core and substrate. E_c is the transverse electric field (along the y -axis) at the grating surface and $\int_{-\infty}^{\infty} E_y^2 dx$ represents the integral of the square of the electric field over the transverse direction.

The peak reflectivity R for a grating of length L can be expressed as:

$$R = \tanh^2(\kappa L) \quad (6.2)$$

The linewidth $\Delta\lambda$, or full bandwidth, can be expressed as:

$$\Delta\lambda = \frac{2\lambda N}{Ln_g} \left[1 + \left(\frac{\kappa L}{\pi} \right)^2 \right]^{\frac{1}{2}} \quad (6.3)$$

Thus, it can be seen that increasing the length of grating to increase the reflectivity of the grating decreases the bandwidth. The expected reflectivity for gratings designed for the Er^{3+} system is illustrated in Figure 6.1.

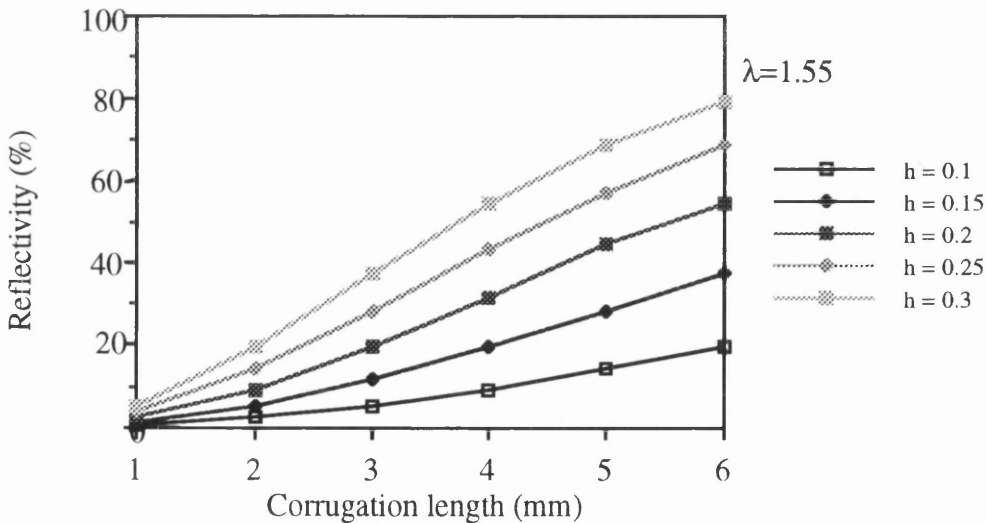


Figure 6.1 Reflectivity of gratings for different lengths and corrugation amplitudes.

The model is based on the wavelength 1.53 μm , the peak absorption in the Er^{3+} doped $\text{SiO}_2\text{-P}_2\text{O}_5$ planar devices, with a waveguide thickness of 6 μm and a refractive index difference of 0.75% between the guide and the substrate. To produce this type of grating a period of 527 nm is necessary. To produce a grating for use with the Nd^{3+} system at 1.05 μm a period of 362 nm is necessary.

6.2.2 Holographic system

The holographic technique is good for defining submicron gratings over a large area (1 cm^2) in a short period of time. In this set-up the output light from an argon ion laser operating on the 457.9 nm line is split into two beams of equal intensity using a 50-50 beam splitter. The two beams are incident on mirrors which are equidistant from the beam splitter. The two beams are reflected, such that they interfere at the sample surface. Figure 6.2 shows the holographic arrangement used for producing gratings.

The period of the interference fringes Λ , is given by

$$\Lambda = \frac{\lambda_o}{2n \sin \theta} \quad (6.4)$$

where λ_o is the wavelength of the two beams incident on the sample, at an angle θ symmetrically about the normal to the sample, and n is the refractive index in which angle θ is measured, usually air.

For grating fabrication, 1 mm thick Homosil grade silica samples were cut into squares of 20x20 mm^2 . The photoresist employed was Shipley S1400-31 which was diluted with a thinner in the ratio of 1:2. For resist gratings on glass substrates, the reflection at the resist-glass interface is small enough not to have any significant effect on the grating quality. The reflection arising from the rear glass-air interface of the substrate is, however an order of magnitude larger. this tends to deteriorate the grating through light scattering and the support of vertical standing waves in the photoresist-glass system. The effect can be suppressed by using ARC-XL, a commercially available anti-reflection coating.

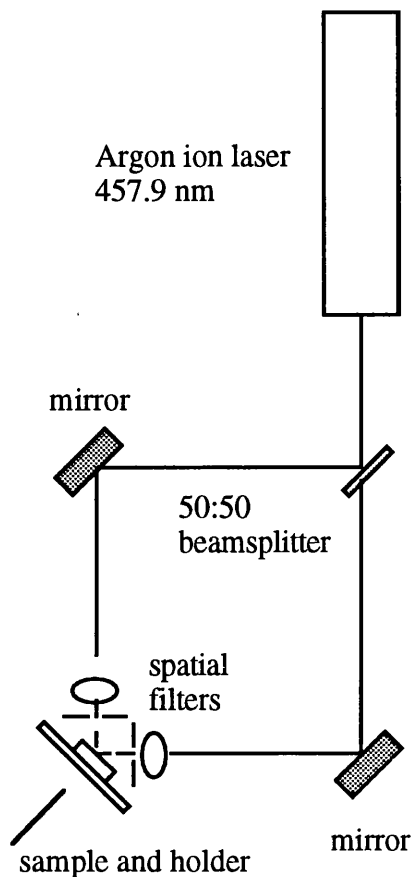


Figure 6.2 Laser holography set-up.

Gratings were fabricated in the following manner. Samples were cleaned using the standard process. ARC was applied to the sample through a syringe with a 0.45 μm filter and spun for 60 s at 5000 rpm. The sample was then baked at 130 $^{\circ}\text{C}$ for 30 minutes. The thinned S1400-31 (1:2) was then used to liberally cover the sample and spun at 4000 rpm for 30 s to leave a resist thickness of approximately 0.12 μm . The sample was then baked at 90 $^{\circ}\text{C}$ for 30 minutes. Following this the sample was stored in a light tight dry box for transfer to the holographic laboratory.

The alignment of the two beam interference was such that the arrangement provided a grating period of 527 nm. Spatial filters were inserted in order to improve spatial beam quality. The power of the argon laser was about 20 mW in each beam, measured after the spatial filters. After exposure by the interference method (typically 30 s), samples were developed in a 1:2 solution of the developer and RO water for 15 s.

The sinusoidal resist grating crests were then shadow-masked by evaporating a 15 nm layer of NiCr at an angle of 65 $^{\circ}$ (chosen to give a 1:1 mark space ratio). In this way the

NiCr layers covered the top and one side of each grating crest. The uncovered resist and ARC layers were removed using a low pressure O_2 etch for 5 minutes. The silica was then etched by a low pressure CHF_3 etch which gave an etch rate of 30 nm/minute. The process is illustrated in Figure 6.3.

The dry-etched samples were then boiled in N-methyl-2-pyrrolidone (NMP) to remove the remaining layers of resist and ARC to leave the grating structures to be overgrown with the SiO_2 - P_2O_5 core layer. Figures 6.4 shows a typical example of the final grating structure in the silica substrate.

6.2.3 Electron beam system

The electron-beam writing system does not depend on a mask. Instead, patterning is directly produced on the resist coated sample, by either deflecting the electron beam or shifting the stage. The e-beam writer used was a Phillips EBPG5-HR which uses a vector scan principle with a gaussian beam such that the beam is scanned only across the areas of interest. Owing to the size of the patterns it was necessary for the stage to be mechanically moved, otherwise deflecting the e-beam would have caused deflection aberrations. R. Harkins is to be thanked for his assistance in the e-beam writing and sample processing.

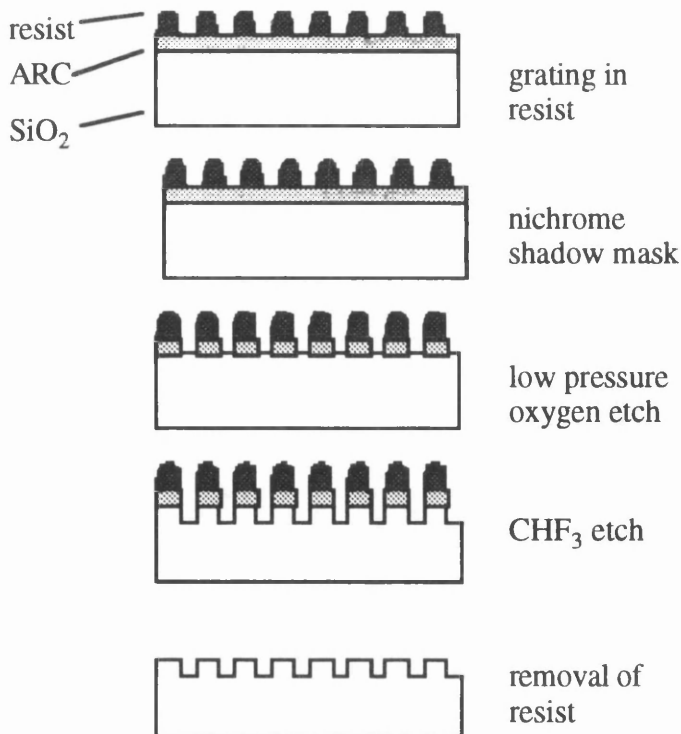


Figure 6.3 Schematic of the processing steps involved for the holographic system.



Figure 6.4 SEM photograph of gratings formed by the holographic technique.

For the e-beam system it is necessary to design the pattern to be transferred to the e-beam writer. This requires a number of programs which must be used to create the data, then translate it into e-beam readable format and finally to control the e-beam as it writes the job. For the large pattern sizes investigated it was preferable to use Sigraph-Optik, a Siemens software package, to design the grating pattern. The output from Sigraph produces industry standard binary Gdsii files which the beamwriter cannot understand. As a result it is necessary to translate the data into machine readable format using the program CATS (Computer Aided Transcription System). Finally, the program BWL (Beam Writer Layout) is used to control the e-beam as it writes the job and to control global parameters such as spot size, dosage etc.

A 3" Si wafer with a 10 μm thermal oxide was used as the substrate in these experiments. Before writing the pattern it was necessary to prepare the substrate, after which the sample was coated with e-beam sensitive resist. The resist recipe was determined to give very high resolution features which were good for metal lift-off using metal thicknesses of 60 nm or less. This is necessary as the resists used do not provide suitable masks for dry etching. The first layer of resist was 4% BDH PMMA (poly methyl methacrylate) spun at 5000 rpm for 60 s. This is a mixture of xylene (solvent) with 4% of the total weight being PMMA. The thickness of the layer was 70 nm. The sample was then baked at 120 $^{\circ}\text{C}$ for 2 hours. The sample was then

coated with 4% Elv (elvacite) resist which was spun at 5000 rpm for 60 seconds to provide an additional thickness of 100 nm. Finally, the sample was placed in an oven at 120 °C and baked overnight.

Initial samples which were patterned by the e-beam were found to have stitch errors as shown in Figure 6.5. This was due to the thermal oxide acting as an insulator causing charge to build up which subsequently deflected the e-beam. To overcome this problem 30 nm of chrome was evaporated onto the sample before writing.

On the 3" wafer 6 sites consisting of 5 mm square grating structures, as illustrated in Figure 6.6, were written. Due to the physical size of the gratings it was necessary to choose an e-beam spot size such that the features of the pattern could be reproduced and within a time which would not be overly long. The spot size was chosen to be 40 nm. The grating period chosen was 530 nm. As a result the resolution (or beam step size) was 21.2 nm which is divisible into the grating period, a prerequisite for defining the pattern. A useful rule of thumb which was followed was to ensure that the spot size (40 nm) was about twice the resolution (21.2 nm) and that the resolution itself was approximately one tenth of the minimum desired feature size (265 nm). Having determined the parameters for the e-beam the dose was varied to produce a mark:space ratio of 1:1. Figure 6.7 and Figure 6.8 are examples of gratings written with dosages of 342 $\mu\text{C}/\text{cm}^2$ and 200 $\mu\text{C}/\text{cm}^2$ respectively. In the former case the gratings are overexposed whilst in the latter the gratings are underexposed. Figure 6.9 shows a sample with a dosage of 220 $\mu\text{C}/\text{cm}^2$ which produced gratings with 1:1 ratios and no stitching errors. The chrome was subsequently removed from the sample and developed in 3:1 IPA:MiBK for 1 minute 45 seconds at 23 °C. This is a relatively slow development but produces high contrast and good resolution patterns. To provide a suitable mask for dry etching 30 nm of NiCr was evaporated onto the developed sample. A 30 second O₂ ash was undertaken to remove any residual resist before evaporating the metal to ensure good 'lift-off'. The sample was subsequently placed in an acetone bath for 4 hours at 45 °C, such that the resist with the thin metal covering was removed to leave the NiCr pattern. A 10 minute low pressure CHF₃ RIE was then performed to produce an etch depth of 0.3 μm . Finally, the NiCr was removed and the sample overgrown with the SiO₂-P₂O₅ core layer for device analysis.

The devices produced by both grating fabrication techniques were tested by fibre-launching into channel waveguides. A fibre connected broadband white light source was coupled into the waveguides and the transmission spectra measured on a spectrum analyser. Unfortunately, no reflectivity was measured, which could be due to the

spectrum analysers resolution being limited to 0.1 nm, especially as the gratings were designed with linewidths of approximately 0.1 nm.

An interesting alternative to etched gratings however, has been the development of photosensitive Bragg reflectors⁷. In particular germanium doped fibres have been shown to exhibit excellent photosensitivity. A peak absorption at 240 nm relating to a germania defect has enabled gratings to be formed in fibres by externally interfering two UV beams. It is still an active area of debate as to what causes the increase in refractive index. It is thought that oxygen-deficient germania releases an electron on exposure to UV which is free to move within the glass matrix until it is retrapped⁸. The same phenomenon has been transferred to planar technology⁹.

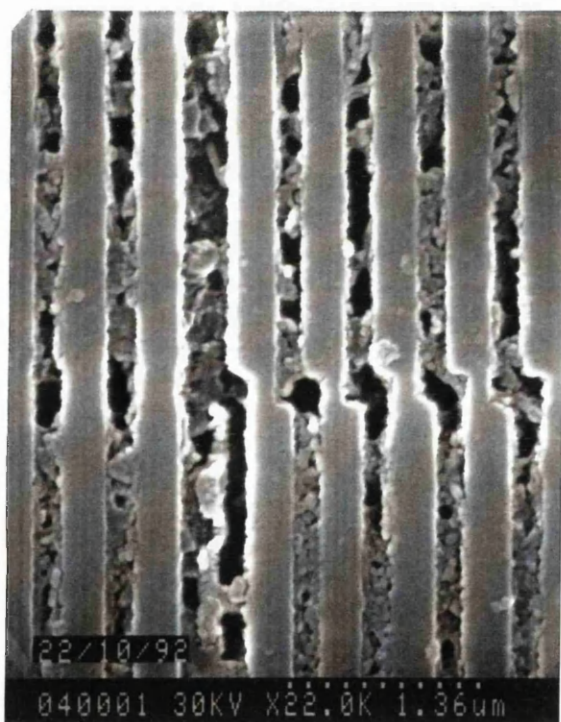


Figure 6.5 SEM photograph of grating stitch errors .

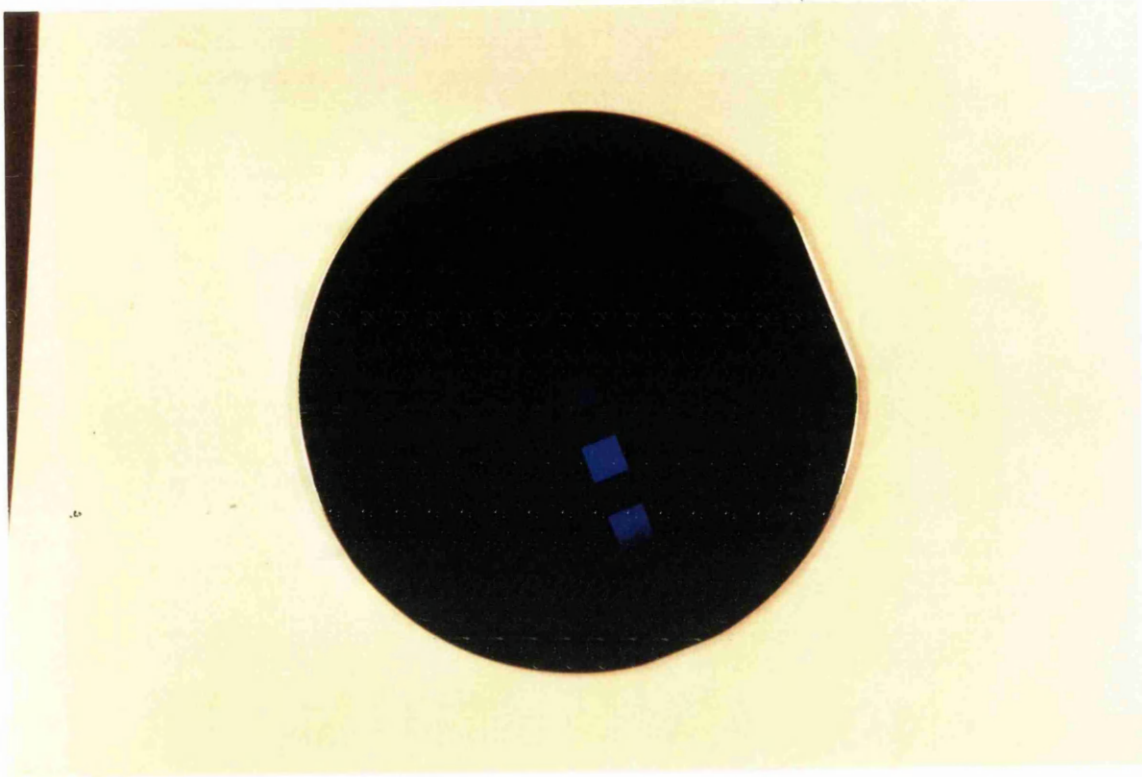


Figure 6.6 Photograph of gratings formed over selective areas by the e-beam technique.



Figure 6.7 SEM photograph of overexposed gratings formed by the e-beam technique.

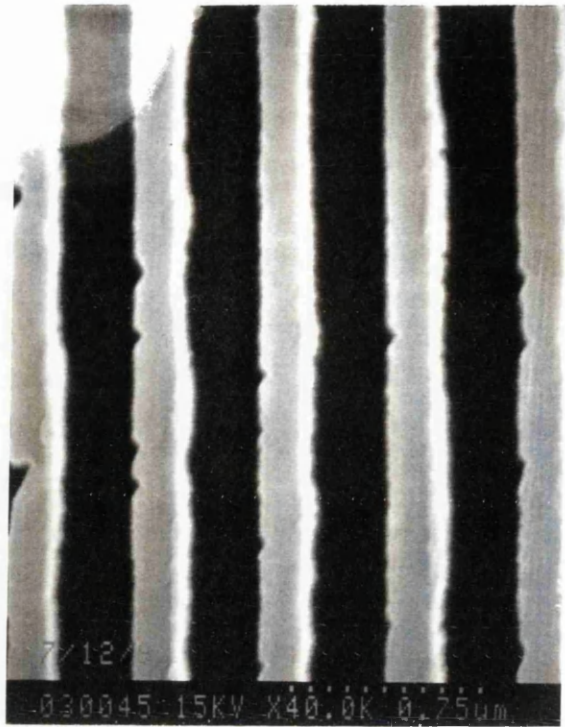


Figure 6.8 SEM photograph of underexposed gratings formed by the e-beam technique.

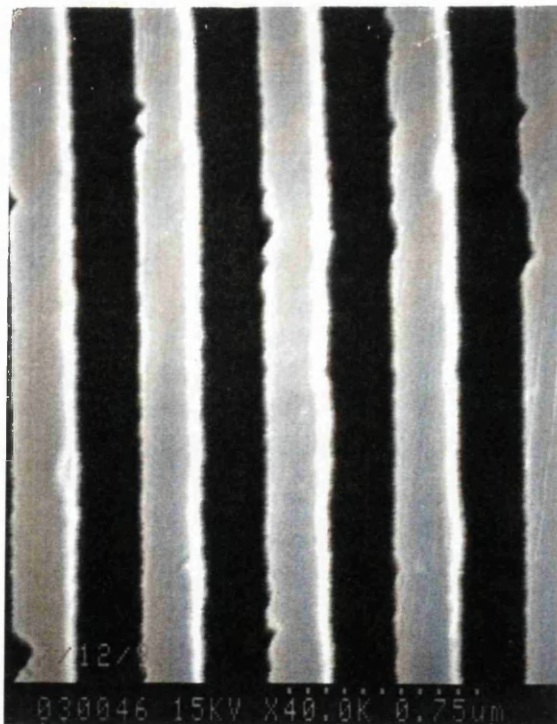


Figure 6.9 SEM photograph of correctly exposed gratings formed by the e-beam technique.

To increase the photosensitivity hydrogen has been found to be a good defect former in germania-doped glass. To achieve this, two techniques have been adopted namely, hydrogen loading¹⁰ and flame brushing¹¹. In the former the sample is placed in a hydrogen chamber and in the latter the sample is heated by an oxy-hydrogen flame in a hydrogen-rich atmosphere. Of particular importance for Er^{3+} - P_2O_5 codoped silica planar waveguides was the photo-induced large refractive index change introduced by exposing to 193 nm light. Recently, an Er^{3+} doped planar waveguide laser was formed with Bragg gratings with a cavity free spectral range (FSR) of 3 GHz¹².

GeO_2 doped silica waveguides have been fabricated with an index difference of 0.75% to match that of standard core material for rare earth doping. The samples were subsequently, exposed to 240 nm radiation at Porto University, by Paulo Vicente Da Silva Marques. An area of $1 \times 1.5 \text{ cm}^2$ was irradiated with 248 nm light from a KrF excimer at an irradiance of $400 \text{ mJ/cm}^2/\text{pulse}$ and a pulse repetition of 50 Hz for 10 minutes (Note that higher energy pulses resulted in laser ablation). The samples were not hydrogen treated but still resulted in an index increase of 5×10^{-4} . This gave an indication of the GeO_2 level to be approximately 13 wt%. At Porto University, a hydrogen chamber has recently been built and it is intended that hydrogen loading will be further investigated. A possible future device is to have photo-induced Bragg gratings on the passive GeO_2 - SiO_2 section integrated with rare earth doped P_2O_5 - SiO_2 section for a single longitudinal mode planar laser.

To provide integration, techniques have been developed to form active devices, which are phosphorous based, on the same substrate as passive devices which are germanium/boron based. The following section describes the techniques with which active and passive layers can be integrated using FHD.

6.3 Selective area doping

Much discussion has taken place about the feasibility of forming transparent or lossless devices on the same motherboard. A device of particular importance is a lossless power splitter which is based on a passive splitting device, preceded by an integrated amplifier. The amplifier produces gain, which compensates for the splitting losses.

Research has concentrated on both vertical and regional selective area doping using both the solution and aerosol doping techniques. Vertical selective area doping is of particular importance for the erbium amplifier as it allows the peak doping level of the erbium ions to be coincident with the maximum intensity of the waveguide mode¹³. As

a result, a more efficient pump system is possible producing amplifiers with improved gain-pump power characteristics¹⁴.

A multi-stage process, can be employed for both doping techniques to form vertical selective area doped structures. The deposition parameters were chosen such that 1 μm of glass was produced per traversal. First of all, 2 traversals of passive materials were deposited. The deposited soot was removed to the furnace for consolidation. The sample was then replaced in the deposition chamber and a further 2 μm deposited. Note that to maintain the same refractive index for the aerosol sample the PCl_3 flow rate had to be increased. Finally, the sample was replaced in the deposition chamber and a further 2 μm deposited and consolidated. This process is time consuming but it does confine the rare earth ions to the centre of the waveguide owing to the fact that the rare earth ions are 'locked' and do not diffuse. A potential drawback is the extra thermal treatment, which we have already shown affects the fluorescent lifetimes.

Employing the aerosol doping technique, vertical selective area doping can also be achieved in one step. Typically, 6 traversals took place, during the third and fourth traversals, the carrier gas flow rate for the aerosol delivery to the torch was initiated and the nebulised rare earth transported to the torch. Once again the PCl_3 flow rate was increased during the active layer depositions to compensate for the reduction in refractive index when incorporating the rare earth. Due to diffusion of the rare earth, Secondary Ion Mass Spectroscopy (SIMS) profiles highlighted that instead of all the rare earth remaining in the middle section approximately 80% remained¹⁵. The advantage of this doping regime however is both the speed and ease of fabrication, as well as the reduction in thermal cycling of the rare earth doped sample to reduce the onset of clustering.

Regional selective area doping can be achieved employing both doping techniques. Once again the aerosol was found to be more flexible. By interrupting the standard aerosol delivery during each traversal at the same point on the sample it was possible to form passive and active layers on the same substrate. The system could also introduce different dopants on the same substrate by using aerosol deliveries with varying dopants. The major drawback however, was that distinct boundaries could not be formed. This was as a result of the size of the flame incident on the substrate. By tailoring the shape and size of the flame it was possible to reduce this boundary to a few mm.

A multi-stage process was investigated with the aim of producing a sharp boundary between the active and passive regions (Figure 6.10). Rare earth doped films were

deposited and consolidated. Standard photolithographic procedures were employed to pattern the planar sample and the subsequent unmasked areas etched back to the thermal

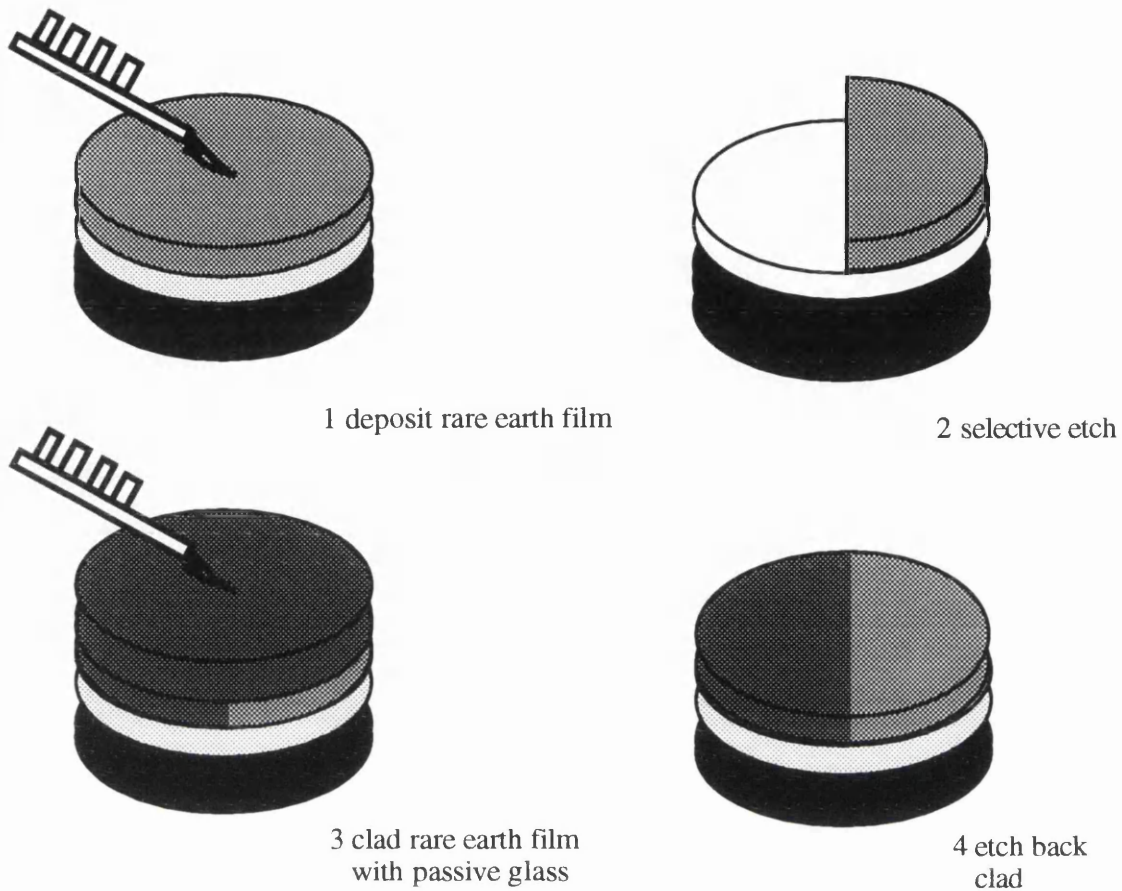


Figure 6.10 Multi-step fabrication process for achieving regional selective area doping.

oxide layer. A thick passive $\text{SiO}_2\text{-P}_2\text{O}_5$ clad layer was then deposited onto the sample ensuring that planarisation took place. The final stage involved either etching or planar polishing the clad back to provide selective areas. As mentioned, owing to the fact that rare earth ions are 'locked' into the consolidated glass it was possible to form distinct boundaries. Figure 6.11 demonstrates this point. For this particular structure, a $\text{SiO}_2\text{-P}_2\text{O}_5$ layer doped with Eu^{3+} was fabricated. Implementing the processes detailed it was possible to produce half of the sample doped with Eu^{3+} . Consequently, the sample was tested using the prism coupler with the 465 nm line from an argon ion laser. Since Eu^{3+} absorbs at 465 nm and fluoresces in the red it was possible to demonstrate the selective area doping. Of particular note is the sharp interface between the passive and active sections which is much more highly controllable than the one step process.

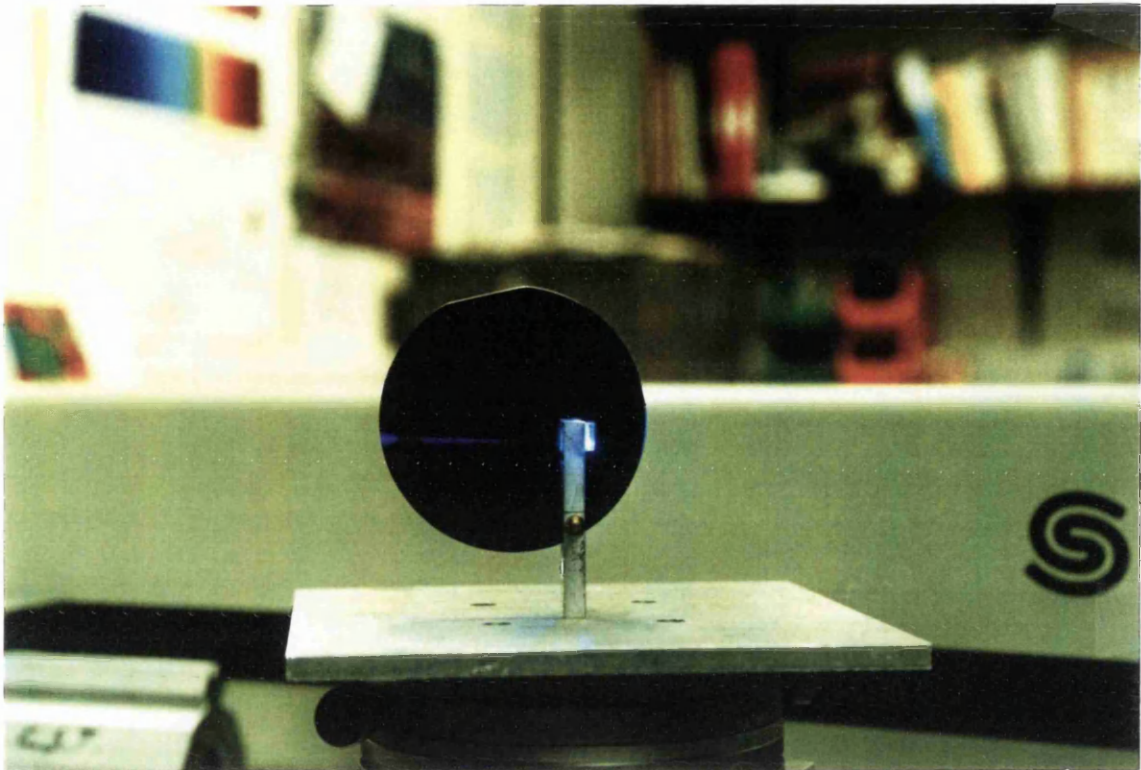


Figure 6.11 Photograph of regional selective area doping

6.4 Waveguide devices

6.4.1 Multimode interference (MMI) couplers

Compact and rugged $1 \times N$ splitters compatible with fibre systems, can be formed using FHD and RIE. The integrated-optic devices are generally formed from either Y-branches or directional couplers¹. However, to fabricate a 1×8 splitter it is necessary to have 7 units of each device with the result that the physical dimensions of the splitter becomes large. To form ultracompact devices and thus, increase the number of devices on the motherboard it is possible to form multimode interference (MMI) coupling devices. Of particular interest was the MMI centre fed symmetric power splitter¹⁶ (Figure 6.12).

The design of MMI couplers is based on ray tracing methods, where the incident light expands in the multimode region due to diffraction, followed by multiple reflections at the waveguide edges. For the MMI coupler discussed only the symmetric modes are excited and the number of modes is determined by the width W , of the multimode section. From analysis (assuming the sample only supports one guide in the transverse

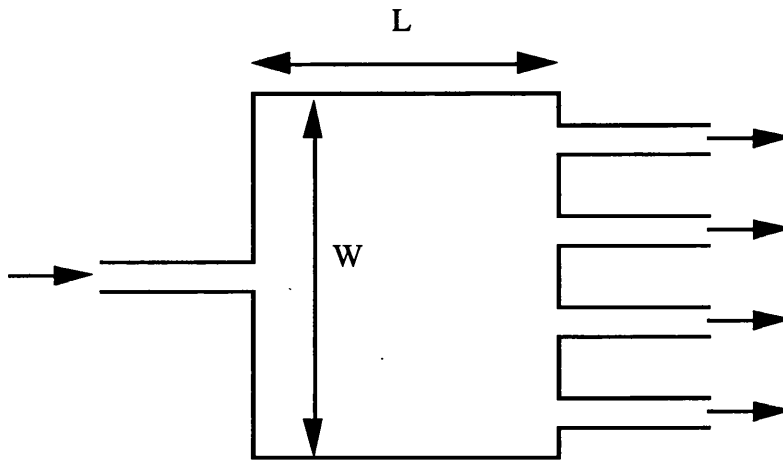


Figure 6.12 Schematic of MMI centre fed symmetric power splitter.

direction and neglecting both leaky and radiation modes) it can be shown that a symmetric pattern is repeated periodically at intervals of:

$$\Lambda = \frac{nW^2}{\lambda_0} \quad (6.5)$$

where n is the refractive index of the waveguide and λ_0 is the free space wavelength. It follows, that N images of the field from the input guide are formed at:

$$z = \frac{\Lambda}{N} \quad (6.6)$$

The images are equally spaced across the multimode guide with a pitch of:

$$p = \frac{W}{N} \quad (6.7)$$

Consequently, to form a $1 \times N$ splitter we design the device such that the length of the multimode section is $L = \Lambda/N$, with the single mode waveguide outputs placed at $p = W/N$. To ensure no coupling at the outputs it is advantageous to have at least a separation of $10 \mu\text{m}$ between the guides. By placing S-bends at the output it is possible to create spacings of $250 \mu\text{m}$ between the guides for fibre compatibility. Numerical simulation of the structures were undertaken using the beam propagation method (BPM). A typical result for a 1×4 structure is given in Figure 6.13.

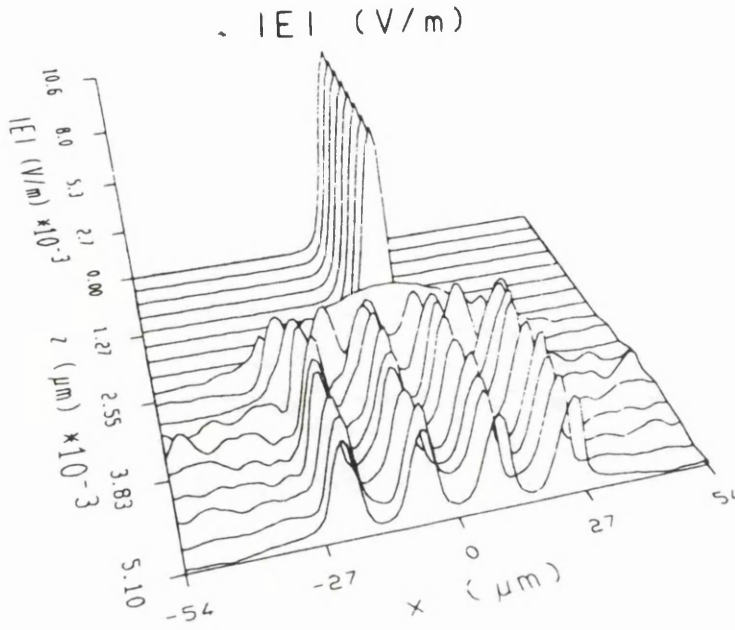


Figure 6.13 BPM simulation of 1x4 MMI coupler.

MMI couplers were fabricated with designs based on the preceding analysis (Figure 6.14).

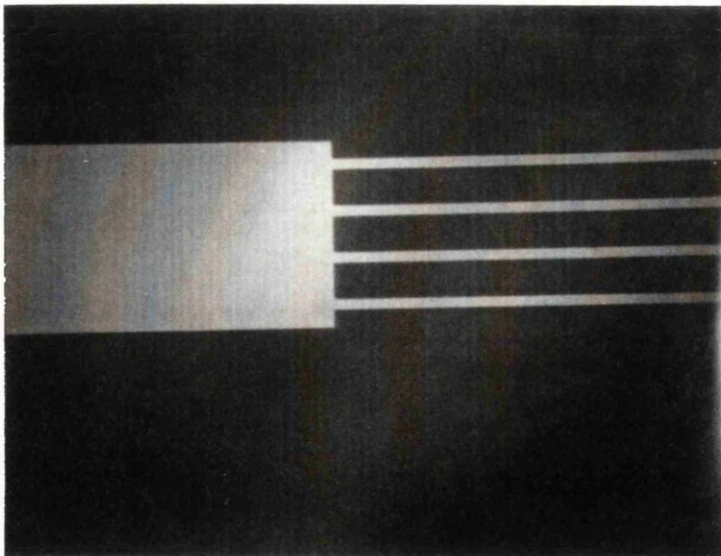


Figure 6.14 Photograph of output of 1x4 MMI coupler.

To test the MMI couplers the samples were placed in the fibre loss kit, such that the samples could be aligned in the visible and subsequently tested in the infra-red. A fibre-

pigtailed laser diode at 1.54 μm was butt coupled against the waveguide input and the resulting output measured on an infra-red sensitive camera. However, when measuring the outputs it was not possible to resolve each output, independently. The major problem seemed to be the output waveguide spacing for the devices from centre to centre was only 15 μm such that the edge to edge spacing between the 6 μm output waveguides was 9 μm . It is hoped that further work can be conducted to test such devices with adequate output waveguide separation.

6.4.2 Ring resonators

A ring resonator, whether in its integrated¹⁷ or fibre-loop form¹⁸, is a useful optical device that can allow high power confinement at resonance frequencies and act as wavelength (or frequency) filter with considerably high selectivity. Essentially a resonant cavity formed by a closed channel waveguide ring or a fibre-loop, the ring resonator has found diverse usage in optical telecommunications, lasers and lensing applications. During the studies particular interest was paid to passive ring resonators for linewidth control of an Er^{3+} doped fibre laser and an integrated Nd^{3+} doped silica planar ring resonator. Ring resonators on planar silica are compatible with fibres and can be accurately fabricated to produce compact and rugged devices for narrow linewidth output.

A fibre ring resonator generally involves a coupling section between two fibres with one fibre forming a closed loop. The coupling section in fibre form, is extremely fragile and sensitive to twists, bends and tensioning, such that it is necessary to carefully package. As a result the resonator length is limited. For the integrated device the minimum resonator length is determined by the refractive index difference between the core and clad. Usually, radiation losses for straight waveguides are negligible for well-confined modes that are from cut-off. However, because of the distortions in the optical field as guided waves travel through a bend, radiation (bending) losses become significant. Bending losses can be reduced by increasing the refractive index difference, such that the field is better confined. Also, losses due to bending will decrease as the radius of curvature is increased. For, silica waveguides with $\Delta n = 0.25\%$ the minimum bending radius (radius at which the bending loss is negligible) is 25 mm, whereas waveguides with $\Delta n = 0.75\%$ the minimum bending radius is 5 mm. Consequently, the devices with a refractive index of 0.75% were fabricated with a radius of 7.5 mm for the s-bends and ring itself. The total length of the ring resonator was 10.7 cm.

For a ring resonator it is preferable if it has a wide free spectral range (FSR), a high finesse (F) for good wavelength selectivity, high extinction ratio for low crosstalk and low insertion loss¹⁹. The FSR is given by:

$$f_{\text{FSR}} = \frac{c}{n_{\text{eff}}L} \quad (6.8)$$

where c is the light velocity, n_{eff} is the guide effective index and L is the loop path length. Hence, it can be seen that the FSR is proportional to the inverse of the path length. Therefore, the widest FSR obtainable is dictated by the minimum ring radius for a maximum acceptable value of bending losses. This was the criteria for setting the waveguide radius to 7.5 mm.

Instead of a ring structure a race-track structure was designed²⁰. This has potential disadvantages as the abrupt straight to curved transitions introduce additional losses, increased path length which results in larger losses and reduced resonance spacing. However, for a circular resonator the input guide follows the ring concentricity for a fraction of the circumference. As a result, the coupler section is highly asynchronous due to the differing radial positions of the two guides. A solution to this is to increase the refractive index of the resonator section, or to form a vertical integrated ring resonator²¹.

The finesse (ratio of resonance spacing to bandwidth) for a ring resonator is described as

$$F = \frac{f_{\text{FSR}}}{\Delta f_{\text{FWHM}}} = \frac{\pi\sqrt{\sigma}}{1-\sigma} \quad (6.9)$$

where Δf_{FWHM} is the full width half maximum (FWHM) of the resonance peaks and σ is a function of the coupler fractional loss and the waveguide propagation loss. Consequently, to achieve a high finesse it is preferable if the coupling coefficient is low and the loss of the resonator is low.

The ring resonator structure was designed taking into consideration the points given above. Figure 6.15 illustrates the final design of the ring resonator. The waveguide dimensions were $7 \times 7 \mu\text{m}^2$. The resonator was designed with two coupling sections such that the output from the first coupler could be employed for monitoring the response. For ease of fabrication the coupler sections were designed with a separation of $4.5 \mu\text{m}$ from edge to edge (pitch of $11.5 \mu\text{m}$). To estimate the coupling coefficients for such devices, assuming a wavelength of $1.55 \mu\text{m}$, theoretical studies were based

on the Kumar method²². Once values had been obtained simulations on the BPM design package were conducted for the coupler sections. Figures 6.16 and 6.17 indicate 3-D contour plots for the coupler section with a power transfer of 20% for the upper plot and a power transfer of 70% for the lower plot. As a result it was possible to tabulate the power transfer for different values of coupling lengths.

Coupling length, l (mm)	Power transfer at 1.55 μm
2	20%
3	34.1%
4	53.2%
4.5	62.5%
5	71.4%

Table 6.1 Coupling length vs Power Transfer

Owing to the size of the resonator structures it was only possible to accommodate three resonators (coupling lengths of 3, 4 and 5 mm) on the 3" Si wafer, as well as a few directional couplers and straight waveguides for characterisation.

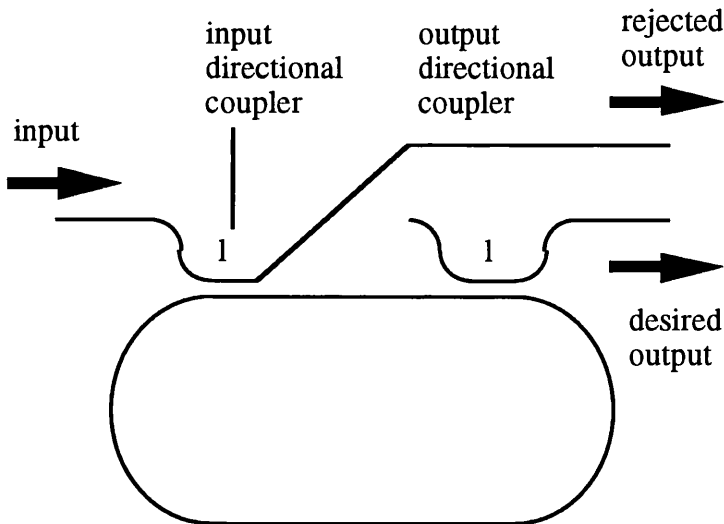


Figure 6.15 Schematic of ring resonator design.

The resonators were fabricated employing the usual procedures. The halides were tailored such that an index difference of 0.75% was achieved. Standard photolithographic techniques and a CHF_3 RIE were then used to form $7 \times 7 \mu\text{m}^2$ channel waveguides. A $20 \mu\text{m}$ thick $\text{SiO}_2\text{-P}_2\text{O}_5\text{-B}_2\text{O}_3$ cladding layer with a refractive

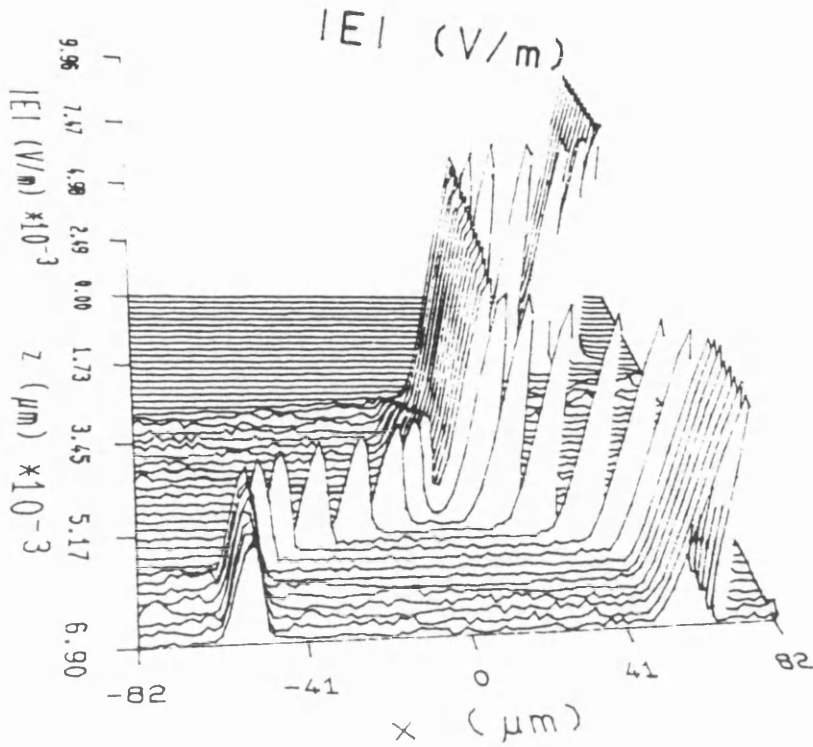


Figure 6.16 BPM simulation for directional coupler with coupling length of 2mm.

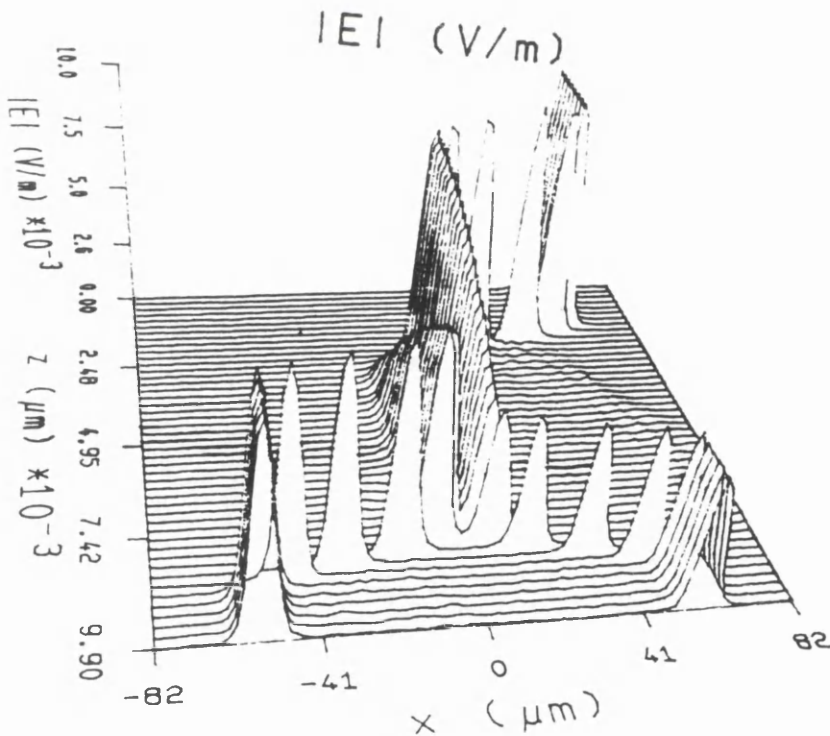


Figure 6.17 BPM simulation for directional coupler with coupling length of 5mm.

index matched to that of the buffer layer was then formed by FHD. Finally, the waveguides were cut to a length of 5 cm.

To test the produced devices the samples were transferred to Dr N. Langford of the Department of Physics, Strathclyde University, since they possess a suitable narrow linewidth source. Unfortunately, at the point of writing measurements have not been carried out. It is hoped that resonators will be tested and results reported.

Another resonator configuration has been designed to form a Nd³⁺ doped silica planar waveguide laser. Figure 6.18 illustrates the basic design. Points of particular interest are the wavelength division multiplexing (WDM) directional coupler and the intersection. The resonator design was based on an open loop form²³ such that the coupler was designed to have a low coupling ratio at the pump wavelength (20%) and a high ratio at the signal wavelength (98%). This was so the pump light at 804 nm propagates into the ring resonator and excites the Nd³⁺ ions, while a small fraction of the 1050 nm light is extracted from the resonator. It was also necessary, to adopt this design as the coupling length at 804 nm for the waveguide parameters is extremely long (11.6 cm) for the pump wavelength. The intersection was also necessary to extract the output light. To reduce the cavity loss created by the intersection it was designed to have an intersection angle of 62.19⁰²⁴. Once again coupling lengths were estimated employing the Kumar method followed by BPM simulations. For the structures, the waveguide dimensions were 6x6 μm² and the waveguide separation was 4 μm edge to edge (pitch 10 μm). For low losses the resonator was also designed with radii of 7.5 mm.

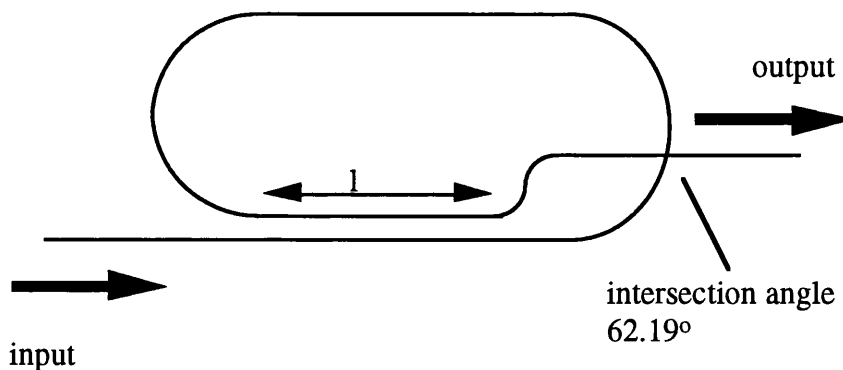


Figure 6.18 Schematic of ring resonator design.

Once again due to time constraints it was only possible to design the structures. However, a mask with the relevant structures is due to be produced in the foreseeable future. A possible addition to the resonator is to selectively dope the structure such that the coupling section and the output waveguide is designed to be passive whilst the majority of the ring is active to produce sufficient gain for lasing at 1.05 μm.

References

- 1 Kawachi M., *Opt. and Quant. Electron.*, 1990, **22**, 391.
- 2 Kashyap R., Wyatt R. and McKee P. F., *Electron Lett.*, 1993, **29**, 1025.
- 3 Maxwell G. D., Kashyap R., Sherlock G., Collins J. V. and Ainslie B. J., *Proc. IEE - 'Planar Silicon Hybrid Optoelectronics'*, London, 1994.
- 4 Yi-Yan A., Wilkinson J. A. H. and Wilkinson C. D. W., *IEE Proc.*, Pt. H, 1980, **127**, 335.
- 5 Ishii M., Hibino Y., Sugita A. and Tamamura T. *Electron Lett.*, 1993, **29**, 1684.
- 6 Kogelnik H., *Theory of Dielectric Waveguides in Topics in Applied Physics*, **7**, Integrated Optics, Springer Verlag, 1975.
- 7 Hill K. O., Fujii Y., Johnson D. C. and Kawasaki B., *Appl. Phys. Lett.*, 1978, **32**, 647.
- 8 Kashyap R., *Optical Fibre Techn.*, 1994, **1**, 17.
- 9 Maxwell G. D., Kashyap R., Ainslie B. J., Williams D. L. and Armitage J. R., *Electron Lett.*, 1992, **28**, 2106.
- 10 Hill K. O., Bilodeau F., Malo B., Albert J., Johnson D. C., Hibino Y., Abe M. and Kawachi M., *Opt. Lett.*, 1993, **18**, 953.
- 11 Lemaire P., Atkins R. M., Mizrahi V. and Reed W. A., *Electron. Lett.*, 1998, **13**, 1191.
- 12 Kitagawa T., Bilodeau F., Malo B., Thériault S., Albert J., Johnson D. C., Hill K. O., Hattori K. and Hibino Y., *Electron Lett.*, 1994, **30**, 1311.

- 13 Ramussen T., Lumholt O., Polvsen J. H. and Bjarklev A., *Electron. Lett.*, 1993, **29**, 455.
- 14 Armitage J. R., *Appl. Opt.*, 1988, **27**, 4831.
- 15 Bebbington J. A., Barbarossa G., Bonar J. R. and Aitchison J. S., *Appl. Phys Lett.*, 1993, **62**, 337.
- 16 Heaton J. M., Jenkins R. M., Wright D. R., Parker J. T., Birbeck J. C. H. and Hilton K. P., *Appl. Phys. Lett.*, 1992, **61**, 1754.
- 17 Adar R., Shani Y., Henry C. H., Kistle R. C., Blonder G. E. and Olsson N. A., *Appl. Phys. Lett.*, 1991, **58**, 444.
- 18 Ezekiel S. and Balsamo R., *Appl. Phys. Lett.*, 1977, **30**, 478.
- 19 Stokes L. F., Chodorow M. and Shaw H. J., *Opt. Lett.*, 1988, **27**, 4104.
- 20 Walker R. G. and Wilkinson C. D. W., *Appl. Opt.*, 1983, **22**, 1029.
- 21 Suzuki S., Shuto K. and Hibino Y., *IEEE Photon. Techn. Lett.*, 1992, **4**, 1256.
- 22 Kumar A., Kaul A. N. and Ghatak A. K., *Opt. Lett.*, 1985, **10**, 86.
- 23 Kitagawa T., Hattori K. Hibino Y., Ohmori Y. and Horiguchi M., *Proc. ECOC'92, Berlin, 1992*, **3**, 907.
- 24 Kominato T., Kitoh H., Katoh H., Hibino Y. and Yasu M., *Technical Digest of Fourth Optoelectronics Conference, 1992*, **16B4-1**.

Chapter 7 Conclusions and future work

7.1 Conclusions

The work carried out on this project has been concerned with the application of FHD technology, for fabricating planar silica devices. The devices of particular interest were rare earth doped silica waveguide laser structures. To achieve these goals, material and processing parameters were investigated to provide low loss, inexpensive and high yield devices.

The FHD system was developed to provide increased flexibility and reproducibility. A heater below the turn table was installed to provide accurate temperature control of the substrate. The deposition chamber was coated with Xylan and the equipment within the chamber designed to withstand the residual HCl, to prevent particle contamination. A localised extract provided a stable and uniform deposition, preventing fluctuations in the parameters such as thickness and index uniformity. Fused quartz torches of various designs were developed for both passive and active depositions. An extra port was incorporate to act as a shroud providing directionality to the flame and reducing the temperature of the torch nozzle to prevent the risk of surface defects. The residual HCL was safely disposed of, with a closed loop scrubber unit deigned and installed. Steps are now in progress to house the deposition laboratory in a class 10,000 clean room.

A horizontal loading furnace enabled batch loading of devices, to provide accurate test devices. Contamination problems from the devitrification of the fused quartz furnace tube were decreased by regular replacement of the liners and placing samples below Si wafers for protection. Helium and oxygen were transported to the furnace to provide different sintering atmospheres.

To incorporate rare earth dopants into the glass matrix phosphosilicate glasses were fabricated by FHD. It was realised at an early stage that it was necessary to have as high as possible phosphorous pentoxide level, to increase the solubility of the rare earth ions. The optimum fusing conditions of high temperatures and short durations also constrained the deposition parameters¹. Problems inherent in the glass system were subsequently encountered and solutions established. The flame temperature and substrate temperature were optimised to reduce the diffusion of P₂O₅ from the silica

Chapter 7 Conclusions and future work

matrix and at the same time provide the deposited soot with sufficient mechanical strength to prevent oxide particles flaking off. Sintering conditions were also adapted to provide low loss, bubble free planar waveguides.

Suitable cladding material for high phosphorous pentoxide silica cores were investigated. To provide material with thick, low sintering temperatures and refractive indices matched to that of the thermal oxide buffer layer, $\text{SiO}_2\text{-P}_2\text{O}_5\text{-B}_2\text{O}_3$ layers were fabricated. Residual gas trapping and diffusion of B_2O_3 were highlighted. To prevent bubbles caused by gas trapping, suitable sintering conditions were developed. The discontinuity at the cladding and thermal oxide layers was reduced by tailoring the temperature of the flame. It was also highlighted the variation in refractive index for the samples final temperature on removal from the furnace.

A standard set of procedures were adopted to test the homogeneity of planar film thickness and refractive index. Prism coupler measurements as well as the Pliskin etch highlighted a 17% variation in thickness across a 3" wafer. However, the inhomogeneity in the refractive index was below 0.1%. By controlling the torch traversal speed it was possible to reduce the film thickness variation to 6%. The prism coupler measurements found that the film refractive index was proportional to the halide flow rates. Of particular importance, the prism coupler provided qualitative information pertaining to the planar sample losses. Using this simple technique it was possible to decide which samples were suitable for further processing, without having to rely on more involved techniques such as the three prism technique.

To fabricate channel waveguides standard photolithographic techniques were employed. A low pressure CHF_3 etch was generally used and provided low loss channel waveguides with reduced etch wall roughness. It also reduced the redeposition of non-volatile rare earth products. The major drawback was the slow etch rate of $2.1 \mu\text{m/hr}$. To overcome this hurdle without compromising the etch quality further etching processes were tested. A high power C_2F_6 plus O_2 etch process to increase the fluoride to carbon ratio did increase the etch rate, however a suitable mask was not found. An etch rate of $7.8 \mu\text{m/hr}$ was achieved employing a high power CHF_3 plus C_2F_6 etch. To etch a depth of $8 \mu\text{m}$ it was necessary for a NiCr mask of 2000 \AA to be deposited onto the sample. This thickness posed problems and as a result the resolution of the process was limited to $2 \mu\text{m}$.

An optical microscope was installed on the Loadpoint machine to enable accurate cutting of waveguides. Provided cladded waveguides were processed a resinoid blade provided facets with polished quality in a fraction of the time. The versatility of the

Chapter 7 Conclusions and future work

system allowed channel waveguides of widths approximately 25 μm to be defined, alleviating the extra procedures necessary for channel waveguide fabrication. This was beneficial for quick assessment of rare earth doping levels using a broadband white light source.

To provide swift analysis of channel waveguides, a fibre loss kit was developed. This provided insertion loss measurements at point wavelength sources of 632.8, 1317 and 1553 nm. Spectral measurements were also possible using the white light source. Insertion losses for 5.8 cm long rare earth doped channel waveguides were measured to be as low as 1.5 dB at 632.8 nm.

Rare earth doped $\text{SiO}_2\text{-P}_2\text{O}_5$ films were fabricated using two techniques, namely solution and aerosol² doping. Both techniques were adapted from the fabrication of rare earth doped fibres. However, owing to the shorter lengths experienced on a planar format, a larger concentration of the rare earth was necessary to produce waveguide lasers.

To optimise the solution doping process it was necessary to determine the conditions necessary to incorporate the rare earth ions into the glass matrix in a reliable and uniform manner. The in-plane and out-of-plane scatter were minimised by providing a structure partially fused at 925 °C for 10 minutes and which was carefully dried after immersion in the rare earth solution.

Aerosol doping a novel technique, developed during the course of the project, enabled rare earth ions to be incorporated directly. Thus, avoiding the extra steps necessary for solution doping. To produce uniform depositions with adequate doping levels it was necessary to tailor the deposition parameters. The N_2 gas flow used to nebulise and transport the rare earth aqueous solution was maintained at 3 l/min providing a delivery rate of 0.15 ml/min, whilst not compromising the flame shape. The doping concentration incorporated into the glass was dependent on the solution strength. To prevent condensing of rare earth ions before the reaction zone, a novel torch design was developed. When the aerosol was introduced to the reaction the refractive index difference in relation to the substrate was lower by approximately 10 %. Moreover the film thickness was reduced by 15 %. The differences were due to the flame being cooler and subsequently inhibiting the hydrolysis.

Loss measurements of rare earth doped films were investigated using the prism coupler technique. The qualitative measurements highlighted propagation loss as a function of fusing temperature. For a sample with an Er^{3+} concentration of 0.36 wt%, with a

Chapter 7 Conclusions and future work

relative index difference of 0.75 % between film and substrate, the propagation loss was ~2 dB/cm when fused at 1250 °C. For a similar structure fused at 1375 °C the propagation loss reduced to below 0.5 dB/cm. The loss decreased as a result of the decreased volume scattering.

To deduce doping levels and doping homogeneity of Nd³⁺ and Er³⁺ doped SiO₂-P₂O₅ channel waveguides fluorescence, absorption and fluorescence lifetime measurements were obtained.

Doping levels of channel waveguides, formed by cutting ridges, were measured by correlating data from the absorption peaks to extinction coefficients. Fluorescence measurements detailed the emission peak wavelengths. Irrespective of doping technique or level, the salient feature was the effect of the high P₂O₅ concentration. This resulted in the emission peaks being shifted to shorter wavelengths.

Of particular importance was the codoping of Al³⁺ for aerosol doped samples. Even although the maximum Al³⁺ doping level was 0.04 wt%, the FWHM was increased to 24 nm for the Nd³⁺ ⁴F_{3/2}-⁴I_{11/2} transition. The fluorescence and absorption peaks for rare earth doped SiO₂-P₂O₅ films were also moved to shorter wavelengths. Similar solution doped samples codoped with Al³⁺ concentrations of 2 wt% exhibited no change in spectral response compared to rare earth doped SiO₂-P₂O₅ films. Consequently, it was postulated that the Al³⁺ ions were incorporated into the glass matrix in a more homogeneous manner using the aerosol technique.

Fluorescent lifetime measurements provided important information pertaining to the effective lifetime of the upper lasing level. Much of the work concentrated on Er³⁺ doped SiO₂-P₂O₅ samples. However, measurements of the Nd³⁺ system did provide typical lifetime measurements of 300 μs.

The differential of the natural logarithm was measured to highlight ion-ion interactions for the Er³⁺ system. The slow decay component was observed to be 5 ms, whilst the fast decay component became more pronounced for increased Er³⁺ levels³. Aerosol doped samples incorporating Al³⁺ provided the greatest reduction in the fast decay component, without seriously reducing the etch rate⁴. Similar results were witnessed for solution doped samples, however, the Al³⁺ doping level was larger and had the undesired effect of reducing the etch rate.

Nd³⁺ doped planar waveguide lasers at 1.05 μm, were fabricated using both the solution⁵ and aerosol⁶ doping techniques. CW oscillation was achieved for 0.38 and

Chapter 7 Conclusions and future work

0.5 wt% Nd³⁺ solution doped SiO₂-P₂O₅ channel waveguides. For the former, the lasing threshold was 20 mW of absorbed power and the slope efficiency was recorded to be 2.6 %. Output powers of over 1 mW were also measured. Similar devices have been reported by NTT, however the devices exhibited higher thresholds and lower slope efficiencies. A model was also developed to determine the optimum power extraction efficiency as a function of the output pump mirror reflectance. Subsequently, an output mirror with a reflectance of 80 % was butted to the waveguide output, producing an increased slope efficiency of 10 %⁷. The higher solution doped SiO₂-P₂O₅ channel waveguides provided output powers greater than 2 mW, but measurements were restricted owing to the limited pump powers available.

Nd³⁺ aerosol doped SiO₂-P₂O₅ channel waveguide lasers were reported for the first time. Al³⁺ was also used as a codopant. The lasing threshold was 22 mW and the slope efficiency was recorded to be 2.5 %. However, without further analysis it is still not possible to determine which doping regime is superior, although it would appear that the aerosol method is a good alternative to solution doping.

An Er³⁺ solution doped SiO₂-P₂O₅ channel waveguide laser at 1.534 μm was fabricated. The doping level was 0.3 wt% and the length of the cavity was 33 cm based on a spiral design. To achieve lasing it was necessary to have high reflectivity mirrors at both input and output. As a result, the lasing threshold was only 23 mW absorbed power whilst the slope efficiency was 0.04 %. Researchers at NTT observed lasing for higher doped waveguides with a reduced waveguide length. Although, a better performance was reported, the lasing did not take place at the peak of the fluorescence but rather at 1.6 μm due to reabsorption effects.

A major drawback in fabricating the waveguide lasers was the method of providing feedback implementing external dielectric mirrors. To provide monolithic integrated waveguide lasers, grating structures acting as Bragg reflectors were investigated. Two techniques (holographic and electron beam writing), were used to form gratings over selective areas of the substrate. The gratings were defined into the substrate due to problems encountered for dopant diffusion in cladded waveguides. However, photosensitive gratings have been successful in providing Bragg reflectors for both SiO₂-GeO₂ fibre and waveguide technologies. As a result SiO₂-GeO₂ doped waveguides were exposed to an KrF laser and produced an index increase of 5x10⁻⁴. It is expected that hydrogen treating the waveguides will increase the photosensitivity.

Both the solution and aerosol techniques were used to form regional and vertical selective area doping of planar waveguides. Although, the aerosol doping provided the

Chapter 7 Conclusions and future work

possibility of one step processing the boundaries were not as distinct as one might hope. This was resolved by using multi-step procedures. A possible application is to have photo-induced Bragg gratings on the $\text{SiO}_2\text{-GeO}_2$ passive section integrated with a rare earth doped active section.

To emphasise the versatility of silica-on silicon waveguides, passive waveguides were investigated. Multi-mode interference couplers, ring resonators and pressure sensors⁸ were fabricated using FHD and RIE.

In conclusion, rare earth doped waveguide lasers have been fabricated employing both the solution and aerosol doping techniques⁹. Such devices have the potential for applications in future all optical communications networks, for both local and wide area networks.

7.2 Future work

Within the report many potential areas for future work have been proposed. To increase the yield of the planar fabrication process, a major up-grade to the deposition laboratory is now almost complete.

Material analysis to understand the $\text{SiO}_2\text{-GeO}_2\text{-B}_2\text{O}_3$ system is still necessary. Factors such as deposition parameters (substrate temperature etc.) and fusing conditions (atmosphere etc.) have still to be optimised. This will have significance for future photosensitive devices. It is imagined that waveguide structures will be able to be defined by exposing to UV light, thus eradicating the need to RIE certain waveguide structures.

Interdiffusion between the core and cladding material was observed during the course of this project. A possible solution was to deposit a SiO_2 capping layer on the channel waveguides before depositing the cladding layer. Analysis is still to be determined to the success in preventing the diffusion of the P_2O_5 . Failing this, trenches could be formed in the buffer layer by RIE and the subsequent core material deposited on top. Owing to the viscous nature of the deposited glass it would flow into the trenches to minimise the surface area. The residue of core layer on top of the waveguide would either be removed by RIE or optical polishing.

To form an integrated waveguide laser employing passive Bragg reflector sections and a rare earth doped section is still to be realised. The ease of forming selective area

Chapter 7 Conclusions and future work

doped sections has been shown. It is envisaged that photosensitive gratings will be able to produce the required feedback for both the Nd^{3+} and Er^{3+} systems.

Another key device for future development is a transparent 1xN splitter. An active section would provide the required amplification to compensate for the splitting losses. The active section would provide suitable increased signal gain by incorporating a coil path design for waveguides of longer length. The splitter itself would be formed from Y-branches, directional couplers or MMI couplers. Another device, would be to incorporate a passive waveguide division multiplexer for a long length waveguide amplifier, enabling the multiplexing of the pump and signal wavelengths.

More analysis should be carried out to compare the solution and aerosol doping techniques. In particular, doping homogeneity of the rare earth ions should be determined by measuring the fraction of clustered ions for samples of similar composition and thermal history. For aerosol doping other codopants such as La^{3+} , Yb^{3+} and Ga^{3+} to reduce the ion-ion interactions could be investigated.

Gain measurements as a function of doping concentration have still to be determined. It has already been established that the amplifier efficiency is reduced for very high rare earth concentrations. Consequently, to optimise the optical gain it is necessary to compare the trade-off between the loss and the rare earth concentration.

Ring resonator designs, for narrow linewidth and laser applications have been detailed in the report. The resonators have still to be characterised and could provide suitable planar lightwave circuit devices for all optical telecommunications.

Signal processing circuits incorporating elements such as delay lines are feasible using FHD and RIE. These devices require long lengths of low loss waveguides. By forming relatively high Δn waveguides it is possible to achieve small bend radii for spiralled waveguide designs and subsequently compact devices.

References

- 1 Bonar J.R., Bebbington J.A. and Aitchison J.S., Proc. IPR, Dana Point, 1995.
- 2 Bebbington J.A., G.Barbarossa, Bonar J.R. and Aitchison J.S., Appl. Phys. Lett., 1993, **62**, 337.
- 3 Bonar J.R., Bebbington J.A., Aitchison J.S., Maxwell G.D and Ainslie B.J., Proc. IEE - 'Planar Silicon Hybrid Optoelectronics', London, 1994.
- 4 Bonar J. R. and Aitchison J. S., to be submitted for publication in Appl. Phys. Lett.
- 5 Bonar J.R., Bebbington J.A., Aitchison J.S., Maxwell G.D and Ainslie B.J., Electron. Lett., 1994, **30**, 229.
- 6 Bonar J.R., Bebbington J.A., Aitchison J.S., Maxwell G.D and Ainslie B.J., Electron. Lett., 1995, **31**, 99.
- 7 Bonar J.R., Bebbington J.A., Aitchison J.S., Maxwell G.D and Ainslie B.J., Proc. CLEO, Anaheim, 1994.
- 8 Taneya Naya A., Bonar J.R., Bebbington J.A., De La Rue R. M. and Uttamchandani D., Proc. IEE - 'Microengineering and Optics', London, 1994.
- 9 Bonar J. R. and Aitchison J. S., to be submitted for publication in IEE Proc. Special Issue On Guided-Wave Optics On Silicon.